ABSTRACT

Title of dissertation: SOLID OXIDE FUEL CELL AND
GAS TURBINE HYBRID CYCLES
FOR AEROSPACE POWER AND PROPULSION

Lucas Pratt
Doctor of Philosophy, 2022

Dissertation directed by: Professor Christopher Cadou
Department of Aerospace Engineering

Hybrid propulsion systems combining gas turbine and solid oxide fuel cells (GT/SOFCs) have the potential to substantially reduce carbon emissions from 737-class aircraft. Many turbine/fuel cell hybrid cycles have been proposed for ground-based energy conversion at the utility scale, and some work has investigated small-scale (<500 kW) fuel cell-based energy conversion systems for aircraft (mostly auxiliary power units). However there is relatively little known about large hybrid engine/fuel cell systems capable of providing main propulsive power in large (i.e. 737-class) aircraft. This work takes several important steps toward filling this gap.

First, it develops an analytical model of a GT/SOFC system that provides insight into the trends and tradeoffs associated with varying design parameters across a wide design space. Key insights that emerged from this modeling effort are: a) Increasing the fraction of fuel processed by the fuel cell always increases efficiency. b) A tradeoff between fuel cell efficiency and specific power determines the optimum range of the vehicle. This tradeoff is heavily influenced by the polarization curve

of the SOFC. This optimum operating point is different from the maximum power point. c) The GT/SOFC could be used to increase the cycle's flow specific work, enabling a smaller core to drive the same size fan. This premise is investigated in more detail later in the thesis. d) The fraction of fuel processed by the fuel cell is limited by the ability to cool it. An analytical expression for this limit is derived but in general the maximum power output of the fuel cell is limited to less than half of the total system power output for most hybridization schemes.

Second, this work develops an improved thermodynamic model of the hybrid turbine and fuel cell system. The model accounts for off-design performance of the turbomachinery as well as sufficient details of the transport and electrochemistry in the fuel cell to predict the effect of specific design changes (physical dimensions, flow rates, pressure, temperature, etc.) and operating conditions on power output, energy conversion efficiency, and system mass. The model is implemented using a NASA-developed tool called Numerical Propulsion System Simulation (NPSS) that is emerging as a standard in modern engine development. While third-party NPSS fuel cell modules are available, they are not suitable for fuel cell design because key performance parameters like utilization, efficiency, and specific power are inputs. Our module predicts fuel cell performance from its geometric attributes (channel length, width, height, number) and electrochemical attributes (i.e. temperature, pressure and composition effects on the polarization curve). Such capability is computationally expensive but essential for predicting GT/SOFC performance over varying flight conditions. This work implemented a) 'guardrails' to prevent solver divergence due to self-reinforcing high or low temperatures, b) an adaptive Newton-solver damping scheme to improve convergence, c) an electrochemical performance map to find close initial conditions, and d) the option for methane as an additional fuel, amongst other alterations. Taken together, these changes reduced execution time from weeks to hours and greatly improved stability making the thermodynamic model a much more useful tool for design and analysis.

Third, the NPSS system model is used to assess the viability of two possible hybridization schemes. The first is a 'parallel' hybrid system where an SOFC powers an electric motor that assists the turbine in driving the main fan. The second is a 'turboelectric' hybrid system where all of the propulsive power is provided electrically by a fuel cell working in tandem with a mechanical generator attached to the gas turbine. The results show that a parallel hybrid can reduce fuel consumption by 27%, but requires a reformer/fuel cell that achieves $> 1\text{kW}\,\text{kg}^{-1}$ to achieve range parity with a conventionally-powered B737. This occurs because the thermodynamic efficiency of the system increases by 10% and the propulsive efficiency increases by 10% due to the higher bypass ratio made possible by the increase in flow specific work associated with hybridization. The turboelectric system reduces fuel consumption by 12% when 25% of power is generated by the SOFC, but requires a reformer/fuel cell that achieves $> 1.2\text{kW}\,\text{kg}^{-1}$ to achieve range parity with a conventionally-powered B737. This higher specific power requirement occurs because the gas turbine operates at a lower $OPR = 15$ vs. $OPR = 24$ to enable recuperation via a heat exchanger. The heat exchanger also improves the thermodynamic performance of both the Brayton cycle and the SOFC (by reducing preheating requirements) even at 30% effectiveness, but adds mass and complexity.

Fourth, this work investigates the potential impacts of introducing the fuel cell exhaust—which is hot and contains large amounts of water and combustible reformate—on the Brayton cycle. The system modeling efforts show that the fuel cell exhaust can constitute up to 70% of the total mass flow rate through the system and up to 50% of the total net heat release. Therefore, the effect of the fuel cell exhaust on the operation of the main combustor is expected to be substantial both for integration with traditionally injected fuels, and influencing trades for the SOFC subsystem design choices that affect that exhaust (e.g. fuel utilization). Subsequent chemical kinetic simulations implemented in Cantera show that SOFC exhaust adiabatic flame temperatures can reach as high as 2200K, laminar flame speeds may vary by as much as 500% across a range of fuel utilization targets, ignition delay times with hydrocarbon/air mixtures can reach the millisecond range, and mixed SOFC exhaust can achieve extinction strain rates of over 300,000s^{-1} in pressures reasonable for gas turbines. These results suggest that aircraft GT/SOFCs may also require new combustor designs for effective hybridization.

SOLID OXIDE FUEL CELL AND GAS TURBINE HYBRID CYCLES FOR AEROSPACE POWER AND PROPULSION

by

Lucas Merritt Pratt

Dissertation submitted to the Faculty of the Graduate School of the
University of Maryland, College Park in partial fulfillment
of the requirements for the degree of
Doctor of Philosophy
2022

Advisory Committee:
Professor Christopher P. Cadou, Chair/Advisor
Professor Raymond J. Sedwick
Professor Kenneth H. Yu
Professor Chunsheng Wang
Professor Eric D. Wachsman

Dedication

For Muñeca and Samson.

Acknowledgments

As with most large projects spanning years of effort, this dissertation involved substantial assistance from many different parties.

First I must thank the members of my committee that reviewed and approved this dissertation, both for their direct work here as well as their prior guidance in classwork (Dr. Yu, Dr. Sedwick, Dr. Wang) and research collaborations (Dr. Wachsman). They have all made indelible marks on my thought processes as an engineer and scientist. In particular though, I thank my advisor Dr. Christopher Cadou for his tutelage, support, and example over the years, as well as his efforts to bring this specific work to fruition.

However, both my classwork and research would not have been possible without the aid and comraderie of my labmates; Colin Adamson, Wiam Attar, Steven Cale, Andrew Ceruzzi, Branden Chiclana, Daanish Maqbool, Stephen Vannoy, Carnell Bolden, and Chris Lamb. I also appreciate the efforts of my direct predecessor on this line of inquiry, Dan Waters, on whose shoulders I stand most firmly.

Additionally, I want to recognize the support of the undergraduates I worked with closely during this project; Kyle Spawn, Lizo Odharo, Ben Robinson, Bradley Harris, Jerry Liu, Bafoday Koroma, and Nikolai Smith. Thank you for the opportunity to teach you all.

Outside the University of Maryland, I want to thank Tom Lavelle at NASA Glenn for his help in getting my footing with NPSS, and I also appreciate the discussions with (and data from!) Chuck Lents at Raytheon Technology Research

Center. I furthermore thank Dr. Gregory Jackson and Akhil Ashar at the Colorado School of Mines for their in-depth discussions of fuel cell modeling. I must also thank Dr. Mark Lewis, Dr. Bhavya Lal, and others at the Science and Technology Policy Institute for their help and encouragement in applying to this program, as well as for providing many opportunities to further develop my technical background in Aerospace prior to graduate school.

At the level of organizations, critical financial support for this research and my degree came from the Office of Naval Research (award number N000141410721), the Department of Defense through the National Defense Science and Engineering Graduate Fellowship, and the Advanced Research Projects Agency-Energy through the REEACH program.

However the most important acknowlegments must be to my friends and family. I cannot overstate the importance of their support both during this program and throughout my life. However, my wife Thanh Tran deserves acknowledgment as the single most important pillar encouragement, standing strong throughout this process of strange classtimes, long nights, and nigh-incomprehensible jargon. Thank you, and I love you.

Table of Contents

List of Tables

List of Figures

List of Abbreviations

AFT	Adiabatic Flame Temperature
AGR	Anode Gas Recirculation
BLI	Boundary Layer Ingestion
BOP	Balance of Plant
CGR	Cathode Gas Recirculation
CORSIA	Carbon Offsetting and Reduction Scheme for International Aviation
ESPG	Energy Storage and Power Generation
ESR	Extinction Strain Rate
FC	Fuel Cell
GT	Gas Turbine
HEX	Heat Exchanger
HWB	Hybrid Wing Body
ICAO	International Civil Aviation Organization
IDT	Ignition Delay Time
KE	Kinetic Energy
L/D	Lift-to-Drag Ratio
LHV	Lower Heating Value
LSM	Lanthanum Strontium Manganate
NAS	National Academy of Sciences
NASA	National Aeronautics and Space Administration
OPR	Overall Pressure Ratio
PEMFC	Polymer Electrolyte Membrane Fuel Cell
PR	Pressure Ratio
QFD	Quality Function Deployment
RPK	Revenue-Passenger-Kilometer

RSS	Root-Sum-Square
SAF	Sustainable Alternative Fuels
SL	Sea Level
SOA	State of the Art
SOFC	Solid Oxide Fuel Cell
TIT	Turbine Inlet Temperature
YSZ	Yttria-Stabilized Zirconia

Chapter 1: Introduction

1.1 Motivation[i]

This dissertation presents several different analyses of a hybridized system that combines a gas turbine engine with a solid oxide fuel cell stack for aircraft propulsion. In this first section however, we discuss why this project is worth pursuing.

At its heart, flight is a power-intensive activity that requires an aircraft to counteract the ever-present force of gravity along with progressively more and more drag from the atmosphere as an aircraft moves faster. In order to supply this power, an aircraft needs to carry some source of energy which it expends gradually—usually a fuel.[ii] As such, modern aircraft, moreso than almost any other kind of vehicle, including large naval vessels (see Figure 1.1), often devote a large proportion of their mass to carrying fuel; this proportion can reach upwards of 40% for aircraft that need to fly for long distances or periods of time [1, p. 25].

According to the second law of thermodynamics, only a portion of an energy

---

[i] A similar narrative for modern motivations and current promising technological options is available from a 2016 National Academies study on this topic [1] as well as from papers by Epstein [2], and Epstein and O'Flarity [3].

[ii] "Fuel" may be defined as an energy source that becomes part of the momentum-imparting exhaust in a propulsion system. By contrast, an energy source such as a battery weighs the same throughout its use. Unless otherwise stated, the terms "fuel" or "jet fuel" will refer to either a kerosene-analog (e.g. Jet-A) or a shorter hydrocarbon chain mixture (e.g. AVgas), which are used by nearly all modern crewed aircraft not designed to demonstrate an alternative energy source.

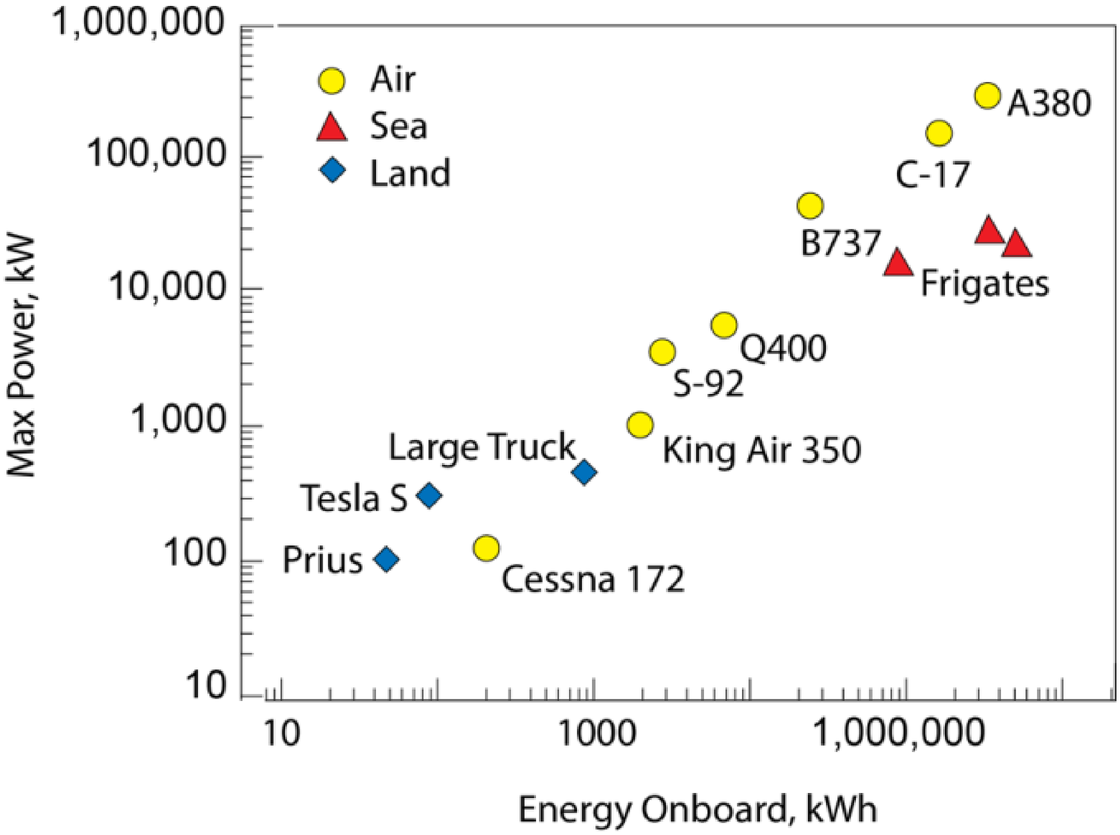

Figure 1.1: Range of vehicle energy storage and power generation capacities. Reproduced from the National Academy of Sciences, Figure 2.1 [1, p. 23].

source is converted into usable power, with the proportion of usable power to total power referred to as “efficiency.” Thus, more efficient conversion allows the use of less fuel to fulfill the same power requirements. On aircraft where these requirements are substantial, improving fuel efficiency is particularly important. Furthermore, both aircraft owners and operators as well as the world at large have practical incentives to improve fuel efficiency in order to minimize fuel usage, or “burn,” as much as possible.

For aircraft owners and operators, the first incentive relates to the cost of fuel. In 2018 alone, 95 billion gallons of fuel were purchased by the commercial airline industry [4, p. 27]. Since fuel makes up such a large percentage of their operating costs (approximately 20-30% of their annual spending from 2014-2019 [5]), fluctuations in fuel price heavily impact profit margins. Therefore, lowering the amount of fuel necessary for any particular mission—for example, carrying one hundred passengers from New York to Los Angeles within four to five hours—will reduce both the marginal costs of operation and the corresponding sensitivity to a shifting fuel price, all else being equal.[iii] Similarly, since fuel makes up a large portion of an aircraft’s carrying capacity, requiring less fuel allows this space to be allocated elsewhere. This extra space opens up possibilities for performance improvements such as increased operating range, loiter time, and flight speed, depending on operator preference. As a result, the goal of improving fuel efficiency drives technology development in what is a highly competitive industry [1, p. 3].

[iii] This statement assumes that the means by which fuel burn is reduced does not significantly affect the operating costs (whether capital costs or marginal costs via maintenance etc.) of the aircraft. This may not be realistic as the SOFC components in the GT/SOFC hybrid would likely qualify as expensive and immature.

Moving beyond the cost incentive, reducing greenhouse emissions is another major motivator for improving fuel efficiency, as the fuel burned by aircraft represents a substantial source of greenhouse gases (905 million tonnes of carbon dioxide by airlines in 2018) and other pollutants (e.g. nitrous oxides[iv]). When tallying the emissions of aircraft worldwide, including those produced by passenger airliners, cargo transports, and military aircraft, the total amount makes up approximately 2.0-2.5% of all human carbon dioxide emissions [6]. At face value, 2.0-2.5% sounds like a relatively insignificant source of emissions to focus our concern—albeit this percentage is out of an immense overall body of emissions! However, if we focus on the United States as per Figure 1.2, aircraft represent 9.3% of all transportation-related carbon dioxide emissions in the United States [7, p. ES-13]. Additionally, the air transportation sector tends to provide a market for more extreme or expensive technologies to be adapted later into other pollution-generating sectors. This tendency is due to the high performance requirements for aircraft incentivizing new approaches that may readily transfer to less immediately-demanding secondary applications. Examples of these sorts of transfers may be seen in terrestrial power generation [8].

Furthermore, various organizations such as the United Nations International Civil Aviation Organization (ICAO) have issued increasingly-stringent fuel economy and emissions standards for future aircraft that make fuel efficiency an explicit requirement for primarily profit-driven commercial operators [1, p. 15]. The most

---

[iv] Pollutants besides carbon dioxide are not *necessarily* dependent on strict energy efficiency, except insofar that their release scales with how much fuel is burned.

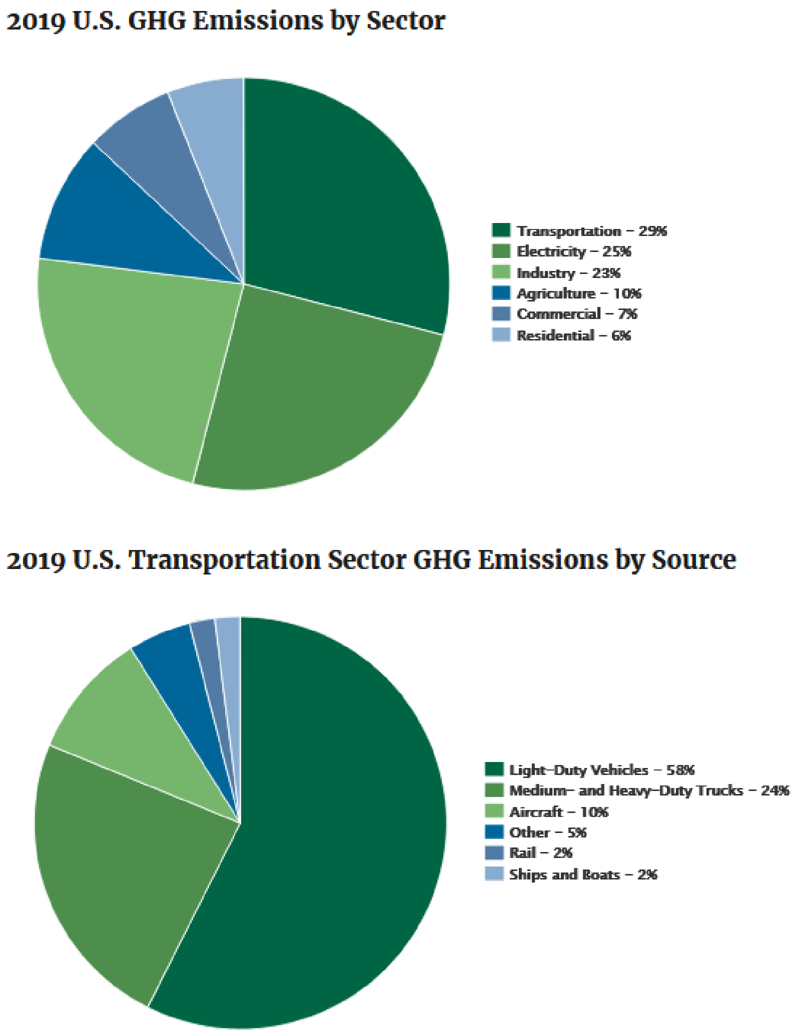

2019 U.S. GHG Emissions by Sector

2019 U.S. Transportation Sector GHG Emissions by Source

Note: Totals may not add to 100% due to rounding. Transportation emissions do not include emissions from non-transportation mobile sources such as agriculture and construction equipment. "Other" sources include buses, motorcycles, pipelines and lubricants.

Figure 1.2: United States Greenhouse Gas (GHG) emissions by overall sector (top) and transportation sector (bottom). Reproduced from the U.S. Environmental Protection Agency [9].

recent ICAO guidance, the Carbon Offsetting and Reduction Scheme for International Aviation (CORSIA) [10], established voluntary carbon-reduction standards through 2026, and mandatory standards for 2027 and beyond [4, p. 49]. Likewise, many individual nations, including the United States, have their own ever-tightening emissions standards [11, p. 13-25].

Whether to cut costs or increase performance, using fuel in an efficient and clean manner is hardly a new goal, and there has been continuous improvement in aircraft operating efficiency. Lee et. al. noted that there has been a 20-30% improvement in efficiency between successive generations of aircraft and an overall improvement of 60% from 1969-2009 in terms of carbon dioxide emissions per revenue-passenger-kilometer[v] (RPK), though much of this has come from step-change improvements in technology [6]. Similarly, the National Academies of Sciences (NAS) found an approximate 2% reduction in aircraft fuel burn per seat-mile (a metric similar to RPK) since 1970 (see Figure 1.3). About half of this improvement came from development and refinement in aircraft technology (such as weight reduction and aerodynamics) and half from performance improvements in the engines that directly burn the fuel in question. At an industry level, commercial aircraft operators have improved route planning and have optimized flying conditions (e.g. flight altitude, speed) to reduce the amount of fuel consumed, while still providing similar overall services [1, p. 22-24; 6; 12, p. 614].

These broad trends of incremental efficiency improvement will likely persist

---

[v] The metric of revenue-passenger-kilometer is used as a normalization of performance in the airline industry, specifically referring to a paying passenger (i.e. not a crew member) traveling a kilometer. For example, an aircraft emitting 10 tons of carbon dioxide to carry 10 paying passengers 100 kilometers implies using 10 tons of CO_2 for 1000 RPK, or 0.01 tons of CO_2 per RPK.

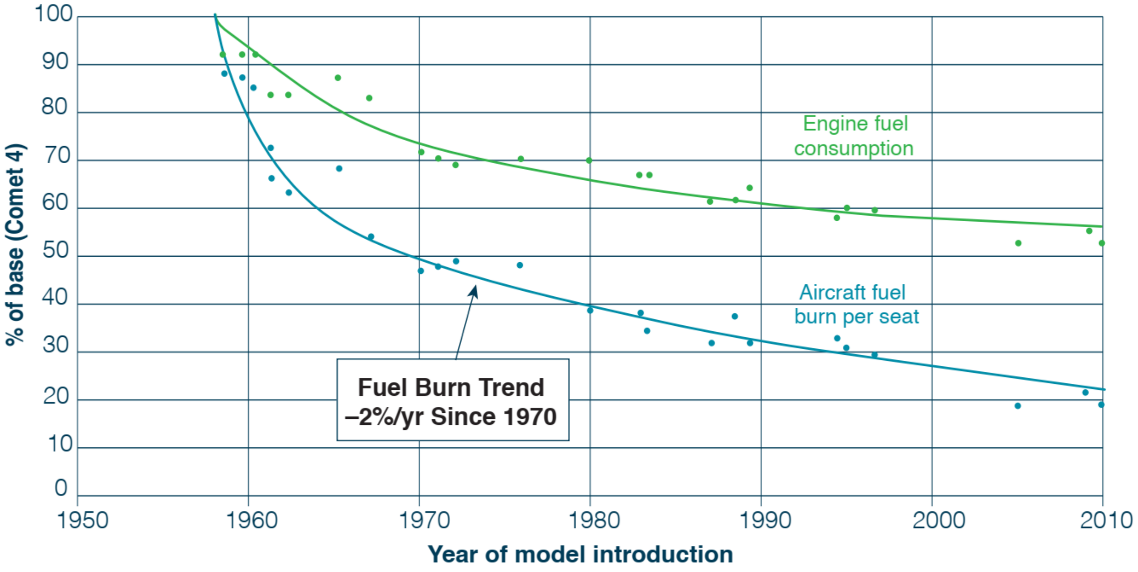

Figure 1.3: History of commercial aircraft fuel burn per seat-mile. Reproduced from the National Academy of Sciences, Figure 2.3 [1, p. 24].

into the future to further reduce marginal fuel burn (and their accompanying emissions) by the aircraft sector. However, the rate of those marginal improvements can also be expected to drop off into the future for the same class of technology. This can be seen in the efficiency trends of individual turbofan components such as high- and low-pressure compressors and turbines [13]. Another promising path for aircraft emissions reduction is the production of sustainable alternative fuel (SAF). SAFs minimize net carbon emissions by reducing the amount of "new" carbon dioxide emitted by the current use of fossil fuels, though they do not necessarily reduce fuel costs or reduce fuel burn by the aircraft [4, p. vi]. SAF candidates[vi] generally tend to be biofuels produced from an agricultural feedstock, and have been shown to be technically feasible for drop-in use on current aircraft. However, they face implementation issues, mostly pertaining to sufficient production of fuel at an economically reasonable cost, such that it is still important to reduce fuel burn as much as possible [2].

Furthermore, depending on the degree of SAF scaleup possible, SAF utilization may not be enough to meet modern emissions goals or stabilize the marginal costs of fuel for aircraft operators. The US Energy Information Administration projects a 31% increase in jet fuel consumption by 2050 as demand grows faster than expected fuel efficiency improves [7]. Unfortunately, ICAO projections of technology growth suggest that in order to achieve the CORSIA goal of carbon neutrality, the majority of any emissions reductions will need to be the result of SAF introduction and market-based measures (see Figure 1.4) [14, p. 17-19]. Given the anticipated problems with SAF scaleup, meeting the CORSIA goal will likely require beating the projected technological capabilities as much as possible.

Putting aside industry development and optimization by SAF producers and aircraft operators as important topics beyond the scope of this work, we will focus instead on the technological opportunities to reduce fuel burn. Historically speaking, tens of billions of dollars in technological investments in engines (or perhaps more abstractly, propulsion systems) have paid off, yielding improvements in both performance (two to four times power-to-weight ratio) and efficiency (up to three times) in the 50 years since the Boeing 707 was introduced [2]. Recall also from Figure 1.3 that about half of the reduction in fuel burn is from engine development specifically. As such, we will next discuss the nature of this technological improve-

---

[vi] Biofuels and other options for SAF are evaluated in part by a life-cycle analysis (LCA) to determine whether their production is an improvement—much less achieving carbon-neutrality—over traditional fossil fuels. Unfortunately, LCA processes are inconsistent and uncertain across the industry [4].

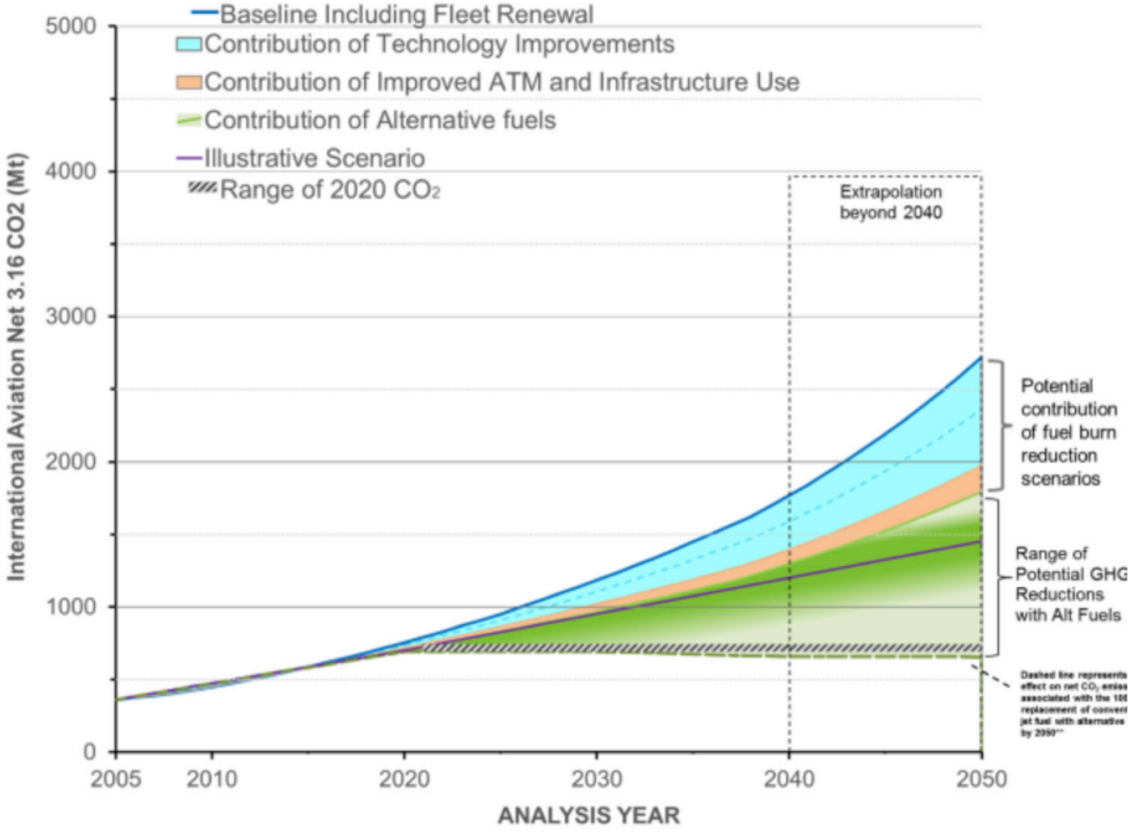

*Illustrative case would require high availability of bioenergy feedstocks, the production of which is significantly incentivized by price or other policy mechanisms

** 100% replacement of alternative jet fuel would require a complete shift in aviation from petroleum refining to biofuel production and a substantial expansion of the agricultural sector, both of which would require substantial policy support

Figure 1.4: Aircraft CO2 Emissions from International Aviation, 2005 to 2050, Updated to Include Alternative Fuels Life Cycle Emissions Reductions. Reproduced from the International Civil Aviation Organization, Figure 5 [14, p. 19].

ment, starting first with the specific considerations that are largely limited to the aircraft application. Then, we will address the broad range of different solution paths for the problem. Third, we will analyze our technology of interest—the gas turbine / solid oxide fuel cell hybrid.

1.2 Specific Considerations for Aircraft

For relatively self-contained systems like aircraft, it is important to consider propulsion systems as a whole composed of both an energy conversion system (e.g. the engine) and an energy source (e.g. the fuel and tank); both aspects have substantial impacts on overall performance. A collective term for these is an "energy storage and power generation" system, or ESPG, represented in Figure 1.5. An ESPG will have its own performance metrics of specific power and specific energy taking into account proportional sizes of each subsystem. Additional cost metrics for capital costs or fuel costs may also be considered, but will generally be beyond the scope of this work.

Appendix C provides an overview of the generic problem of designing an ESPG system for any given application. However, the specific constraints of a use case, here for aircraft, can drive technology development, and lead to different design philosophies even for fundamentally similar technologies. Without getting into the details of specialized missions for individual aircraft, we can still discuss some of the most important constraints including size and weight effects, variations with altitude, and a large propulsive power requirement that is now gradually shifting

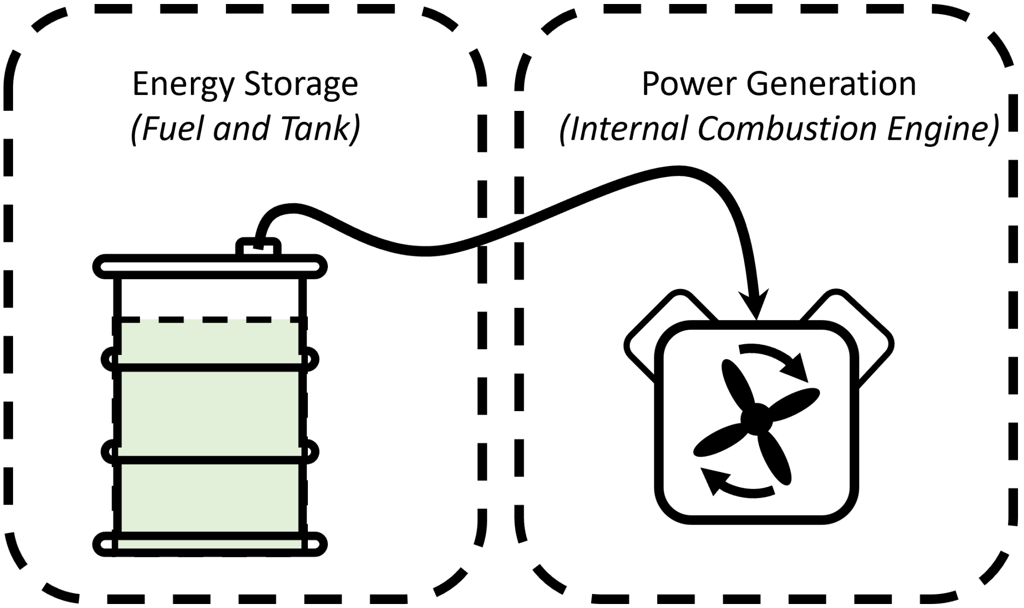

Figure 1.5: Basic ESPG Representation.

towards electrical loads.

Arguably the most important constraints on an ESPG system design for aircraft are the mass and volume they require. Unlike most ground-based vehicles, the performance (specific power, efficiency, etc.) of flying vehicles like aircraft and rockets is particularly sensitive to overall mass and volume. For example, adding weight requires flying at a higher angle of attack to support the additional load, resulting in increased induced drag. Similarly, increasing the overall volume of the aircraft increases profile drag. The vehicle's drag polar provides a simple tool for determining how changes in vehicle weight here affect induced drag. The use of a drag polar is discussed in Section 2.3 in greater detail. Similarly, volume effects can be accounted for via parasitic drag analysis and other methods.[vii]

Since aircraft need to carry all of the components of their ESPG in almost all conceivable cases,[viii] there is an interdependent relationship between the size and weight characteristics of the ESPG and the performance required by the overall system. An ESPG with a higher specific power and specific energy requires less mass and space to provide the necessary power. Similarly, increasing the efficiency of the power generation system reduces the amount of fuel needed for the mission. Oftentimes however, more efficient devices *tend* to be larger and heavier as well [15, 16], resulting in scenarios where more efficient PG devices are not necessarily optimal.

Also related to the effects of mass, many ESPG systems expend the material used for energy storage, causing the mass of the ESPG to decrease over the course of a mission. All fuel-based ESPGs fall in this category. The progressive reduction in mass can provide a substantial benefit to operating time and range, as the power required to remain in flight goes down as the vehicle gets lighter. For example, for the same aircraft with a 30% fuel mass fraction, expending the fuel in-flight confers an almost 20% greater range than one that does not (e.g. a battery) [17, p. 8]. This effect increases exponentially as the proportion of ESPG mass devoted to energy storage increases.

[vii] In general, minimizing additional profile drag is a challenge of effective integration of the ESPG and the airframe—which can lead to net-positives in cases where strategies such as boundary layer ingestion (BLI) can be implemented.

[viii] One could argue that a solar-electric aircraft carries only a power-generation system, with energy ”stored” in sunlight, or hydrogen in the sun. However, while the specific energy could be considered effectively infinite (since sunlight is weightless), the specific power of the collecting solar panels is far too low (fundamentally limited by the available solar energy flux to the Earth of approx. $1.36\mathrm{kW\,m^{-2}}$ [**?**]) to be useful for almost any aircraft.

ESPGs on aircraft are also constrained by the variation of their performance with operating conditions, especially altitude. Open-cycle heat engines such as turbofans make use of the ambient air that they pass through, and the performance the engines provide varies due to these air conditions. The ambient air conditions also affect the amount of drag the aircraft experiences at any given speed. In general, lower altitudes have denser, hotter, and higher pressure air; for a given aircraft, these conditions result in higher drag on the airframe, but also higher engine thrust performance and somewhat lower efficiency—with the opposite scenario at cruise altitudes.

Nevertheless, the same engines need to operate in both regimes, providing at different times a peak power capability for takeoff and landing, and a peak efficiency at cruise where the aircraft often spends the most flight time [3]. While the engine demands and capabilities can scale similarly for open-cycle heat engines (one reason they are usually chosen), the same capability is required of any alternative engine as well.

The third characteristic constraint is the form or forms of the ESPG system's power output. As discussed in Appendix C, the fundamental power requirement for aircraft lies with generating the necessary force to maintain flight. This force is produced by using power (almost always generated from an energy source on the aircraft[ix]) to increase the momentum of the ambient air (and often some fuel) around the aircraft in the opposite direction of the required force, regardless of the precise method.

However, secondary (i.e. non-propulsive) power requirements for control surfaces, sensors, environmental control systems, communications, wing ice protection, entertainment systems, etc. are also present. These are often provided by off-takes of shaft power or pressurized bleed air from the main engines (see Figure 1.6) or an auxiliary power unit (APU), representing additional forms of ESPG power output.

Since aircraft usually employ heat engines of some kind for their main propulsion systems, the efficiency of the engine tends to scale up well enough such that the majority of secondary electrical power and motive power both come from the same conversion system. An APU for engine starting, stationary power, or emergency backup use is often present as well, but usually operates at a lower power level and efficiency. Practically, many designs use shaft power from the main engine to drive multiple subsystems, such as hydraulic control surfaces or a mechanical generator to produce electricity.

Electrical power may be applied to a wide range of secondary applications on aircraft, and large-scale production holds additional promise for propulsion due to the ease with which it may be used for boundary-layer ingestion and distributed propulsion schemes. For secondary systems such as environmental control, wing ice protection, and engine starting, hydraulic, pneumatic, and mechanical loads have been progressively replaced or augmented by electric power or controls for better efficiency and reduced maintenance requirements [19,20]. As such, an aircraft ESPG

[ix] Exceptions would be aircraft run off of solar panels, or beamed power, neither of which (to the author's knowledge) are in widespread use today—though demonstrators of each do exist.

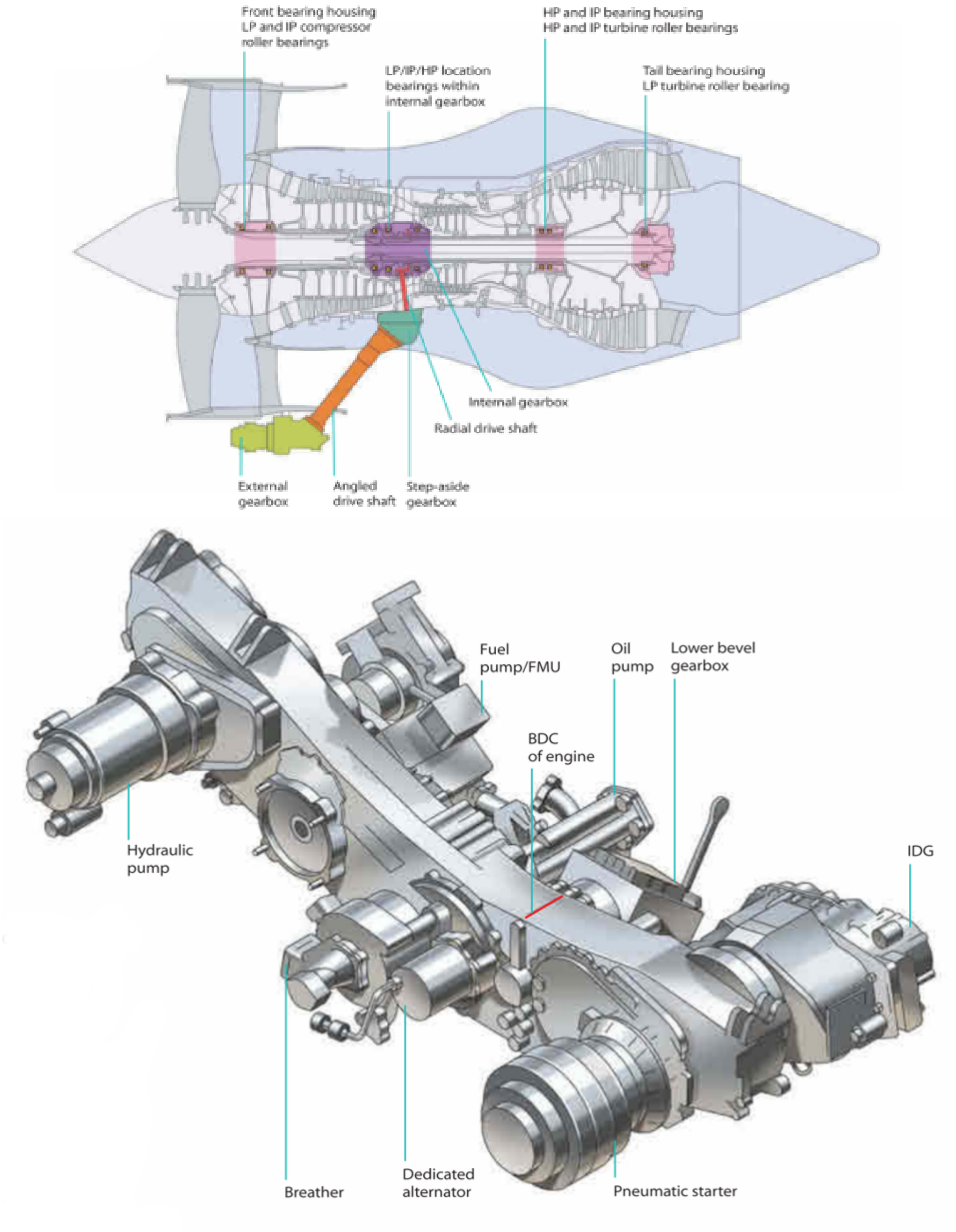

Figure 1.6: (Top) Schematic of turbofan with Accessory Gearbox and connections highlighted; (Bottom) Accessories gearbox including the Integrated Drive Generator (IDG) for electricity generation. Reproduced from [18].

system generally supplies a large propulsive load as well as some mix of secondary shaft and (increasingly) electric power. However, if electric power is employed by the propulsion system as well, then 100% electric power generation scenarios are foreseeable.

At this point, we have a good sense of the underlying motivations for improving ESPGs on aircraft, and application-specific constraints. Armed with this knowledge, in the next section we will discuss reasonable paths to accomplishing this goal.

1.3 Choosing a Reasonable Path Forward

Many different ESPG types have been used on aircraft, from hydrocarbon-fueled internal combustion engines and gas turbines, to battery-electric, solar-electric, and even human-powered aircraft. However, the largest class of aircraft that collectively burns the most fuel are large[x] single- or twin-aisle passenger and transport aircraft; and in fact, these classes generate more than 90% of aircraft carbon dioxide emissions (see Figure 1.7). In these missions (and in many other applications besides), the propulsion system is almost always a ducted turbofan engine [1, p. 27]. For this reason, we focus our attention on the underlying technologies of, variations of, and replacements for, the ducted turbofan.

Many paths are conceivable. A 2014 journal paper by Epstein [2] argued that there is substantial water still left in the well for turbofans to further improve, and suggested several high priority paths of improvement for further development, in particular envisioning an evolution towards smaller, higher performance gas turbine[xi]

---

[x] Here a “large” aircraft is roughly defined as one capable of carrying greater than 100 passengers

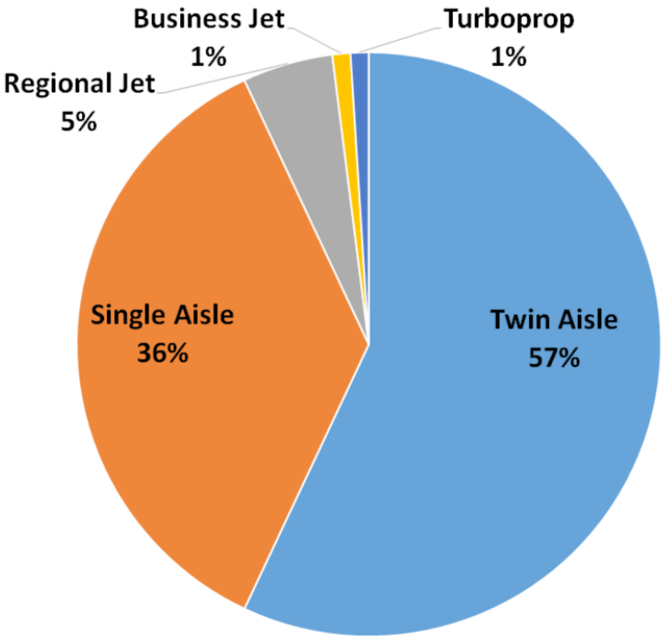

Figure 1.7: Global civil aviation fuel consumption by aircraft class. Reproduced from the National Academy of Sciences, Figure 1.1 [1, p. 17].

cores driving larger and higher-propulsive-efficiency fans.

Other technology options discussed include batteries and fuel cells, along with a variety of energy storage alternatives to kerosene-based jet fuels. In general, Epstein finds that energy sources besides hydrocarbon fuels lack sufficient energy density. Similarly, alternative thermodynamic cycles, fuel cells with electric motors, or hybridized systems are not clearly beneficial for the application. Fuel cells in particular are noted (at least based on current technology) to be unattractive on the basis of their comparatively-high weight alone.[xii]

In addition, a 2016 National Academy of Sciences (NAS) report [1] iden-

---

[xi] A quick introduction to the fundamentals of gas turbine operation and performance is provided in Appendix A.

[xii] One of the goals of this dissertation is to show how fuel cells may be used to reduce fuel burn, and the thresholds at which their use becomes beneficial.

tified four high-priority approaches for further research into the problem of airliner/transport aircraft propulsion in the 10-30 year timeframe, or "N+3" in the NASA terminology representing roughly three generations ahead of aircraft development. Two of these approaches are broader in scope relating to (1) integration of the airframe and propulsion systems and (2) further development and scaleup of SAF. The remaining approaches are a prioritization of both gas turbine technology[xiii] and turboelectric propulsion, stating that the former has a potential for a 30% efficiency improvement over modern (2016) capability, while the latter is "...probably the only approach for developing electric propulsion systems for a single-aisle passenger aircraft that is feasible in the time frame considered by the committee" [1, p. 6].

More specifically, the report notes that gas turbine engines may be improved both in terms of thermodynamic[xiv] as well as propulsive efficiency, continuing historical trends since the introduction of the jet engine—see Figures 1.8 and 1.9 from the NAS report. Based on different cited analyses, the NAS estimated that a 30% improvement over the best engines today was possible, with about twice as much of the gains coming from propulsive efficiency improvements over thermodynamic ones.

Alternatively, the report suggested that an approximately 7% improvement in overall efficiency (the result of multiplied thermal and propulsive efficiencies) was possible per decade starting from the current peak of approximately 40% [1, p. 41].

[xiii] It should be noted that Epstein [2] was also a lead author on this National Academies report, so their agreement should not be considered independent.

[xiv] The "motor" thermodynamic efficiency accounts for all core fluid power (often used directly for propulsion) as shaft power that may be deliverable to a propulsor [2]. This concept is useful for comparing between different engine cycles and configurations (turbofan, turboprop, etc.).

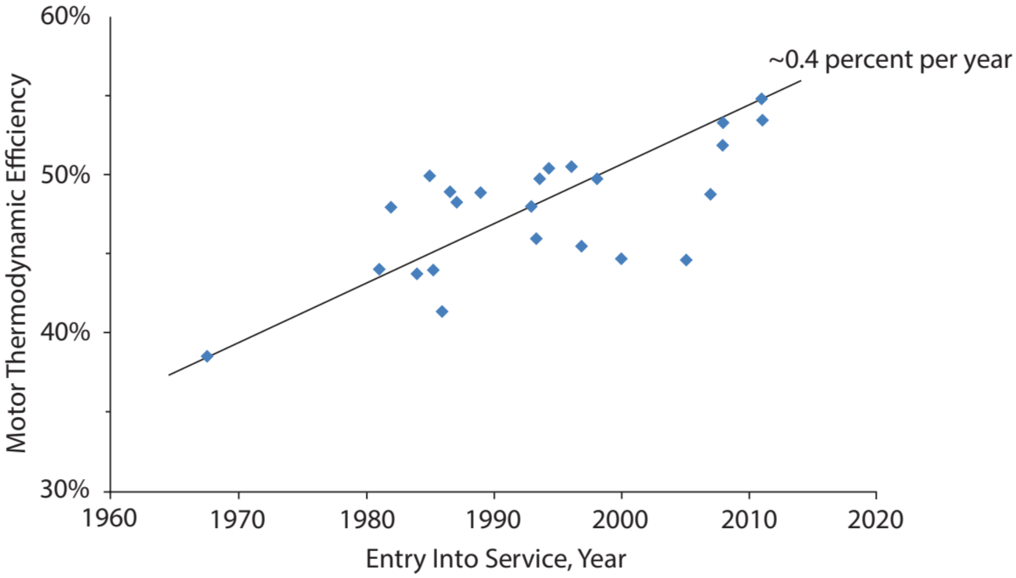

Figure 1.8: Trend with time of the "motor" thermodynamic efficiency[xiv] of commercial aircraft turbofans at cruise. Reproduced from the National Academy of Sciences, Figure 3.3 [1, p. 38].

However, this last estimate is likely from the linear extrapolation of Figures 1.8 and 1.9, which prima facie present data that may be just as easily fit with a decaying curve instead, more indicative of diminishing returns on investment. Additionally, the performance of the main turbofan components (e.g. compressor, turbine, TIT limits etc.) have also seen diminishing returns to their improvement over time [13]. As such, the 7% estimate is likely to be highly optimistic.

The second engine technology focus, turboelectric systems, was found to be promising amongst various electric propulsion concepts by minimizing reliance on high performance battery technology. Instead, a turboelectric propulsion system uses a gas turbine core to convert some or all of the fuel into electricity via a generator. In turn the electricity from the generator is used to drive fans using electric

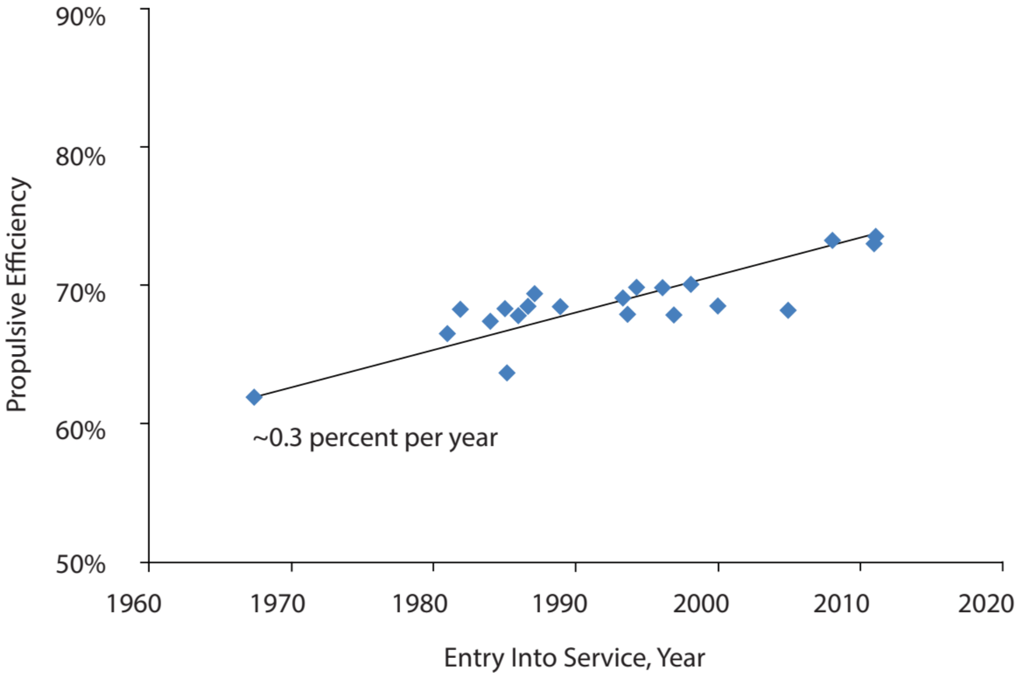

Figure 1.9: Trend with time of commercial aircraft turbofan propulsive efficiency at cruise, Figure 3.4 [1, p. 38].

motors. While the initial energy conversion process is less efficient due to compounding losses in the additional conversions from shaft power to electricity and back again, this may be more than recouped by better positioning the electrically-driven fans for BLI and distributed propulsion [1, p. 56]. Beyond the thermodynamics, the improvements to drag and efficiency need to more than make up for the impact of the additional weight of electric motor, generator, and power-handling components necessary to make this system run. See Figure 1.10 later for illustrations of these components in the "Turboelectric" system.

Other technologies mentioned by the NAS include high-power batteries, superconducting motors, and fuel cells. It was determined that investment in these topics will continue regardless so aircraft-specific research may be prioritized when the state of the art (SOA) is sufficiently advanced [1, p. 21].

Another forward-looking review from NASA Glenn Research Center [21] considered the breadth of several "N+3" concept designs (by NASA, Boeing, General Electric, Northrup Grumman, Georgia Tech, and Massachusetts Institute of Technology) to identify and prioritize the different propulsion technology requirements for operation by 2035. The range of concepts encompassed a number of different configurations, though mostly concentrated on advanced turbofans and turboelectric designs. Electric motors and advanced combustor design appeared to be the most important technical targets for success, with battery and fuel cell technology having the lowest probability of achieving design targets, though the analytical method used was acknowledged to not track the interdependent relationship of electric technologies [21, p. 7-8]. Also considered important were more advanced computational tools to reduce risk and accelerate the process for adoption of new technologies. This dissertation contributes to this category of research.

In general, NASA concurred with the NAS that fuel cells and pure battery power would be unlikely to be appropriate for the "N+3" timeframe except as augmentations to electricity production. However NASA also noted that fuel cells might be more appropriate for the next generation, "N+4" thereafter for propulsion as well. The findings of this report can be considered in some ways a more-grounded update of a 2004 article by Sehra and Whitlow from NASA forecasting future propulsion concepts. The article took the view that propulsion would eventually be based on all-electric systems powered by hydrogen fuel cells [22].

Some more promising, though also more speculative, directions were considered in the Boeing SUGAR study Phase II report [23] which was a follow-on to the Boeing contribution to the review by NASA Glenn [21]. The Phase II report focused on advanced concepts that were potentially feasible for the 2040-2050 "N+4" time frame even if the underlying technologies were still immature. The resulting recommendations diverged from the propulsion configurations suggested in Phase I and instead favored a gas turbine and solid-oxide fuel cell (GT/SOFC) hybrid system using a cryogenic liquid natural gas fuel supply along with additional BLI propulsors and unducted fans.

From these sources, in particular the National Academies report [1] as a representative of the recent consensus of the field, it appears as though the basic architecture of aircraft propulsion—turbofan engines with yet-higher bypass ratios using liquid hydrocarbon jet fuel—will remain the preferable choice for the immediate future. More speculative shifts to turboelectric systems are also suggested to push the effective bypass ratio (plus other quite promising BLI benefits) of the same fundamental Brayton heat cycles even further with the promise of maximized aerodynamic advantages. Other options are generally considered speculative.

The historical trends presented in Figures 1.8 and 1.9 combined with explicit industry projections [14, p. 19] suggest that we can expect improvements to traditional turbofan engines to be evolutionary rather than revolutionary with increasingly-difficult progress as time goes on. If we do not wish to rely so heavily on the advances of the SAF industry to meet the majority of our emissions goals—and address the fuel price sensitivity of commercial aircraft operators at all substantially—it is perhaps worth focusing on the more future-looking ideas for aircraft propulsion and power.

The argument against some of these options has been that development will continue on the required technologies (such as fuel cells, superconductors, etc.) regardless, and aircraft designers can pick up the baton once the technology is more mature [1, p. 21]. On the other hand, one might also anticipate for some cases that the specific needs for aircraft, such as minimal size and weight, are different enough from other applications that developments for those other applications won't transfer effectively—a power plant on the ground cares little that the new cheap and efficient fuel cell it uses is twice as heavy, for example. Adding insult to potential injury, highly conservative and safety conscious commercial operators will need substantial assurance that new technologies are safe to operate. What this means in practice is that years of work will be required beyond the initial introduction of the technology before it is common in the aviation marketplace. As such, we may want to begin investigations into more speculative topics sooner rather than later in order to make those initial technology introductions as soon as possible.

The Boeing SUGAR Phase II study [23] and its support for a hydrocarbon-fueled GT/SOFC hybrid system to provide power and propulsion on aircraft is a main motivation of this dissertation. While the GT/SOFC is only one of several of the more-speculative directions considered for improving aircraft propulsion, consistently it has been found to be a promising path—though not ready for real-world use. The primary roadblocks are sufficient improvement in the performance of the underlying SOFC both in terms of specific power and reliability. Two goals of this dissertation are to provide a detailed framework for evaluating such concepts and to quantify the levels of fuel cell performance improvement (specific power and efficiency) to improvements in overall efficiency and carbon emisssions at the vehicle level.

1.4 GT/SOFC Hybridization

A hybridized ESPG system is the result of combining different energy storage and/or power generation methods that can operate synergistically in some way to enhance overall performance beyond the sum of its parts. The turboelectric systems described in the previous chapter are examples of hybrid electric systems. Figure 1.10 shows six different architectures that hybrid propulsion systems can follow including turboelectric.

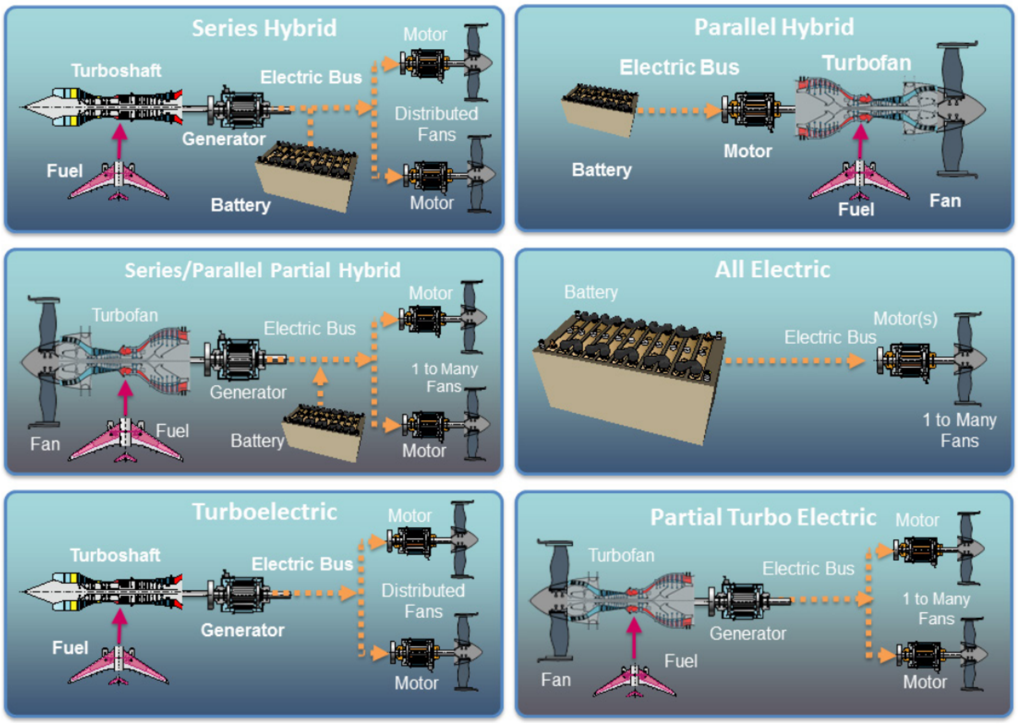

Figure 1.10: Electric Propulsion Architectures, reproduced from Figure 4.1 [1, p. 52].

Each architecture includes the use of electrical power for at least part of the propulsive power. In these cases, electrical power is drawn from either a battery or a mechanical generator attached to a gas turbine—or both! Propulsion is achieved either via distributed fans or the GT-linked turbofan—or again both at once. The batteries presented in Figure 1.10 serve as both energy storage and conversion devices and can be replaced by other energy storage and conversion device. Notably, one option would be an SOFC with a fuel tank that offers substantially greater specific energy than the battery.

The SOFC itself is an electrochemical technology most often used for static power generation—and designed accordingly. However, systems may also be designed for transportation and even use on aircraft to provide electrical power.

The GT/SOFC hybrid concept further optimizes the use of the SOFC as a power source by combining the Brayton cycle of a gas turbine with the topping-cycle of the SOFC.[xv] A basic diagram of the configuration is provided in Figure 1.11. A certain fraction of high pressure air from the GT compressor is bled from the compressor and diverted to the SOFC components where it is further split between the fuel reformer (leading to the SOFC anode), the cathode, and a cooling bypass duct. All three flows (anode, cathode, and cooling bypass) are eventually directed back into the Brayton cycle via the combustor along with any remaining airflow from the compressor. Power generated from the SOFC will take the form of direct current electrical power initially, while in most devices the Brayton cycle power output is originally shaft work which can be converted to other forms in a

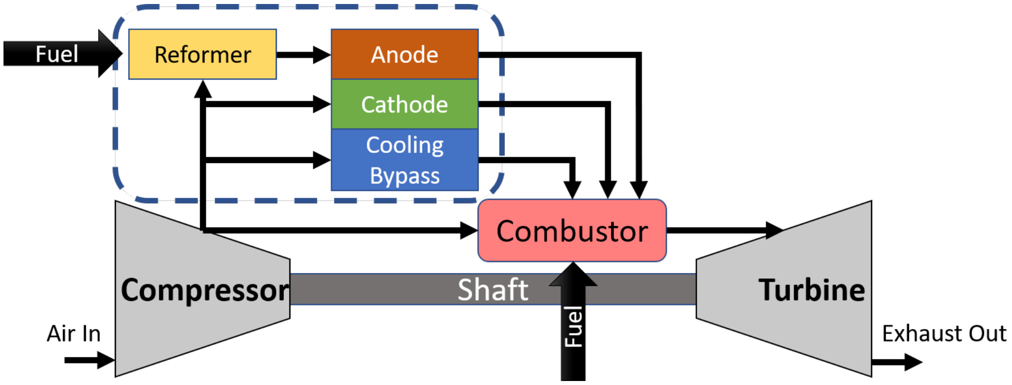

Figure 1.11: Basic Configuration of GT/SOFC. SOFC components in dashed region.

number of ways.

While both GTs and SOFCs can generate power from the same energy sources, SOFCs typically offer higher efficiency power generation than a GT at the same conditions. The fundamental reason for this is that the SOFC operates isothermally at a (relatively) low temperature which avoids or minimizes inefficiencies associated with material temperature limits, combustion inefficiencies, and irreversibilities from heat rejection present in high performance heat engines. [24, p. 87]. Figure 1.12 provides the theoretical efficiency trend of the isothermal fuel cell in comparison to the maximum-efficiency Brayton cycle (equivalent to the Carnot cycle in terms of efficiency, but producing infinitesimally little work) and the Brayton cycle producing the maximum work *per unit of material flow through the system.*[xvi] The range of SOFC operating temperatures is shown, broadly from 550°C to 1000°C [24, p. 478]. Modern state-of-the-art turbine inlet temperatures are split between approximately 1300K for uncooled turbine blades, and 2000K for air-cooled turbine blades [25,

---

[xv] Primers on gas turbines and fuel cells are each available in Appendices A and B respectively.

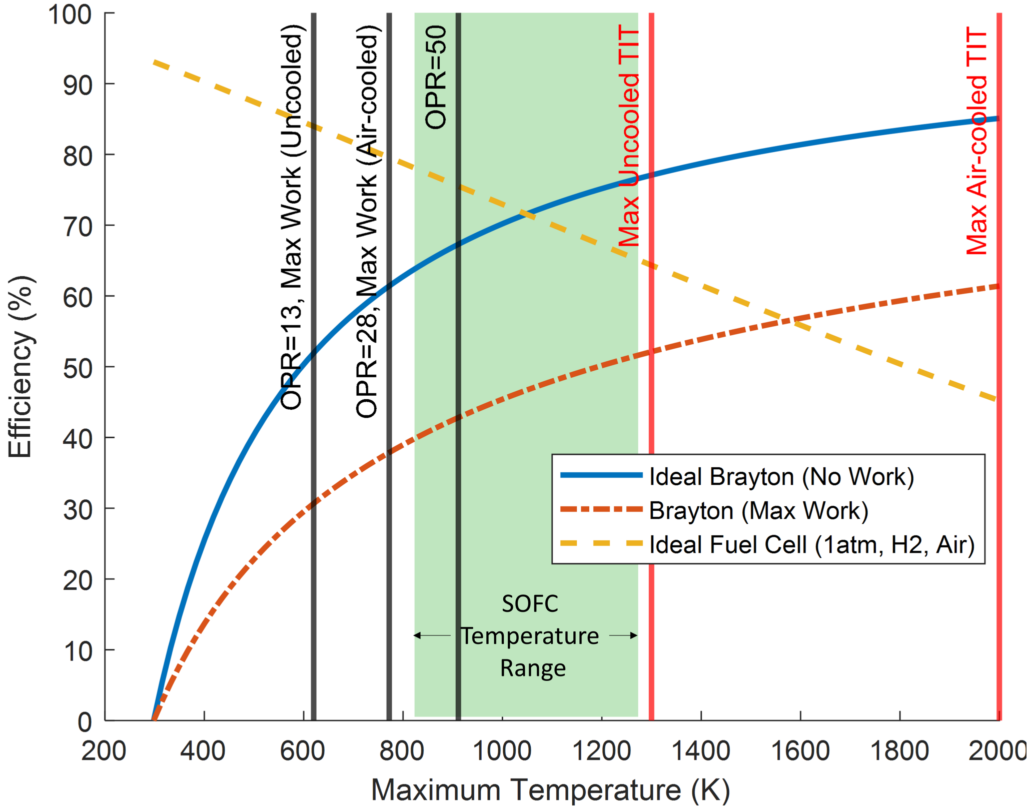

Figure 1.12: Ideal efficiencies of gas turbines and fuel cells as a function of maximum operating temperature. The cycle entrance temperature is 300K. The black vertical lines indicate the compressor outlet temperature at different overall pressure ratios (OPRs). The intersections of the curves with the maximum cycle temperatures (indicated by the vertical solid red lines) give the maximum efficiencies of Brayton cycles. The intersection of the yellow dashed curve with the left boundary of the green shaded region gives the efficiency of an ideal H_2-air fuel cell.

Fig. 2]. Some ideal compressor exhaust temperatures are provided for the optimal (maximum work per unit of material flow) compression ratio for the uncooled and air-cooled TIT limits, as well as a state-of-the-art OPR of 50.

Looking at Figure 1.12, we see that the upper limits on SOFC and Brayton-

---

[xvi] This diagram does not include an equivalent SOFC "Max Work" scenario since all of the inefficiencies of a fuel cell's operation are a result of the material performance characteristics, similar to performance map characteristics of the GT compressor and turbine components. A very large fuel cell with very low current density will yield nearly the ideal efficiency while producing useful power from a unit of material flow through the system.

cycle efficiencies are not substantially different within their respective ranges of operating temperatures. The optima are however on opposite sides of the temperature space: low temperatures result in higher fuel cell efficiency while high temperatures result in higher Brayton-cycle efficiencies. Drawing significant power from a given real system of either cycle also drops the efficiency of operation[xvii]. However, the lower temperature SOFCs can generally achieve greater efficiencies than Brayton-cycle devices that usually design closer to the "Max Work" case [24, p. 86-88].

There are a number of advantages associated with placing an SOFC inside the Brayton cycle. First, the gas turbine acts to replace some of the additional balance-of-plant (BOP) infrastructure usually required to operate fuel cells such as pumps and blowers. These can account for about a quarter of the total mass of a purely FC-powered aircraft [26]. Second, a GT/SOFC also provides a means of recovering waste heat and unburned fuel from the SOFC by discharging the fuel cell exhaust directly into the gas turbine's combustor. This recuperative effect enables the SOFC to be designed with less concern for achieving high fuel conversion enabling it to be smaller and lighter.

Third, the high temperature environment required by the SOFC is naturally achieved inside the hot-section of the gas turbine. Heating starts in the compressor (see compressor)exhaust conditions in Figure 1.12) and can can be continued using

---

[xvii] Thermodynamically, a "Max Work" efficiency line for an SOFC is equivalent to the ideal case—an arbitrarily large SOFC can generate a small amount of power per unit of active area that is near the ideal efficiency. Practically however, we are often interested in the max-work-per-unit-flow scenario as it correlates with a reduced size of the device. To address the same consideration for the SOFC would target the work-per-unit-reacting-surface, which requires many additional analytical considerations of the different inefficiency sources. See Section 3.3.5 for an accounting of these inefficiencies.

waste heat if necessary.[xviii] For the "Max Work" OPR values, some additional heating is required to achieve the SOFC operating temperature. This can often be achieved using the waste heat produced by a the SOFC itself. Higher OPR values (which also increase the efficiency of the Brayton cycle) can achieve SOFC operating temperatures without any additional heating whatsoever. This benefit at higher OPR is balanced against the efficiency benefits of lower temperature SOFC operation, and as we'll see in Chapter 2, the reduced fuel cell waste heat absorption capacity with higher compressor exhaust temperatures.

Fourth, Figures 1.13 and 1.14 show that operating a Ni-YSZ SOFC at post-compressor pressures drives up the power density via increases in adsorption rates and alterations to transport processes within the electrodes.[xix] Higher pressure operation also provides a small improvement to ideal efficiency since the Nernst potential increases with the partial pressure of reactants [27].

While Figure 1.13 shows that increasing pressure offers diminishing returns, this also means that the performance of the pressurized SOFC is less affected by a change in altitude (as from takeoff to cruise operating conditions) than the Brayton cycle [28].[xx] The net result at cruise altitude (approx. 35kft) is that the specific

---

[xviii] These same high-temperature conditions (as well as a restriction to pure hydrogen fuel) prevent a similar integration of more-technologically-mature polymer electrolyte membrane fuel cell (PEMFC) technology. Additionally, a PEMFC requires substantial temperature control to within 20°C, vs. approximately 100°C for an SOFC stack. Finally, the PEMFC's susceptibility to poisoning by carbon restricts its use to difficult-to-carry pure hydrogen fuel, further penalizing its use on aircraft.

[xix] These effects can also be seen in modeling results as part of this work in Figures 3.16 (for power density) and 3.17 (for efficiency).

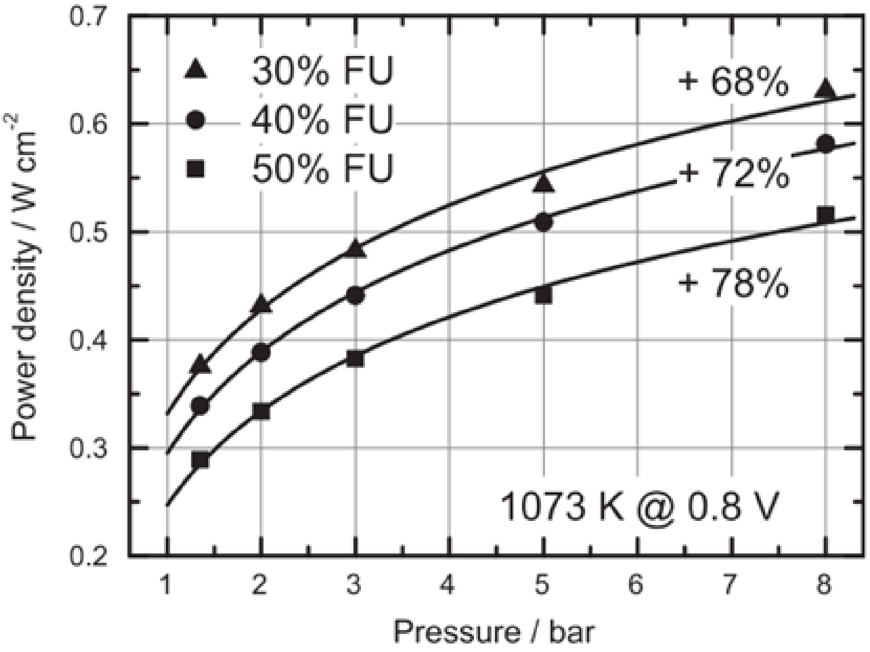

Figure 1.13: Power density vs. pressure for different fuel utilizations at constant temperature and voltage for Ni-YSZ based SOFCs. Reproduced from Henke et. al. [27].

powers of the Brayton and fuel cell cycles are comparable [29].

Furthermore, in the combined GT/SOFC system the same unit of material flow—mostly air for a typical aircraft engine with some amount of fuel—can be used to extract more power (i.e. a higher *flow* specific power) than is possible with the Brayton cycle alone. The reason for this increased capability is that the fuel cell in the topping cycle does not depend on a change in temperature like heat engine cycles, even if one occurs due to heat release from irreversible losses during operation

---

[xx] Strictly speaking, the Brayton cycle's performance does not drop with ambient pressure, and for a given hot-side temperature limit will actually improve with altitude as the ambient temperature falls. However, for a single Brayton cycle device of a given size (say a jet engine), the amount of power that can be produced is limited by the air density, which drops with altitude as well.

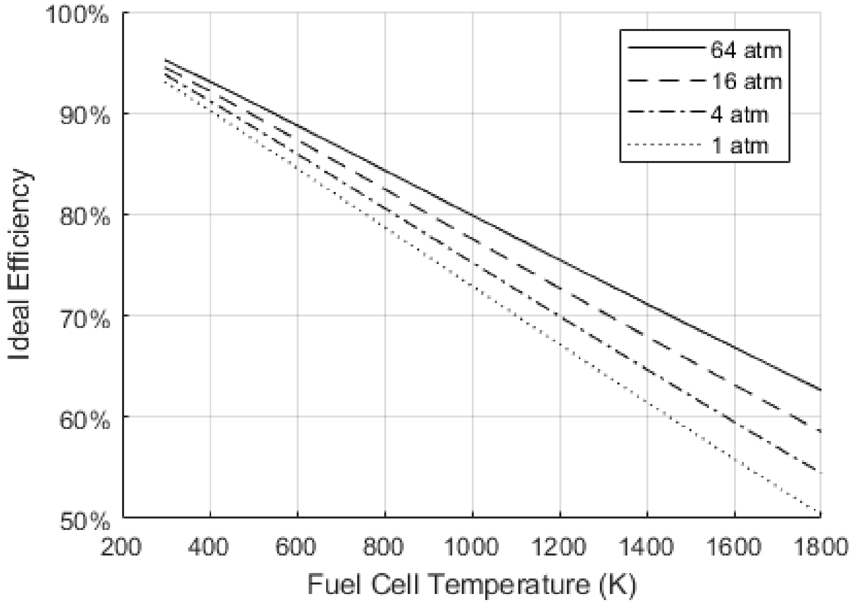

Figure 1.14: Ideal fuel cell efficiency (Open-Circuit) at varying operating temperature for different operating pressures. Anode: 100% H2 gas, Cathode: Air.

of the fuel cell.[xxi]

The total power that can be extracted from a unit of material flow is still limited by the amount of SOFC waste heat generated and the stoichiometry of the fuel chemistry, but all modern jet engines are currently operated "fuel lean" to limit operating temperatures below structural material limits. As such, there is the *stoichiometric* capacity for additional power extraction with additional fuel.

[xxi] Consider the alternative where we use another Brayton cycle instead of a fuel cell as the topping cycle. An optimal Brayton cycle can be tuned through the pressure ratio to provide a maximum flow-specific power based on the cold and hot side material temperature limits. If the bottoming Brayton cycle of the

1.5 Current State-of-the-Art

A large body of work exists for GT/SOFC hybrids intended for large ground-based electrical power generation. These studies show that integration can achieve overall system efficiencies ranging between 50%-90% [17, p. 20]. An expansive 2018 review of the hybrid cycle focused ground-based applications—including mobile and transportation applications such as for train engines—is available from Azizi and Brouwer [30]. While summaries from the perspective of aircraft researchers are available [17, 31], studies for ground-based power production tend to be difficult to apply to aircraft use cases since static power plants have effectively no mass or volume constraints (see section 1.2). As such, there is relatively little sensitivity to making the thermodynamic cycle even more complex (such as with high-effectiveness recuperating heat exchangers or condensers, for example Yi et. al. [32]) if the overall efficiency is improved by even a small amount. In general these are computational studies, but there are a few experimental systems built as demonstrators such as one by the German Aerospace Center (DLR) [27, 33, 34].

Research on GT/SOFC hybrids for aircraft specifically has progressed over the last several years such that it represents a more substantial body of work. In this section, we will provide a summary of the sub-field focused specifically on aircraft. Indeed, an overall observation is that many studies focusing on aircraft grapple with the questions of just which components or cycle optimizations can be effectively carried over to the aircraft application.

First, there is a distinction to be made between studies of SOFC (and other fuel-cell) systems on board aircraft, and those for GT/SOFC hybrids. The former lack many or all of the hybrid synergies previously discussed, though their set of BOP components (such as a compressor or recuperator—if present) may perform many of the same functions. The range of possible configurations is broad, so at times the definition may be blurred, and authors (e.g. Eelman et. al. [35]) may not highlight or even recognize a distinction. In addition, some findings from the non-hybridized SOFC studies on aircraft are applicable to the GT/SOFC. As such, some of those works are also discussed here. Interestingly, there have been more experimental/demonstrator and even operational non-hybridized fuel cell systems on (usually small UAV) aircraft. Examples include the Ion Tiger, a PEMFC-based demonstrator by the Naval Research Laboratory [36], and the Lockheed Martin Stalker XE UAS which is an example of an operational battery/SOFC hybrid that extends the range of an otherwise pure-battery solution [37]. While blowers and fans are present in these examples, power extraction is not based on a heat cycle or related to substantial changes in pressure.

There are also a variety of intended purposes for the GT/SOFC on board the aircraft. First, the GT/SOFC takes the place of the traditional gas turbine APU producing secondary power, rather than being used for propulsion. Alternatively, if the GT/SOFC is used for propulsion, some studies consider all-electric propulsion systems using the GT/SOFC as the electric power source (following the Series Hybrid architecture from Figure 1.10), while other studies use the GT/SOFC for duct propulsion directly in addition to electric power production (i.e. the Series/Parallel Partial Hybrid from Figure 1.10). In this last case, the electrical power can be used to either add to the propulsive power by some means, or be employed for some secondary purpose. Table 1.1 organizes the GT/SOFC studies in this literature review by these categories, with rows collapsing similar studies from the same group. This dissertation focuses on the latter two propulsion-focused categories.

The first takeaway from the Table is that all of these published studies are modeling studies rather than experimental. However, among those studies, there is a wide range of model complexity and parameters addressed. Gas turbine performance may be modeled as ideal theoretical components [38, 39], or derive an efficiency from a performance map of real or simulated components. The fuel cell has been modeled as everything from a simple constant efficiency reactor to full electrochemical models with transport through the MEA and at least one-dimensional transport along the fuel and oxidizer channels. Note that fixed efficiency models are too crude to properly assess hybrid GT/SOFC over the range of operating conditions experienced over a mission and that higher fidelity models are required.

At the level of implementation, modeling efforts are carried out using a range of platforms depending on what aspect of the problem is of most interest. MATLAB/Simulink is a common general-purpose choice, but aircraft-focused platforms have also been used, particularly the Numerical Propulsion System Simulation (NPSS) language. Other specialized platforms include gPROMS (a process systems modeling software), Flight Optimization System (FLOPS), and SysFuel. The first of these might generally be applied to ground-based power plants, while the latter two are aircraft-specific modeling platforms. The choice of platform should be unimportant for identical mathematical representations of the system. At a practical level however, the details of how each platform operates means that mathematical representations of the systems will usually be at least slightly different. This complicates efforts to compare results generated using different platforms and to generate computational libraries that can be shared between platforms.

Regarding aircraft APU applications, an in-depth review article from 2018 by Fernandes et. al. provides a recent picture of the sub-field covering academic articles, theses, reports, and patents [40]. The general takeaways from the review were that many of the immediate issues with the technology remained with the foremost conclusion being that “hybrid” systems (any combination of SOFC and heat cycle including GT/SOFCs) generally did not reach the necessary weight-to-efficiency ratio. Fuel choice also remained an open question. The authors predicted that applications in smaller and unmanned vehicles were possible in the short- to medium-term future, and that the focus would be on all-electric applications in larger aircraft in the long-term. Finally, they also cited increased complexity and unproven reliability of the SOFC systems as remaining concerns for aerospace use.[xxii]

The main challenges identified by Fernandes et. al. for SOFC-APU systems also apply generally to other GT/SOFC systems in aircraft. Therefore, we should address the state-of-the-art in more detail. The first concern is fuel choice, with one of two paths generally considered: hydrogen or hydrocarbons. Pure hydrogen gas provides the most energy per unit of fuel mass and the best SOFC performance, but faces very challenging storage problems due to its physical characteristics: Whether

---

[xxii] Reliability concerns for the SOFC are generally acknowledged as an unknown for this application (Stoia et. al. consider it in the context of the recycle blower necessary for their system [41]) but are otherwise minimally addressed even though it is a substantial topic for SOFC researchers [42].

as a gas or as a cryogenic liquid, the low volumetric density relative to hydrocarbons adds drag penalties, from both the sheer size of the fuel storage on board the aircraft and the heavier high-pressure/cryogenic storage tanks. The alternative, hydrocarbons (usually jet fuel in order to ease introduction into modern fuel distribution infrastructure), are dense and readily stored in thin-walled fuel tanks. To be used by the SOFC however, such a fuel needs to be desulfurized (either on the ground or on the aircraft) and reformed into "syngas" which is a mixture of hydrogen gas and carbon monoxide [40]. Most studies at least acknowledge or briefly consider the trades between these two options with, with several studies considering carrying hydrogen just for the fuel cell in addition to jet fuel [43–47]. If a hydrocarbon fuel is chosen however—as it is in the majority of studies found—the method of reformation is another research topic.

Reforming is a chemical process that breaks hydrocarbon fuels into H_2 and CO. The process is usually accomplished by one of three methods: steam reforming (SR), autothermal reforming (ATR), and partial oxidation (POx), which exist on a continuum of greater to lesser degree of water injection respectively. Methane steam reforming consists of the three reactions in Equation 1.1. For larger hydrocarbon fuels (e.g. jet fuels), a thermal/oxidative decomposition, or "cracking," process yields shorter hydrocarbons like methane for these reactions. These preceding reactions are more complex, but generally result in predictable distributions of products [48].

$$CH_4 + H_2O \rightarrow CO + 3H_2 \ \ \Delta H = 206\,\mathrm{kJ\,mol^{-1}} \tag{1.1a}$$

$$CO + H_2O \rightarrow CO_2 + H_2 \;\; \Delta H = -41\,\mathrm{kJ\,mol^{-1}} \tag{1.1b}$$

$$CH_4 + 2H_2O \rightarrow CO_2 + 4H_2 \;\; \Delta H = 154\,\mathrm{kJ\,mol^{-1}} \tag{1.1c}$$

Steam reformation is endothermic, requiring large amounts of heat and molar steam/carbon ratios in the 2.5:1 to 3:1 range. Optimum operating temperatures for the most complete conversion of the fuels to syngas are in the range of 800°C-900°C. Autothermal reforming adds the additional reaction in Equation 1.2

$$CH_4 + 1/2O_2 -> CO + 2H_2 \;\; \Delta H = -24.5\,\mathrm{kJ\,mol^{-1}} \tag{1.2}$$

An ATR operates at higher temperatures (950°C-1100°C) and can be accomplished with overall $\Delta H \approx 0$ by adding a relatively small degree of air or other source of oxygen such that this reaction balances the other largely endothermic processes. In the most extreme case, Partial oxidation uses no additional water injection. Instead some of the fuel reacts with air under fuel-rich conditions to make the heat *and* water needed to run reactions in Equation 1.1. Partial oxidation, especially over a heavy-metal catalyst such as platinum (i.e. "catalytic partial oxidation" or CPOx) is faster than steam reforming and requires a smaller reactor. However, as less water is provided for reformation (i.e. the steam-to-carbon ratio drops) from SR to ATR to CPOx, the process becomes less efficient—both energetically and in terms of complete conversion—as more of the fuel's combustion enthalpy is expended to provide the heat and water needed to run the reactions.

The question is which process is best for use on aircraft. Ji. et. al. [49]

discusses a variety of seam reforming issues and includes a discussion of optimization on aircraft e.g. [50] and exhaust gas recirculation, whether from cathode (CGR) or anode (AGR) exhaust flows [51,52]. Steam injection with carried water is considered by Stoia et. al., but found to be universally not-worth-the-weight [41], with a similar result found by Ibarreta and Sung [50]. As an additional wrinkle, reforming can also be performed or continued inside the SOFC itself since the nickel-based anode catalysts of high-temperature fuel cells are often active for the reformation reactions as well, particularly the Water-Gas Shift reaction in Equation 1.1b [24, p. 435-436].

After fuel choice, the second looming issue is whether a sufficient specific power within the SOFC may be achieved. As part of this balance of efficiency and specific power, GT/SOFC hybrids can have a wide range of configurations. Recuperation increases the efficiency of the GT while exhaust recirculation within the fuel cell subsystem can improve SOFC and reformer performance. In practice, the performance improvements offered by these more complicated configurations trade against the additional mass and volume they require.

In the direction of simplicity, there are also "turbineless" hybrid systems ([28, 49]) that drive the compressor via the SOFC electric power and a motor. The advantage of these systems is that the temperatures exiting the combustor can be much higher without the presence of the relatively-fragile turbine. All of the power available in the Brayton cycle is harnessed by expanding the exhaust through a nozzle. Among the challenges for a turbineless hybrid is an even further decrease in propulsive efficiency vs. an equivalent turbojet, since the difference in exhaust velocity and flight speed will be even greater.

Optimizations can also be made in terms of high-level system settings such as fuel utilization within the fuel cell—while high fuel utilization makes the most of higher SOFC efficiency, achieving that utilization requires larger and heavier SOFC components. For example, Yi and Kim made the point about the optimal fuel cell utilization of a GT/SOFC hybrid being reduced versus a traditional fuel cell [53], and variation of utilization with altitude for the same design [28]. On the other hand, Braun et. al. suggest a high fuel utilization target of 88% by the SOFC to minimize the fuel burn objective used for an aircraft APU system [51]. Finally, technology improvements or design choices may be made at the SOFC stack level that tailor them to the aircraft application [46].

In addition to weight concerns, the physical volume of the SOFC components is another source of drag.[xxiii] The fact that the redox fuel/air reactions must occur on a surface makes fuel cells inherently less compact than an equivalent combustion chamber. An analysis by my own research group found that profile drag can easily become the more substantial component, though this is highly dependent upon the choice of GT/SOFC integration to the airframe [29]. In a similar vein, Litherland et. al. also address the drag of an SOFC-carrying pod [54]. An ideal GT/SOFC integration method remains to be identified but Blended-Wing-Body (BWB) aircraft designs may be more suitable than traditional engine-pylon configurations [23].

At another level of the problem, studies consider different operating conditions, which if modeled with some level of complexity will change the operating

---

[xxiii] This volume concern is separate from (and additive to) any increase in volume requirements due to the use of low-density hydrogen fuel.

performance of the fuel cell components as well as that of the turbomachinery. Cruise conditions for the given aircraft are taken to be the representative condition in most cases since it is the majority of flight time and fuel burn, and as such the most beneficial target for improving performance. Some studies also add takeoff as a bracketing high-performance-requirements condition [31]. In the most rigorous cases, a full mission analysis is sometimes considered, integrating performance (e.g. fuel burn rate) over the course of an entire flight to address the performance of the GT/SOFC over the overall journey [51].

Finally, to date, little work has been performed considering the potential impacts of SOFC exhaust streams' reintegration into an aircraft combustor: a recent conference paper by Cadou and myself appears to be the only discussion of the topic for aircraft known [55].

Table 1.1: Summary of Previous Studies for Fuel Cell Power and Propulsion Systems on Aircraft. Rows represent efforts by different research groups, with their works collapsed together.

	Authors	Platform	Reformer	Fuel	FC Model	GT Model	Max Power (kW)	Max Efficiency	Notes
APUs	Braun et. al. [51]	gPROMS, ITAPS	ATR (AGR)	Jet A	Zero-D	Proprietary	300	70%	Uses CGR and AGR; 4.7%-6.7% fuel reduction
	Gummalla et. al. [56]	gPROMS, ITAPS	ATR (AGR)	Jet A	Zero-D	Proprietary	2×150	70%	Integration study for [51]
	Eelman et. al. [35]	MATLAB	Steam	Kerosene	Unspecified	Unspecified	370	70%—75%	Addresses Component Mass, Recovers H_2O
	Freeh et. al. 2004 [57]	NPSS	Steam	Jet A	Zero-D	Performance Maps	200	40.6%	Model Development Paper
	Freeh et. al. 2005 [58]	NPSS	ATR	$C_{12}H_{23}$	Zero-D	Performance Maps	440	73%	Part-power and altitude effects
	Steffen et. al. [59]	NPSS	ATR	Jet A	Zero-D	NASA Design Code	440	62%	Averages SOFC perf. wrt. depletion; Detailed Mass Model in [60]
	Dollmayer et. al. [61]	SysFuel	ATR	Jet A	ChemCAD Model	Constant η	700	59%	0.25kW kg^{-1} SOFC breakeven point
	Rajashekara et. al. [38,39]	Unspecified	ATR	Jet-A	Zero-D	Idealized	440	79%	Idealized Analysis
	Whyatt and Chick [52]	Unspecified	ATR (AGR)	Jet-A	ChemCAD Model	Constant Efficiency	972	76%	Breakeven Point Not Achieved
	Borer et. al. [54]	FLOPS	Unspecified	JP-8	Subcontractor	N/A	60	62%	SOFC-only Pod Drag Study
All-Electric	Himansu et. al. [62]	MATLAB	N/A	H_2	Zero-D	Constant Efficiency	50	Unreported	High Cell Voltage Optimal for HALE
	Aguiar et. al. [63]	gPROMS	N/A	H_2	Quasi-1D	Constant Efficiency	140	66%	For HALE; Applies Intercooling; Rigorous Electrochemistry
Power and/or Propulsion	Waters et. al. [29,31,64]	NPSS	CPOx	JP-5	Quasi-1D	Performance Maps	500	42%	Rigorous Electrochemistry
	Bradley et. al. [23,65]	NPSS	IR-SOFC	Jet-A/LNG	Proprietary	Performance Maps	780	N/A	Boeing SUGAR studies
	Valencia et. al. [66]	MATLAB	N/A	H_2, kerosene	Zero-D	Constant Efficiency	N/A	-71% TSFC	Includes Mass Model
	Chakravarthula et. al. [28]	Simulink	IR-SOFC	LNG	Quasi-1D	Constant Efficiency	Unreported	Unreported	Turbineless Hybrid, Complex Electrochemistry
	Ji et. al. [49]	Unspecified	CPOx	Tetradecane	Zero-D	"Lumped Parameter"	N/A	$\approx 66\%$	Turbineless Hybrid
	Okai et. al. 2015 [43]	Simulink	N/A	H_2 for SOFC	Unspecified	Constant Efficiency	Unspecified	58%	Different SOFC and GT fuels
	Okai et. al. 2016 [44]	Simulink	N/A	H_2 for SOFC	Zero-D	Constant Efficiency	Unspecified	58%	Mass Breakeven Points for [43]
	Okai et. al. 2017 [45]	Simulink	N/A	H_2 and jet fuel	Zero-D	Constant Efficiency	7500	60%	Compares fuel options
	Hashimoto et. al. [46,47]	Simulink	N/A	H_2 for SOFC	Zero-D	Constant Efficiency	75	64%	Designs lightweight SOFC

1.6 Objectives and Approach

In this work, we will consider several different directions of analysis for hybrid GT/SOFC systems on aircraft. In the first chapter, we will derive a relatively simple analytical performance model that takes into account the basic topping-cycle of the GT/SOFC. We will couple this performance model with a variation of a previously-derived range/endurance model for aircraft to identify basic relationships between system performance and the performance of individual SOFC components that will inform our further analyses.

The second chapter will expand on the simple analysis using an improved NPSS system model that takes into account the physical design of the SOFC and varying performance of the GT components for different system configurations. In contrast to previous work using this model that considered generation of secondary electrical power (ie. the SOFC as a replacement for an APU), we will address configurations where 100% of the power output is electrical, and configurations where the electrical power assists the fan enabling larger bypass ratios. We will also develop new component models for exhaust gas recirculation and heat recuperation. The former is important for fuel reforming while the latter improves the overall efficiency of the cycle.

A third chapter will consider the effects of introducing fuel cell exhaust into the main combustor. High concentrations of H_2 and CO in the fuel cell exhaust could lead to substantial changes in combustion characteristics such as local flame speed and extinction strain rate which, in turn, could influence the stability of the combustor—and possibly enable operation at lower overall equivalence ratios than previously possible without combustion instability.

1.7 Remaining Challenges

For completeness, there are some immediate open questions that should be mentioned, but will not be considered in this dissertation. First, while NPSS is capable of predicting transient performance, it is an additional level of complexity that is not considered in this work. However, considering the changes in temperature and heat transfer requirements over the operating range of a typical aircraft mission, this is an important consideration that deserves future analysis.

Second, the reliability of any replacement power and propulsion system needs to be approximately similar to that of modern aircraft engines; an in-flight shutdown rate of approximately 0.020 for extended operations and 0.002 per 1000 hours of operation is the current state of the art in turbofans. The same goes for maintainability; currently turbofans have reached 6,000-14,000 hours before removal for overhaul (i.e. time-on-wing) [2]. As future-looking technologies, reliability and maintainability have not been strongly examined in the aircraft application, which is unfortunately different from modern usages of fuel cells for long-term baseload power where startup/shutdown cycling is few and far between. For fuel cells this cycling process is a substantial component of degradation [67]; however, research continues on different SOFC materials that are more resistant to cycling as well as tolerance to lower-temperature and lower-voltage operation [68].

Additionally, acceptable pricing of the SOFC systems is also a difficult question since SOFCs have not had the same level of commercial cost optimization that other technologies such as batteries have received. However, if a GT/SOFC system is to approach the capabilities of modern turbofans, manufacturers have tended to be willing to spend about 15-22% of the total cost of the airplane consistently since the 1980s, such that a new technology should ideally avoid net engine manufacturing cost [2]. A full techno-economic analysis is however beyond the scope of this thesis.

Chapter 2: Ideal Parametric System Analyses

The goal of this chapter is to establish a simplified analytical model that can provide high-level guidance to designing GT/SOFC systems, as well as help set performance targets of individual components necessary in order to realize improvement in the aircraft as a whole—whether that be a reduction in fuel burn or an increase in range and endurance. We will start with a derivation of an ideal GT/SOFC "cycle" followed by an integration with an aircraft range and endurance equation before generating results. As applicable background for this chapter, a brief introduction to the gas turbine and the Brayton cycle which it approximates may be found in Appendix A. A similar introduction to the fuel cell is available in Appendix B.

It should be noted that this is not the first example of a cycle derivation or model provided in the literature, though other works such as by Chinda and Brault [69] and Tarroja et. al. [70] take different approaches and levels of their complexity for ideal analysis. In this chapter, the focus is on providing a more intuitive understanding of the cycle operation rather than extracting specific performance predictions, especially for the fuel cell components. These questions are left for Chapter 3 which considers the design of particular GT/SOFC systems.

2.1 GT/SOFC Analytical Model

Thermodynamically, the GT/SOFC involves an SOFC operating within the heat addition step of the GT's Brayton cycle – specifically between stations 3 and 4 (see also Figure A.3) such that both waste heat and unburned fuel from the SOFC exhaust can be accounted for as part of the heat addition. Physically, this might be represented by the GT-SOFC in Figure 2.1 where power is extracted from the turbine and electricity from the SOFC in lieu of thrust power produced by accelerating hot working fluid through a nozzle. This configuration matches some turboelectric concepts where electric power production is maximized.

This ideal analysis assumes the system to be at rest such that no ram drag nor inlet compression (nor expansion of exhaust through a nozzle) are present.[i] Accordingly, the flow velocities inside the different components are presumed to be low ($M << 0.3$) such that the total temperatures and pressres are equivalent static temperatures and pressures at each stage of the cycle. The full open cycle of a gas turbine engine core, in accordance with Aerospace Recommended Practice 755A [71, p. 263], proceeds from stations 0 to 9. As such, the conditions at the compressor inlet at station 2 match the conditions at station 0 (subscript "amb") and the free-power turbine outlet condition at station 6 is equivalent to station 9. With the static pressure matching at both ends of the cycle, the result is that

$P_2 = P_6 = P_{amb}$, and we need only consider stations 2 through 6 during the analysis.

The cycle developed here will use assumptions of a calorically-perfect gas as well as ideal isentropic compression and expansion during the applicable stages of the cycle. Furthermore, it is assumed that the addition of fuel does not substantially change the specific heat c_p or specific heat ratio γ between any given points in the cycle [71, p. 269]. Similarly, the difference in mass flow rates across the compressor and turbine (and as such the work they require and produce respectively) is presumed to be small. These assumptions are appropriate for most GT systems where the fuel mass flow rate is relatively small ($AFR \approx$30-60 [71, p. 247]), but the applicability of this assumption can be checked against the AFR found to achieve the target heating in the cycle derived here.

To start, consider the flow-specific work of a simple Brayton cycle w_{GT}, which is the power produced $\dot{W}_{GT}$, normalized by the mass flow rate of the working fluid $\dot{m}$. The flow-specific work for a calorically-perfect working fluid is given by Equation 2.1 when considered in terms of heat input and output, or Equation 2.2 when considered in terms of work input and output.

$$w_{GT} = \frac{\dot{W}_{GT}}{\dot{m}_{tot}} = q_{in} - q_{out} = c_p(T_4 - T_3) - c_p(T_6 - T_{amb}) \tag{2.1}$$

---

[i] For an aircraft, this might normally be too extreme a simplification; however for our purposes the power output does not become thrust directly such that the distortion of performance is reduced. The actual required condition for the turboelectric system posed in Figure 2.1 might only be that the momentum of the flow $\dot{m}v$ at inlet and outlet of the GT/SOFC is the same to achieve zero-thrust for any given flight condition. A line of analysis for the ideal full extractable turbine power may be found by solving for the turbine temperature ratio (and associated pressure ratio via isentropic relations) via Mattingly's Equation 5.29 after setting the thrust to zero [71, p. 282].

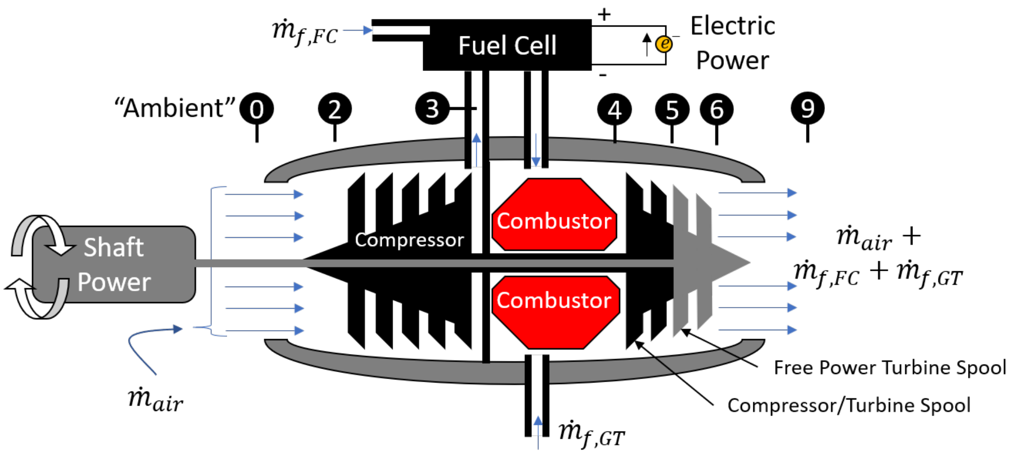

Figure 2.1: GT/SOFC Configuration in Ideal Analysis with mass flow sources and power outputs.

$$w_{GT} = \frac{\dot{W}_{GT}}{\dot{m}_{tot}} = w_{out} - w_{in} \approx c_p(T_4 - T_6) - c_p(T_3 - T_{amb}) \tag{2.2}$$

Note that equation 2.2 assumes that the mass flow rates through the compressor and turbine are approximately equal or $m_{\dot{air}} >> m_{\dot{fuel}}$. This is a reasonable assumption for most gas turbines.

The heat input for this cycle q_{in} is given by equation 2.3 where Δh equals the specific enthalpy released when a certain mass flow rate of fuel $\dot{m}_f$ is burned with a certain mass flow rate of air $\dot{m}_{air}$ that together make up the total mass flow rate $\dot{m}_{tot}$. The temperature reached is related to the fuel enthalpy h_{fuel} and the air-to-fuel ratio $AFR = \dot{m}_{air}/\dot{m}_f$. Substuting Equation 2.3 into Equation 2.1 gives Equation 2.4.

$$q_{in} - q_{out} = \frac{\dot{Q}}{\dot{m}_{tot}} = \frac{\dot{m}_f h_{fuel}}{\dot{m}_{air} + \dot{m}_f} = c_p(T_4 - T_3) \tag{2.3}$$

$$w_{GT} = \frac{\dot{m}_f h_{fuel}}{\dot{m}_{air} + \dot{m}_f} - c_p(T_6 - T_{amb}) \tag{2.4}$$

A gas turbine's performance is generally determined by its overall pressure ratio OPR and the maximum temperature at the combustor exhaust or the turbine inlet temperature (TIT) leading to $T_4 = TIT$. Since we are presuming an ideal gas turbine, we use isentropic relationships to convert between temperature and pressure in a given component. This leads to Equation 2.5 which relates the turbine inlet and exhaust temperatures to the ratio of pressures at the two stations.

$$\frac{TIT}{T_6} = \left(\frac{P_4}{P_9}\right)^{\frac{\gamma-1}{\gamma}} = (OPR)^{\frac{\gamma-1}{\gamma}} \rightarrow T_6 = TIT\,(OPR)^{\frac{1-\gamma}{\gamma}} \tag{2.5}$$

Substituting this into Equation 2.4 gives Equation 2.6.

$$w_{GT} = \frac{\dot{m}_f h_{fuel}}{\dot{m}_{air} + \dot{m}_f} - c_p(TIT(OPR)^{\frac{1-\gamma}{\gamma}} - T_{amb}) \tag{2.6}$$

Equation 2.6 is appropriate for a generic gas turbine cycle; however in a GT/SOFC there is a split between fuel introduced in the FC and fuel introduced directly into the GT combustor[ii] each of which will provide different degrees of heating for the bottoming Brayton cycle.

Recall that the heat provided to the GT combustor from the FC will be the

---

[ii] Fuel added directly into the combustor effectively serves to add whatever enthalpy necessary to achieve the target TIT.

result of waste heat and chemical energy from unburned reactants, which will total to be some proportion of the original fuel enthalpy. Assuming no heat losses to the outside environment for simplicity, the proportion of useful electrical power produced by the FC ($\dot{W}_{FC}$) to the fuel enthalpy passed through the fuel cell ($\dot{m}_{f,FC}h_{fuel}$) is defined as the fuel cell efficiency η_{FC} (Equation 2.7).

$$\eta_{FC} = \frac{\dot{W}_{FC}}{\dot{m}_{f,FC}h_{fuel}} \tag{2.7}$$

The total fuel flow rate includes the flow through the fuel cell $\dot{m}_{f,FC}$ and the flow directly into the GT combustor $\dot{m}_{f,GT}$ such that $\dot{m}_{f,FC} + \dot{m}_{f,GT} = \dot{m}_f$. The ratio of the two flow rates is given by $\sigma_{FC} = \dot{m}_{f,FC}/\dot{m}_f$. The heat contributed to the GT cycle by the fuel introduced into the fuel cell is: $(1 - \eta_{FC})\dot{m}_{f,FC}h_{fuel}$.

Substituting in these variables and the AFR into Equation 2.3 for the flow-specific heat input q_{in}, as well as the isentropic temperature relation for T_3, we can find the relationship between cycle station temperatures T_{amb} and T_4, and the fuel/air streams, shown in Equation 2.8. Additionally, this equation can be rearranged to solve for the TIT (T_4) as shown in Equation 2.9.

$$\frac{h_{fuel}(1 - \sigma_{FC}\eta_{FC})}{AFR + 1} = c_p\left(TIT - T_{amb}\left(OPR\right)^{\frac{\gamma-1}{\gamma}}\right) \tag{2.8}$$

$$TIT = \frac{h_{fuel}(1 - \sigma_{FC}\eta_{FC})}{c_p(AFR + 1)} + T_{amb}\left(OPR\right)^{\frac{\gamma-1}{\gamma}} \tag{2.9}$$

Substituting in Equation 2.9 for T_4 and the FC fuel ratio, OPR, and AFR into

Equation 2.6 and simplifying leads to Equation 2.10 which gives the specific work per unit flow produced by the gas turbine portion of the GT/SOFC.

$$\boxed{w_{GT} = \frac{h_{fuel}\left(1 - \sigma_{FC}\eta_{FC}\right)}{AFR + 1}\left(1 - (OPR)^{\frac{1-\gamma}{\gamma}}\right)} \tag{2.10}$$

Returning to the fuel cell, recall Equation 2.7 for the fuel cell efficiency and note that the useful work generated by the fuel cell as electrical power, $\dot{W}_{FC}$ is unspecified. To rectify that, first consider the actual thermodynamic efficiency of electricity production from the fuel and oxidant reactions, η_{elec} which is generally represented in the cell voltage after all reversible and irreversible losses are accounted for. A baseline approximation of η_{elec} can be calculated per Li [24, p. 99] based on the thermoneutral voltage V_{tn} and the ratio of operating voltage V_{oper} as shown in Equation 2.11 where n is the number of electrons transferred per redox reaction of the fuel, F is Faraday's constant, and Δh is the enthalpy change of the reaction per **mole** of reactant.

$$\eta_{elec} = \frac{V_{oper}}{V_{tn}} = \frac{V_{oper}}{-\Delta h/(nF)} \tag{2.11}$$

In the case of an SOFC operating on pure hydrogen fuel, the lower heating value (LHV) of the combustion reaction with air is -241.8 $\mathrm{kJ\,mol^{-1}}$ [24, p. 50] with two electrons transferred per molecule of fuel, or equivalently 1.253 V. The resulting η_{elec} for a reasonable operating voltage of 0.75 V is 60%. It is possible to do a similar calculation for hydrocarbon fuels. In general, thermoneutral voltages go down with increasing carbon content. For example, the thermoneutral voltage for methane is 1.154 V, while it is 0.839 V for dodecane (a kerosene surrogate). At the same operating voltage of 0.75 V, these yield thermodynamic efficiencies of 65% and 90% respectively!

That larger hydrocarbons yield greater efficiencies may seem unintuitive at first glance since hydrogen is traditionally considered to be the 'better' fuel. However, this is due to the lower amount of energy stored in the hydrocarbon fuel *per mole of hydrogen that may be generated in the resulting syngas.* There are conditions built into this result that are helpful to consider.

First, the presumed operating voltage depends on the chemical condition of the fuel entering into the SOFC with a general performance range set by the dominant reaction (i.e. the fastest charge transfer reaction) taking place at the electrodes. Even for hydrocarbon fuels, the dominant reaction tends to be the elemental hydrogen redox reaction if it is present even in small amounts [72, p. 2386]. This hydrogen is provided by reforming the fuel into a syngas mixture via reaction with some source of oxygen (e.g. air, steam) before that flow enters the fuel cell anode (see Section 1.5).

Second, the process of fuel reformation itself consumes some degree of the electron transfer capability within the fuel (on a molar basis) *if* any elemental oxygen is added to the fuel stream without first reacting across the MEA. This is because the added oxygen consumes part of the fuel streams capacity to absorb oxygen from the cathode, and only this second oxygen source yields electrical power. The addition of oxygen for reformation outside the fuel cell's redox reaction lowers the effective value of n in Equation 2.11, driving up the thermoneutral voltage and lowering the efficiency.

The optimal solution is to perform fuel reformation without adding any new oxygen. This may be achieved using anode gas recirculation (AGR) in which exhaust gas (carrying steam produced at the MEA) from the anode exit is rerouted upstream and back into the reformer [73]. This may be an effective idea with the caveat that the reformation reaction then required (the Water-Gas Shift reaction in Equation 1.1b) is endothermic and will require an additional source of heat (e.g. a smaller amount of atmospheric air reacted with the fuel, as in the ATR method) to operate the system. Internal reformation (via all of the reactions of Equation 1.1) inside the fuel cell anode may also be possible if a suitable catalyst (like Nickel) is present. However, the internal reformation process still requires some initial water to be present, and the rates of reaction are strongly dependent on temperature [24, p. 435-436]. .

If we consider a kerosene-analogous jet fuel using a CPOx reactor (as in this work), we can apply an AFR within the CPOx of between 6 and 9 (in terms of mass) depending on the temperature and pressure conditions [64]. This corresponds to roughly 36% and 54% of outside oxygen supplied for reformation respectively. This reduces the effective n by the same proportion since that oxygen capacity is not available for the transfer of oxygen inside the MEA. A CPOx is the simplest but least efficient reformation option. In this case, if we take the more optimistic (i.e. low AFR) case of $AFR = 6$ for a CPOx and use that to moderate the number of electrons transferred in Equation 2.11, we find $\eta_{elec} = 54\%$ for the 0.75 V operating voltage.

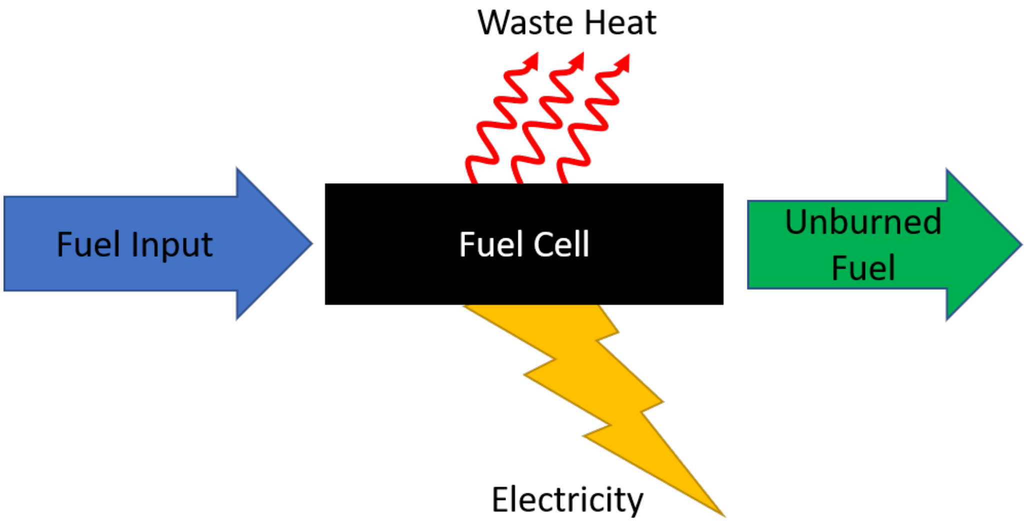

Figure 2.2: Representation of idealized fuel cell energy inputs and outputs for GT/SOFC cycle analysis.

A second consideration is that the fuel cell "burns" fuel progressively as it flows along the fuel cell's surface (anode) leading to some amount of fuel that is converted into products ($\dot{m}_{f,FC,burned}$) by the time the fuel flow leaves the FC. An idealized visualization of this breakdown is presented in Figure 2.2. This enables us to represent the power produced by the fuel cell using Equation 2.12.

$$\dot{W}_{FC} = \dot{m}_{f,FC,burned} h_{fuel} \eta_{elec} \tag{2.12}$$

We can also represent the degree of fuel conversion nondimensionally in terms of a "utilization" $U_{FC} = \dot{m}_{f,FC,burned}/\dot{m}_{f,FC}$, i.e. the proportion of fuel introduced into the fuel cell that is reacted by the fuel cell (with the enthalpy released as electric power or waste heat). Substituting these terms into Equation 2.7, leads to Equation 2.13. This is interesting in that it shows that one must have high electrical conversion efficiency *and* high utilization to achieve high fuel cell efficiency. However improving each aspect has different impacts on thermal management and mass of the SOFC.

$$\eta_{FC} = \eta_{elec} U_{FC} \tag{2.13}$$

We can also derive an expression for the *specific* fuel cell electrical power generation w_{FC} which is the power produced by the fuel cell $\dot{W}_{FC}$ normalized by the total mass flow rates of air and fuel (Equation 2.14). Note that this is the same normalization performed for the GT portion of the cycle.

$$w_{FC} = \frac{\dot{W}_{FC}}{\dot{m}_f + \dot{m}_{air}} \tag{2.14}$$

Now that we have two expressions for the useful electrical work from the fuel cell $\dot{W}_{FC}$, we can combine Equations 2.12 and 2.14, substitute the utilization and air-to-fuel ratio into the expression, and solve for the fuel cell specific work:

$$\boxed{w_{FC} = \frac{\eta_{elec} U_{FC} \sigma_{FC} h_{fuel}}{AFR + 1}} \tag{2.15}$$

For the purposes of the analysis in this chapter, we will not delve any further into the inner workings of the fuel cell. Instead, we will take the efficiency and utilization as design parameters (or performance targets) after establishing the rest of the GT/SOFC cycle. In that vein, we define the system thermal efficiency of a GT/SOFC system as the total extracted power divided by the maximum available fuel power in a manner that is similar to Equation 1 from Braun [51].

$$\eta_{sys} = \frac{\dot{W}_{GT} + \dot{W}_{FC}}{\dot{m}_f h_{fuel}} \tag{2.16}$$

Dividing both numerator and denominator of the right hand side of Equation 2.16 by the sum of the mass flow rates of air and fuel gives an alternate expression for the system thermal efficiency of the system in terms of the AFR and the specific power of the turbine and fuel cell:

$$\eta_{sys} = \frac{\left(w_{GT} + w_{FC}\right)\left(AFR + 1\right)}{h_{fuel}} \tag{2.17}$$

The specific work of the fuel cell and gas turbine can replaced with Equations 2.15 and 2.10 respectively, and after simplification leads to a new expression for the system thermal efficiency in terms of the electrical efficiency and utilization of the fuel cell, the overall pressure ratio of the turbine, and the ratio of the fuel mass flow rate of fuel through the fuel cell to the total fuel mass flow rate (σ_{FC}). Note that as with the traditional Brayton cycle, the system thermal efficiency is independent of the station 4 maximum temperature (i.e. TIT).

$$\boxed{\eta_{sys} = \left(1 - (OPR)^{\frac{1-\gamma}{\gamma}}\right) + \eta_{elec} U_{FC} \sigma_{FC} (OPR)^{\frac{1-\gamma}{\gamma}}} \tag{2.18}$$

One of the most important points to note in Equation 2.18 is that the system thermal efficiency is the addition of two terms. The first term is just the thermal efficiency of the Brayton cycle, which is dependent only on the pressure ratio. This is the bottom floor of the GT/SOFC system thermal efficiency, since the second term consists of the fuel cell terms (all taking values between zero and one) and a pressure ratio term, also always between zero and one for any pressure ratio above one. The takeaway is that the system thermal efficiency of a GT/SOFC is always greater than that of a gas turbine alone with the same design parameters, no matter the efficiency or size of the SOFC subsystem. A more efficient or proportionally-larger SOFC yields better benefits, but there is still a benefit even if the SOFC subsystem is less efficient than the gas turbine cycle.

Equation 2.18 can also be rearranged to yield an expression for the electrical efficiency:

$$\eta_{elec} = \frac{\eta_{sys} + (OPR)^{\frac{1-\gamma}{\gamma}} - 1}{U_{FC}\sigma_{FC}(OPR)^{\frac{1-\gamma}{\gamma}}} \tag{2.19}$$

We can also solve for other interesting quantities such as the AFR by solving Equation 2.17 for AFR and substituting the specific work terms and Equation 2.18 for η_{sys} to yield Equation 2.20. Furthermore, the total specific power comes from the addition of the specific work terms from Equations 2.15 and 2.10 to create Equation 2.21). The ratio of work produced by the fuel cell to that of the gas turbine cycle comes from the division of those terms instead in Equation 2.22. Hereafter we will define Equation 2.22 as θ.

$$AFR = \frac{h_{fuel}\left(1 - \eta_{elec}U_{FC}\sigma_{FC}\right)}{c_p\left(TIT - T_{amb}(OPR)^{\frac{\gamma-1}{\gamma}}\right)} - 1 \tag{2.20}$$

$$w_{FC} + w_{GT} = c_p \left(TIT - T_{amb} \left(OPR \right)^{\frac{\gamma-1}{\gamma}} \right) \left[\left(1 - \left(OPR \right)^{\frac{1-\gamma}{\gamma}} \right) + \frac{\eta_{elec} U_{FC} \sigma_{FC}}{1 - \eta_{elec} U_{FC} \sigma_{FC}} \right] \tag{2.21}$$

$$\theta = \frac{w_{FC}}{w_{GT}} = \frac{\eta_{elec} U_{FC} \sigma_{FC}}{\left(1 - \eta_{elec} U_{FC} \sigma_{FC} \right) \left(1 - \left(OPR \right)^{\frac{1-\gamma}{\gamma}} \right)} \tag{2.22}$$

Of particular importance is the total specific power, Equation 2.21, which consists of three major terms. The first is the heat addition to the Brayton cycle, $c_p \left(TIT - T_{amb} \left(OPR \right)^{\frac{\gamma-1}{\gamma}} \right)$ with the square brackets containing the final two terms. These last two terms are first the Brayton cycle efficiency $\left(1 - \left(OPR \right)^{\frac{1-\gamma}{\gamma}} \right)$, and a factor consisting of the SOFC design variables that will always evaluate to a value greater than zero. Similarly to Equation 2.18 for the system thermal efficiency, this arrangement implies that the presence of the SOFC subsystem at any size or efficiency will increase the specific work of the GT/SOFC system.

At this point we have relationships for a GT/SOFC thermodynamic cycle as a function of basic design parameters, omitting the electrochemical details of fuel cell operation. However given reasonable fuel cell metrics for electrical efficiency, fuel utilization, and the proportion of fuel sent to the fuel cell in the cycle in place of those electrochemical details, we can implicitly determine performance for the whole cycle collectively with the traditional Brayton cycle parameters of ambient and maximum temperature conditions along with the overall pressure ratio.

The next section will discuss how we might represent this cycle graphically.

2.2 GT/SOFC Cycle Representation

A traditional representation of a Brayton cycle is through a plot of temperature and entropy, the so-called "T-s diagram," an example of which is provided in Figure A.3. One may be constructed from the ambient and maximum temperatures of the cycle (T_2 and T_4 respectively) and the overall pressure ratio. In the GT/SOFC cycle considered here, the fundamental processes of the Brayton cycle remain unchanged but the there are now several sources of isobaric heat addition: (1) the net waste heat emitted by the reformer/fuel cell during fuel reformation and electricity generation Δh_η, (2) the enthalpy remaining in the fuel not consumed by the SOFC Δh_U, and (3) the enthalpy in the additional fuel added directly to the gas turbine combustor Δh_c. The latter is adjusted to complete the isobaric heat addition to T_4.

The net heat released inside the fuel cell due to inefficiencies in the electrochemical oxidation process in the fuel cell can be inferred by replacing η_{elec} with $11 - \eta_{elec})$ in Equation 2.15 leading to:

$$\Delta h_\eta = \frac{(1 - \eta_{elec})\, U_{FC} \sigma_{FC} h_{fuel}}{AFR + 1} \tag{2.23}$$

Similarly, the enthalpy of the fuel that is not oxidized in the fuel cell and is later burned in the combustor can be inferred by replacing U_{FC} with $(1 - U_{FC})$ in Equation 2.15 leading to: .

$$\Delta h_U = \frac{(1 - U_{FC})\, \sigma_{FC} h_{fuel}}{AFR + 1} \tag{2.24}$$

The sum of Δh_η and Δh_U is the net contribution of the fuel cell to the heat addition to the cycle. Both of these heat additions can be expressed as temperature and enthalpy additions to the cycle. These are plotted consecutively in T-s space starting from the compressor exhaust temperature. Note that these heat additions are *average* temperature changes considering effects on the entirety of airflow through the system; where flow necessarily splits inside the SOFC for example, there may be different local temperatures or cycle paths.

Finally, there should be some representation of the "work" performed by the fuel cell.

On a T-s diagram, work into and out of the ideal Brayton cycle is represented by differences in temperatures between stations 2 → 3 and 4 → 6 respectively. For the calorically perfect assumption, the net useful work produced by the Brayton cycle is the difference between the work output and input (see Equation 2.2). The problem is that part of the "work" done by the fuel cell is electrochemical in nature (associated with driving electrons against a potential) and therefore not fully relatable to the *pdv* work of the Brayton and other thermally-based power cycles that the temperature changes in T-s diagrams represent. The solution is to capture the heat addition associated with the reformer/fuel cell assembly in the T-s plane while adding a third orthogonal axis to capture the energy change.[iii]

An example of such a cycle diagram for the GT/SOFC is presented in Figure 2.3. The inputs used to generate it are presented in Table 2.1. Also indicated on

---

[iii] Energy on this third axis is reported in temperature units assuming a calorically perfect gas (per $\Delta H = c_p \Delta T$) in order to be consistent with, and to permit comparisons to, the temperature axis in the traditional T-s space.

the diagram are different components of heating between stations 3 and 4, as well as the compressor-linked-turbine $\dot{W}_{t,c}/\dot{m}c_p$ and free-turbine $\dot{W}_{t,f}/\dot{m}c_p$ work components between stations 4 and 6. The diagram shows that the specific work of the fuel cell and turbine are roughly equal ($\theta = 0.998$). It should be noted, however, that the assumed efficiency of electrical conversion inside the fuel cell $\eta_{elec} = 0.71$ corresponds to approximately 0.9 V which may be unreasonably high once reversible and irreversible losses are taken into account. Additionally, the heat released inside the fuel cell (the red line) does not bring *all* of the flow up to the cell operating temperature of 625°C (898 K)—an appropriate temperature for the intermediate-temperature SOFCs being considered here. This is why the fuel cell operating temperature lies beyond the red region of the heat release profile that is associated with electrochemical conversion.

Table 2.1: Baseline Inputs for GT/SOFC Cycle Results, unless otherwise stated.

Variable	Value	Units
OPR	15	n/a
γ	1.4	n/a
c_p	1006	$\mathrm{J\,kg^{-1}\,K^{-1}}$
h_{fuel}	5.55×10^7	$\mathrm{J\,kg^{-1}}$
TIT	1600	K
T_{amb}	251.8	K
T_{FC}	898	K
U_{FC}	0.7	n/a
σ_{FC}	0.7	n/a
η_{elec}	0.6	n/a

However, this operating constraint is not guaranteed, and represents a physical limitation within the assumptions of this ideal cycle.[iv] Specifically, if energy is to be conserved within the cycle (and not cooled by some other means such as fan

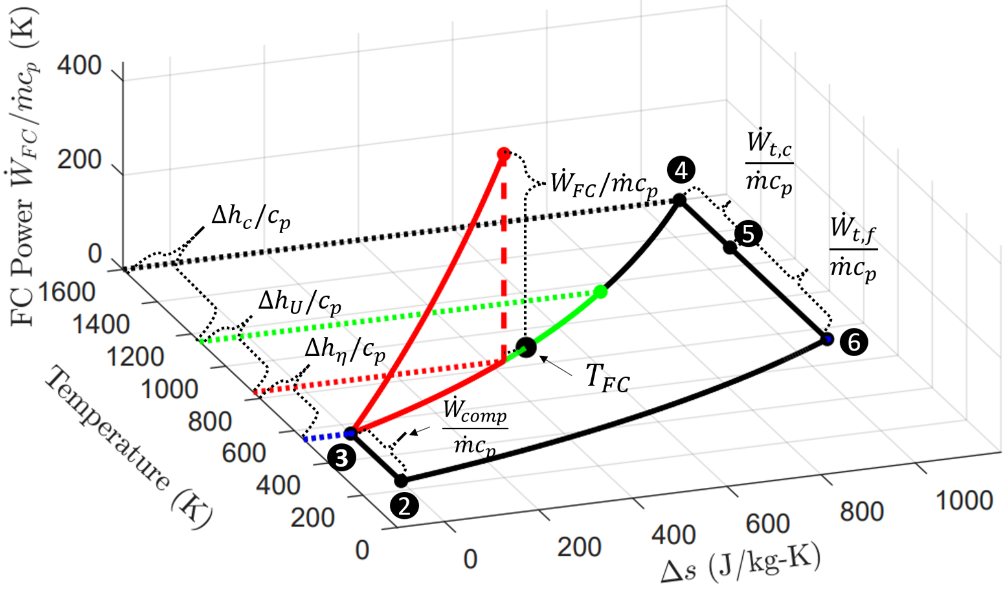

Figure 2.3: Sample T-s diagram of a hybrid GT/SOFC Cycle based on inputs from Table 2.1.

.

bypass air), the isothermal assumption for the fuel cell is broken if the required absorption of waste heat Δh_η drives the temperature of all flow through the system above the safe operating temperature of the fuel cell. Temperatures may be locally maintained at the operating temperature inside the fuel cell anode and cathode up to this point, but more heat release after that point will necessarily increase the temperature. This limitation is illustrated in Figure 2.4. Note in the figure that the average temperature of the total air flow rate through the system ("combined flow") is the relevant value plotted in T-s space in the GT/SOFC cycle diagram.

This physical limitation is not absolute; the idealized fuel cell stage considered here includes any fuel reformation process. Some reformation methods may be operated at a higher temperature than the SOFC (for example, CPOx reformers)

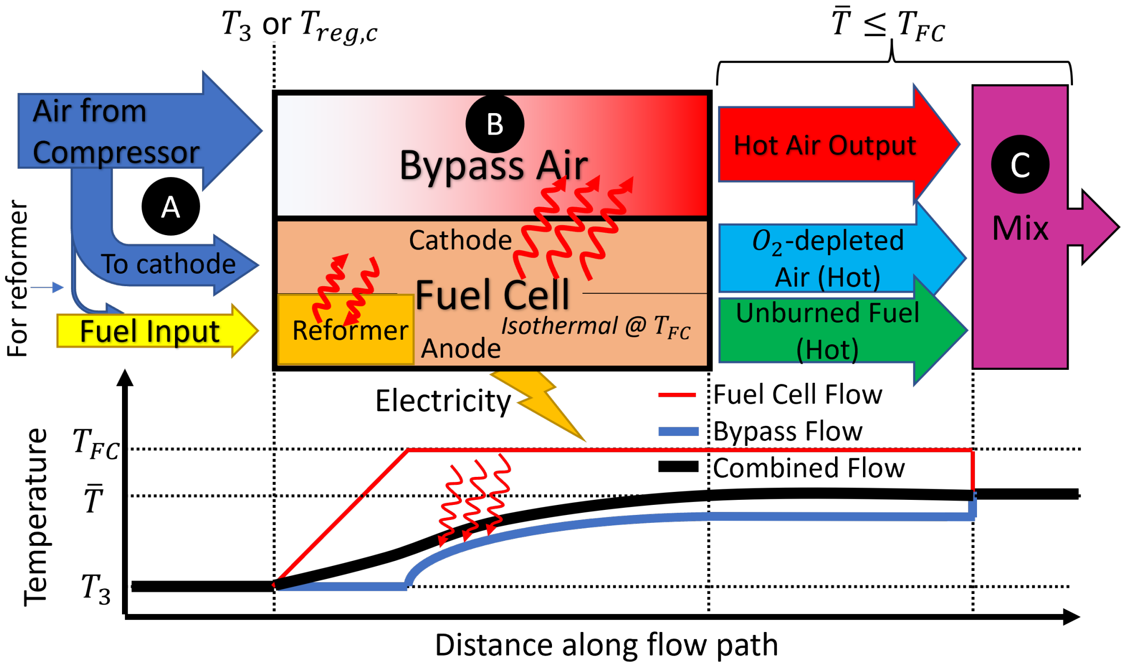

Figure 2.4: Conceptual sketch of GT/SOFC cycle fuel cell heat loss limit.

that might allow for a higher temperature exhaust via a counterflow heat exchanger. However, from a practical perspective the excess heat produced in the fuel cell during reformation is minimized as much as possible to improve efficiency. Furthermore, an effective heat exchanger for this scenario is likely complicated—though not without value! For this chapter considering ideal analysis, the fuel cell operating temperature is considered an instructive limit regardless.

To account for this limit, we can mark a limit based on one of our design variables, for instance the fuel cell efficiency η_{elec} which will linearly control the amount of heat released within the fuel cell. If the design electrical efficiency is

---

[iv] Near-equivalent descriptions are mentioned in the literature as well, such as by Ji. et. al., but put in terms of compressor vs. SOFC outlet temperatures to enable air cooling [49]. This particular study did not vary fuel cell characteristics, leading to specific operating limitations of pressure ratio and flight Mach number.

below this minimum limit, then the GT/SOFC cycle will be non-physical.

Once again considering the calorically-perfect gas assumption, we can determine the limiting specific heat release Δh_{lim} to be the enthalpy that reaches the fuel cell operating temperature T_{FC}. Equation 2.25 provides this relationship, after a substitution for the compressor exhaust temperature via the isentropic relationships.

$$\Delta h_{lim} = c_p \left(T_{FC} - T_{amb}(OPR)^{\frac{\gamma-1}{\gamma}} \right) \tag{2.25}$$

Combining this equation with Equation 2.23 for the specific heat released based on the other cycle inputs, and substituting for the AFR via Equation 2.20, we can derive Equation 2.26 providing the minimum physical fuel cell electrical efficiency, $\eta_{elec,min}$. Note however that this expression could be instead solved for any of the other fuel cell design variables (U_{FC}, σ_{FC}) if preferred, but the value of η_{elec} is generally more constrained by fuel cell material characteristics than the other design variables.

$$\eta_{elec,min} = \frac{T_{FC} + \left(\sigma_{FC} U_{FC} - 1\right) T_{amb}(OPR)^{\frac{\gamma-1}{\gamma}} - (TIT)\, \sigma_{FC} U_{FC}}{\sigma_{FC} U_{FC} \left(T_{FC} - TIT\right)} \tag{2.26}$$

In practice, this equation should only come into play to indicate if the design conditions are non-physical in terms of maintaining fuel cell operating temperature.

2.3 Range Modeling

Alone, the GT/SOFC cycle immediately indicates some straightforward behavior: first, per Equation 2.18, the system efficiency always rises with increasing OPR, as well as with increasing fuel cell efficiency, utilization, and fuel proportion through the fuel cell—with the caveat of the fuel cell cooling limitation from Equation 2.25. However this conclusion ignores the tradeoffs for improving these characteristics, which for the most part will be an increase in mass due to the addition of the fuel cell components.

Those tradeoffs have large impacts on vehicle range and endurance[v]. We will explore these by modifying the Breguet range equation [74, p. 152; 71, p. 41]for aircraft with GT/SOFC propulsion systems. This derivation is an extension of a similar analysis by Daniel Waters [31, p. 203].

One may design a range equation for a wide array of different analytical scenarios and assumptions. In this case, we will consider an aircraft flying at a constant velocity v and altitude, with the GT/SOFC power output scaling to match the demand. This last condition implies a constant thrust-specific fuel consumption (TSFC). The effect of energy conversion system weight is captured by representing the lift to drag ratio of the aircraft using a drag polar. Increases in weight result in increases in angle of attack and reduced lift/drag ratio.

In contrast with the prior work by Waters where the TSFC referred only to the GT performance (as SOFC electric power was used for secondary purposes), here

---

[v] For our purposes here, the presumed speed of the aircraft is constant such that range implies endurance and vice versa. As such, we will only derive a range equation for simplicity.

the TSFC is determined from the performance of the full GT/SOFC cycle for the given scenario. More specifically, this derivation applies the electric power generated to propulsion, and limits the total mass of the system m_{tot} such that a larger engine mass m_{eng} leaves less mass for the full fuel capacity $m_{f,ini}$, rather than increasing the overall mass as the propulsion system becomes heavier. This setup is intended to maintain the overall expected handling performance for the given airframe, and helps illustrate the tradeoffs between fuel-storage and GT/SOFC mass. Furthermore, this approach is similar to that followed by Okai et. al. [45].

Building off of Appendix A.1 by Waters [31, p. 204], consider a fundamental expression for the range R of a fuel-burning aircraft provided in Equation 2.27.

$$R = \int_{m_{fin}}^{m_{ini}} v \frac{\mathrm{d}m}{\dot{m}_f} \tag{2.27}$$

Here m_{fin} is the final aircraft mass (with all fuel expended) while m_{ini} is the initial aircraft mass, fully loaded with fuel. Since the fuel flow rate is the only substantial mechanism for changing the aircraft mass, we can track the other contributions separately (i.e. $m_{ini} = m_{f,ini} + m_0 + m_{eng}$, with m_0 representing the aircraft's structure and payload mass) allowing us to rewrite Equation 2.27 in terms of just the fuel mass for Equation 2.28.

$$R = \int_{0}^{m_{f,ini}} v \frac{\mathrm{d}m_f}{\dot{m}_f} \tag{2.28}$$

With a given structure/payload and total mass for an aircraft, we only need to establish an engine mass and a fuel flow rate based on our GT/SOFC cycle. Starting with the fuel flow rate, we assume that the aircraft is in straight, level, and constant speed flight so that the propulsive power $\dot{W}_{prop}$ exactly equals the power to overcome drag D or $\dot{W}_{prop} = vD$. The thrust power is created from the GT/SOFC cycle's electric power, moderated by some propulsive efficiency η_{prop} of the distributed fans necessary to convert the electrical power into a change in momentum of surrounding air. Per Equation 5.13 by Hill and Peterson, except replacing the thermal efficiency with our system efficiency, we find Equation 2.29 for the fuel flow rate [74, p. 151].

$$\dot{m}_f = \frac{vD}{\eta_{sys}\eta_{prop}h_{fuel}} \tag{2.29}$$

Presuming steady flight, we can also quickly reframe Equation 2.29 in terms of the thrust-specific fuel consumption (TSFC) in Equation 2.30, which normalizes the fuel flow rate by the produced thrust of the system.

$$TSFC = \frac{\dot{m}_f}{D} = \frac{v}{\eta_{sys}\eta_{prop}h_{fuel}} \tag{2.30}$$

A standard treatment in aircraft design is to express the lift and drag with non-dimensional coefficients of lift $C_L = \frac{L}{\frac{1}{2}\rho v^2 S}$ and drag $C_D = \frac{D}{\frac{1}{2}\rho v^2 S}$ respectively, and then relate those coefficients using a "drag polar" (that relates the coefficients to each-other) of the form $C_D = C_{D,min} + K\left(C_L - C_{L,min}\right)^2$ [75, p. 262].[vi] Here ρ is the air density, S is the wing area. The variables K, $C_{D,min}$, and $C_{L,min}$ are all fitted parameters for a particular airframe.

[vi] Other forms of the drag polar may also be used, but they all include some reference to the lift force such that the general steps of this derivation remain appropriate.

Replacing the drag in Equation 2.29 with the drag polar and expressing the lift force L using a lift coefficient C_L yields Equation 2.31.

$$\dot{m}_f = \frac{v\left(C_{D,min} + K\left(\frac{L}{\frac{1}{2}\rho v^2 S} - C_{L,min}\right)^2\right)\frac{1}{2}\rho v^2 S}{\eta_{sys}\eta_{prop}h_{fuel}} \tag{2.31}$$

In order to maintain a constant altitude, the lift must equal weight such that $L = mg$, where g is the acceleration due to gravity. The mass however changes from the initial mass over the course of the flight as the fuel is expended, with the engine and structure/payload masses remaining constant. Additionally, from the GT/SOFC cycle we can substitute in the system efficiency (Equation 2.18). Together, these alterations yield Equation 2.32.

$$\dot{m}_f = \frac{v\left(C_{D,min} + K\left(\frac{m_f+m_0+m_{eng}}{\frac{1}{2}\rho v^2 S}g - C_{L,min}\right)^2\right)\frac{1}{2}\rho v^2 S}{\left(\eta_{elec}U_{FC}\sigma_{FC} + (1-\eta_{elec}U_{FC}\sigma_{FC})\left(1-(OPR)^{\frac{1-\gamma}{\gamma}}\right)\right)\eta_{prop}h_{fuel}} \tag{2.32}$$

The fuel flow rate is now determined in terms of design constants, the fuel mass, and the mass of the engine which has thus far been unspecified, but is required for establishing the initial fuel mass in any case. We can make an estimation of the engine mass by presuming that the engine needs to be designed to provide the maximum required power, i.e. the power required at full fuel load $\dot{W}_{prop,ini}$. The basic mass relationship shown in Equation 2.33 is through the GT/SOFC structure-specific power $p_{GT/SOFC}$.

$$m_{eng} = \frac{\dot{W}_{prop,ini}}{p_{GT/SOFC}} \delta_{fans} \tag{2.33}$$

The specific power of the GT/SOFC represents the total power produced, normalized by the total mass of the system. As a substantial simplification, we can consider both the power produced and the mass to be sums of the gas turbine and fuel cell contributions to each characteristic, as in Equation 2.34. An additional multiplicative mass factor δ_{fans} is included to account for the additional mass of the electrical control system, propulsor fans, and motors necessary to convert the electrical power to momentum in the flow.[vii]

$$p_{GT/SOFC} = \frac{\dot{W}_{GT} + \dot{W}_{FC}}{m_{GT} + m_{FC}} \tag{2.34}$$

If we recall the dimensionless variable θ defined in Equation 2.22 as the relationship between the flow-specific power produced by the fuel cell and gas turbine, we can apply the same relationship to the non-normalized powers such that we can put the fuel cell power produced in terms of the gas turbine power via $\dot{W}_{FC} = \theta \dot{W}_{GT}$, such that $\dot{W}_{prop,ini} = (1 + \theta)\, \dot{W}_{GT}$.

We can also provide reasonable values of the structure-specific powers of the gas turbine $p_{GT} = \frac{\dot{W}_{GT}}{m_{GT}}$ and fuel cell[viii] $p_{FC} = \frac{\dot{W}_{FC}}{m_{FC}}$ components. Structure-specific power values are often available in the literature for real systems (modern turbofans are currently approximately 15kW/kg [2]), or can be modeled separately, for example

---

[vii] These masses might also be included in $p_{GT/SOFC}$, but they are not directly dependent on the GT/SOFC cycle characteristics, instead scaling primarily with the overall power produced.

as in Waters [31, Ch. 4.3].

With the structure-specific powers, we can substitute for the masses in Equation 2.34 as well as the maximum propulsive power in terms of θ and the gas turbine power contribution. The result after all GT power contributions cancel is Equation 2.35, which leaves the specific power of the combined GT/SOFC system in terms of θ and the individual component specific powers alone.

$$p_{GT/SOFC} = \frac{1+\theta}{\frac{1}{p_{GT}} + \frac{\theta}{p_{FC}}} \tag{2.35}$$

Returning to the GT/SOFC "engine" mass from Equation 2.33, first recall that $\dot{W}_{prop} = vD$. The maximum power required in Equation 2.33 can be found by substituting for the drag D again with the drag polar form as in Equation 2.31, except with the static value for the mass of m_{ini}. Substituting both the propulsive power and GT/SOFC specific power from Equation 2.35, we arrive at Equation 2.36.[ix]

$$m_{eng} = \frac{v\left(C_{D,min} + K\left(\frac{m_{ini}}{\frac{1}{2}\rho v^2 S}g - C_{L,min}\right)^2\right)\frac{1}{2}\rho v^2 S\left(\frac{1}{p_{GT}} + \frac{\theta}{p_{FC}}\right)}{1+\theta}\delta_{fans} \tag{2.36}$$

With the GT/SOFC engine mass established, we can substitute this expression

---

[viii] The specific power of the fuel cell is taken to be that of the whole stack with supporting interconnects, etc. and will vary as a function of multiple variables including the electrical efficiency and the utilization

[ix] This mass formulation bears a close resemblance to that used by Okai et. al. [44], with the addition of θ and without consideration of power conditioning or fan mass. Since these latter components are (arguably) linearly-dependent on the power produced, they are encapsulated in the single correction factor δ_{fans}.

into the fuel flow rate (Equation 2.32) which is in turn substituted into the range equation (Equation 2.28). Finally, recall that the upper limit of integration $m_{f,ini}$ in Equation 2.28 is solvable via $m_{f,ini} = m_{ini} - m_0 - m_{eng}$.

The resulting range equation is provided below in Equation 2.37, though the expressions that result in constants (θ, m_{eng}, $m_{f,ini}$) are left un-substituted for simplicity.

$$R = \int_0^{m_{f,ini}} \frac{\left(\eta_{elec}U_{FC}\sigma_{FC} + (1-\eta_{elec}U_{FC}\sigma_{FC})\left(1-(OPR)^{\frac{1-\gamma}{\gamma}}\right)\right)\eta_{prop}h_{fuel}}{\left(C_{D,min} + K\left(\frac{m_f+m_0+m_{eng}}{\frac{1}{2}\rho v^2 S}g - C_{L,min}\right)^2\right)\frac{1}{2}\rho v^2 S}\,\mathrm{d}m_f \tag{2.37}$$

If we carry out this integration, using now the un-substituted η_{sys} from Equation 2.18 for compactness, we reach Equation 2.38. This expression provides a single performance metric (an aircraft's range) through which we can compare the overall effect of different GT/SOFC cycle design parameters on a notional aircraft.

$$R = -\frac{\eta_{sys}\eta_{prop}h_{fuel}}{\sqrt{KC_{D,min}g}}\tan^{-1}\left(\sqrt{\frac{K}{C_{D,min}}}\frac{\left(C_{L,min}\frac{1}{2}\rho v^2 S - g\left(m_f+m_0+m_{eng}\right)\right)}{\frac{1}{2}\rho v^2 S}\right)\Bigg|_{m_f=0}^{m_f=m_{f,ini}} \tag{2.38}$$

Note that in order to use Equation 2.38, θ, m_{eng}, $m_{f,ini}$, and AFR need to be substituted for as well along the way.

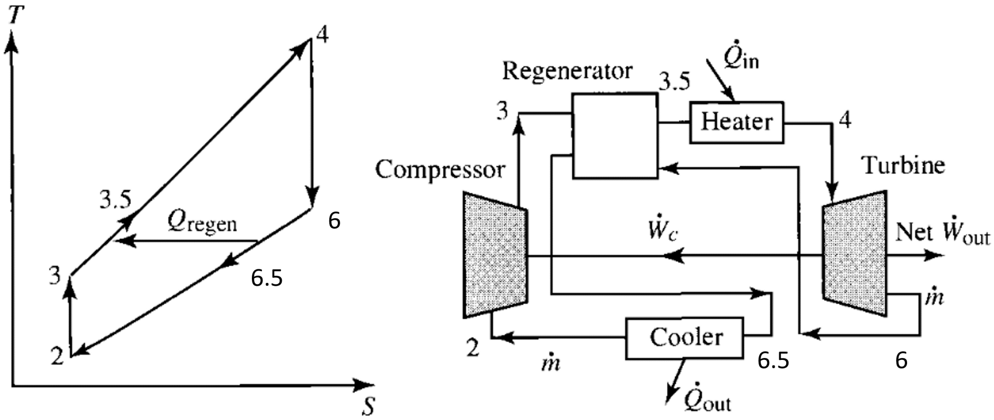

Figure 2.5: Ideal Brayton cycle with recuperation, T-s diagram and block diagram. Reproduced from Mattingly [71, p. 256] with minor modification of station numbers to match Figure 2.7

2.4 Recuperation

One common strategy for improving the efficiency of the Brayton cycle, with or without fuel cell components, is *recuperation.*[x] This section will provide an analysis that includes this strategy into the previous GT/SOFC cycle derivation. Recuperation, illustrated in Figure 2.5, places a heat exchanger (HEX) between the compressor and turbine exhausts (stations 3 and 9 respectively in Figure 2.5) allowing waste heat in the turbine exhaust to preheat the compressor exhaust before it enters the combustor lowering the amount of fuel needed to raise the flow temperature to the turbine inlet temperature. The cycle is illustrated in Figure 2.5) [71, p. 252-257]. Note, however, that recuperation only works if the turbine exhaust is hotter than the compressor exhaust.

---

[x] An alternative term for this process is "regeneration" (usually used in power plant contexts) and the equivalent component a "regenerator" instead of a recuperator.

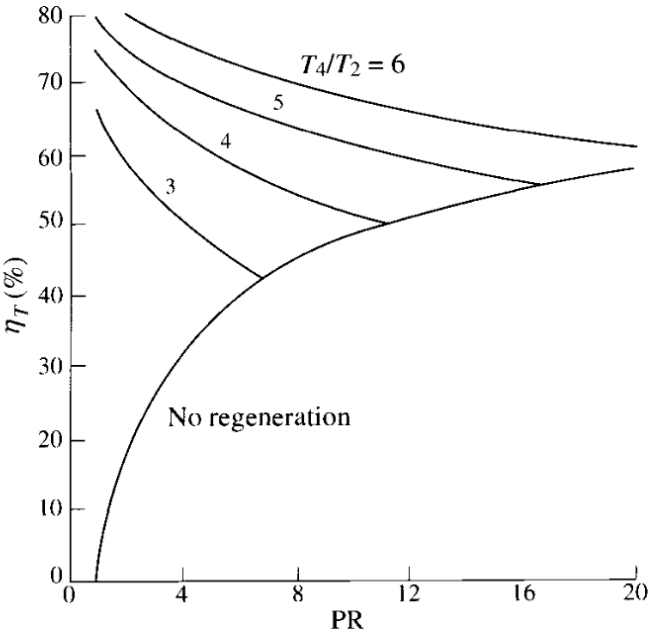

Figure 2.6: Efficiency of ideal Brayton cycle with recuperation at varying pressure and temperature ratios. Reproduced from Mattingly [71, p. 256]

Presuming a perfect recuperating heat exchanger, the resulting ideal thermal efficiency η_T can be calculated from Equation 2.39 [71, p.257]. At low pressure ratios PR, the efficiency improvements can be substantial—and in fact recuperation is common in ground-based power generation with steam turbines. However the advantage drops away rapidly with increasing pressure ratios at any given maximum-to-ambient temperature ratio, as can be seen in Figure 2.6. For context, the temperature ratio of modern jet engines can be between 5–8 for a $T_4 = TIT$ of 1600K, depending on operating altitude (which determines T_2).

$$\eta_T = 1 - \frac{(PR)^{(\gamma-1)/\gamma}}{T_4/T_2} \tag{2.39}$$

Ground applications of GT/SOFC systems often incorporate some kind of recuperation process as part of the overall cycle [76]. At least one analysis comparing system configurations with and without the recuperative cycle show that it is effectively a trade between higher pressure ratios (for the GT components) and higher weight/comnplexity (for recuperator) [32]. Although the concept has also been considered for many years in un-hybridized aircraft applications [77–79], recuperation tends to be difficult to implement. This is because air-to-air heat exchangers with high effectiveness (i.e. approaching ideal behavior) are large, heavy, and add substantial complexity to the flowpath. These disadvantages are much less problematic in ground-based scenarios. Furthermore, the recuperation strategy depends upon a relatively low overall pressure ratio to maintain the exhaust temperature difference, which goes against the standard trends for aircraft turbomachinery to target higher pressure ratios for greater compactness and flow-specific work[xi] in addition to improved efficiency.

However, in the case of an airborne GT/SOFC, there still could be an optimal middle-ground since GT/SOFC systems already require additional flow path complexity, and provide enhancement to the flow-specific work. On the other hand, the heat added to the flow via recuperation contributes to the cooling limitation discussed in Section 2.2.

[xi] A similar thermodynamic strategy for improving the flow-specific work of the Brayton cycle is called *reheat*. Reheat adds more energy to the flow after the turbine used to drive the compressor, but before the additional power extraction turbine [71, p. 252-257]. Since the first turbine's exhaust is still at higher pressure than ambient, the additional heating functions as a second Brayton cycle at a lower OPR. Operating with reheat dodges turbine temperature limits to extract more work per unit of flow through the system, but lowers the system efficiency since the reheat stage is less efficient with the lower OPR. Reheat is usually applied in scenarios like afterburners for combat aircraft rather than airliners, so the process is not considered further here.

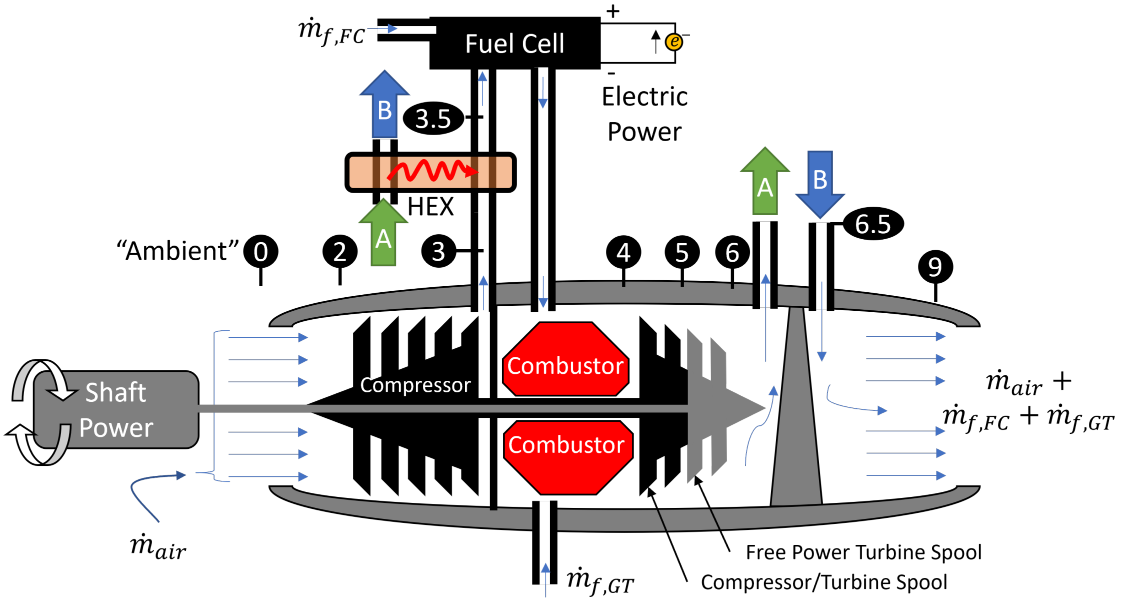

Figure 2.7: GT/SOFC Configuration with Recuperator in Ideal Analysis with mass flow sources and power outputs. Arrows "A" and "B" denote connected flow locations and direction

Without further preamble, we can consider a recuperating HEX placed into the GT/SOFC cycle, perhaps as depicted in Figure 2.7. Using the same assumptions as Section 2.1, we can represent the thermal efficiency of the baseline Brayton cycle with recuperation in terms of the work produced $\dot{W}_{GT}$ and the cycle heat input $\dot{Q}_{in}$ in Equation 2.40 per Mattingly [71, p. 22].

$$\eta_T = \frac{\dot{W}_{GT}}{\dot{Q}_{in}} \tag{2.40}$$

With the presumption that the fuel mass flow rates are relatively small, we can again approximate that the mass flow rates through the compressor, combustor, and turbine are equal. As such, following Equation 2.2 the flow-specific work produced by the Brayton cycle may be written as the difference between the work input (compressor) and output (turbine), differences in enthalpies across the components, differences in temperatures across the components (assuming constant specific heats).

However, the flow-specific heat $q_{in} = \dot{Q}/\dot{m}_{tot}$ that is added varies from Equation 2.3 in the starting temperature: instead of starting at the compressor exhaust temperature T_3, it begins at the cold-side recuperator exhaust temperature $T_{3.5} = T_3 + \Delta T_{comp}$. Also recalling that $T_4 = TIT$, we can generate Equation 2.41. Noting that the heat output will be similarly impacted, we can also generate Equation 2.42 from a similar process through $T_{6.5} = T_6 - \Delta T_{turb}$.

$$q_{in} = \frac{\dot{Q}_{in}}{\dot{m}_{tot}} = \frac{\dot{m}_f h_{fuel}}{\dot{m}_{air} + \dot{m}_f} = c_p(TIT - T_{3.5}) \tag{2.41}$$

$$q_{out} = \frac{\dot{Q}_{out}}{\dot{m}_{tot}} = c_p(T_{6.5} - T_{amb}) \tag{2.42}$$

In turn, both recuperator exhaust temperature differences are calculated from the (here given) effectiveness ϵ, which is the ratio of the actual heat transfer rate achieved by the HEX to the maximum possible heat transfer rate between the two flows (Equation 2.43).

$$\epsilon = \frac{\dot{Q}_{HEX}}{\min\left(\dot{m}_1 c_{p_1}, \dot{m}_2 c_{p_2}\right)(T_6 - T_3)} \tag{2.43}$$

Here $\dot{m}_1$ and $\dot{m}_2$ are the flow rates on each side of the heat exchanger. However in this analysis so far we have made the assumption that the fuel mass flow rate is relatively small such that the flow rates through the compressor and turbine are taken to be equal. Similarly, the specific heat of air has also been taken to be constant, such that $c_{p_1} = c_{p_2}$. As a result, noting that because of these assumptions $\dot{Q}_{HEX} = \dot{m} c_p \Delta T$ and that $\Delta T_{comp} = \Delta T_{turb}$, Equation 2.43 simplifies substantially to a ratio of temperature differences, $\epsilon = \Delta T / (T_6 - T_3)$ through which we may substitute and solve for $T_{3.5}$ (Equation 2.44) and $T_{6.5}$ (Equation 2.45).

$$T_{3.5} = \epsilon \left(T_6 - T_3\right) + T_3 \tag{2.44}$$

$$T_{6.5} = T_6 - \epsilon \left(T_6 - T_3\right) \tag{2.45}$$

Substituting Equation 2.44 into Equation 2.41 and 2.45 into Equation 2.41 as using isentropic relationships (see Equation 2.5) to write temperatures in terms of pressures leads to Equations 2.46 and 2.47

$$q_{in} = c_p \left(TIT \left(1 - \epsilon \left(OPR\right)^{\frac{1-\gamma}{\gamma}} \right) + T_{amb} \left(OPR\right)^{\frac{\gamma-1}{\gamma}} \left(\epsilon - 1\right) \right) \tag{2.46}$$

$$q_{out} = c_p \left(TIT \left(OPR\right)^{\frac{1-\gamma}{\gamma}} \left(1 - \epsilon\right) + T_{amb} \left(\left(OPR\right)^{\frac{\gamma-1}{\gamma}} \epsilon - 1 \right) \right) \tag{2.47}$$

We can now return to the same process as the previous GT/SOFC cycle derivation, equating the two expressions for q_{in} from Equation 2.46 and the FC-parameter left-hand-side of Equation 2.8 which represents the heat addition. The result is Equation 2.48.

$$\frac{h_{fuel}(1-\eta_{elec}U_{FC}\sigma_{FC})}{AFR+1} = c_p\left(TIT\left(1-\epsilon\left(OPR\right)^{\frac{1-\gamma}{\gamma}}\right)+T_{amb}\left(OPR\right)^{\frac{\gamma-1}{\gamma}}\left(\epsilon-1\right)\right) \tag{2.48}$$

From here we may derive other quantities of interest as before, including AFR, w_{FC}, θ, and η_{sys}, which are provided in Equations 2.49, 2.50, 2.51, and 2.52 respectively. The flow-specific gas turbine work for this scenario (w_{GT}) reduces to Equation 2.1, which is appropriate since the only changed characteristic of the Brayton cycle are the different contributions to the heating between stations 3 and 4.

$$AFR = \frac{h_{fuel}\left(1-\eta_{elec}U_{FC}\sigma_{FC}\right)}{c_p\left(TIT\left(1-\epsilon\left(OPR\right)^{\frac{1-\gamma}{\gamma}}\right)+T_{amb}\left(OPR\right)^{\frac{\gamma-1}{\gamma}}\left(\epsilon-1\right)\right)} - 1 \tag{2.49}$$

$$w_{FC} = c_p\left(TIT\left(1-\epsilon\left(OPR\right)^{\frac{1-\gamma}{\gamma}}\right)+T_{amb}\left(OPR\right)^{\frac{\gamma-1}{\gamma}}\left(\epsilon-1\right)\right)\frac{\eta_{elec}U_{FC}\sigma_{FC}}{1-\eta_{elec}U_{FC}\sigma_{FC}} \tag{2.50}$$

$$\theta = \frac{w_{FC}}{w_{GT}} = \frac{TIT\left(1-\epsilon\left(OPR\right)^{\frac{1-\gamma}{\gamma}}\right)+T_{amb}\left(OPR\right)^{\frac{\gamma-1}{\gamma}}\left(\epsilon-1\right)}{TIT\left(1-\left(OPR\right)^{\frac{1-\gamma}{\gamma}}\right)+T_{amb}\left(1-\left(OPR\right)^{\frac{\gamma-1}{\gamma}}\right)}\left(\frac{\eta_{elec}U_{FC}\sigma_{FC}}{1-\eta_{elec}U_{FC}\sigma_{FC}}\right) \tag{2.51}$$

$$\eta_{sys} = \eta_{elec} U_{FC} \sigma_{FC} + \left(1 - \eta_{elec} U_{FC} \sigma_{FC}\right) \beta \tag{2.52a}$$

$$\beta = \frac{\left(1 - (OPR)^{\frac{\gamma-1}{\gamma}}\right)\left(TIT - T_{amb}(OPR)^{\frac{\gamma-1}{\gamma}}\right)}{(OPR)^{\frac{\gamma-1}{\gamma}}\left(TIT\left(\epsilon(OPR)^{\frac{1-\gamma}{\gamma}} - 1\right) - T_{amb}(OPR)^{\frac{\gamma-1}{\gamma}}\left(\epsilon - 1\right)\right)} \tag{2.52b}$$

These equations reduce to their equivalents in Section 2.1 when $\epsilon = 0$.

A GT/SOFC with a recuperator is subject to the same turbine inlet tempeature limit as the non-recuperated cycle investigated in Section 2.2. This, in turn, limits how much heat may be released within the SOFC. Following the same process for derivation, consider that the heat addition limit Equation 2.25 is bracketed again by the SOFC operating temperature, but now on the low-temperature side by the recuperator exhaust temperature instead of the compressor exhaust's. This leads to Equation 2.53 where T_3 is replaced by $T_{3.5}$ as per Equation 2.44, and re-written in terms of OPR and ambient conditions using isentropic relations.

$$\Delta h_{lim} = c_p\left(T_{FC} - \epsilon\left(TIT(OPR)^{\frac{1-\gamma}{\gamma}} - T_{amb}(OPR)^{\frac{\gamma-1}{\gamma}}\right) - T_{amb}(OPR)^{\frac{\gamma-1}{\gamma}}\right) \tag{2.53}$$

With an expression for the heat limit, we may again combine this equation with Equation 2.23 for the specific heat released based on the other cycle inputs, and substituting for the AFR with recuperator via Equation 2.49, leads to Equation 2.54 for the minimum physical fuel cell electrical efficiency, $\eta_{elec,min}$. Note again that this expression could be solved for the other fuel cell design variables if preferred.

$$\eta_{elec,min} = \frac{A - \sigma_{FC} U_{FC}}{\sigma_{FC} U_{FC} \left(A - 1\right)} \tag{2.54a}$$

$$A = \frac{T_{FC} - \epsilon \left(TIT\right) \left(OPR\right)^{\frac{1-\gamma}{\gamma}} + T_{amb} (OPR)^{\frac{\gamma-1}{\gamma}} \left(\epsilon - 1\right)}{TIT \left(1 - \epsilon (OPR)^{\frac{1-\gamma}{\gamma}}\right) + T_{amb} (OPR)^{\frac{\gamma-1}{\gamma}} \left(\epsilon - 1\right)} \tag{2.54b}$$

The cycle diagram presented in Figure 2.3 is modified to illustrate the effect of recuperation in Figure 2.8 for an effectiveness of $\epsilon = 0.8$ and other parameters identical. The blue segments illustrate the effects of the recuperator which occur at the compressor and turbine exhausts. The heat transfer that occurs via the HEX, Δh_ϵ, is also shown normalized by the specific heat of air at constant pressure.

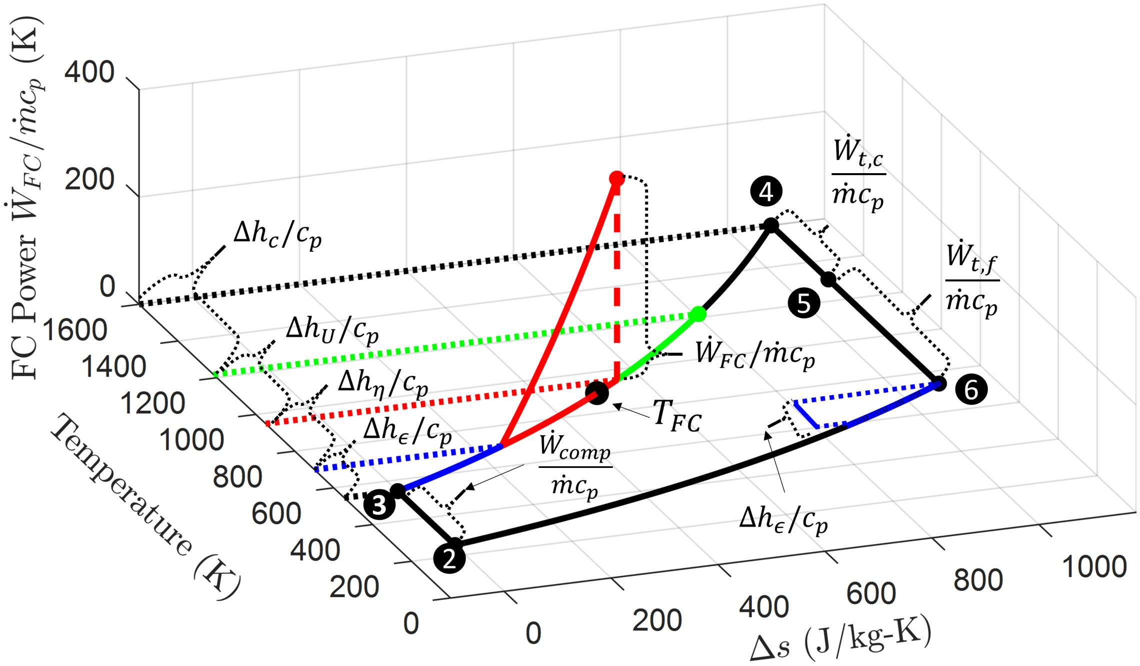

Figure 2.8: Example T-s diagram of GT/SOFC cycle with recuperation based on inputs from Table 2.1 and a HEX effectiveness of $\epsilon = 0.8$.

Immediately we can see that in comparison to the scenario without recuperation (Figure 2.3), the heat added after the compressor exhaust (station 3) pushes the temperature after heat release within the fuel cell above the fuel cell operating temperature T_{FC} of 898K. As discussed earlier, this set of parameters is not a physically viable operating condition.

2.5 Results and Discussion

With analytical equations for the GT/SOFC cycle in hand, let us next examine some results, both qualitative and quantitative. As done for the derivations, we'll first look at the basic cycle, then consider range analysis results and the impacts recuperation can have on the cycle.

2.5.1 GT/SOFC Cycle Model

There are many places to begin an analysis of the GT/SOFC cycle since there are many questions that may be asked. These include but are not limited to global performance questions like optimizations of efficiency and specific power per unit flow rate, internal characteristics like the amount of power produced by the SOFC relative to the turbine, etc.

We will start with a qualitative description of the effects of some specific design variables on the GT/SOFC cycle that may be freely specified. They are the amount of fuel diverted through the fuel cell σ_{FC}, the fuel cell utilization U_{FC}, and the overall GT pressure ratio OPR. See Table 2.1 for a more complete list of design parameters. The values of σ_{FC} and U_{FC} are always between zero. OPR is limited by the practical capabilities of turbomachinery—higher OPR hardware is generally more expensive and exists in the range of $OPR \approx 1 \leftrightarrow 50$ with higher capabilities at the state-of-the-art for aircraft use. All other variables in Table 2.1 are broadly constrained by higher- or lower-level design choices (e.g. fuel cell operating temperature and fuel enthalpy), materials limitations (TIT), or operating conditions.

Consider Figure 2.9, which shows GT/SOFC cycles for three different OPR values and all other values specified in Table 2.1.[xii] Some immediate observations we can make are that the usual characteristics of Brayton cycle apply normally, with increasing compressor exhaust temperatures and lower changes in entropy achieved with increasing OPR.

We also see that as OPR increases, the heat release within the SOFC (red along the Brayton cycle outline) drives the fuel cell exit temperature toward the SOFC operating temperature limit (large black dot). Increasing OPR also increases the power extracted from the turbine (stations 5 to 6, per Figure 2.8) which reduces the amount of power produced by the SOFC (red dashed line rising from the Brayton-plane) relative to the power produced by the turbine. In most ground-based GT/SOFC systems, pressure ratios are low as they are applied to a steam-generating Rankine cycle such that the increased importance of the SOFC contributions for ground power production is consistent. At the same time, the system thermal efficiency increases with OPR as the Brayton cycle turbine is operated more efficiently.

Instead of viewing each scenario as a cycle plot, we can generate contour diagrams, with the axes representing some design variables of interest. Figure 2.10 shows contours of system thermal efficiency as a function of σ_{FC} and OPR. Cases in

---

[xii] Unless otherwise noted, the baseline variable values used in all results match Table 2.1.

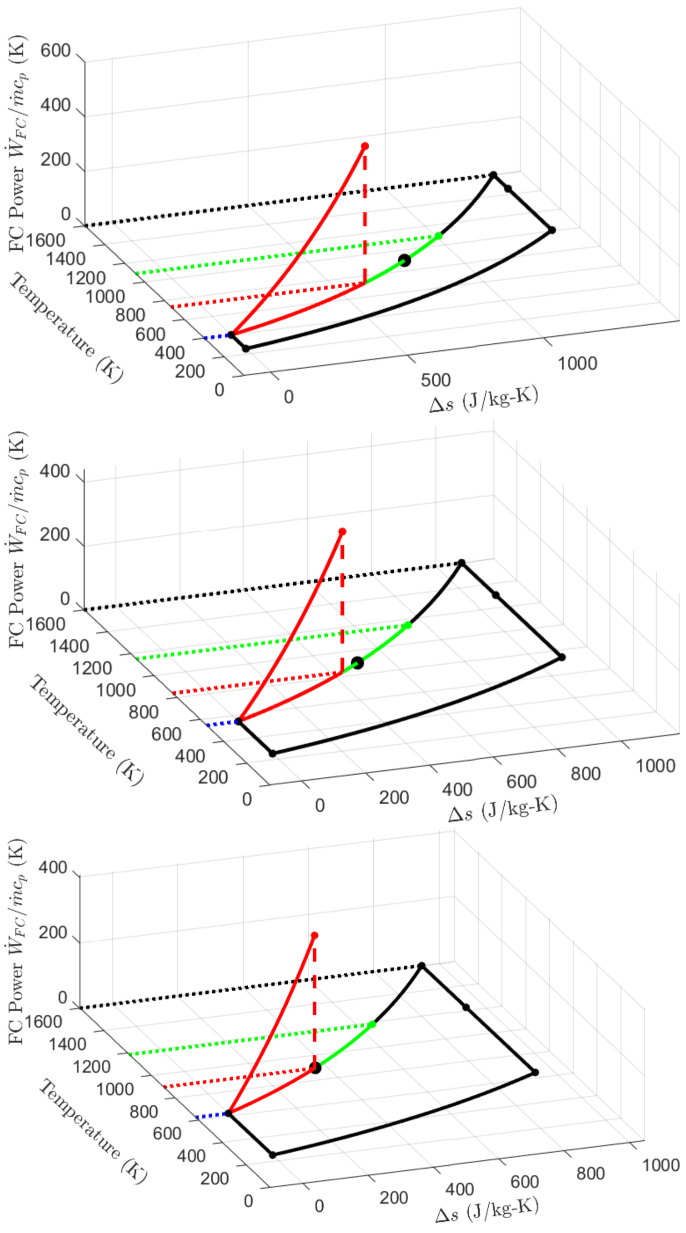

Figure 2.9: GT/SOFC T-s cycle diagrams for $OPR = 5{,}15{,}24$ (top to bottom). The corresponding system thermal efficiency are $\eta_{sys} = 55\%{,}67\%{,}73\%$ respectively. The red portion of the curve show the heat addition associated with chemical reaction in the fuel cell. The green portion shows the heat addition in the combustor from fuel that was not converted in the furel cell. The large black dot shows the FC operating temperature.

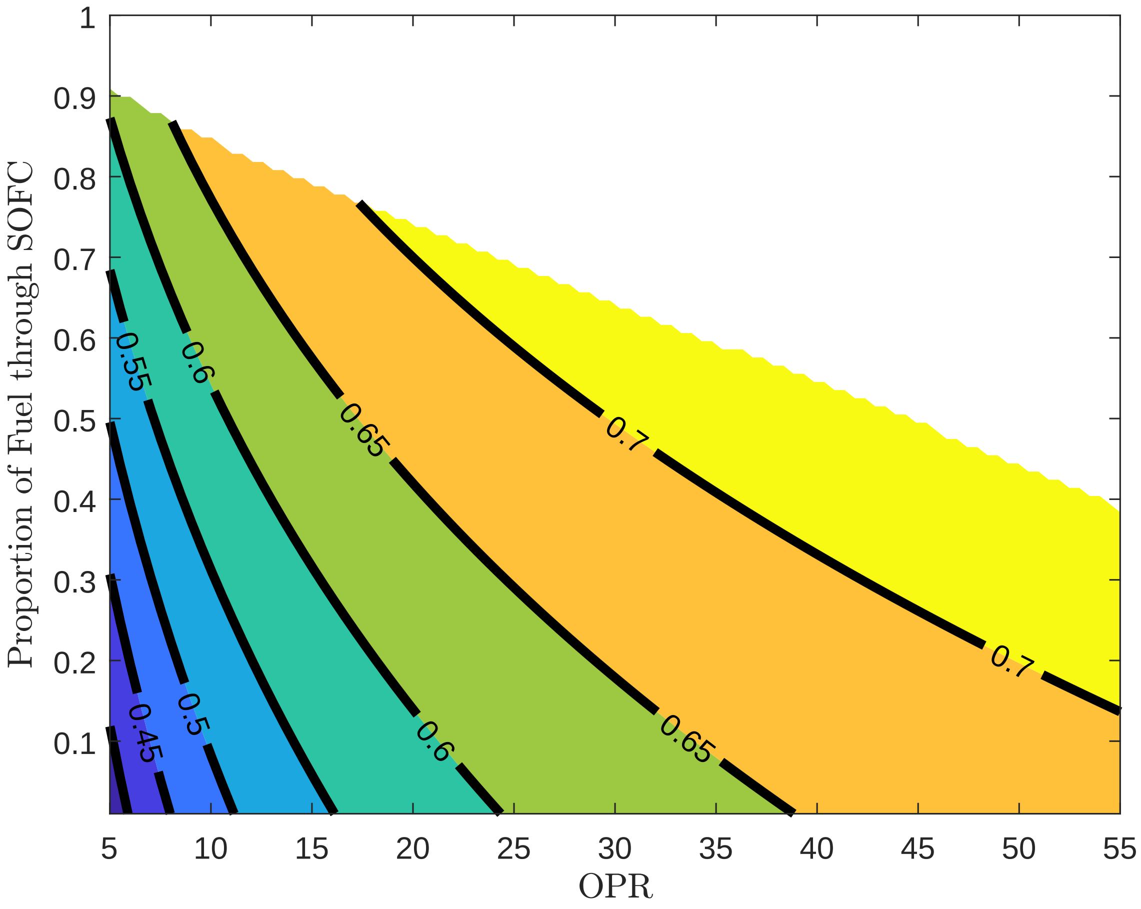

Figure 2.10: System thermal efficiency (η_{sys}) as a function of overall pressure ratio (OPR) and proportion of fuel through the fuel cell (σ_{FC}). The values of other system parameters are given in Table 2.1.

which the SOFC exit temperature exceeds the isothermal SOFC temperature limit are excluded and shown on the plots as blank white space.

There are several immediate observations. First, we see the approximately linear decrease of the temperature limit cutoff as OPR increases: raising OPR raises the fuel cell inlet temperature meaning that less fuel will have to be converted in the fuel cell to reach the isothemal operating limit T_{FC}. Note that the relationship is not exactly linear (see Equation 2.26) but appears so in this case.

Next, note the general trend that higher values of both OPR and σ_{FC} improve the system thermal efficiency. This makes sense because the Brayton cycle's efficiency increases with OPR and the fuel cell is more efficient than the Brayton cycle. The slope of the contours indicate that system efficiency is more sensitive to OPR when OPR and σ_{FC} are low and becomes slightly more sensitive to σ_{FC} as OPR increases. To see this, notice how the direction of the gradient vector (which is perpendicular to the contours) changes as one moves around in the space.

Turbomachinery limitations in cost or achievable efficiency favor lower OPR values, but even a relatively modest $OPR = 24$ (seen in engines powering modern regional airliners) can achieve $\eta_{sys} = 70\%$. This is substantially greater than the thermodynamic efficiencies of modern turbofans (see Figure 1.8).

While the system efficiency results appear promising, efficiency is only one metric of a thermodynamic cycle's performance. Another is the total flow-specific work which is presented in Figure 2.11. The figure shows that there is a particular value of OPR that maximizes flow specific work for any given σ_{FC}. The flow specific work increases as σ_{FC} increases while the optimum value of OPR decreases. An optimum OPR also exists for $\sigma_{FC} = 0$ (i.e. a pure GT without a fuel cell subsystem) and finding it is a standard optimization problem for the Brayton cycle [71, p. 253]. The decrease in optimum OPR with increasing σ_{FC} reflects the fact that as the more efficient fuel cell contributes more to the system's overall power, it is less necessary for the turbomachinery to be efficient. The results also indicate that there is a tradeoff between efficiency (see Figure 2.11) and flow specific work: System thermal efficiency increases as one increases OPR and decreases σ_{FC} whereas flow specific

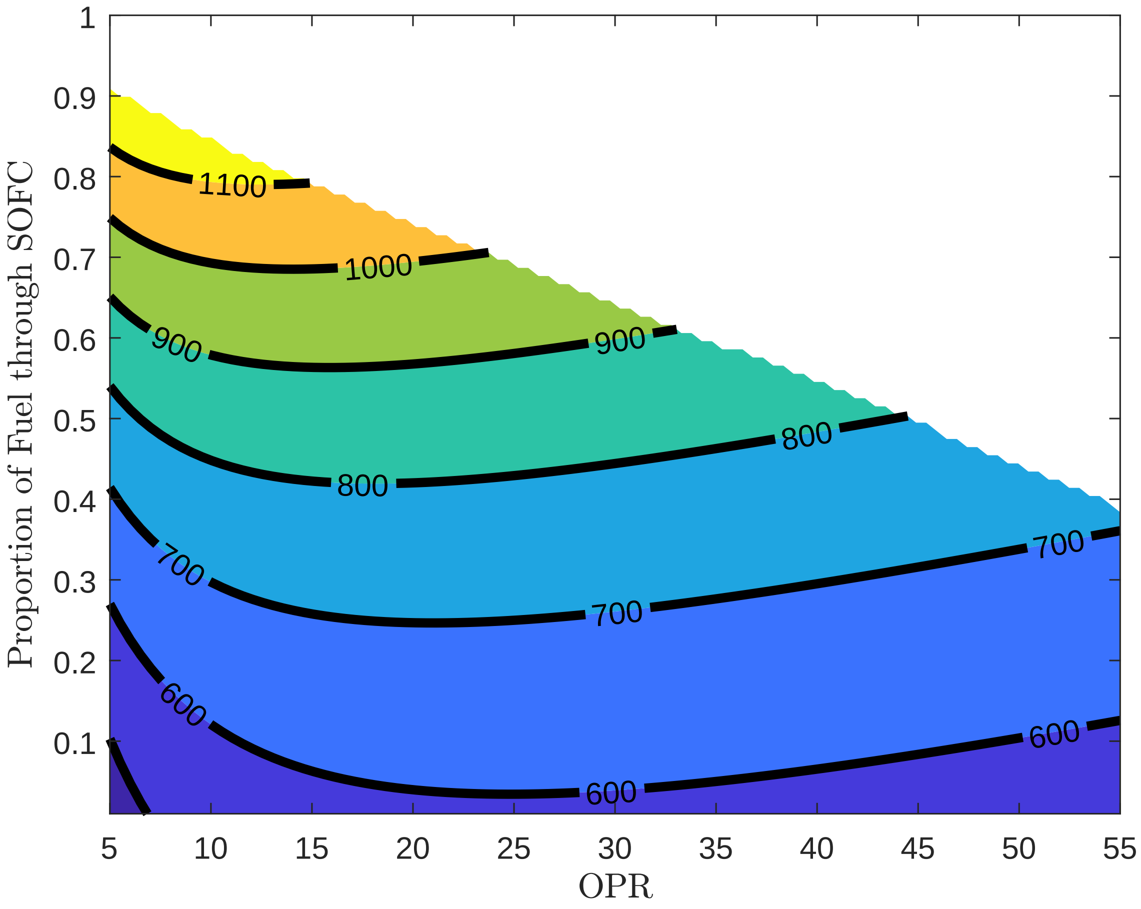

Figure 2.11: Total flow-specific work ($\frac{\dot{W}_{GT}+\dot{W}_{FC}}{\dot{m}_{tot}}$) as a functino of overall pressure ratio (OPR) and proportion of fuel through the fuel cell (σ_{FC}). The values of other system parameters are given in Table 2.1.

work increases as one increases σ_{FC} and moves OPR toward the optimum value.

Gradient vectors in the space point mostly upward indicating that the flow-specific work is much more sensitive to the value of σ_{FC} than the OPR. For example, a value of $\sigma_{FC} = 0.6$ results in an over 50% improvement in flow-specific work over that of a baseline GT alone! *This is an encouraging result, since higher flow-specific work leads to a relatively more compact engine. We should note that in this case we may only achieve a smaller inlet size, considering that more power generation by* *the fuel cell will generally require a proportionally larger (and heavier) fuel cell.*

The effect of varying OPR and $sigma_{FC}$ on the relative proportion of power generated by the fuel cell and gas turbine subsystems is presented in Figure 2.12. While an optimized design will also take into account other factors like mass (see the range model in Section 2.5.2) and turbomachinery efficiencies, we can see that the power split becomes more sesitive to OPR as σ_{FC} increases. We can also see that the maximum allowable value of σ_{FC} decreases with OPR reflecting the constraint imposed by the maximum SOFC operating temperature. This does not necessarily indicate that hybridization becomes less favorable with increasing OPR since the system thermal efficiency also increases (see Figure 2.10).

The variation of air-to-fuel ratio (AFR) with OPR and σ_{FC} is illustrated in Figure 2.13. The immediate use for this information is to confirm that we are operating in a reasonable range for our constant specific heat assumption. Unsurprisingly, AFR is lowest when most fuel is injected through the SOFC subsystem at low OPR (emphasizing the SOFC contribution), and highest in the opposite scenario that emphasizes the gas turbine.

With cycle performance broadly established, we can now move on to the overall effects these different cycle impacts have on aircraft operating range.

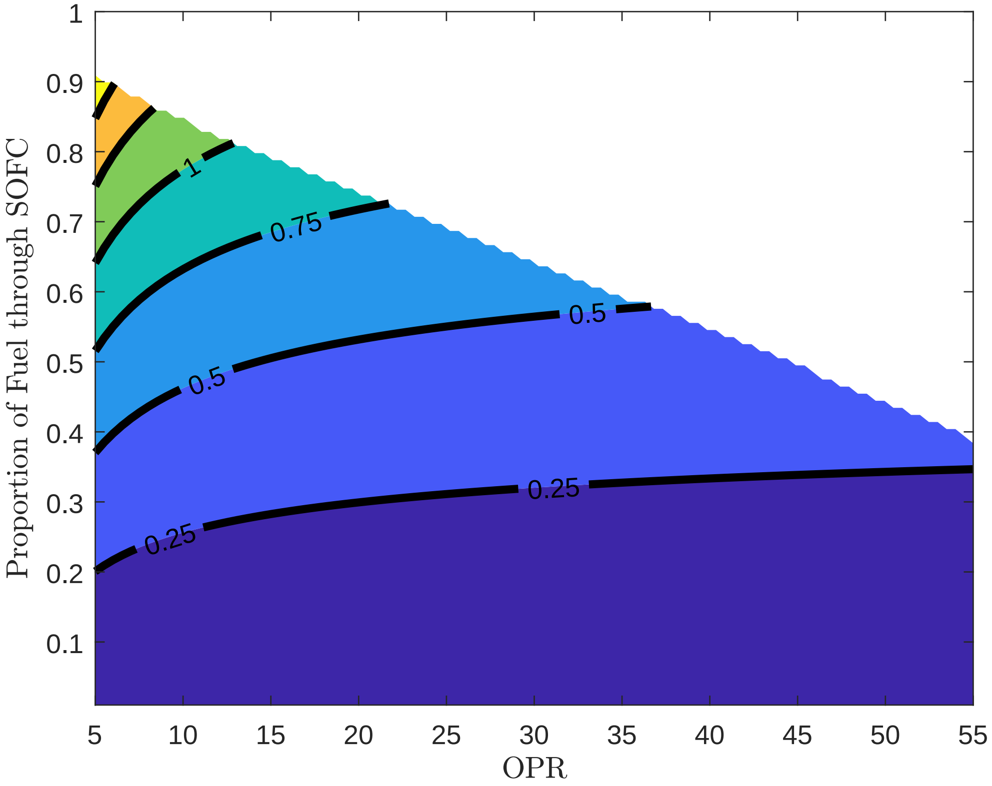

Figure 2.12: Ratio of fuel cell to gas turbine specific work as a function of overall pressure ratio (OPR) and proportion of fuel through the fuel cell (σ_{FC}). The values of other system parameters are given in Table 2.1.

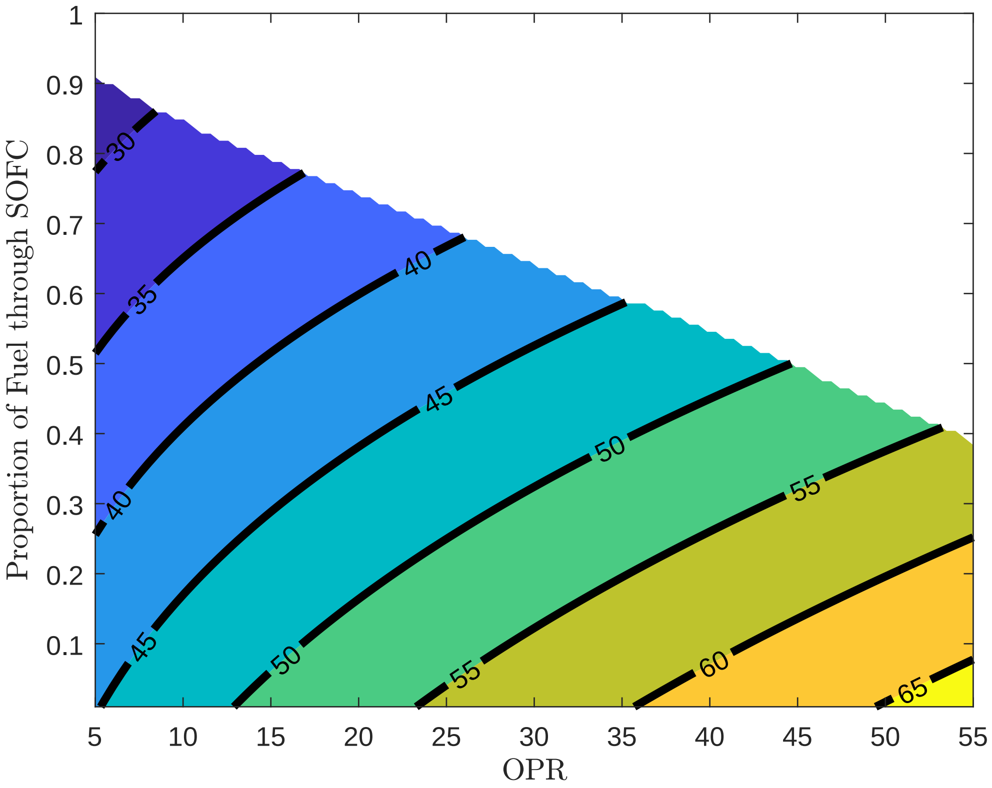

Figure 2.13: Required system-level Air/Fuel ratio (AFR) for varying OPR and proportion of fuel through the fuel cell.

2.5.2 GT/SOFC Range Model

In looking at the range modeling results, we use the same default system parameters as before in Table 2.1. Additional variable values regarding aircraft mass breakdown and airframe performance in Table 2.2. Where available, these values match those provided in prior work for a regional transport jet such as the ERJ-145 [64]. As before, and in the discussion that follows, both sets of default values only vary where explicitly stated.

Table 2.2: Baseline Inputs for GT/SOFC Range Model Results, unless otherwise stated.

Variable	Value	Units
η_{prop}	0.8	n/a
p_{GT}	3.37	$\mathrm{kW\,kg^{-1}}$
p_{FC}	1.00	$\mathrm{kW\,kg^{-1}}$
m_0	15000	kg
m_{tot}	20524	kg
v	237.29	$\mathrm{m\,s^{-1}}$
ρ	0.3806	$\mathrm{kg\,m^{-3}}$
S	50	$\mathrm{m^2}$
δ_{fans}	1.5	n/a
$C_{D,min}$	0.016	n/a
$C_{L,min}$	0.1	n/a
K	0.09	n/a

Figure 2.14 shows range (comuputed using Equation **??**) as a function of OPR and σ_{FC}. First of all, the range values are much higher than seen in actual aircraft of this class. For example, the ERJ-145LR has a range of 2,873 km whereas the range estimate here is a little under 11,000 km for GT alone (a pure Brayton cycle) at an $OPR = 23$ with no fuel cell. This factor of 3-4 difference might be

accounted for by the (1) ideal turbomachinery efficiency, (2) lack of safety margin, taxi/takeoff/landing fuel usage, and (3) an optimistic value of propulsive efficiency expected for driven fans.

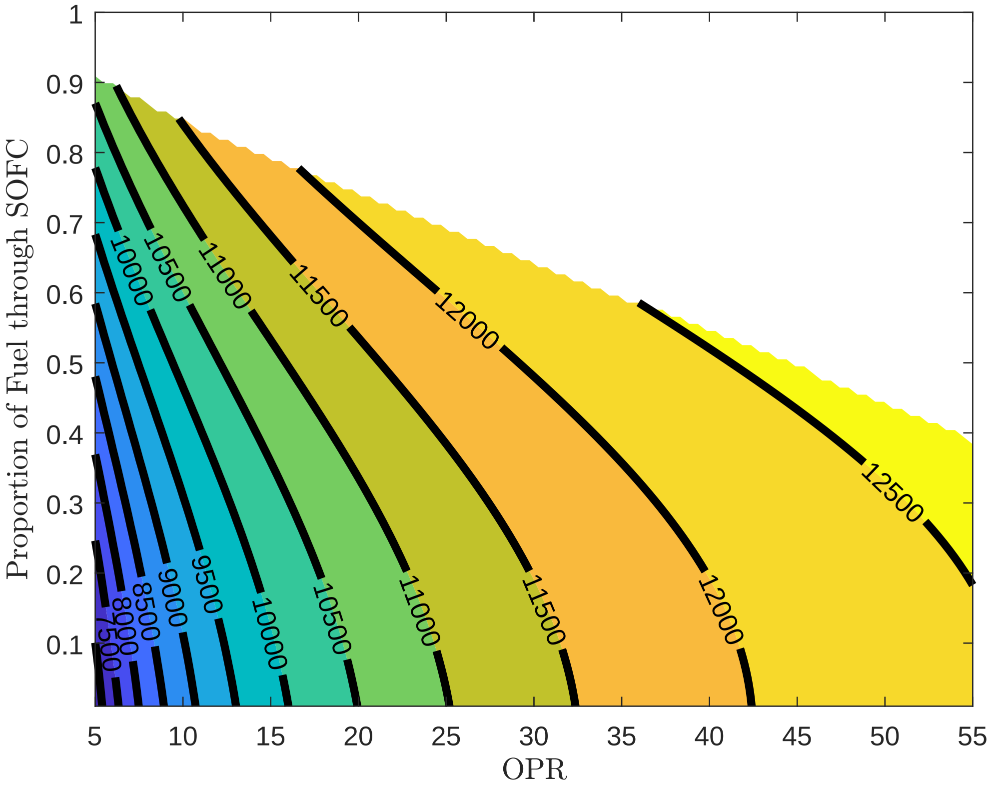

Figure 2.14: Range as a function of overall pressure ratio (OPR) and proportion of fuel through the fuel cell (σ_{FC}) for a reformer/fuel cell element with a specific power of $1kW/kg$ and turbomachinery with a specific power of $3370W/kg$. The values of other system parameters are given in Table XXX.

In any case, for this ’toy’ model the greatest interest is in the performance trends. Immediately, we can see that the range follows the same general trend as efficiency illustrated in Figure 2.10 of the previous section: range increases with increasing OPR and σ_{FC} but is much more sensitive to OPR. However, the shapes of the curves are different: the efficiency contours in Figure 2.10 are concave up whereas the range contours here (Figure 2.14) are concave down.

The total weight of the ESPG (ie. energy conversion system plus fuel) upon which Figure 2.14 is based is constant as is its power output. What changes as one moves vertically in the space (ie. as one adds fuel cell components) is the distribution of weight between the turbomachinery, fuel cell, and fuel. Since ESPG power output remains constant, adding fuel cells reduces the size of the turbomachinery needed. However, since the specific power of the turbomachinery is greater than that of the fuel cell, fuel mass must also be reduced in order to maintain constant ESPG weight. Figure 2.15 shows how fuel capacity varies in the OPR–σ_{FC} space. The greatest amounts of fuel (and so the smallest ESPG) can actually be found at the extremes of the σ_{FC} limits, with either no SOFC (i.e. $\sigma_{FC} = 0$) or nearly all fuel passing through the SOFC first. However, the variation in general is not substantial, only varying about 200 kg over the entire space. Note also that these limits do not confer the greatest range; the range capability is a function of the cycle efficiency of the system, as well as the amount of fuel carried.

Since for a range calculation we are now considering the masses of our ESPG components, other variable trades can be particularly important. For example, consider the effects of fuel cell electrical efficiency and specific power which trade against each other via the choice of SOFC operating voltage: increasing stack operating voltage increases efficiency but decreases current and thus specific power. Figure 2.16 illustrates the effect of fuel cell efficiency and specific power on range for $OPR = X$ and $\sigma_{FC} = Y$. Unsurprisingly, range increases with increasing fuel cell

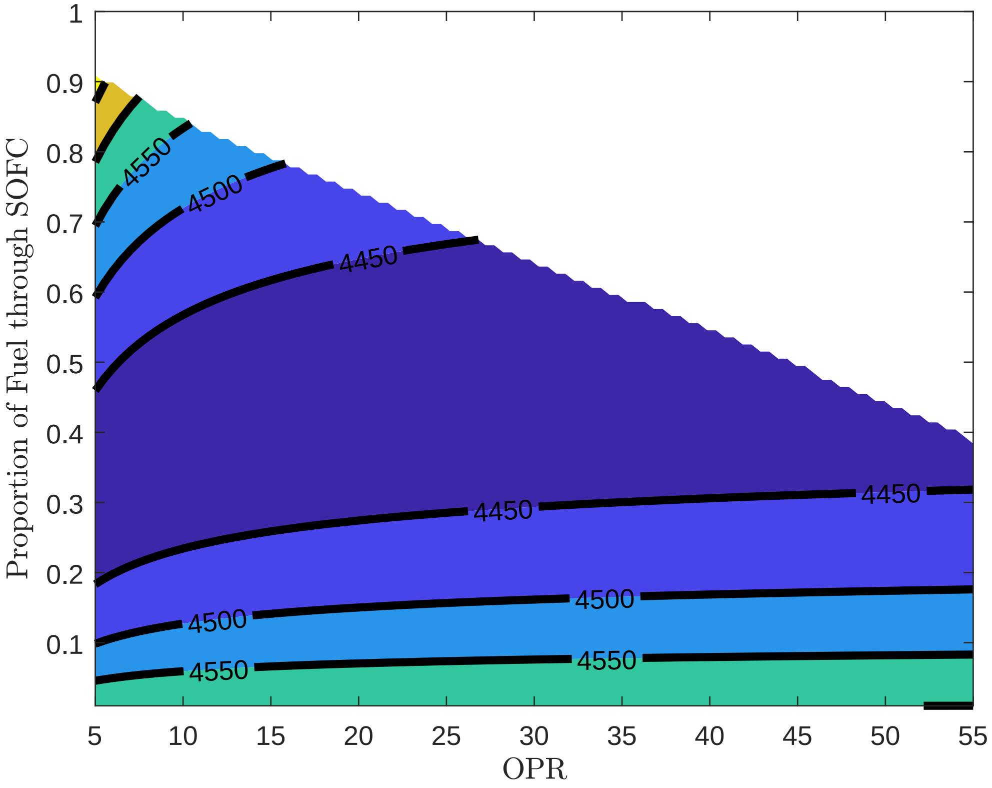

Figure 2.15: Maximum fuel capacity (kg) as a function of overall pressure ratio (OPR) and proportion of fuel through the fuel cell (σ_{FC}) for a reformer/fuel cell element with a specific power of $1kW/kg$ and turbomachinery with a specific power of $3370W/kg$. The values of other system parameters are given in Tables 2.1 and 2.2.

specific power and cell efficiency. Range is most sensitive to fuel cell specific power when specific power is low but gets progressively less sensitive to specific power as it increases and by $1600\mathrm{W\,kg^{-1}}$ is equally sensitive to efficiency and specific power. As indicated earlier, efficiency and specific power are not independent of each other in a fuel cell which means that a single cell cannot access all portions of this space. *Note that the plot has excluded values below a minimum efficiency which corresponds to the heat release limit for the chosen value of* $\sigma_{FC} = 0.5$, *since specific power does*

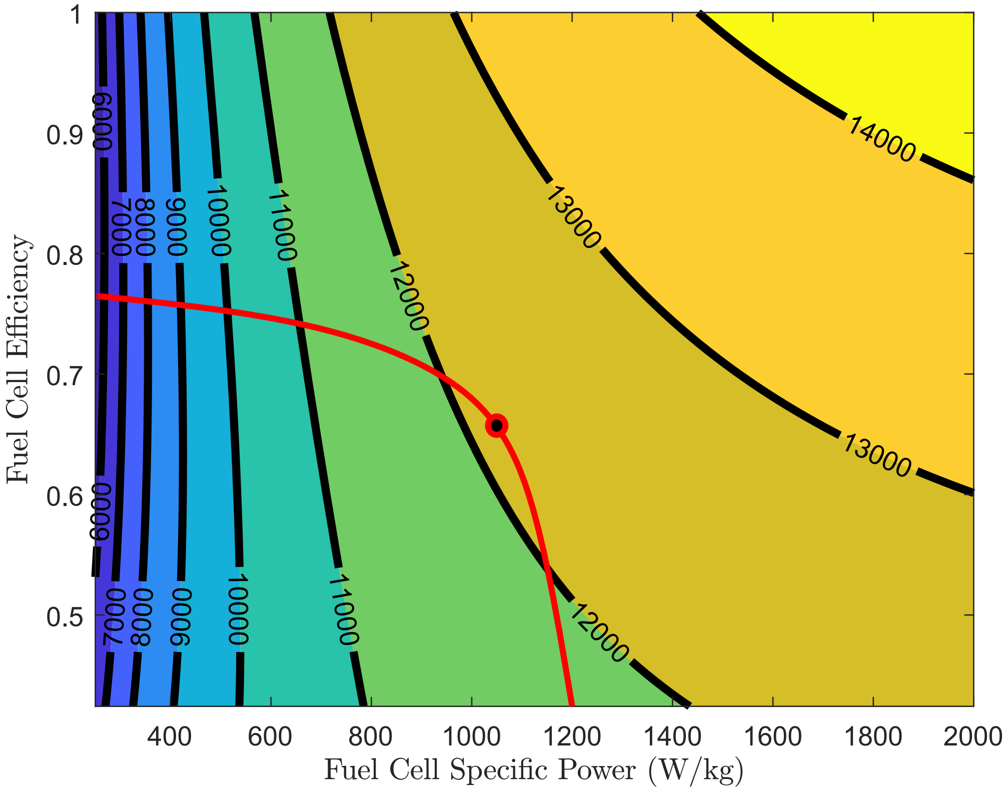

Figure 2.16: Aircraft range as a function of SOFC efficiency and specific power for a hybrid power system with $OPR = 15$ and $\sigma_{FC} = 0.7$. The values of other system parameters are given in Table 2.1. Overlaid on this space is a notional SOFC performance curve along with the SOFC operating point (indicated by the red circle with black dot) that maximizes range.

not impact the cycle performance.

|

The notional curve shown on Figure 2.16 represents the SOFC polarization curve; in a fuel cell stack, varying the operating voltage effectively changes the efficiency per Equation 2.11. The result is a larger current density in the same physical SOFC active area, and—to a point—greater electrical power generation that increases the device's specific power. With some conversion of per-active-area SOFC performance to stack mass, we can map this onto with any empirical polarization curve for the SOFC operating condition (i.e. temperature and pressure). Depending on the specific performance and conditions, we can determine an range-optimal operating voltage, as indicated by the black dot on the curve.

In a similar efficiency and fuel cell specific power space, we can generate a plot of the fuel mass necessary for these different variables, yielding Figure 2.17. While there are small effects from the variation in efficiency across the space changing the expected engine mass through changes in the resulting θ, the fuel cell specific power is far more impactful in terms of the amount of fuel available—at least at this location in the OPR/σ_{FC} space.

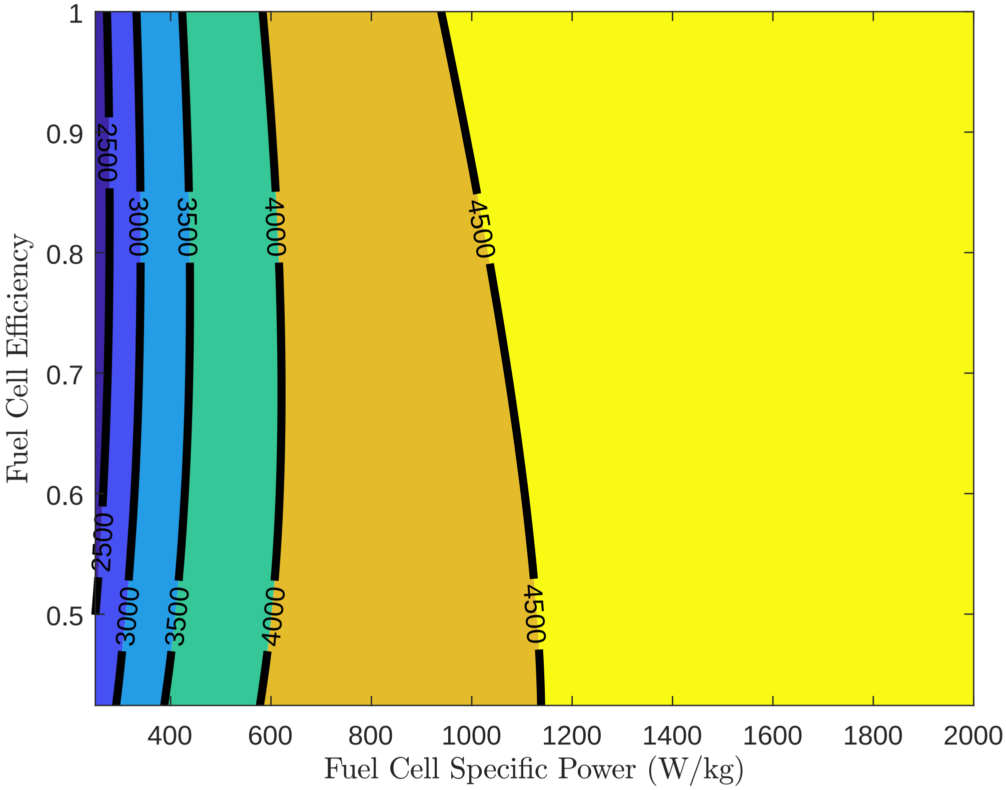

Figure 2.17: Maximum fuel capacity (kg) as a function of SOFC efficiency and specific power for a hybrid power system with $OPR = 15$ and $\sigma_{FC} = 0.7$. The values of other system parameters are given in Table 2.1.

2.5.3 Recuperation Results

The presence of the recuperator in the GT/SOFC system has several significant effects. First, the system thermal efficiency is improved when the turbine exhaust (T_6) temperature is substantially higher than the compressor exhaust temperature (T_3), i.e. at low pressure ratios or high T_4/T_{amb} values. When the temperature relationship is reversed (i.e. $T_6 < T_3$), the recuperator actually becomes harmful to performance and should be bypassed. Second, the upper limit on σ_{FC} is reduced since the heat passed into the compressor exhaust by the recuperator lowers the amount of waste heat that may be absorbed below the SOFC operating temperature. These effects are seein in Figure 2.18, which overlays contours for 50% recuperation onto an equivalent scenario to Figure 1.12.

We can also discuss the impact of a recuperator for a continuous range of effectiveness rather than just a single value. Consider Figure 2.19 which shows the system thermal efficiency as a function of recuperator effectiveness and σ_{FC}. The figure shows that both variables have similar substantial positive impacts on the system thermal GT/SOFC efficiency; at the same time parts of the space are restricted again by the SOFC operating temperature limit.

This is unsurprising, since both strategies (SOFC integration and recuperation) pre-heat the compressor exhaust flow before it reaches the combustor. The difference is that the integrated SOFC draws additional energy from fuel injected into the cycle before adding waste heat and enthalpy into the combustor, effectively augmenting the Brayton cycle power output with thermodynamically “free” SOFC

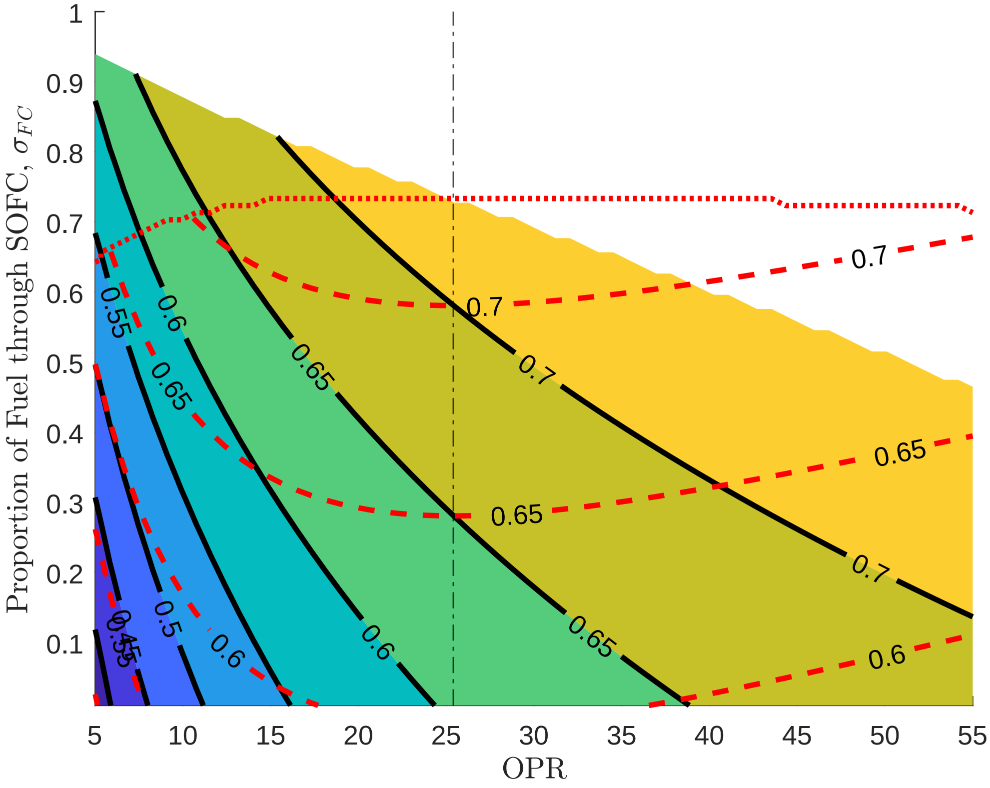

Figure 2.18: GT/SOFC cycle efficiency as a function of OPR and σ_{FC} with red dashed contours corresponding to 50% effective recuperation and black solid contours corresponding to 0% recuperation. Dash-dotted vertical line indicates OPR at which turbine exhaust becomes colder than compressor exhaust. The values of other system parameters are given in Table 2.1.

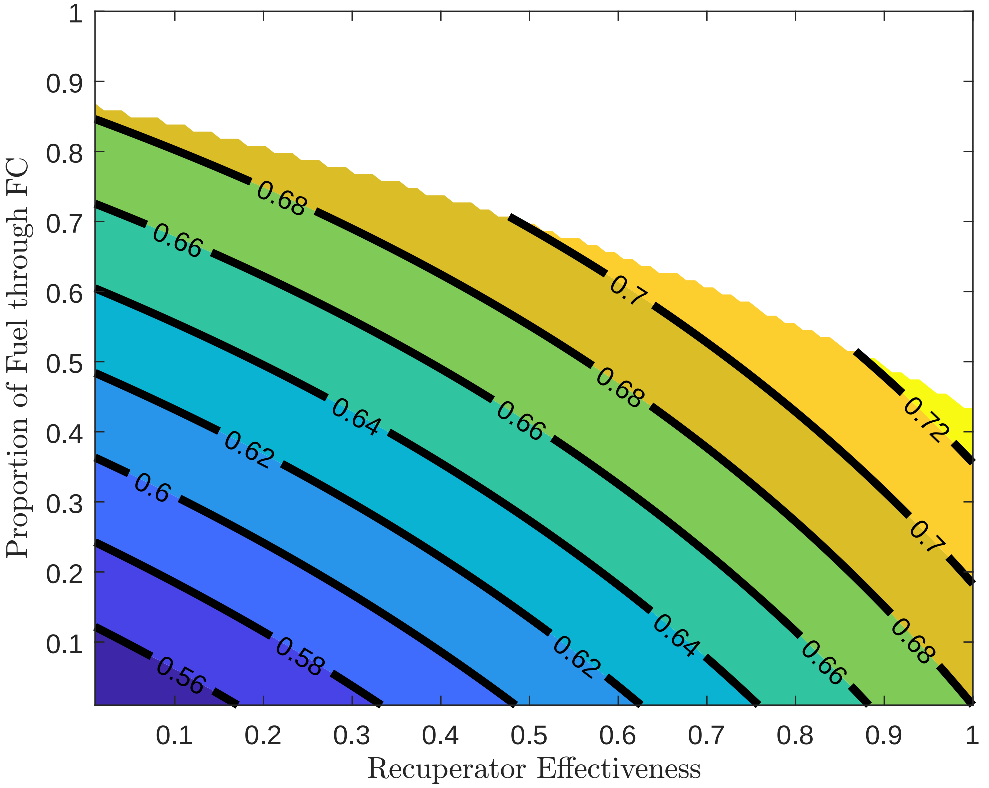

Figure 2.19: GT/SOFC cycle efficiency as a function of recuperator effectiveness and σ_{FC} The values of other system parameters are given in Table 2.1.

output.[xiii] In contrast, recuperation recovers waste heat from the turbine exhaust into the compressor exhaust. Per Equations A.1 and A.2, this results in a direct and equivalent lowering of both $\dot{Q}_{in}$ and $\dot{Q}_{out}$ from the heat cycle. While their difference (and so the work produced) is the same, the efficiency (dependent only on $\dot{Q}_{in}$) is improved.

This difference is also observable in the resulting work per unit of flow. Consider Figure 2.20 which shows substantial increases in flow-specific work as the relative size of the SOFC (ie. σ_{FC}) increases. As expected for a recuperated Bray-

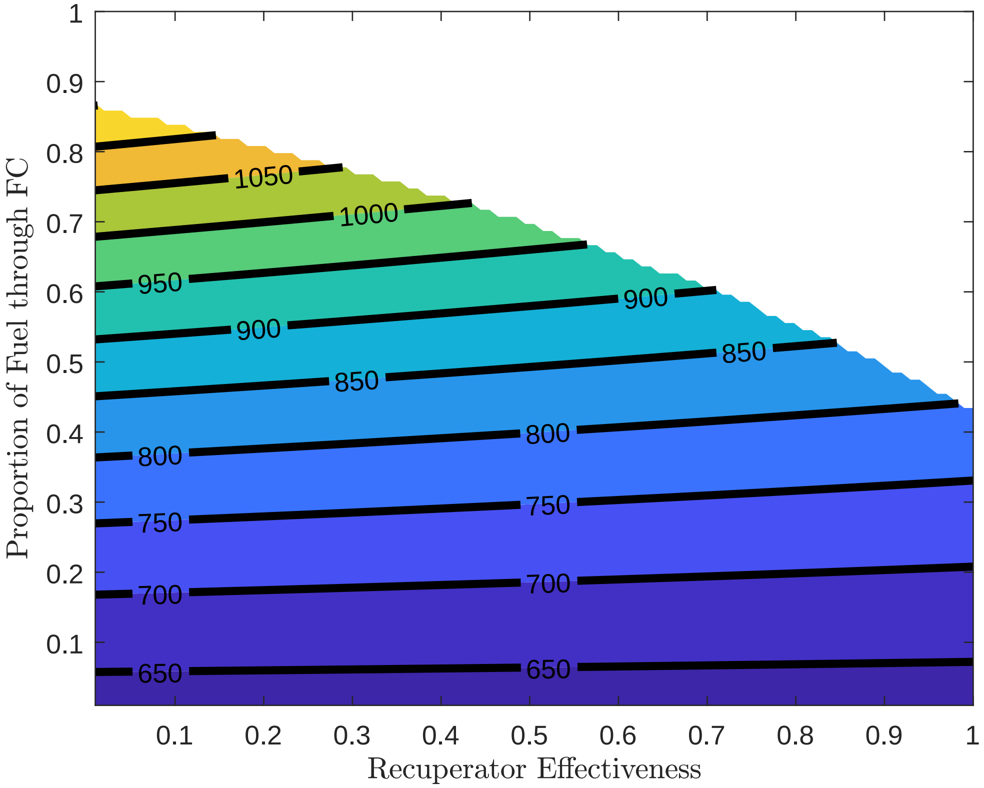

Figure 2.20: GT/SOFC Flow-Specific Power ($\mathrm{kJ\,kg^{-1}}$) as a function of recuperator effectiveness and σ_{FC}. The values of other system parameters are given in Table 2.1.

ton cycle, the flow-specific work is insensitive to HEX effectiveness at small values of σ_{FC}. A small decrease in flow specific work with effectiveness is observed at higher values of σ_{FC}. This is caused by the reduction in the total amount of fuel necessary to reach the TIT with increasing effectiveness of the HEX. Since the total fuel amount is smaller, the constant σ_{FC} represents a progressively smaller SOFC as well. A constant-sized SOFC in such a system would see no change in specific power with varying effectiveness.

To summarize, while recuperation can substantially improve efficiency, it is most effective at lower pressure ratios and higher turbine inlet temperatures. It also competes with the SOFC for “room” to inject waste heat into the cycle thereby limiting the relative size of the SOFC in the hybrid system.

2.6 Conclusions and Future Work

This chapter has presented a detailed analysis of the thermodynamic cycle associated with a hybrid gas turbine/fuel cell where the fuel cell is integrated into the hot section of the engine. The performance of the fuel cell is represented in very simple terms but doing so enabled us to derive analytical relationships for important heat cycle performance characteristics like flow-specific work, thermodynamic efficiency, and the necessary AFR. These relationships allow one to analyze wide swaths of the GT/SOFC design space to inform and guide more complex modeling efforts.

2.6.1 Conclusions

From the cycle, we can also provide some immediate takeaways. First, the integrated GT/SOFC offers the potential for both improved efficiency *and* flow-specific work in the same system. This will be true for any level of SOFC performance, though either a larger or a more efficient SOFC will yield higher efficiency operation. Furthermore, the improvement in flow-specific work from the SOFC integration far exceeds improvements from optimizing the cycle OPR. An increased flow-specific work capability opens the door to smaller core flow rates necessary to produce the necessary power. This concept will be tested later with more complex modeling in Section 3.6.

Additionally, for the surveyed design space where the TIT remains well above the SOFC operating temperature, the SOFC is expected to be roughly the same size or smaller than the GT in terms of power production. The identification and illustration of the cooling limitation to the SOFC operating temperature is a key contribution of this work.

The range analysis performed here is best interpreted in terms of trends, but those trends suggest a capability to trade between SOFC specific power (in terms of system mass) and efficiency (via operating voltage) to achieve the maximum range capability for an aircraft with a given drag polar. While the range was found to be highly sensitive to SOFC specific power, reasonable GT/SOFC configurations were identified that yield improvements over a gas turbine alone.

Finally, recuperation as an efficiency improvement strategy was added to the cycle model. The resulting performance showed that while even greater improvement to efficiency was possible, the recuperator competes with the SOFC in the hybrid system *to store waste heat* , and provides limited utility—and eventually negative utility—at higher pressure ratios.

2.6.2 Future Work

The cycle developed in this chapter is highly simplified, and contains several strict assumptions and important omissions in order to remain reasonably compact and intuitive. However, to better serve in the model's intended role to broadly evaluate the GT/SOFC design space, there are several future improvements that can be identified. Perhaps most fundamentally to the aircraft application, the cycle does not account for countering drag generated at any given flight speed (with associated ram compression), or the thrust of the exhaust—though an approach to perform such an analysis has been identified in the text.

Analytically, the next step might be to evaluate expressions that optimize system flow-specific power or other performance parameters. Thermodynamically, the immediate improvement would be to incorporate engine component efficiencies, as by Chinda et. al. [69] . This may be most easily achieved by re-deriving the equations in terms of temperature ratios τ (see Equation 2.55) to replace the isentropic gas relationships, as per Mattingly [71, Ch. 5]. Furthermore, we can apply trends in turbomachinery efficiency with OPR (usually a negative correlation) or flow rate that may trade off against ideal cycle benefits.

$$\tau_c = \frac{T_3}{T_{amb}} = 1 + \eta_c^{-1} \left(\pi_c^{\frac{\gamma-1}{\gamma}} - 1 \right) \tag{2.55a}$$

$$\tau_t = \frac{T_6}{TIT} = 1 - \eta_t \left(1 - \pi_t^{\frac{1-\gamma}{\gamma}} \right) \tag{2.55b}$$

In the same vein but with device masses, we can expand the recuperation analyses to include the non-negligible mass of the recuperator itself in range or ESPG specific power and energy calculations. Variations in the specific power of the turbomachinery could also apply.

Finally, the cycle analysis generally only applies for a single operating point;

the actual application of the system will be over the course of a full mission, including takeoff, cruise, landing, and all of the steps between. While the analytical model is not an appropriate tool for transient analysis, systems that work over the entire range of mission operating points could be identified.

After that, further system design may be better performed with different tools, leading us into Chapter 3.

Chapter 3: GT/SOFC System Modeling

In Chapter 2, a wide variety of assumptions were made in order to simplify the analysis of the GT/SOFC cycle—not the least of which was a complete neglect of the inner workings of the SOFC. To predict the performance of real systems, more complex modeling is required that takes into account the detailed performance of specific components. This chapter will provide the setup and results from such a model for two promising system configurations.

The GT/SOFC analysis provided in this chapter is performed using the Numerical Propulsion System Simulation (NPSS) modeling framework developed by NASA for which there is a good introduction by Jones [80]. The framework is designed specifically for design and performance modeling of GT engines at aircraft flight conditions. However,it is flexible enough to address a variety of thermodynamic configurations (up to and including nuclear thermal rockets [81]) as well as both steady-state and transient operation.

3.1 Model Setup

To create a system model for a propulsion system, different component models are linked together by flow, bleed, and shaft connections. All flow paths begin with

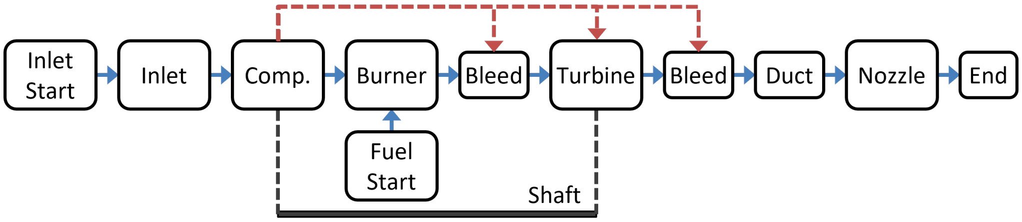

Figure 3.1: NPSS model schematic of a turbojet. Reproduced from Waters [31, fig. 47].

an Inlet Start component, and end with a Flow End component. Flow conditions are calculated by determining flow conditions through successive component models along the flow path, all together representing a system such as gas turbine engine. A relatively simple turbojet model example is provided in Figure 3.1.

Systems with multiple flow paths such as turbofan engines may be modeled as well. Elements are executed in a specified linear sequence such that component inputs are already calculated from the outputs of previous components. In the case of loops or heat exchangers where some inputs are from “downstream” component outputs, it is not possible to complete this linear calculation. Analytically this may be possible (see Chapter 2) but not so in NPSS considering that each component model is treated as a “black box”. Instead, the looped characteristic (e.g. heat transfer across an exchanger) may become a system-level solver variable (see Section 3.2). The most common application of this in NPSS is actually for the Shaft components linking compressor and turbine components. In steady operation, the net torque on the shaft should approach zero even though the loads and torques applied to the shaft may occur at many different points along the calculation sequence. As such, effectively all steady-state models include a system-level solver target for this sort of condition.[i]

Once a system model of linked components is established, the model may be run for arbitrary initial conditions in various modes. A particular mode setting changes the way that certain component models operate. Many models have modes distinguishing "Design" and "Off-Design" modes. "On-Design" mode typically changes physical design parameters (i.e. the sizing) of several components in order to achieve a certain performance at a given condition. "Off-Design" mode on the other hand determines performance as a result of the given operating condition for a set of physical design parameters. In normal NPSS practice, an On-Design case is run to "create" a system before Off-Design cases specify the range of performance [80]. Regardless of the mode, each case must be "solved" as a system.

3.2 System Solver

A system model may be run once for a given set of inputs to yield (depending on the mode) an accompanying state (including performance or sizing). However, in most analytical cases, some characteristics must be met for the system to be useful, e.g. zero net torque on a shaft for steady-state operation, or producing sufficient thrust to remain in steady flight. In these cases, an equal number of variables each are set as "independents" and "dependents". Independent variables may be changed

---

[i] This approach works sufficiently for single-characteristic loops, e.g. net torque on a shaft, or heat transfer across an exchanger. The situation is rather more difficult for multiple characteristics, e.g. mixing two flows with varying chemical composition, temperature, and pressure that are determined from downstream conditions. For every additional parameter the size of the Jacobian necessary for the solver increases exponentially.

by the solver in order to yield the targeted characteristic values for the dependent variables. Put another way, independents are "knobs" that may be turned until the dependent "dials" are in their intended position.

Mathematically, the dependent variables represent a system of differentiable functions, taking the independent variables as inputs (i.e. X equations, X unknowns). The different component models are defined independently and may operate at different levels of complexity. However they are still strongly interrelated at the system level. As such, the problem is best described as a system of nonlinear equations that must be solved numerically. NPSS approaches this problem using a quasi-Newton's Method solver that generates a partial derivative matrix (the "Jacobian") via finite-difference methods. The finite-difference methods make small changes in individual variable inputs to a complex system to estimate the partial first derivatives near a given system operating point.

The Jacobian may then be used to help extrapolate the changes necessary to the independent variables to iteratively converge on the desired dependent function results. Furthermore, because of the high computational cost of each system model calculation, the number of finite-difference calculations can be minimized through Broyden updates. Broyden updates adjust the first derivative calculation using the additional information from the next iteration result. Again, greater detail is available from Waters [31, App. B] and Jones [80].

The numerical method of solution for the system level described above allows for the flexibility to run different "black box" component models from a variety of contributors that may only provide information on the component outputs for some given inputs. While this works well for systems with linear flow paths and fast-computing components, NPSS bogs down for computationally-expensive calculations or looped flows where components are both upstream and downstream from each other. Unlike environments working with systems of interrelated equations between components, any “slow” component in NPSS will need to be run in full repeatedly, with an exponential increase in component runs with the number of solver dependent variables. For looped flows, as may be found in recuperating systems, each looped property must be checked for consistency and/or set as part of the global solver’s dependent variables—increasing the size of the Jacobian, and so the number of required calculations, exponentially. Unfortunately, for this work both of these concerns can come into play such that minimizing computational cost and the number of solver variables considered is a constant tension.

For the system configurations presented in this work, a system design is usually built up in progressive complexity, “solving” for turbomachinery conditions before adding smaller or simplified versions of the fuel cell subsystem models, and progressively increasing the size of those subsystems or otherwise slowly altering the characteristic(s) of interest.

3.3 Component-Level Models

The flexibility of NPSS stems from its modularity: information regarding air, fuel, and shaft connections (or other characteristics as applicable) is passed between objects representing different physical components at standardized “port” connec-

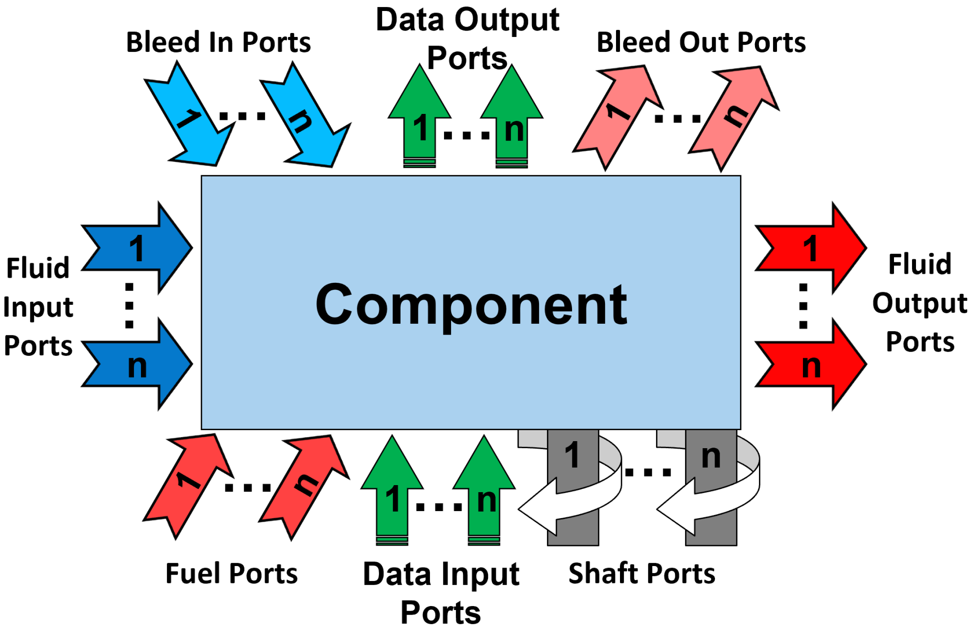

Figure 3.2: Schematic of Generic NPSS Component, including Input/Output Port Types.

tions as depicted in schematic Figure 3.2. NPSS has standard object definitions for GT components like turbines, compressors, inlets, and fans. Customized component models or performance maps may also be written to address the specific needs of the user. Individual component models can vary widely in complexity "inside the box," from lookup tables, to numerical solvers, to wrappers for external codes. Indeed, one of the features of NPSS is that the precise workings of a modeled component can be obscured to better enable different organizations to work on the same model without disclosing intellectual property.

Additionally, many component models can expand their capabilities with the use of "Sockets" which are optional subsidiary calculations that are subordinate only to the component itself. One example of this is the optional pressure-drop socket for the HeatExchanger component. A performance map or other calculation can be associated with the component, passing information back and forth via the socket.

Fluid properties inside and between components may be tracked and calculated using several different thermodynamics packages. We use the Chemical Equilibrium with Applications (CEA) [82] package which allows for arbitrary chemical equilibrium reactions and flow property calculations to be performed at any point as appropriate to the model.[ii]

This work exploits the flexibility of NPSS by using two sets of models. The first set are 'off the shelf' models for standard turbomachinery model components, including compressor and turbine performance maps from the Energy Efficient Engine (E3) program [83] that are included with the standard NPSS distribution. The second set are models of the SOFC subsystem-specific components that have been developed 'in-house' specifically for the GT/SOFC application. The basics of both sets of models have been described in detail in two previous works by Waters [31, Ch. 2] and the author [17, Ch. 8]. However, many of the SOFC subsystem components received updates for the current work, and the standard Heat Exchanger component used here (see Section 3.3.3) is new to this research application and so has not been fully described before.

Table 3.1 lists the standard components, their input/output connections, and provides brief descriptions of their purpose and calculations carried out in the model. Additional information on the standard components is available from the current

---

[ii] The implementation of CEA is not exactly comparable to similar calculations in dedicated chemical equilibrium tools such as CHEMKIN or Cantera. For example, CEA in NPSS will round small equilibrium values to zero which may cause divide-by-zero errors in electrochemistry calculations.

consortium manager (Southwest Research Institute[iii]).

[iii] Current link to consortium page: https://www.swri.org/consortia/numerical-propulsion-system-simulation-npss

Table 3.1: Standard NPSS Component Descriptions.

Component	Inputs			Outputs			Shaft	Description	Calculations
	Fluid	Fuel	Bleed	Fluid	Fuel	Bleed	Connections		
Ambient	0	0	0	1	0	0	0	Provides conditions for speed and altitude	None
Bleed	1	0	n	1	0	n	0	Combines bleed flows	Heat loss
Burner	1	1	0	1	0	0	0	Reacts fuel and airflows	Pressure loss, Combustion
Compressor	1	0	0	1	0	0	1	Compression with losses from shaft work	Scalable performance map
Duct	1	0	0	1	0	0	0	Passes flow between components	Pressure and heat losses
Flow End	1	0	0	0	0	0	0	Terminal component of flow path	None
Fuel Start	0	0	0	0	1	0	0	Initiates fuel stream	None
Heat Exchanger	2	0	0	2	0	0	0	Passes heat between two flows	Set effectiveness or heat transfer
Inlet	1	0	0	1	0	0	0	Calculates performance of engine inlet	Ram pressure recovery and drag
Inlet Start	0	0	0	1	0	0	0	Initiates air stream w.r.t. Ambient	None
Nozzle	1	0	0	1	0	0	0	Converging/Converging-Diverging Nozzle	Compressible flow with losses
Shaft	0	0	0	0	0	0	n	Single physical shaft	Matching rotational torque and speed
Splitter	1	0	0	2	0	0	0	Splits incoming flow into two streams	None except Bypass Ratio
Turbine	1	0	0	1	0	0	1	Expansion with losses giving shaft work	Scalable performance map

The workings of earlier versions of the custom components have been discussed previously in great detail by Waters [31, Ch. 2] and the author [17, Ch. 8]. These are the CPOx Reformer, Fuel Cell Inlet, Solid Oxide Fuel Cell, and Combiner components. These components have not been altered substantially in terms of the physical modeling they carry out. However, they have received many under-the-hood changes and bug-fixes for substantial improvements to stability, calculation speed, and operating modes to better perform within NPSS. These changes are elaborated explicitly in Appendix D. Finally, two new custom components were also developed specifically for this work to represent a generator and an electric motor.

Given the centrality to this work of the components used to incorporate the reformer and fuel cell, the workings of all (even standard NPSS components or those originally developed by Waters) are described next in greater detail.

3.3.1 Electric Motor

Schematic illustrations of the electric motor is presented in Figure 3.3. The motor applies torque to a shaft in response to electric power input and efficiency. The amount of torque applied is calculated to match the useable electric power input in proportion to the rotational speed of an attached Shaft component. The mass of the motor is estimated based on its power output and an assumed specific power. The electric motor is presumed to be $16\mathrm{kW\,kg^{-1}}$, following the High Efficiency Megawatt Motor project from NASA Glenn Research Center [84, 85]. Associated converter/inverter power electronics ($19\mathrm{kW\,kg^{-1}}$ per Hall et. al. for an

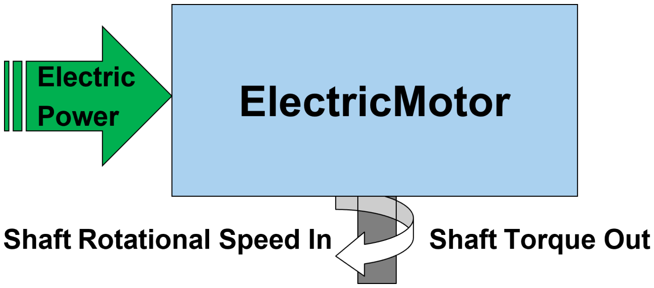

Figure 3.3: Schematic illustration of NPSS custom electrical components.

optimistic 2035 target [86]). Together, the overall component has a specific power of 8.7kW kg^{-1}. An efficiency of 95% has been assumed, taking account of the efficiency of both the motor and power electronics.

3.3.2 Generator

Schematic illustrations of the electric motor and generator components are presented in Figure 3.4. The motor applies torque to a shaft in response to electric power input based on the rotational speed of an attached Shaft component. The generator does the opposite, outputting electric power in response to torque and rotational speed of the attached Shaft. The mass of each component is estimated based on its power input/output and an assumed specific power. The specific power of a state of the art electric motor is not the same as that of a state of the art generator. In this work, the generator presumes a specific power of 6.55kW kg^{-1} to include the mass of the generator itself (10kW kg^{-1} SOA per Madonna et. al. [19]) and converter/inverter power electronics (19kW kg^{-1} per Hall et. al. for an optimistic 2035 target [86]). The electric motor is presumed to be 16kW kg^{-1},

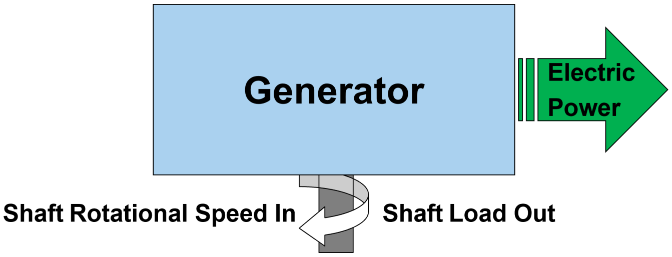

Figure 3.4: Schematic illustration of NPSS custom electrical components.

following the High Efficiency Megawatt Motor project from NASA Glenn Research Center [84, 85].

3.3.3 Heat Exchanger

The HeatExchanger component (shown as a schematic in Figure 3.5) is an off-the-shelf component module provided with NPSS. The model calculates basic heat transfer between two parallel (i.e. co-current) streams. This calculation assumes no particular scaling or geometry besides parallel flow. However, pressure losses on each side may also be supplied through a subordinate calculation via an NPSS socket component (see Section 3.3) or as a direct pressure loss value setting. , This component does not calculate counter- or cross-current heat exchanger performance.

The calculation is carried out according to Kays and London [87] for a steady-state condition only. The calculation may be operated in two modes, using either an effectiveness or absolute rate of heat flux rate $\dot{Q}$ as a given parameter applied to the two streams. In the former case, the effectiveness rating will imply the heat energy passed between the two streams as a function of their temperature and heat

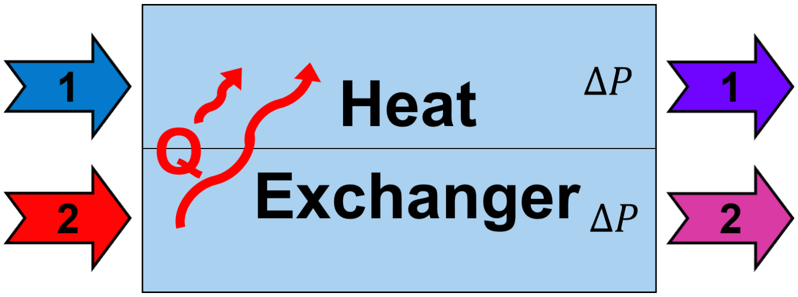

Figure 3.5: Schematic of NPSS HeatExchanger Component, including Input/Output Port Types.

capacity; in the latter the heat transferred will imply an effectiveness.

While not necessarily aligned with an On-Design or Off-Design mode (see Section 3.3) , in this work we use the heat transfer rate input mode during the design process to achieve a target outlet temperature. The required effectiveness becomes an output during the design process. While Using the effectiveness mode during subsequent off-design calculations may be reasonable since this characteristic can be reasonably stable for different flow conditions, at least as used here with the constraints of similar flow rates on both compressor- and turbine-exhaust sides.

3.3.4 Catalytic Partial Oxidation Reactor (CPOx)

The catalytic partial oxidation reactor model (hereafter referred to as the "CPOx") component serves to reform hydrocarbon fuel species into some proportion of syngas species (i.e. H_2, CO) to enable the SOFC to begin reacting with the fuel. As described in the Introduction, a CPOx reactor is the most compact—though least efficient in terms of conversion—reformation method. The CPOx model

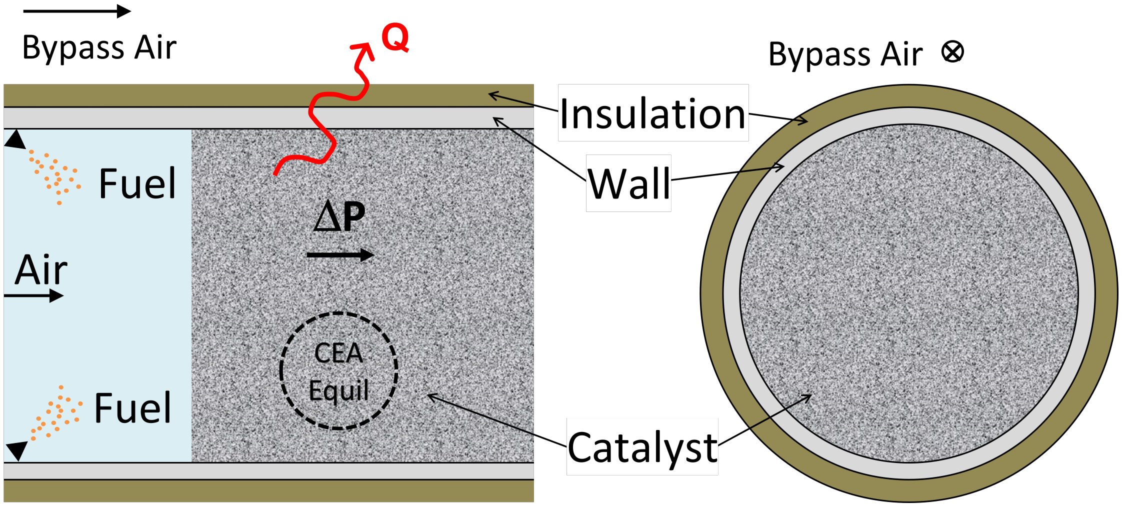

Figure 3.6: Geometry of single catalytic partial oxidation reactor. Component includes multiple cylinders surrounded by cooling bypass air.

described in this section has only been modified slightly from the prior development by Waters [31, p. 68], with those modifications elaborated in Appendix D.

The presumed geometry of the CPOx is that of a number of circular tubes containing an alumina foam catalyst, represented in Figure 3.6. The outside of each tube is surrounded by a layer of insulation to moderate heat loss. All of the tubes are contained in a duct through which bypass air is passed for cooling and pass-through to the fuel cell inlet and SOFC.

As depicted in Figure 3.7, the CPOx model splits incoming air into bypass and CPOx streams. Fuel is combined with the CPOx air stream ahead of the reaction zone (lower path in light purple). The reaction zone itself is divided into a number of segments along a quasi-1D flow path.

The CPOx takes inputs of air and fuel conditions, and determines an appropriate AFR for the fuel passing through the reaction zone (“reax” in Figure 3.7).

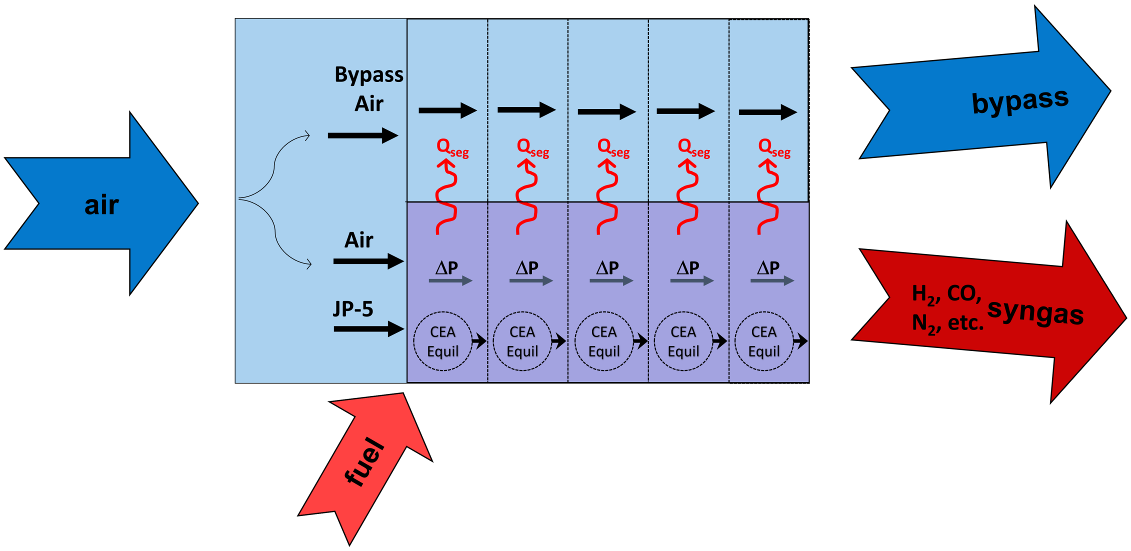

Figure 3.7: Schematic of NPSS Catalytic Partial Oxidation Reactor Component. Quasi-1D segments and processes illustrated.

An appropriate AFR is defined to be marginally greater than a limiting-value that forms soot [88]. Soot is elemental carbon that remains in the mixture of air and fuel after the equilibrium is calculated (i.e. post-burning). The soot formation limit depends on the temperature and pressure of the reformer exhaust. In general, increasing the temperature decreases the limiting AFR while increasing the pressure raises the limiting AFR [64]. The lowest appropriate AFR values (i.e. just above that of soot formation) are preferred as this results in the greatest concentration of fuel species in the anode flow.

For performance, a table of AFR values across a range of output temperatures and pressures has been pre-calculated. Computationally, the CPOx element starts at an initial guess for the AFR, then adjusts the AFR based on the tabulated result based on the exhaust temperature and pressure conditions. The CPOx iterates the calculation until the AFR determined is converged, i.e. varying by less than 1% between iterations.

As part of the calculation of exhaust temperatures and pressures, pressure losses through the alumina foam catalyst are calculated as a quasi-1D segmented calculation, with losses in each segment determined using the Forscheimer equation. Heat losses from the reaction zone to the bypass in each segment are accounted for by Nusselt number correlations . Within each segment, an iterative loop converges upon the exit temperature until energy conservation is satisfied.

3.3.5 Solid Oxide Fuel Cell

The SOFC model used in this work is built directly from that in Waters [31, p. 73]. More detail is available there with modifications as identified here. A basic description of the model, shown schematically in Figure 3.8, is as follows: Three flows are taken as inputs: the anode fuel flow (usually at least partially reformed methane), a cathode oxidant flow (usually air), and bypass air flow that is used for cooling. Within the component, oxygen diffuses to the surface of the cathode where it is ionized picking up two electrons. The oxygen ions (O^{2+}) diffuse through the electrolyte to the anode side where they give up their electrons as they react with H_2 and CO to form H_2O and CO_2 respectively. This reaction is exothermic and generates heat which is partially transferred to the cooling bypass. The electrons on the anode side flow back to the cathode side via the electrical load thereby generating electric power equal to the product of the cell voltage and the current (ie. Vi). The

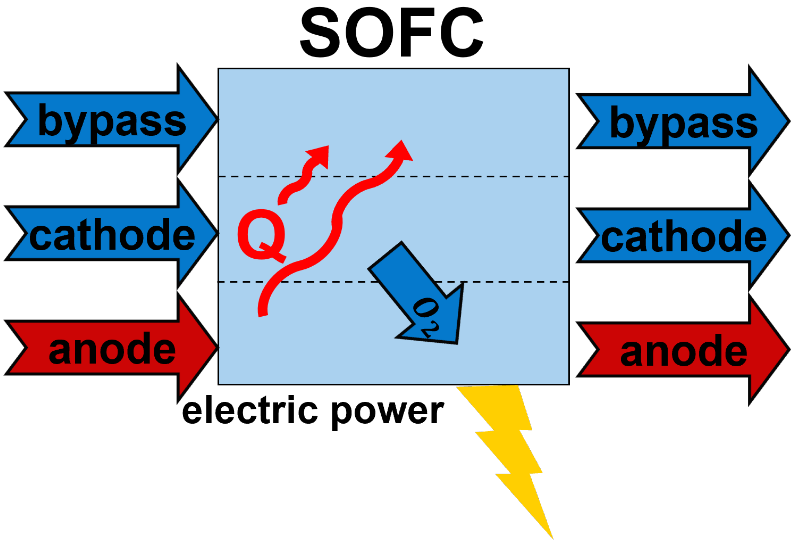

Figure 3.8: Schematic of NPSS Solid Oxide Fuel Cell Component. Figure reproduced with minor modification from Waters Figure 36 [31, p. 73].

component model outputs the state (temperature, pressure, and composition) of the anode, cathode, and bypass flows as well as the electrical power generated. All of these steps are calculated according to physical and electrochemical principles. . The model has been described as "intermediate fidelity" [31, p. 45]since such things like velocity profiles in the channel are not accounted for but property/composition variations 'down the channel'. However, this level of fidelity is higher than that used in most aerospace contexts (see Table 1.1).

3.3.5.1 Calculation Procedure

The SOFC model works at several different levels. First is a generalized geometry and sizing that splits the incoming flows to set flow rates for a single set of anode/cathode channels to simulate in greater detail. Next, the single channel is divided into a number of segments to model varying “down-the-channel” conditions. Inside each segment, an iterative solver determines the SOFC performance at that point and the resulting exhaust conditions.

The SOFC takes the form of a stack with a generalized geometry that is composed of a series of identical ’unit cells’. The intial sizing determines how many of those unit cells are required to provide the desired amount of electrical power from the incoming flow. The conservation equations (mass, energy, momentum, and charge) determines the electrical power produced and the state of the anode and cathode flows exiting the unit cell. The total power of the SOFC is the power produced by one unit cell times the number of unit cells. The state and composition of the SOFC exhaust is assumed to be the same as that of the unit cell. The length of the unit cell can be adjusted to achieve the desired level of utilization. This length along with the size of the unit cell and the number of unit cells are inputs to the SOFC mass model.

The geometry, illustrated in Figure 3.9, is a set of co-flowing anode and cathode channels of a given length separated by MEA layers using a unipolar arrangement. For a single “unit,” there is a number of repeating MEAs-and-channels (“reps”) that determine the ‘height’ of the SOFC stack, while the ‘width’ is set by the number of units placed side-by-side. The top and bottom of the stack has a layer of insulation

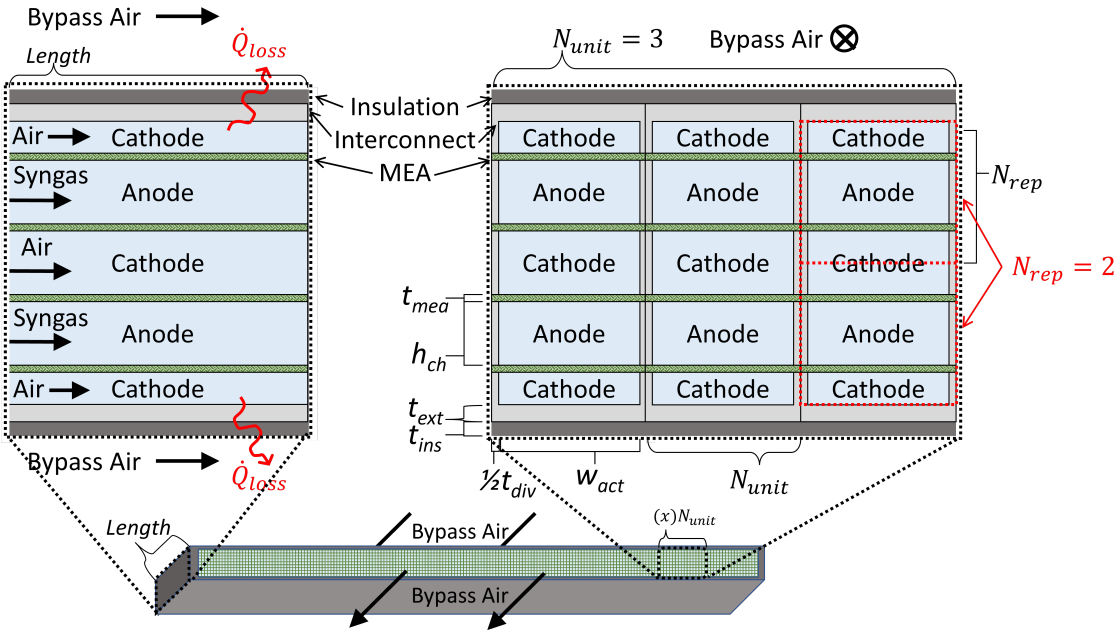

Figure 3.9: SOFC Stack Geometry.

separating the channels from the cooling bypass flow.[iv]

The number of SOFC units and reps determine the total number of channels between which incoming anode and cathode flows must be divided. Given the size of a single channel, a quasi-1D flow calculation determines the internal state and performance as flow progresses down a channel of the SOFC. Three separate flows—anode, cathode, and cooling bypass flows specifically—are considered. As illustrated in Figure 3.10, the channel length is divided into segments. In each segment, several different calculations are performed: (1) pressure loss for anode

---

[iv] In prior work [64], the SOFC was nominally placed as an annulus around a cylindrical gas turbine, and so the sides of the channel were connected such that heat could only transfer to the bypass flow through the top and bottom sides. In this work, this assumption is retained even though the annular geometry is not presumed due to the expected scale of the SOFC being too large to fit in the space without extreme or complete flow disruption (a conclusion of the prior work). The assumption should still hold however so long as the stack aspect ratio (width/height) is sufficiently large enough that the top and bottom faces represent the vast majority of the surface area for heat loss. In practice, this condition is consistently satisfied.

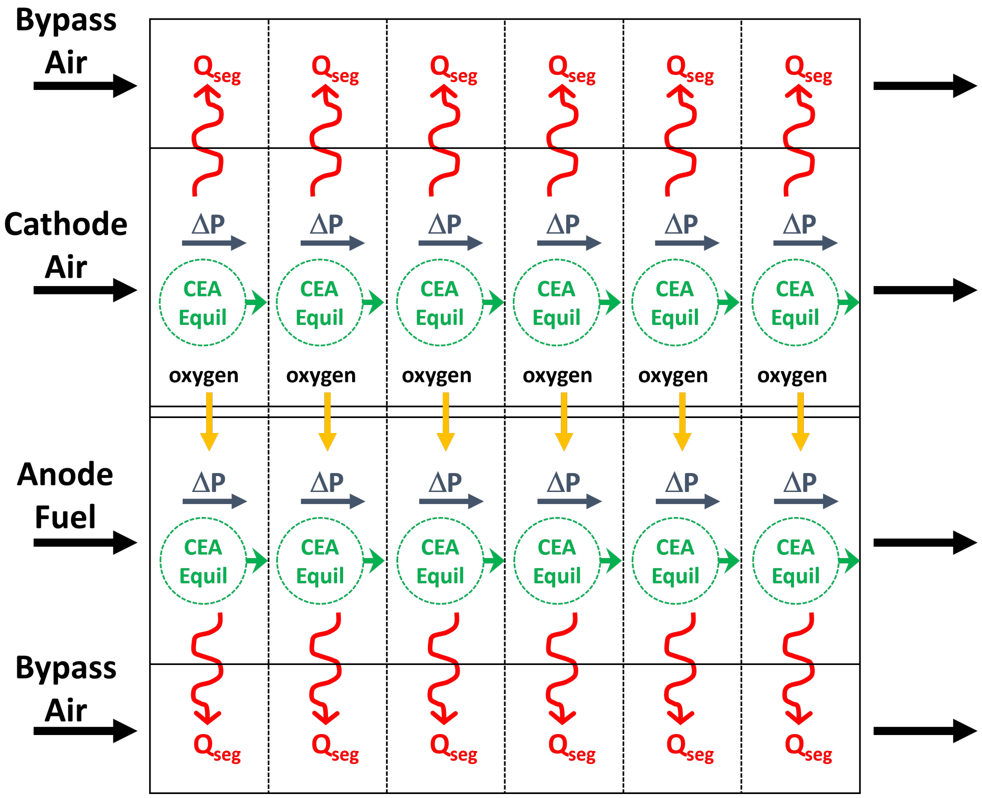

Figure 3.10: SOFC Channel Model Arrangement. Figure reproduced with minor modification from Waters Figure 40 [31, p. 77].

and cathode channels, (2) the electrochemical transfer of oxygen from cathode to anode flow, and the resulting electric power generated, (3) chemical reactions via the Chemical Equilibrium with Applications [82] thermodynamics package built into NPSS, and (4) the heat loss from the anode and cathode each to the bypass flow.

Within each segment, a self-consistent temperature and amount of oxygen transfer is accounted for through an iterative solver that performs each of these calculations per Figure 3.11 with varying anode/cathode operating temperature and SOFC current density. The operating temperature is the result of the balance of heat lost to the bypass air and heat release by reactions within the SOFC. In turn,

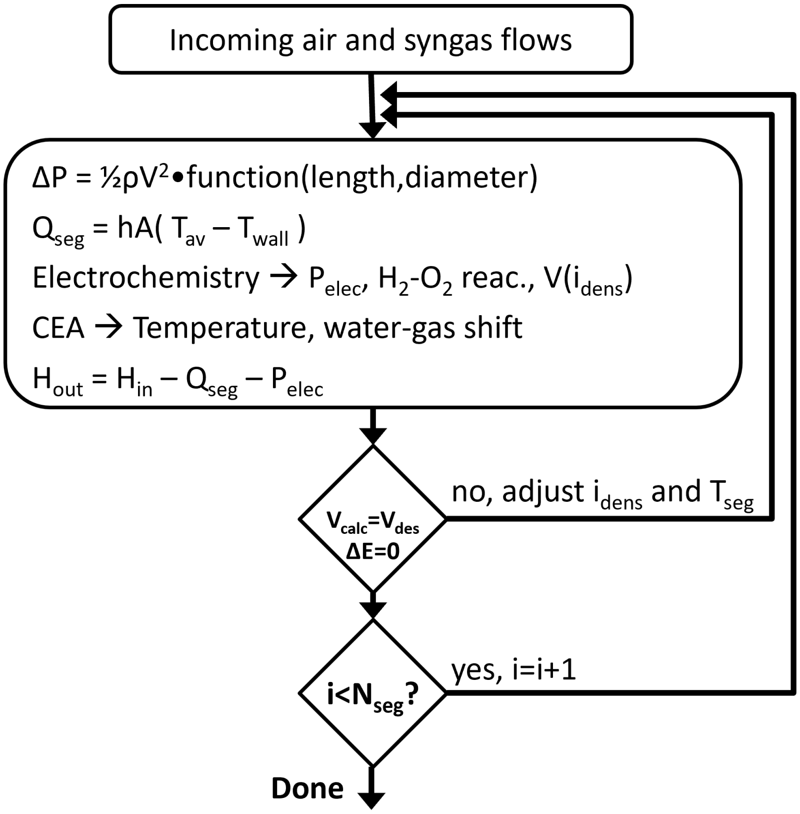

Figure 3.11: SOFC segment solver process diagram. Figure reproduced with minor modification from Waters Figure 41 [31, p. 78].

the current density determines the amount of power generated and heat released, and is the result of the internal conditions including temperature.

The internal adjustments to the current density and operating temperature take the form of another quasi-Newton solver written into the model, fortunately limited to two equations and two unknowns such that an analytical solution exists. A difference approximation is used to determine the four entries to the Jacobian to inform the guesses for the next iteration. Convergence over the iterations is achieved when both energy conservation and the target operating voltage are sufficiently satisfied. The strong and nonlinear interdependence of operating temperature and current density in this system both requires an iterative process and often leads to instabilities over repeated iterations.

3.3.5.2 Electrochemical Model

The nature of the temperature and current density's interdependence is dictated by the electrochemical model of the SOFC, which provides an operating voltage for input operating conditions (temperature, pressure, composition) and a target current density for a given segment of the MEA. Electrochemical models for SOFCs vary in complexity: relatively simple versions use open-circuit voltages with linear relationships of voltage and current density given in terms of slope values called "Area-Specific Resistance" or ASR. ASR values are simplified empirical results rather than physical models, and do not account for conditions beyond the available data.

For both this and prior work however, the SOFC component is expected to encounter widely-varying temperature, pressure, and composition conditions due to the nature of the aircraft application (see Section 1.2). As such, a more physics-based electrochemical model is employed that is based heavily on work by Zhu and Kee [72, 89–95]. The goal of the electrochemical model can be summarized (with greater detail again from Waters [31]) as the means by which the operating voltage of the SOFC is determined for a given current density. This is accomplished by calculating the reversible potential and subtracting several overpotentials (η)

representing irreversible losses. This is summarized in Equation 3.1.[v]

$$V_{cell} = V_{rev} - \eta_{ohm} - \eta_{act,a} - \eta_{act,c} - \eta_{conc} \tag{3.1}$$

The overpotentials considered by the model are: (1) ohmic (η_{ohm}) which accounts for resistive losses of electrons and oxide ions through the MEA, (2) cathode and anode activation ($\eta_{act,c}$,$\eta_{act,a}$) account for activation energy barriers for charge transfer reactions occurring at the respective interfaces, and (3) concentration overpotentials that account for mass transfer limitations through the porous anode and cathode materials. The latter result in lower reactant concentrations at the "active" layers of the anode and cathode near the electrolyte where the majority of charge transfer reactions occur. Ohmic losses are calculated using a temperature-dependent Arrhenius fitting for the ionic conductivity of the electrolyte (YSZ), and the electrical conductivities of the anode (Ni-YSZ) and cathode (LSM). Activation overpotentials for the anode and cathode are found using an iterative solution to the Butler-Volmer equation.

Concentration overpotentials are calculated using the Dusty Gas Model (DGM) [96]. The DGM appears to be preferred over simpler models such as Fick's Law Diffusion or an Advective Diffusion Model (ADM) alone in SOFC applications like this one [97]. The DGM is used to calculate the changes in reactant concentrations from the bulk channel flow to the functional layer of the anode and cathode near the

---

[v] Unfortunately the standard use of the greek letter η for efficiency in an aerospace context, and for overpotentials in a fuel cell context can be confusing. However this work is not *so* interdisciplinary that both uses overlap in any equations. If they do, it will be explicitly noted by subscript.

electrolyte surface, per Figure 3.12 for the anode specifically. In this implementation, linear first-order approximations are made for pressure and mole-fraction differences marching inward from the channel towards the solid electrolyte over a series of steps of size δ. The changes in species composition across the SOFC channel segment (presuming equilibrium) are used to determine the number of moles of each reactant and product species that passes through the anode/cathode interfaces (e.g. $a_2 - a_1$ per Figure 3.12). The diffusion processes accounted for in the DGM result in changes in pressure and species partial pressures across the anode/cathode. Since the SOFC electrochemical reactions generally occur at the functional layer, the concentration overpotential is the difference between the reversible potential calculated using the bulk partial pressures, and the reversible potential calculated using the partial pressures at the functional layer.

The precise implementation of the DGM was improved over the method used in Waters *but some issues remain.* First, Equation 3.2 provides a correction to the derived expression for the first-order concentration changes (Equation 62 in [31]) used in prior work, which includes an extraneous $1/p_-$ term.

$$\frac{x_{k,+} - x_{k,-}}{\delta} \approx -\frac{RT}{p_-}\left(\sum_{l \neq k} \frac{x_{l,-}N_k - x_{k,-}N_l}{D^e_{kl}} + \frac{N_k}{D^e_{k,Kn}}\right) - \nabla p \frac{x_k}{D^e_{k,Kn}} \frac{B_g}{\mu_-} \tag{3.2}$$

Additionally, a single linear pressure differential calculation for the anode and cathode layers was used previously, followed by a first-order approximation of the mole fraction profile over a certain number of steps. However, there is some argument

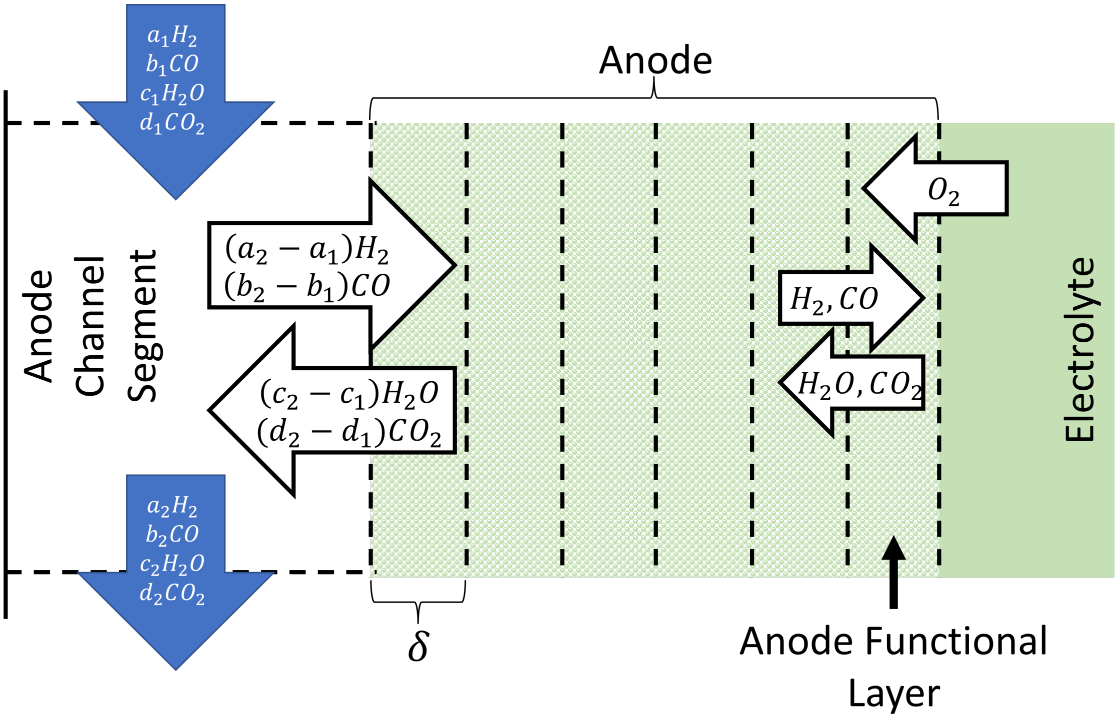

Figure 3.12: Schematic of Dusty Gas Model Implementation (Anode Side Only).

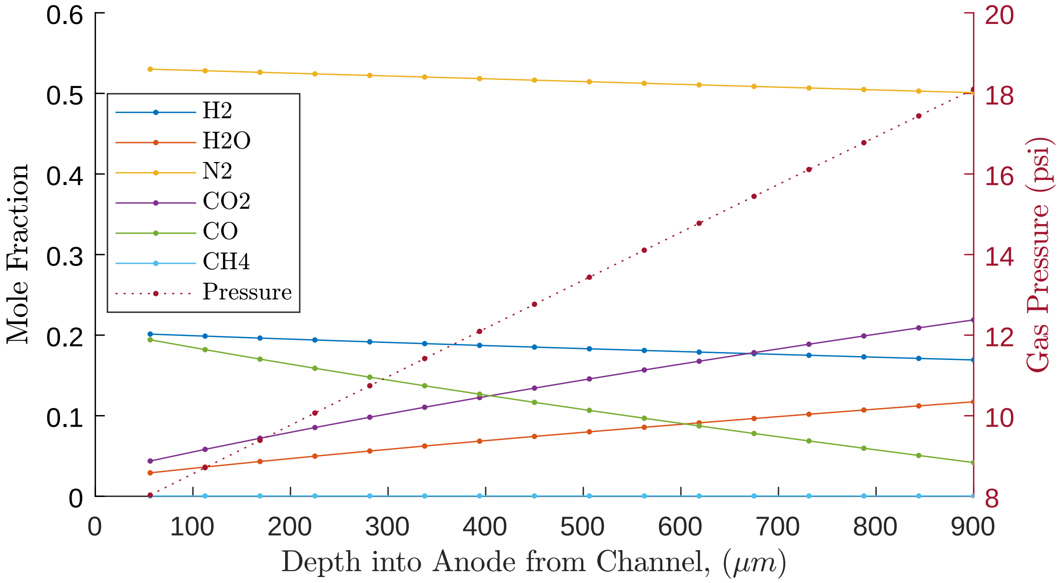

Figure 3.13: Representative Results from Dusty Gas Model for Anode, 0.725V with JP-5 reformate at $AFR = 6$.

regarding the level of complexity appropriate to the DGM implementation used. The most common difference in assumption is with regard to pressures. Fu found that an isobaric assumption was reasonable [98, 99], while Zhu et. al. [91] found that a linear pressure gradient was sufficient for appropriate calculations across the range of operating parameters. In a paper specifically addressing these concerns, Bertei and Nicolella [100] found that at least the uniform pressure assumption was inconsistent with stoichiometry for porous electrodes, especially for multi-component mixtures. The approach taken here, which is to update the pressure gradient in each segment, is consistent with a linear pressure gradient per Zhu et. al. [91] since the mole fraction profile is also linear per each segment.A representative result is provided in Figure 3.13

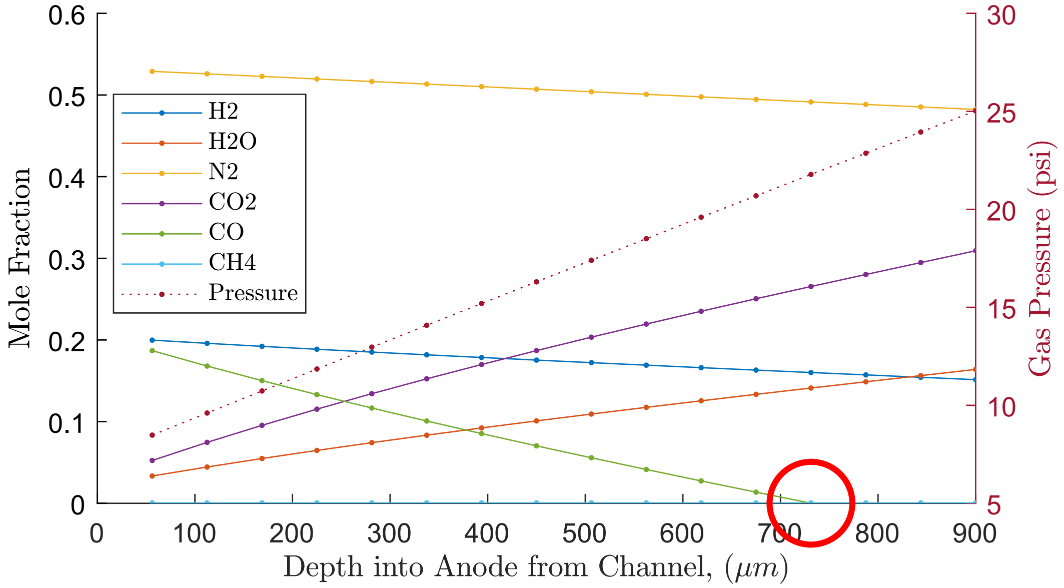

Figure 3.14: Problematic Results from Dusty Gas Model for Anode, 0.625V with JP-5 reformate at $AFR = 6$. Zero-concentration point of CO circled in red.

There is however an observed problem in the implementation of the DGM in this work. At higher current densities, the predicted concentrations of some species—particularly carbon monoxide—drops to zero well before the boundary of the anode as is shown in Figure 3.14. This is non-physical since there must be a concentration of a species in order for diffusion to continue through the boundary.

One possible cause is that internal reformation reactions through the anode are not accounted for except at the anode functional layer at the boundary between the anode and solid electrolyte. However, that explanation has not been confirmed. An alternative path for future work that could address these concerns is to abandon a multi-segment 1-D process. Instead, a linear single-segment model could be used that iterates until convergence on the correct pressure and mole-fraction gradients, per Zhu and Kee [93]. However, this alternative and further troubleshooting is left for future work.

Finally, the reversible potential V_{rev} is determined by the global oxidation reaction for the fuel and oxidant species, which takes account of the bulk concentrations of reactants and products in the anode and cathode channels. This is a slight departure in nomenclature from Waters, where the reversible potential was calculated for the species concentrations at the active layers, which made the concentration overpotential implicit. In this work, a reversible potential is calculated at both the active layer and bulk channel flow, and the difference in voltage identified as the concentration overpotential. Further calculation details and specific electrochemical parameters applied in this work are left identical to Waters [64], and so are not repeated here in detail except if and when they deviate.

The resulting electrochemical performance is illustrated in the polarization curves shown in Figures 3.15 and 3.16. These show the significant sensitivity of performance to operating temperature and pressure, set to be equal in both the anode and cathode. In both figures, increasing the temperature or pressure improves electrochemical performance on JP-5 reformate (reformate $AFR = 6$). Here the effects of operating temperature and pressure variation in Figures 3.15 and 3.16 appear to be similar in magnitude. However, it should be emphasized that the plots use linear steps of temperature (50K increments) and exponential steps in pressure ($\approx$ doubling).

The specific sources of the performance trends shown above can be seen from the variations in overpontentials with temperature and pressure illustrated in Figure

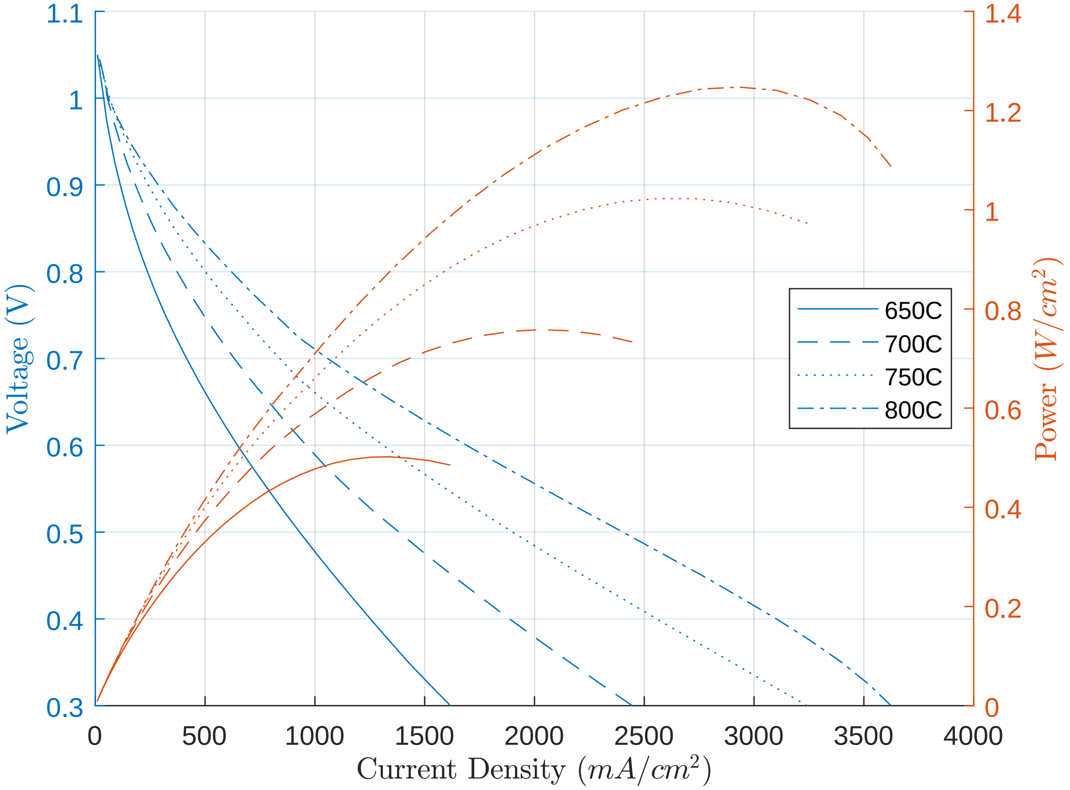

Figure 3.15: Polarization curves of YSZ-based SOFC at varying temperatures and 1 atm pressure, with air and JP-5 reformate at AFR=6.

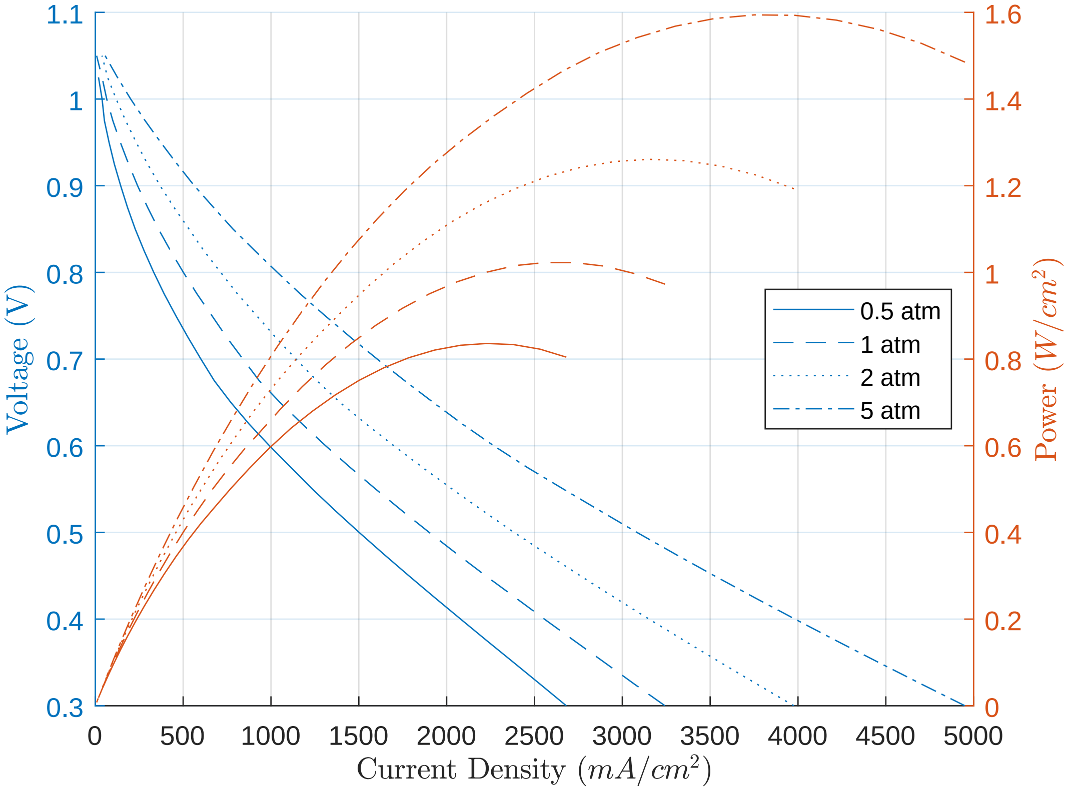

Figure 3.16: Polarization curves of YSZ-based SOFC at varying pressures and 800°C temperature, with air and JP-5 reformate at AFR=6.

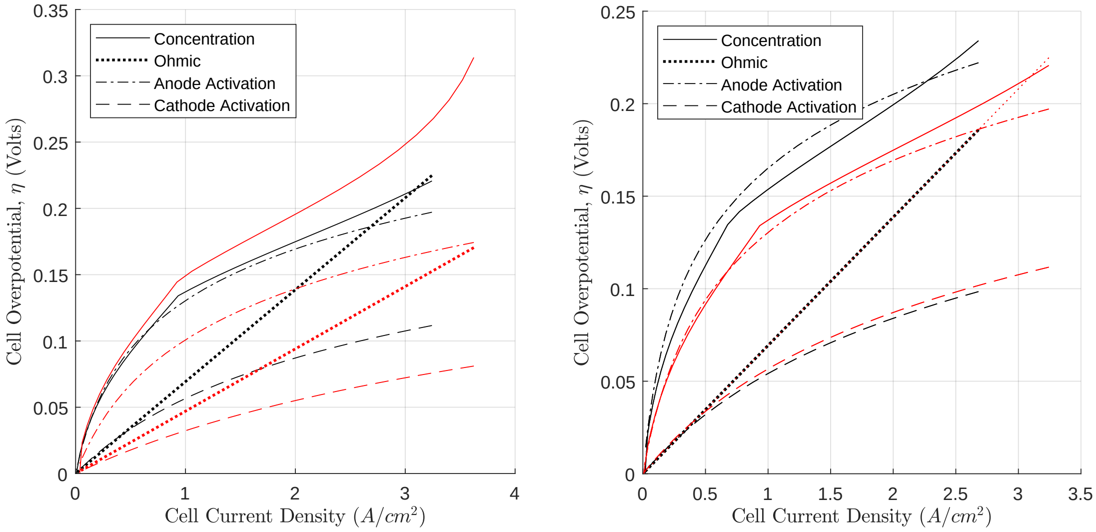

(a) Overpotentials at 1 atm and 750°C (Black) and 850°C (Red)

(b) Overpotentials at 750°C and 1 atm (Black) and 2 atm (Red)

Figure 3.17: Variation of overpotentials with temperature and pressure in YSZ-based SOFC operating on air and JP-5 reformate at AFR=6.

3.17. Notably, the greatest contributing overpotential is due to concentration. In this scenario (and to some degree, all scenarios using a CPOx reformer), the concentrations of fuel species are relatively low ($\approx 3\% H_2$ by mass) because of significant dilution by reaction products (H_2O and CO_2) that form at the anode.

The minor discontinuity in the concentration overpotential trend around 800 $\mathrm{mA\,cm^{-2}}$ corresponds to the non-physical onset of zero-concentration of carbon monoxide shown in Figure 3.14.

Pressure and temperature variations also affect the reversible potential through the Gibbs Free Energy: higher temperatures lower the Gibbs Free Energy for a given reaction (per $\Delta G = \Delta H - T\Delta S$) while higher pressures increase it by increasing the concentration of reactants to products in the reaction equilibrium. Figure 3.18

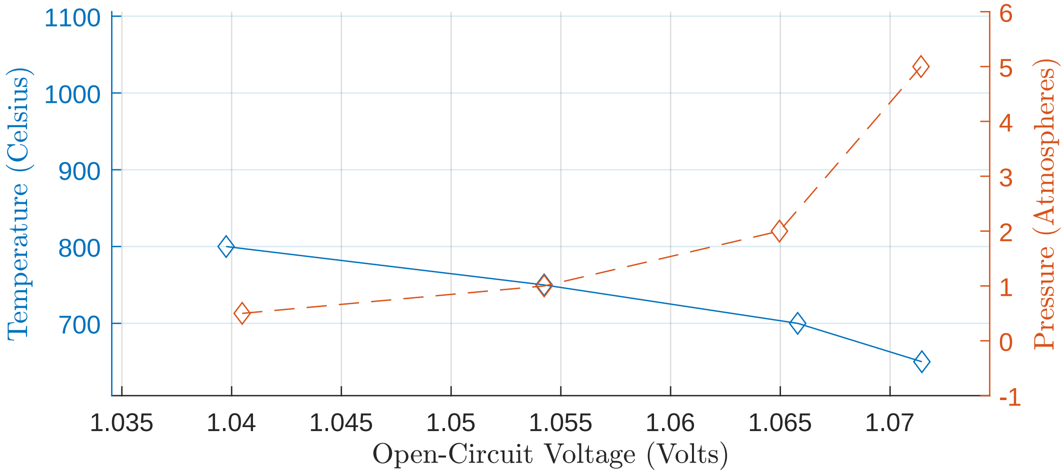

Figure 3.18: Variation in Open Circuit Voltage with Changes in Temperature and Pressure. Shared point represents the same 750°C and 1 atm baseline conditions.

shows that these effects are relatively small amounting to only about 0.03 Volts across the expected range of conditions.

3.3.6 Fuel Cell Inlet

The fuel cell inlet model functions as a heat exchanger placed between the reformer and the SOFC components. The purpose of the inlet is to prevent thermal shock at the entrance of the SOFC by minimizing the difference in temperature between the anode and cathode flows. In the NPSS model, the inlet also splits a fraction of the incoming airflow into a bypass that is used to cool the stack. However, this bypass is assumed not to be in thermal contact between the anode and cathode flows which only exchange heat with each other. This keeps the bypass flow from a) removing heat from the reformer potentially quenching reaction and b) prevents it from heating up enabling it to more effectively absorb heat from the

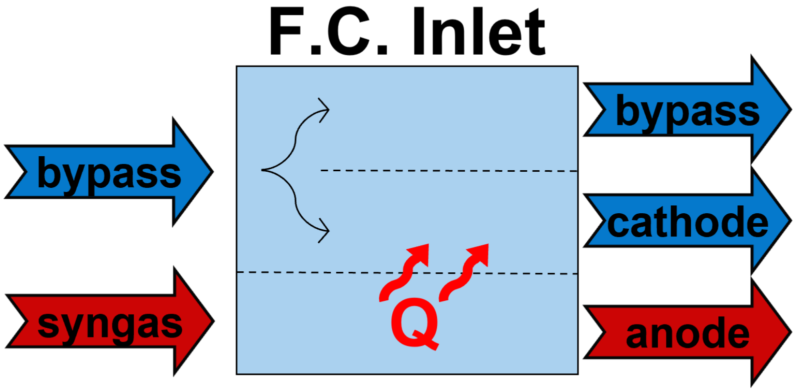

Figure 3.19: Schematic of NPSS Fuel Cell Inlet Component. Figure reproduced with minor modification from Waters Figure 43 [31, p. 90].

SOFC downstream.

The fuel cell inlet is intended to be a physical part of the SOFC stack. As such, in terms of both presumed geometry (see Figure 3.9) and the segmented quasi-1D calculation process, the fuel cell inlet functions similarly to the SOFC model, only with the SOFC electrochemical model removed. Heat exchange is determined through Nusselt number correlations, while pressure drop is found through the same Nusselt number correlations as the SOFC model. Details of both the heat exchange and pressure drop calculations are available in great detail from Waters [31, p. 89] and are not elaborated here.

Several changes have been made to the fuel cell inlet model since this prior work. First, the heat passed to the bypass flow now changes the bypass flow temperature progressively after each segment rather than as a single addition at the end of the component. This allows for a more accurate heat flux calculation within each segment and prevents heat additions that make the co-flow bypass cooling hotter than the inlet flow itself. Second, separate design and off-design modes for the fuel cell inlet have been specified. In the design mode, the SOFC inlet increases in length by adding segments until the temperature difference between the anode and cathode flows is driven below a maximum allowable temperature difference - usually 50K. In off-design mode, the length of the inlet is fixed, and the temperature difference is determined soley by the input conditions.

3.4 Sizing and SOFC Subsystem Design

For a designed system, the physical size of the fluid flows through the system correlate to the physical size and weight of the device(s) containing those flows. In prior work, piecewise models of mass and volume for both turbomachinery and fuel cell components were created and validated. The turbomachinery models are based on work by Onat and Klees [31, Ch. 4; 101], while the fuel cell models are based on a quasi-annular SOFC geometry developed by Waters [31, Ch. 4].

These mass and volume models are used in this dissertation without substantial alteration, but it should be noted that the "unipolar" SOFC channel geometry used in the model does not match the standard practice of planar SOFCs, as are most commonly available. Standard planar SOFC stacks use an additional interconnect layer (also called a "bipolar plate" design) that can make up over half of the total stack mass. This is avoided in the Waters geometry at the potential cost of losses in current collection due to longer electron paths.[vi]

[vi] A further discussion of the unipolar/bipolar distinction by Li is available [24, p. 234].

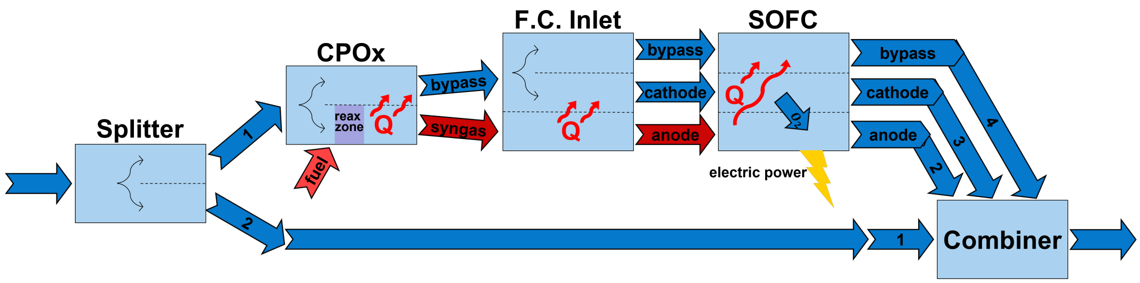

Figure 3.20: SOFC Assembly Diagram, reproduced with minor modification from Waters Figure 30 [31, p. 67].

3.4.1 SOFC Assembly

Together with some off-the-shelf components, the custom SOFC system components are used to represent the SOFC assembly of the GT/SOFC as shown previously in Figure 1.11. Figure 3.20 (reproduced with minor modification from Waters' Figure 30 [31, p. 67]) shows how those components are connected within NPSS. Figure 3.20 also includes a Splitter (a standard NPSS component) that is connected upstream of the CPOx reformer to allow a set fraction of the air flow to bypass the SOFC components. The bypass and SOFC flows are re-combined in the 'Combiner' element prior to entering the combustor.

3.5 Performance Metrics

In prior work, these NPSS models were used for additional secondary power generation (i.e. non-propulsive power) [29, 64]. The performance metric then was the relative fuel flow rate consumed to maintain constant flight versus a baseline traditional jet engine using a mechanical generator for secondary power instead.

Any improvement in efficiency provided by the GT/SOFC was balanced against the impact of the increased weight of the hybrid system on the aircraft's drag polar. Furthermore, drag impacts for notional pylon-based configurations were accounted for as well, further changing the drag to be overcome.

In this work, we are also interested in using the SOFC power for propulsion, and shifting our performance metric where possible to the thrust-specific fuel consumption (TSFC), and a range estimation. The TSFC may be calculated directly from the model outputs of thrust and fuel flow rate (per Equation 2.30), while the range calculation is based on a fuel flow rate equation similar to Equations 2.31 and 2.32, all derived previously. The combined equation for the fuel flow rate is provided in Equation 3.3, and the resulting range provided in Equation 3.4, from carrying out the integration in Equation 2.28. This is actually identical to Equation 2.38 from the analytical modeling chapter, though in that case many of the symbols are implied to be substituted for other analytical expressions. Note that the values for the system thermal and propulsive efficiencies (η_{sys}, η_{prop}) and the fuel combustion enthalpy (h_{fuel}) are derived from the model's instantaneous value of fuel flow rate, and are assumed to remain constant over the course of the flight.[vii]

$$\dot{m}_f = \frac{v\left(C_{D,min} + K\left(\frac{m_f+m_0+m_{eng}}{\frac{1}{2}\rho v^2 S}g - C_{L,min}\right)^2\right)\frac{1}{2}\rho v^2 S}{\eta_{sys}\eta_{prop}h_{fuel}} \tag{3.3}$$

[vii] A more rigorous analysis would use the NPSS model to determine off-design performance for the varying thrust requirements as fuel is expended over the course of the flight, but this is computationally expensive at this time. It is certainly an avenue for future work.

$$R = -\frac{(\eta_{sys}\eta_{prop}h_{fuel})}{g\sqrt{KC_{D,min}}}\tan^{-1}\left(\sqrt{\frac{K}{C_{D,min}}}\frac{C_{L,min}\left[\frac{1}{2}\rho v^2 S\right] - g\left(m_f + m_0 + m_{eng}\right)}{\frac{1}{2}\rho v^2 S}\right)\Bigg|_{m_f=0}^{m_f=m_{f,ini}} \tag{3.4}$$

The TSFC provides information about the marginal cost of the aircraft in terms of fuel expenditure, which is relevant for industry metrics such as fuel burn per seat-mile (recall Figure 1.3). The range estimation accounts for any change in aircraft range capability due to the increase in the mass of the power generation system. In contrast with previous work however, the maximum mass of the aircraft does not change with the mass of the power generating hardware; instead the maximum fuel weight is reduced to accomodate the extra component mass.

This procedure avoids applying the drag polar of the airframe to total aircraft weights outside of the design specification. Additionally, the volume considerations of prior work, while important in their own right, are neglected here by presuming a rough trade of tank volume with GT/SOFC hardware[viii] and a wing structure more optimally designed for a GT/SOFC rather than direct replacement onto an under-wing pylon. With these two changes to the scenario, the thrust required initially in all cases will be constant, and so the TSFC becomes an apples-to-apples metric across our range of inquiry.

The aircraft information used for the range calculations represents a regional transport jet, as previously provided in Table 2.2.

[viii] A quick check is to compare the density of jet fuel (about $0.82\,\mathrm{g\,cm^{-3}}$) with the average density of an SOFC stack (about $4.0\,\mathrm{g\,cm^{-3}}$ per a piecewise estimation in Figure 8 by Tornabene et. al. [60]). The 5x greater density of the stack suggests that trading fuel mass for SOFC mass results in rather more available internal volume to place the SOFC components.

The relative fuel flow rate is still used in this work as well as a metric for the turboelectric GT/SOFC configuration. The relative fuel flow rate is most appropriate there since the configuration only supplies electric power. The conversion of that power production to propulsive thrust is beyond the scope of this work.

3.6 Parallel Hybrid GT/SOFC Model

Prior work with the NPSS model described in this chapter has focused on the efficient production of secondary electrical power from the SOFC to replace off-takes from the main engine shaft or a separate APU. Here we will consider instead applying the power to propulsion, which may take a variety of forms.[ix] In this section we'll consider a "Fan Support" GT/SOFC that supports and augments the thrust produced by an otherwise-standard turbofan by adding more torque to the fan shaft. In the next section we'll instead look at a GT/SOFC that produces only electrical power (to be pithily described as a "Flying Power Plant"), using separate electric motors and fans to produce all thrust.

A sketch of a fan support configuration is provided in Figure 3.21, though on an aircraft, the arrangement is more likely to look closer to the sketch in Figure 3.22. Conceptually, the configuration is closest to the parallel hybrid shown in Figure 1.10. However, instead of a battery providing power to an electric motor on the turbofan shaft, the SOFC provides the electrical power. The likely advantage in this case is that the fuel cell uses fuel with a specific energy ($\approx 15\mathrm{kW\,h\,kg^{-1}}$)

[ix] Using an electrical motor on a shaft to drive a fan is not the only means by which electricity can be applied to propulsion. Just one alternative includes using the electrical power to generate a plasma arc that catalyzes the reduction of NOx pollutants [102].

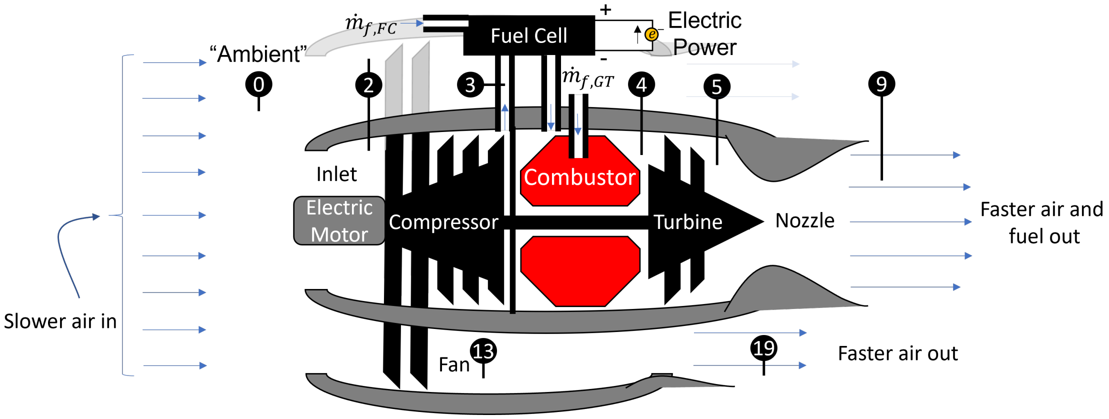

Figure 3.21: Sketch of fan support GT/SOFC system configuration, with station numbering.

an order of magnitude larger than all but the most optimistic battery performance targets ($\approx 1\mathrm{kW\,h\,kg^{-1}}$ per [1, Table 4.1]), and so can more easily provide a greater proportion of total energy to the system—especially over a long-duration flight.

By providing additional torque to the same shaft as the other turbomachinery, the electric motor can relieve some of the demands for power from the turbine. In the literature, "Turbineless" propulsion [28, 49] is the extreme version of the Fan Support model, where the turbine of the GT is replaced entirely by an electrically-driven motor. The result is that all of the energy of the compressed and heated gas may be accelerated through a nozzle to provide thrust directly. However, this may be a substantial amount of power, and supplanting the turbine is comparatively inefficient as, all else being the same, you will have a lower propulsive efficiency by simply increasing the exhaust velocity of the turbofan core.

An alternative is to use the extra power to increase the bypass ratio of a turbofan. Practically, this means the SOFC electrical power can be used to sup-

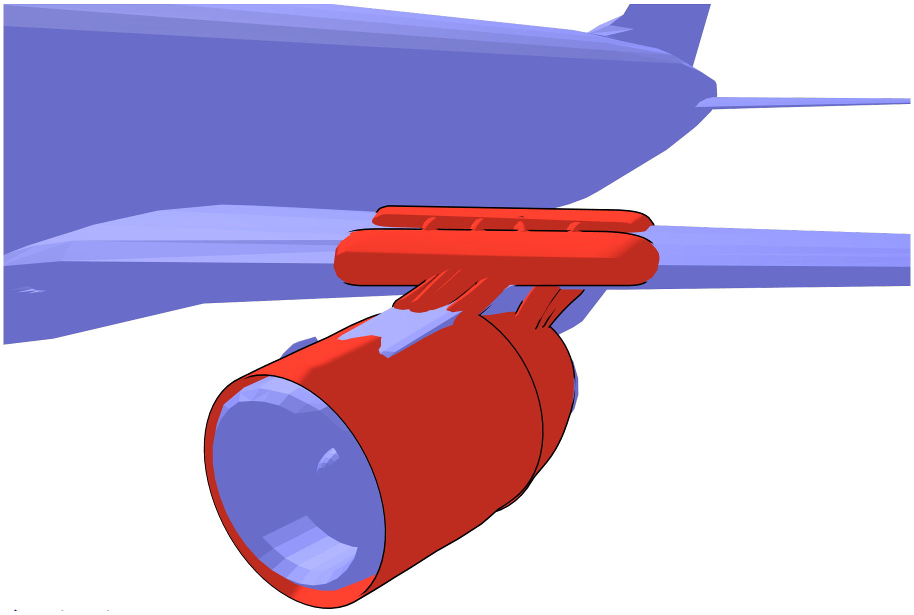

Figure 3.22: Sketch of Notional "On-Wing" Fan Support GT/SOFC. "767-300ER" backdrop 3D model by RTicknor.

port the fan spool (often the same as the low-pressure compressor/turbine spool) through an electric motor in order to reduce demand on the aircraft turbine, potentially lowering temperature requirements and pollution. The bypass ratio may also be effectively increased by the addition of wholly-electric fans elsewhere on the aircraft—especially for BLI schemes where fan placement may counteract drag from the aircraft body [86]. This concept certainly exists in the literature, with an analysis of general electric motor assist by Jansen et. al. [103], and for fuel cells providing the electrical power by Okai et. al. using pure hydrogen fuel [44, 104] and Atreya et. al. [105] considering hydrogen with either PEMFC or SOFC fuel cell technology.

In particular, Jansen et. al. [103] appears to be the most fundamental look, but it specifically uses a electric fan support (i.e. increasing the BPR) in an analysis

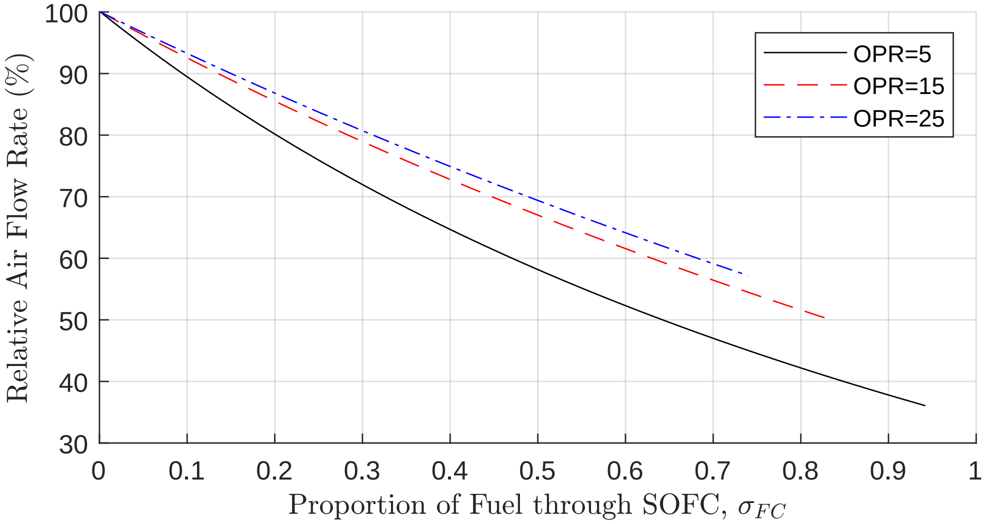

Figure 3.23: Relative Air Flow Rate (%) for GT/SOFC vs. GT Alone at Constant Power Output. Data from Chapter 2 analytical model.

used to bracket the necessary technology for power equipment. Interestingly, the requirements were less and less at lower and lower power levels. This does support the fan-increase method of including electrical power into the propulsion system.

Following this, for a consistent overall power requirement the GT/SOFC engine core flow (i.e. not airflow through the fans) will become smaller such that greater bypass ratios are possible for the same overall engine size. This principle is illustrated in Figure 3.23, which applies the analytical model developed in Chapter 2 using the given default values provided there. As the relative size of the SOFC subsystem is increased (via an increase in σ_{FC}) the required air flow rate drops—more than 60% for $OPR = 5$. Higher pressure ratios see a reduced impact ($\approx 40\%$ at $OPR = 25$) due to the higher flow specific power of the GT and cooling limitations at larger values of σ_{FC}.

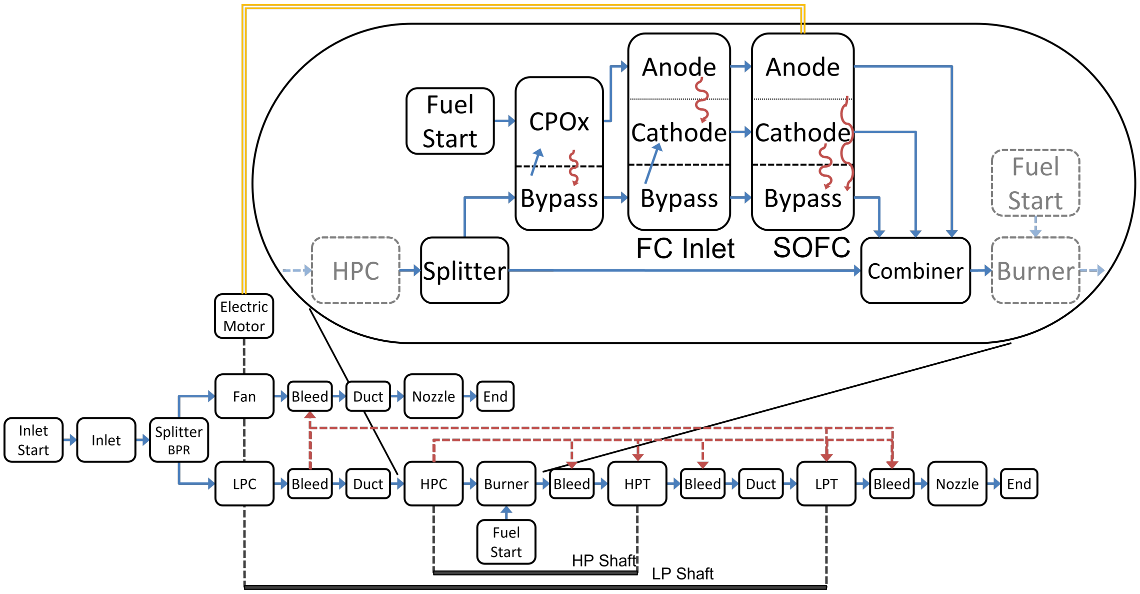

Figure 3.24: NPSS Schematic of Fan Support Model.

In contrast to a turbineless system, increasing the bypass ratio generally improves the propulsive efficiency of the overall turbofan; for a GT/SOFC this compounds with improvements in the thermal efficiency provided inherently by the cycle. Going forward, we will show the design of such a system using NPSS to confirm these trends.

A schematic for the NPSS fan support model is provided in Figure 3.24. The baseline engine is a two-spool turbofan. The most notable changes to the configuration are the inclusion of the electric motor (using power from the SOFC) on the low-pressure ("LP") shaft, the same as the fan. The SOFC subsystem (outlined) branches off in parallel between the high-pressure compressor exhaust and the burner/combustor.

For the purposes of this work, the electric motor has a specific power of 16

$\mathrm{kW\,kg^{-1}}$ and 98% efficiency, drawn from the High Efficiency Megawatt Motor program [84, 85]. As another parameter for bookkeeping mass, the power electronics (for converting SOFC output to appropriate motor input) is taken to have a specific power of 19 $\mathrm{kW\,kg^{-1}}$ [86].

More detailed numerical variable settings for this model are available in Appendix **??**.

3.7 Turboelectric Hybrid GT/SOFC Model

In contrast to the fan support model in section 3.6 that was closely akin to a parallel hybrid from Figure 1.10, the model we develop in this section is similar to the turboelectric or series hybrid systems. This model is also closer to the analytical modeling from Chapter 2, and specifically the sketch in Figure 2.7. The primary difference from the Fan Support configuration is that the GT component of the hybrid is a turboshaft producing electricity, rather than a turbofan producing propulsive thrust. In fact, the core engine cycle is not intended to provide any direct thrust, instead providing wholly electrical power to be used elsewhere on the aircraft for propulsion and/or any other use. Effectively, this is a flying power plant.

A schematic for the NPSS full electric power model is provided in Figure 3.25. Note that there is a single shaft stage for this model, and we will generally approach the system with lower pressure ratio targets to make better use of the recuperator.

The thrust target for this system is low, effectively zero (but non-zero to avoid solver errors); e.g. the core thrust needs only to overcome the drag of the inlet in

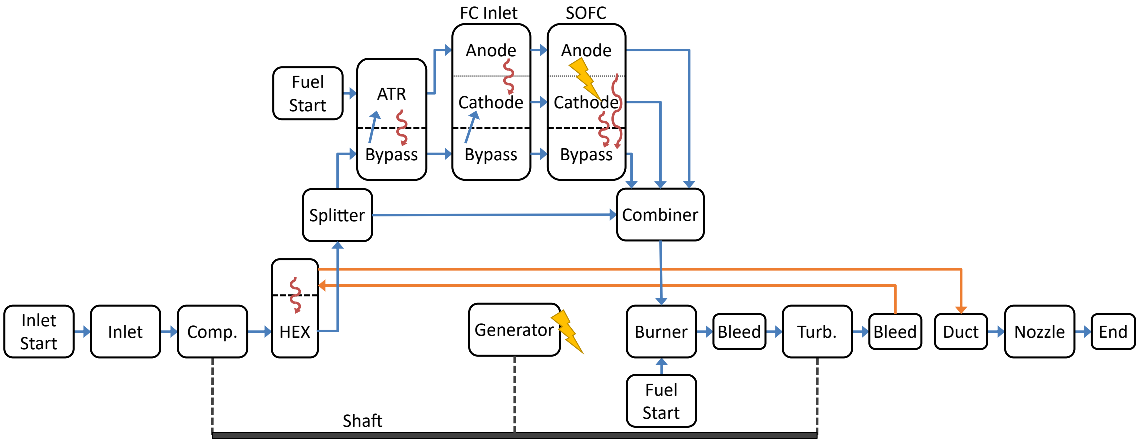

Figure 3.25: NPSS Schematic of Full Electric Power Model.

the flight environment. This is not a strict requirement for such a system (e.g. an electric fan could be placed behind slow core exhaust), but is a good rule of thumb for our purposes in keeping system solutions physically meaningful.

The global NPSS solver process applied for this scenario is available in Figure 3.26. As with other numerical models, NPSS generally approaches scenarios of interest by slow shifts of input parameters after starting from a known converged solution, or relatively simple case. To design the all-electric GT/SOFC configuration, a gas turbine turboshaft engine is designed at the targeted flight condition, initially producing the full electric power demand. Next, a recuperator is added that exchanges heat sufficient to reach a target exhaust temperature $T_{3.5}$.

Once a solution is converged upon, the simplified SOFC model is enabled along with the CPOx fuel stream. The fuel flow rate becomes an independent variable, while the SOFC power output becomes a dependent variable, in turn lowering the turboshaft generator power output target. Note that in the simplified mode, the

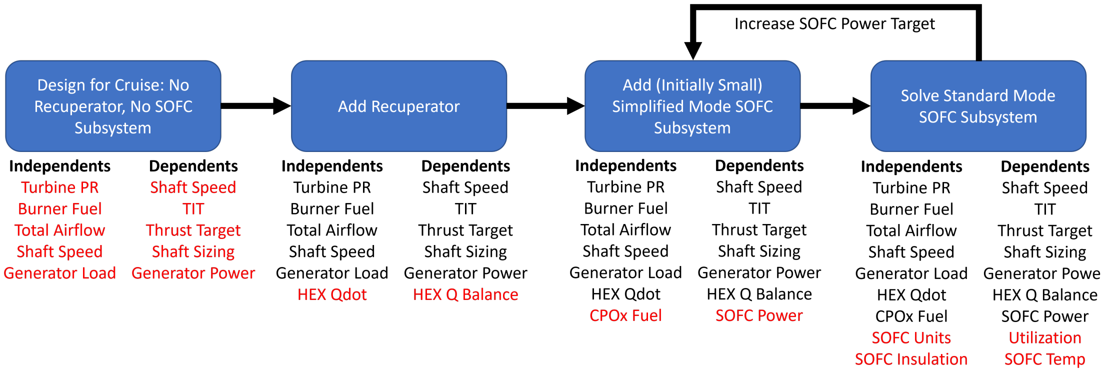

Figure 3.26: Solver Progression for the Full Electric System Model. Red Independent/Dependent entries are added in that stage.

SOFC model power output is determined from a given fuel efficiency such that convergence is relatively quick.

At this point, the standard SOFC model mode is enabled, with SOFC power output now a function of the physical SOFC stack design and electrochemistry, with additional dependent design variables for a target fuel utilization and SOFC operating temperature. Consequently, independent variables for the number of SOFC channels and the thickness of insulation around the SOFC stack are also added, which have direct impacts on the new dependent variables.

For a given set of operating conditions, the SOFC power output target is initially set to a small value to be solved for in both the simplified and standard SOFC modes. Then the SOFC power output is increased, and the solver setup looped back to the simplified mode to converge on the new power target. This process is repeated until non-physical results are encountered.

The scenario used for this system is based on an estimate for a 737-800 [106], with the specific characteristics provided below in Table **??**. The fuel used in this scenario is liquefied natural gas (LNG) which is one of several promising carbon-neutral liquid fuels (CNLF) when produced from biological sources. Mass and power output values are halved, presuming the use of two power generation systems in parallel for emergency redundancy.

More detailed numerical variable settings for this model are available in Appendix **??**.

3.8 Results and Discussion

3.8.1 Fan Support Model

3.8.1.1 SOFC Power Output Sweep

The initial set of results are generated by solving an initial on-design scenario for turbomachinery with a combined OPR of 24 (and specific constant design efficiencies of Engine 3 in Table 5 of Waters, et. al. [64]) for a cruise condition at Mach 0.8 and 10.7 km altitude. For each scenario, the simplified SOFC mode was used to reach an estimated solution for the rest of the gas turbine components before solving with the full SOFC model. For the following results, the SOFC power target is progressively increased even while the overall thrust requirement remains constant. At the same time, the core exhaust velocity is also maintained at the original (i.e. w/o SOFC) turbofan condition such that the turbine exhaust pressure ratio is largely consistent.[x]

The first view of the results is provided in Figure 3.27 which provides the fuel cell subsystem (including the reformer) thermal efficiency, the propulsive efficiency, and the total system efficiency including overall GT/SOFC thermal and propulsive efficiency effects in terms of the total electric power added to the fan/LP-shaft. Additionally, the equivalent non-dimensional parameters from Chapter 2 for the fuel proportion passed into the SOFC σ_{FC} and fuel-cell/gas-turbine power production ratio θ are also provided.

The immediate trends are in line with our general predictions: as the size of the SOFC in the GT/SOFC increases, the propulsive and overall efficiency of the system improves, each about 10% in total for a 1.4MW SOFC. The efficiency of the SOFC subsystem itself is largely consistent across the range, which is also consistent with SOFC stack scaling. Howerver, the absolute efficiency of the subsystem appears to be low, at about 30%, versus the 50%-60% often achievable in other SOFC systems. This low performance is likely due to the reliance on the CPOx reformer, which uses substantial amounts of fuel enthalpy to bring the anode gases to high enough temperatures to drive the reformation process. The anode flow is then cooled to the SOFC operating temperature, and that enthalpy can only be recovered in the turbine.

Finally, the results shown here cover a range from σ_{FC} of zero to 0.7, with a maximum value of unity; as such these results cover most of the available SOFC size

---

[x] Without this solver condition, the core exhaust pressure ratio rises as with “turbineless” systems, harming the overall propulsive efficiency.

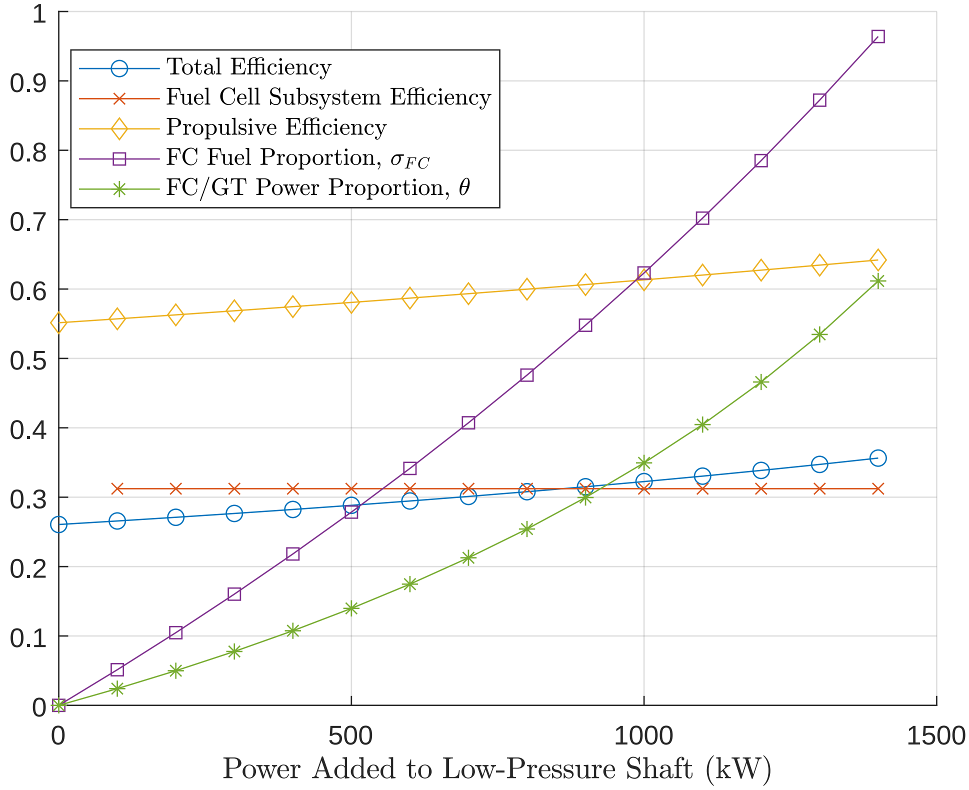

Figure 3.27: Fan-Support GT/SOFC Efficiencies with varying SOFC Power Contribution. Proportional fuel flow into SOFC (σ_{FC}) and FC/GT power generation ratio (θ) included.

ranges for this operating condition. It is not yet cut off by the SOFC cooling limit though nearly all core flow is passed through the SOFC subsystem at this point (see Figure 3.28).

From the analytical model, we predicted that the flow rate of air into the core of the GT/SOFC would drop off as the SOFC components became more prominent, as per Figure 3.23. We also expected the overall airflow rate, as well as the fan bypass ratio, to increase substantially with the added power on the low-pressure shaft. We observe *all* of these trends in the NPSS model results, shown in Figure

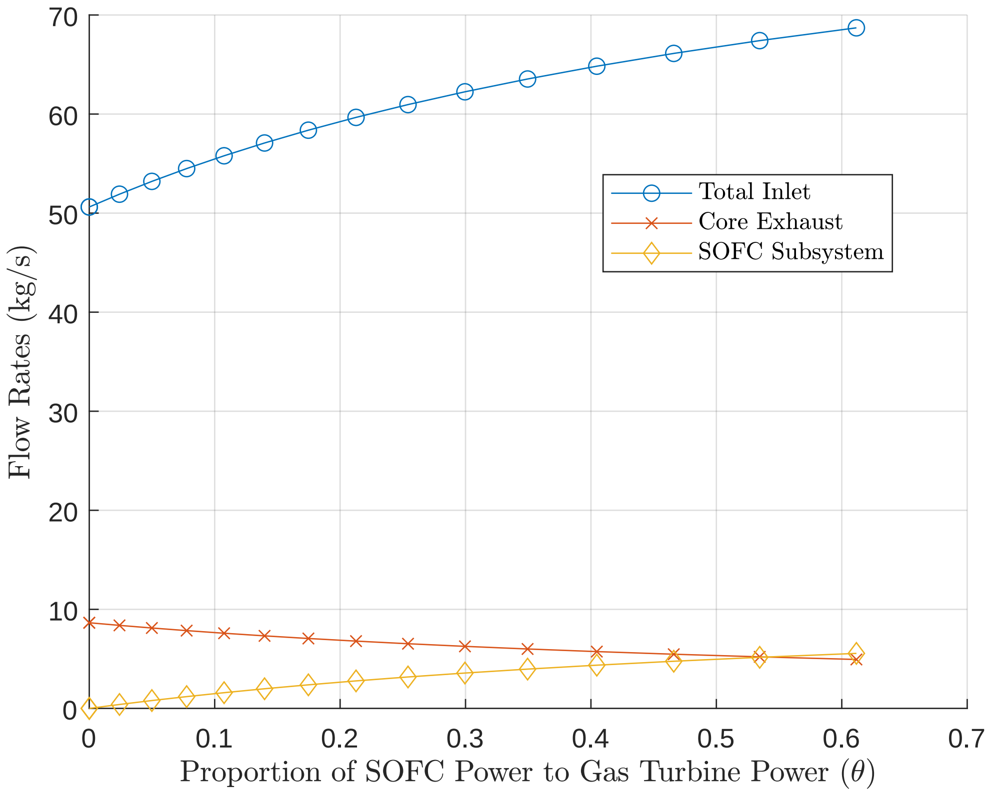

Figure 3.28: Fan-Support GT/SOFC Flow Rates through Main Components. Total inlet flow includes core and fan bypass; core flow includes SOFC subsystem bypass flow.

3.28.

For the data point at the highest value of θ, we should note that the SOFC subsystem is calculated to pass the entire (actually slightly more) core exhaust flow. In other words, there is effectively no flow passing directly from the compressor to the combustor at this system design. As a matter of mass conservation, beyond this point the system would become non-physical as the SOFC subsystem flow is a subset of the core exhaust. However, the amount of flow passed to the SOFC subsystem (for both cooling and cathode flow) is dictated by a constant AFR value of 15, based on the amount of fuel injected into the CPOx. In general, cooling bypass makes up the majority of this flow (see Figure 4.7 for an example from a similar GT/SOFC configuration). As such, lowering this constant AFR to only divert all compressor air into the SOFC subsystem will avoid limiting the growth of the SOFC relative to the GT.

3.8.1.2 System Masses

Greater efficiency is all well and good, but in an aircraft this needs to be balanced against any additional mass such a system requires. Figure 3.29 provides a breakdown of the different parts of the GT/SOFC as the relative prominence of the SOFC increases. Unsurprisingly, the weight of the SOFC subsystem (including reformer, inlet, stack, and ducting) increases as the power supplied increases. However, the lower specific power of the SOFC means that the SOFC components weigh the same as the gas turbine and fan while only providing 15% of the power. The weight of the electric motor is relatively small, though this is at a specific power target ($16\ \mathrm{kW\,kg^{-1}}$) for near future development [84, 85].

3.8.1.3 Performance Metrics

The resulting performance metrics for this power-addition process is provided in Figure 3.30. The immediate observations are that the TSFC (and so the marginal fuel cost for operating the aircraft over a flight) is substantially reduced, to about 80% of the baseline value. The actual range capability however also diminishes—

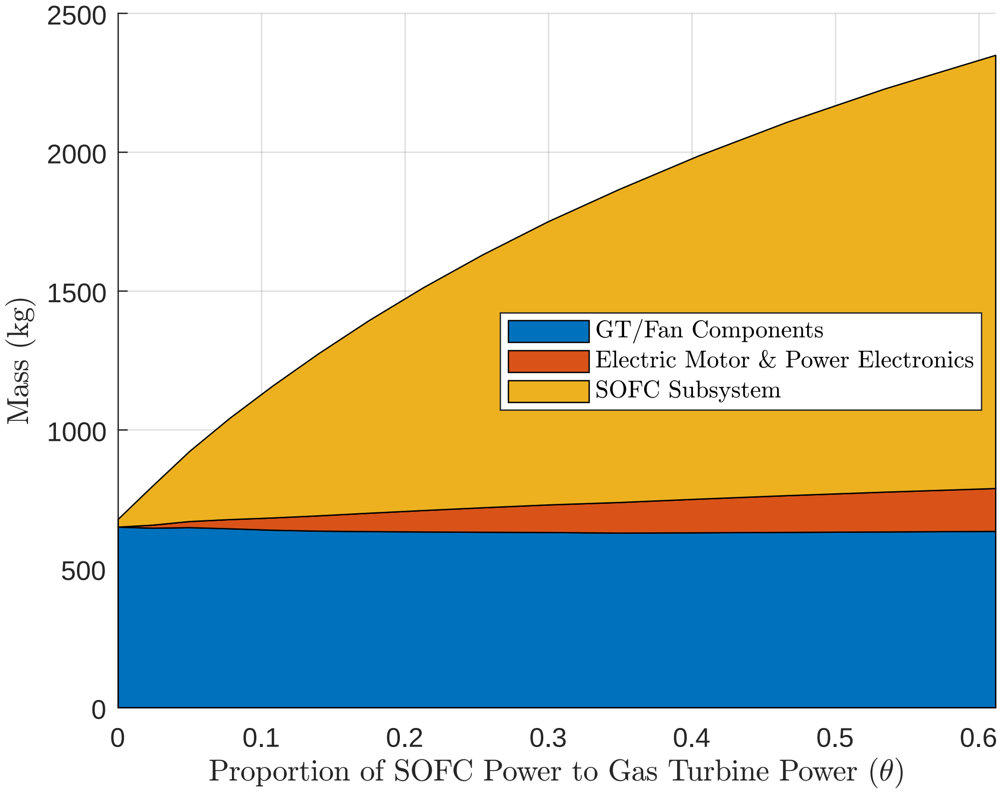

Figure 3.29: Fan-Support GT/SOFC Subsystem Component Masses with varying SOFC Power Contribution.

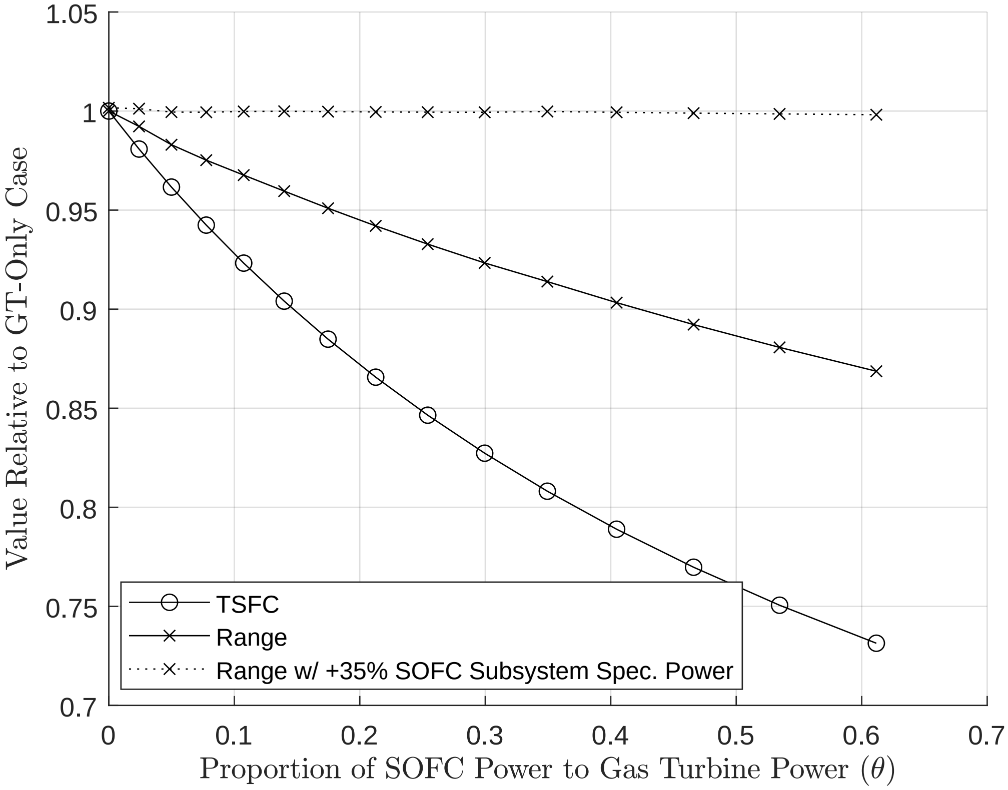

Figure 3.30: Fan-Support GT/SOFC Relative Range and TSFC with varying SOFC Power Contribution. Range results also included for a 35% larger SOFC subsystem specific power to illustrate breakeven point.

i.e. the fuel displaced by the additional mass of the GT/SOFC isn't accounted for by improved efficiency. However, the majority of the additional mass is due to the SOFC subsystem components, especially the SOFC stack. As such, if we (notionally) increase the specific power of the SOFC subsystem 35% from approximately 0.8 $\mathrm{kW\,kg^{-1}}$ to 1.08 $\mathrm{kW\,kg^{-1}}$, the range capability is breakeven as the SOFC is scaled up in this configuration.

This shows existence of a threshold SOFC specific power required to maintain range capability with higher fuel efficiency. The means of achieving this specific power will likely require more power-dense SOFC materials and lightweight interconnect design or underlying material choice. These are however beyond the scope of this dissertation.

3.8.2 Full Electric Power Production Model

3.8.2.1 SOFC Power Output Sweep

The resulting system efficiency and SOFC subsystem efficiency (including the CPOx reformer) is provided in Figure 3.31 as a function of the power generated by the SOFC specifically within the system. The total power output of the system of 4.55MW remained constant for every point, with the load demand on the turboshaft diminishing (and so its physical size, scaling with the E3 program compressor and turbine maps bundled with NPSS) with SOFC power output.

The initial set of results are generated by solving an initial on-design scenario for turbomachinery with an OPR of 15 for a cruise condition at Mach 0.8 and 10.7 km altitude. For each scenario, the simplified SOFC mode was used to reach an estimated solution for the rest of the gas turbine components before solving with the full SOFC model. For the following results, the SOFC power target is progressively increased even while the overall power requirement remains constant. At the same time, the net thrust of the system is maintained at a low value (100 N) in order to prevent the engine intake itself from adding unaccounted drag to the aircraft.

Figure 3.31 provides the fuel cell subsystem (including the reformer) thermal efficiency and the system (combined GT/SOFC) efficiency, here labeled the total efficiency. Additionally, the equivalent non-dimensional parameters from Chapter 2 for the fuel proportion passed into the SOFC σ_{FC} and fuel-cell/gas-turbine power production ratio θ are also provided.

The immediate trends are in line with our general predictions: as the size of the SOFC in the GT/SOFC increases, the propulsive and system thermal efficiency improves about 8% in total. The efficiency of the SOFC subsystem itself is again largely consistent across the range, which is also consistent with SOFC stack scaling. The SOFC subsystem efficiency is still low, about 41%, versus the 50%-60% often achievable in other SOFC systems. This low performance is again likely due to the reliance on the CPOx reformer, but the heat exchanger immediately preceding the flow into the CPOx helps reduce the CPOx reformation burden. This is due to the CPOx performance largely being driven by the temperatures achieved inside the reformer.

Finally, the results shown here cover a range from σ_{FC} of zero to 0.5; as such this system still could grow in the relative size of the SOFC. It is not yet cut off by the SOFC cooling limit and approximately one third of the core flow is not yet passed through the SOFC subsystem at this point (see Figure 3.28).

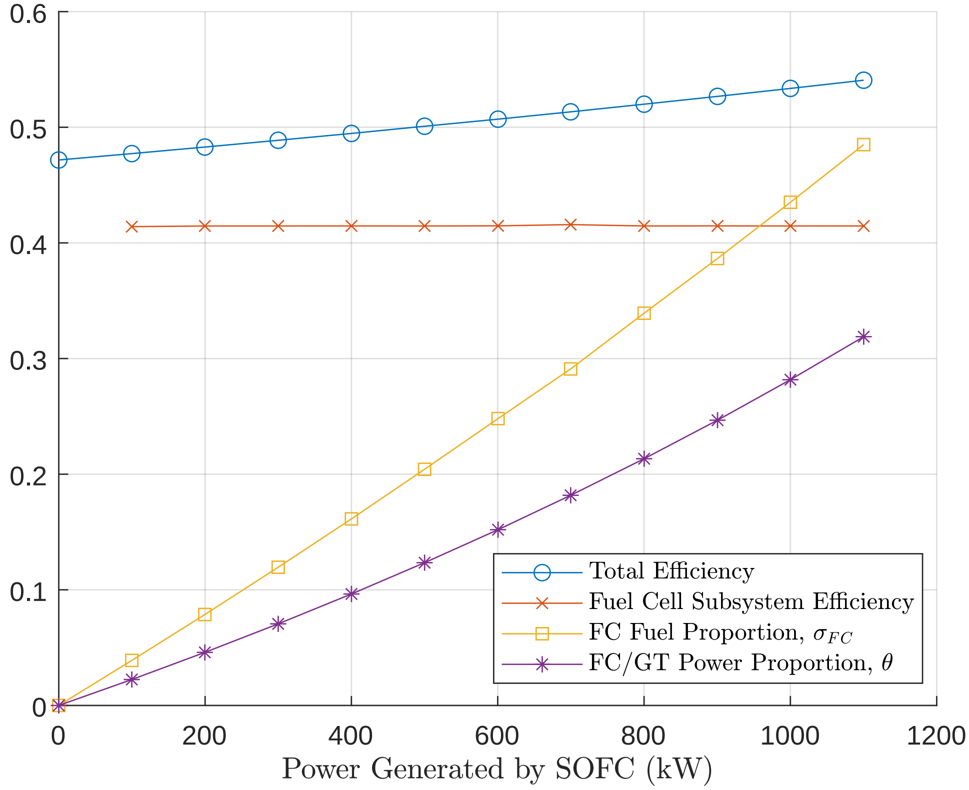

Figure 3.31: Turboelectric Hybrid GT/SOFC Efficiencies with varying SOFC Power Contribution. Corresponding proportional fuel flow into SOFC (σ_{FC}) and FC/GT power generation ratio (θ) included.

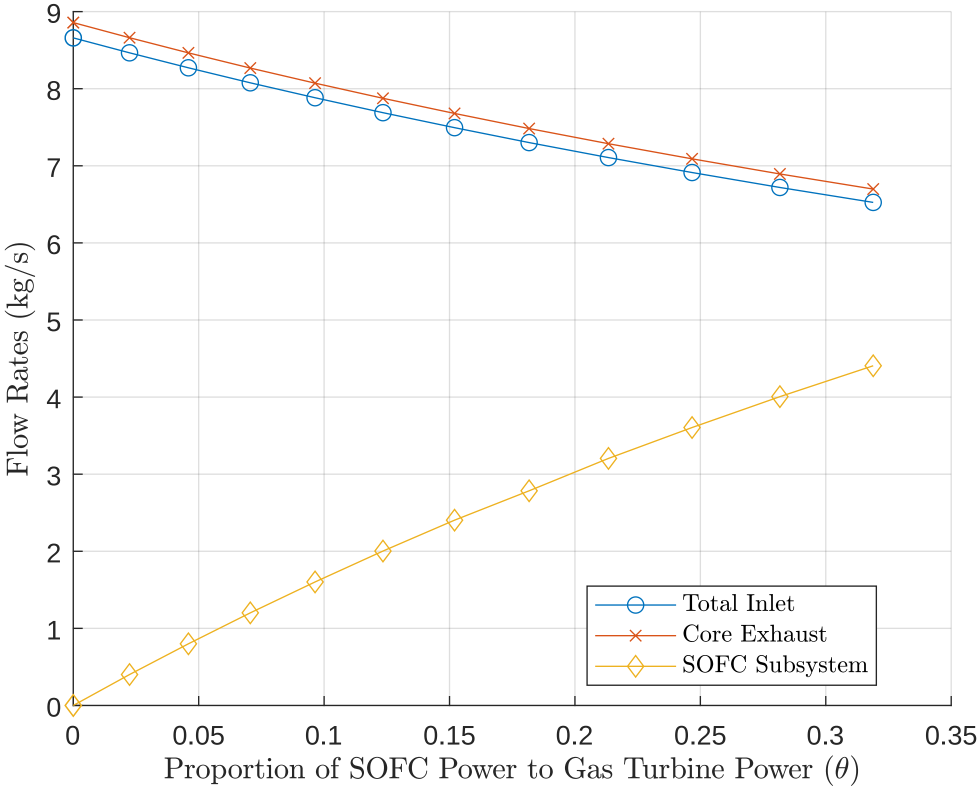

Figure 3.32: Turboelectric hybrid GT/SOFC flow rates through main components. Total inlet flow includes core and fan bypass; core flow includes SOFC subsystem bypass flow.

3.8.2.2 System Masses

The system mass trends for the Turboelectric hybrid, shown in Figure 3.33, are somewhat different from those of the Parallel hybrid. First, the gas turbine and associated generator components reduce in mass as the fuel cell becomes larger since their whole role of producing power (rather than thrust as in the Parallel hybrid case) is reduced ass the fuel cell grows. Surprisingly, the heat exchanger mass is a very small proportion of the total. This result suggested some kind of error to the author, though none has been found. One potential explanation however is that the heat exchanger is sized to operate only at cruise conditions where the overall mass flow rate is relatively small, and the heat exchanger mass requirements are expected to vary linearly with the mass flow rate—all else being equal, such as pressure drop targets.

A second important observation is that the SOFC subsystem in this model is relatively large compared to that of the Parallel hybrid model, almost by a factor of two! This is mainly due to the lower design operating temperature and pressure of the SOFC subsystem in this case, at a trade for better efficiency (41% to 30% in the Parallel hybrid).

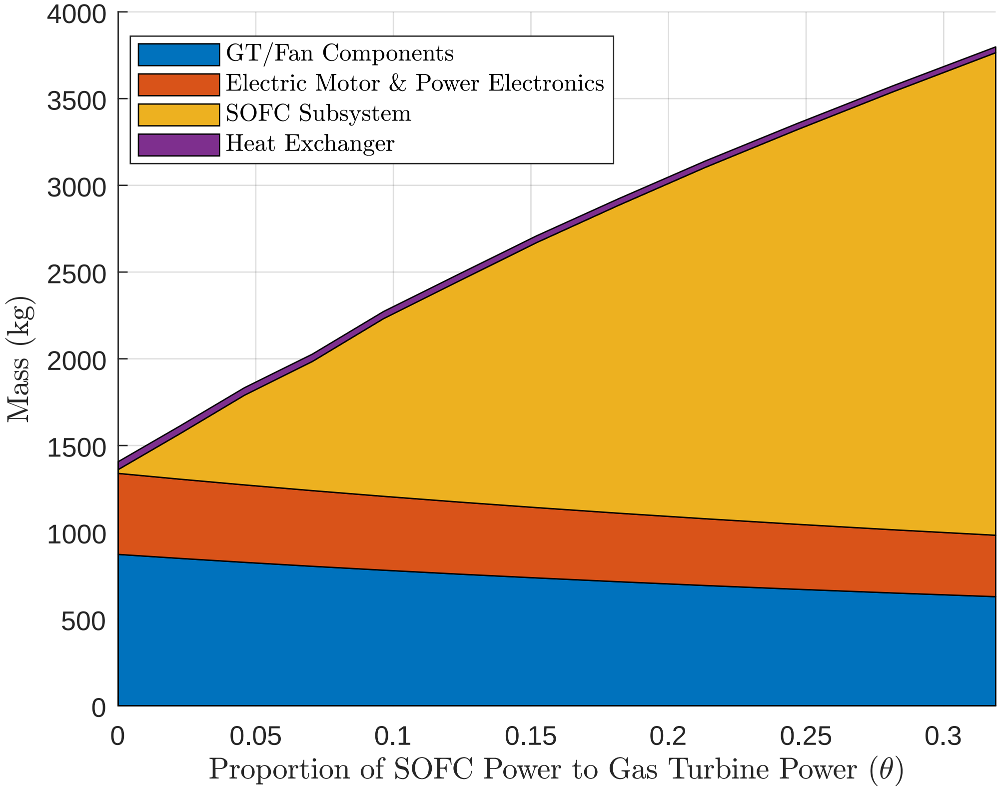

Figure 3.33: Turboelectric Hybrid GT/SOFC Subsystem Component Masses with varying SOFC Power Contribution.

3.8.2.3 Performance Metrics

Finally, the relative range and relative fuel flow rate of turboelectric GT/SOFC is provided in Figure 3.34. The range capability is substantially reduced with increasing fuel cell size, with a break-even value of about 1.2 kW. This represents a 200% increase over the modeled value, suggesting that one should be careful in trading away specific power capability for higher efficiency.

Overall, the turboelectric hybrid provides an alternative form of airborne power that attempts to follow the model of a ground power plant more closely, taking advantage of a heat exchanger as well as the lower overall pressure ratios needed to make use of the heat exchanger. While the resulting HEX is not large, the overall system operates at a lower specific power—though this is also due to the lower temperature and pressure operation of the SOFC components. Additionally, the capabilities of, and other benefits of, electrically driven propulsors (e.g. BLI in the NASA STARC-ABL concept) are not captured in this modeling. As such, it is difficult to give an apples-to-apples comparison with the Parallel Hybrid model performance at this time.

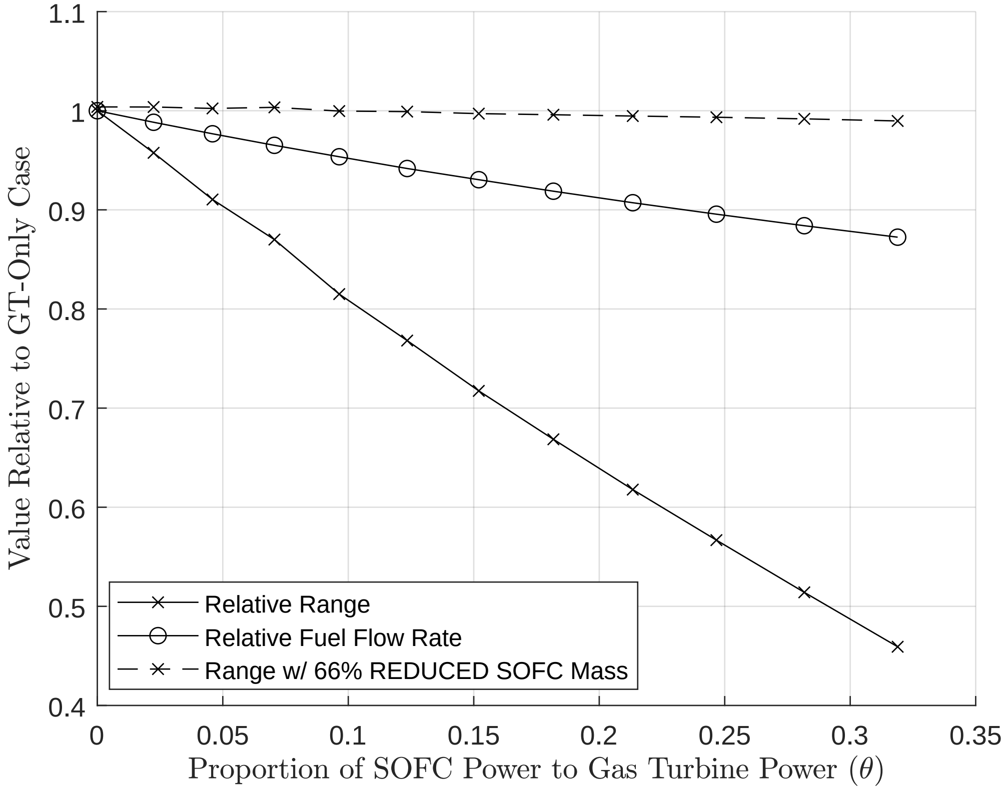

Figure 3.34: Turboelectric GT/SOFC Relative Range and relative fuel flow rate with varying SOFC power contribution. Range results also included for a 200% larger SOFC subsystem specific power to illustrate breakeven point.

3.8.3 Uncertainty and Sensitivity Analysis

In prior work by the author, an extensive sensitivity analysis for a GT/SOFC turbofan (producing secondary power via the SOFC) was performed for many input design variables and varying power levels [17, Fig. 42]. The purpose was to evaluate the degree of output uncertainty for the metric of interest (fractional fuel flow rate) with respect to the many input variables for the model. The most sensitive behavior observed were large effects with SOFC design parameters at very large (and aerodynamically obstructing) sizes for the SOFC subsystem placed radially around the GT. A GT/SOFC system with a similar power level, but less obstructing configuration, showed much lower output uncertainty with SOFC design variables than the GT component or airframe parameters. *A priori* then, we expect similar behavior from this highly similar set of component models.

However, there is still value to finding the sensitivity values for each particular system configuration. In this work particularly, the metrics of interest have changed to TSFC and range, which in addition to the change in system configuration, may alter the results. The uncertainty analysis applies the root-sum-square (RSS) Equation 3.5, where $u_{x_{RSS}}$ is the expected RSS uncertainty in the metric of interest x, u_{y_i} is the uncertainty of any particular input parameter y_i, s_i is the sensitivity of the system to that particular input parameter, and N is the number of input parameters considered. In general, parameters with low sensitivity and/or low uncertainty in the input contribute little to the overall uncertainty.

$$u_{x_{RSS}} = \sqrt{\sum_{i=1}^{i=N} \left(u_{y_i} s_i\right)^2} \tag{3.5}$$

The input parameter uncertainties u_{y_i} will vary by the given input, and matches the assumptions from prior work [17]. Drag polars are assumed to use rounded significant figures such that the actual value may be within ± five-tenths of the last significant figure. Turbomachinery efficiencies are presumed to be accurate within 0.1% per the E3 program performance maps used [107]. By default, all other input uncertainties are assumed to be 5% of their value without additional information.

The parameter sensitivities s_i are effectively first-derivatives of the system performance with respect to the different input parameters. The first derivative is found through by a first-order finite difference calculation, using two operating points: (A) an initial solved state (subscript 0), and (B) a perturbed state solution (subscript 0) from a small ($\approx$ 0.5%) variation in the i^{th} input parameter. The sensitivity is then calculated per Equation 3.6, with a non-dimensional version in Equation 3.7 which can be more useful for comparing the relative impact of each input parameter vs. others.

$$s_i = \left(x_i - x_0\right) / \Delta y_i \tag{3.6}$$

$$s_i = \left(x_i - x_0\right) y_0 / \left(x_0 \Delta y_i\right) \tag{3.7}$$

The results of the Fan Support configuration sensitivity analysis for a 1MW

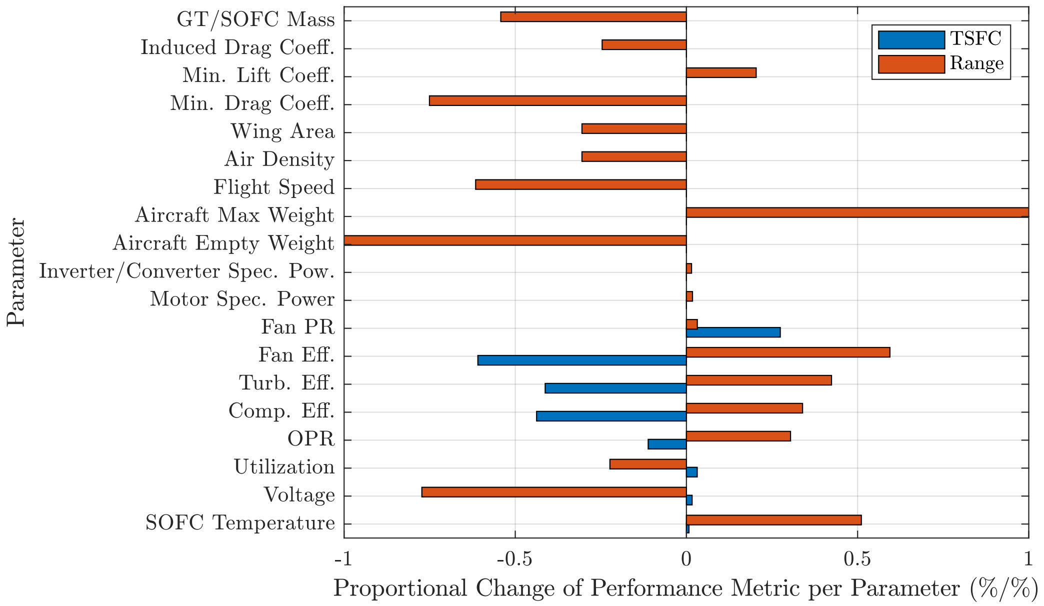

Figure 3.35: Fan-Support GT/SOFC Sensitivity Analysis for 1MW SOFC. Aircraft empty and maximum weight are off-plot, with values of -4.4 and 5.2 respectively.

SOFC are provided in Figure 3.35, which plots the non-dimensional sensitivity parameters. Included in the sensitivity analysis were the most important SOFC parameters (voltage, utilization, and operating temperature) [17]. Additionally included were turbomachinery performance parameters, as well as drag polar and range calculation parameters (see Table 2.2). Note that the range calculation parameters have no impact on the TSFC, so those sensitivities are zero.

The most immediate observations are that the aircraft maximum and empty weights were by far the most impactful parameters by almost an order of magnitude. This is not unreasonable, as these trade directly with the amount of fuel mass available. The fuel mass added or lost impacts the capability of the aircraft at the end of the flight when most of the fuel is already gone, such that the power requirements are much lower than for the rest of the flight.

In comparison to prior work [17], the SOFC is four times the size of the largest system. However drag effects from additional mass or flow obstruction were not present in this scenario, which were the driving factors in that prior work. As such, we expect the TSFC and range to be more impacted than the relative fuel flow rate metric in prior work—but on a more linear scale. Broadly speaking, this is what we observe with most of the SOFC sensitivity coefficients being between 0.2–0.8.

From an optimization perspective, increased utilization and voltage appear to be counterproductive for the range. As seen in Figure 3.30 however, this is because the SOFC needs approximately 35% more specific power for the efficiency improvement to break even with the loss of fuel capacity. On the other hand, increasing SOFC temperature is beneficial to range as it increases the power density of the SOFC, lowering the necessary size of the SOFC. However there is an upper limit to the SOFC operating temperature both practically and materially which the model does not well capture.

For turbomachinery, improving efficiency anywhere is overall beneficial, and to a lesser degree the overall pressure ratio is the same. Interestingly, increasing the fan PR harms the TSFC, likely by damaging the propulsive efficiency of the overall turbofan.

In terms of the uncertainty for the range or TSFC calculations, the TSFC has a fairly small uncertainty of 1.5%. This is unsurprising, as the TSFC has the benefit of disregarding several of the most impactful parameters in the sensitivity analysis. The value could rise slightly if more of the SOFC design variables were included as in prior work, but all of the variables checked previously had similar or lower sensitivity.

On the other hand, the range calculation initially has an RMS uncertainty of 36%. This is primarily due to the large impact of the aircraft maximum and empty weight variation having large impacts on the margin, and the inclusion of more parameters. If just the maximum and empty weight uncertainties are removed, the RMS uncertainty in the range falls to 13%. This may be justified, as the weight characteristics would affect all engine systems. On the other hand, the effects of the uncertainty may be more pronounced for heavier power generation systems that trade fuel capacity for fuel efficiency. This may very well be the case for GT/SOFC systems.

3.9 Conclusions and Future Work

In this chapter, we discussed a detailed simulation method for GT/SOFC systems. The goal is to expand on the simplified analytical findings of Chapter 2 to design and evaluate specific devices that could be constructed. The work presented here with NPSS expanded on prior work for aircraft secondary power generation with the integrated solid oxide fuel cell into. Here the same modeling approach was used for GT/SOFC systems focused on providing main propulsive power, with analysis on two specific configurations.

The first configuration provides direct propulsive force through the GT/SOFC in the form of a turbofan, augmented with an electric motor with electricity provided by the SOFC. The second concerns a 'flying powerplant' producing only electric power from both the SOFC and a mechanical generator attached to the turboshaft. The results build on and confirm trends identified in Chapter 2.1 while removing a number of the analytical assumptions required in that chapter.

More specifically, in the parallel hybrid configuration we found that introducing and increasing the relative size of the SOFC subsystem had several effects. In line with analytical predictions, the necessary core flow rate to maintain the target flight condition was reduced due to a higher flow-specific work for the hybrid system. Furthermore, due to the higher flow-specific work the effective bypass ratio could be increased—more than doubling over the calculated operating points. On balance, this represented an overall moderate increase in total airflow rate, such that overall engine flow area required is not substantially increased. This is an important point for modern aircraft where turbofan size has an effective upper limit for most airframes.

However this does not account immediately for the increased size and weight due to the addition of the SOFC into the system. While the TSFC is observed to decrease with the relative size of the SOFC, maintaining range capability requires a threshold SOFC subsystem specific power around $1 \mathrm{kW\,kg^{-1}}$. This balances both the increased efficiency of the overall thermal cycle, as well as the displaced fuel mass for the additional SOFC components.

In the turboelectric hybrid configuration, we observed similar trends; fuel consumption was reduced by 12% when 25% of power is generated by the SOFC ($\theta = 0.33$). However, in order to achieve an endurance parity with a system without an SOFC it requires a reformer/fuel cell that achieves better than $1.2\mathrm{kW\,kg^{-1}}$. Proportionally, this is a substantial increase (200%) from the mass estimate of the SOFC components. However it should be noted that the SOFC in this system operated at a lower temperature and pressure (due to the lower $OPR = 15$) This higher specific power requirement occurs because the gas turbine operates at a lower $OPR = 15$ vs. $OPR = 24$ to enable recuperation via a heat exchanger. The heat exchanger does improve the thermodynamic performance of both the Brayton cycle and the SOFC (by reducing preheating requirements) even at 30% effectiveness. The mass of the recuperator is however relatively small in these scenarios, and the optimum effectiveness is likely higher. Regardless, the presence of the recuperator introduces substantial complexity to the system.

Future work has a number of potential directions. For both GT/SOFC configurations discussed here, it will also be useful consideration of recirculated flows for anode/cathode recirculation. This will enable substantially more efficient reformer—and by extension, overall SOFC subsystem—performance to increase efficiency and utilization for similar systems.

To achieve this however, a singular ATR/SOFC (or other configuration) model, solver, or map may be desirable in order to take advantage of non-numerical non-linear-execution solution methods. This may also result in better flow-loop capability and ease of integration into other NPSS modeling projects. In particular, creating an easily-integrated and stable set of component or subsystem models would be the most impactful output of this particular modeling project due to the broader uses of NPSS. One indicator of success would be if only a small number of SOFC design parameters will need to operate at the level of the global solver. In this same vein, an SOFC stack performance map can be designed, with an associated performance map [108].

At the level of the individual component models, there are numerous possible directions to improve their accuracy. Design optimizations for SOFC, e.g. variable insulation thickness along length of SOFC to enable better temperature stability is one example, along with axial heat conduction in SOFC and CPOx models. These may have very specific utility and long calculation times such that more complex modeling may want to be performed externally whenever possible. At the system level, it would be useful to apply the NPSS models to determine off-design performance for the varying thrust requirements as fuel is expended over the course of the flight.

In the longer term, what may be the most important problem in GT/SOFC system design is accounting for transient performance. This is not accounted for in the current modeling, which is for steady-state modeling. Transient models will represent an interesting problem due to the large thermal mass of the SOFC components paired with rapid transitions in GT throttle setting and ambient conditions over the course of a flight.

Chapter 4: SOFC Exhaust Reintroduction

As discussed in prior chapters, for ground-based GT/SOFC design the most important consideration is usually minimizing the marginal cost of operation. Practically, this implies operating the hybrid system at the maximum thermal efficiency, which often uses substantial regeneration (see section 2.4) as part of the thermodynamic cycle. Effective use of regeneration requires a low OPR by the GT components (see Figure 2.6), and as such (via Equation 2.22) a low proportion of power provided by the GT vs. the SOFC.

In the scenario described above, it is usually desirable to use a larger SOFC stack such that most of the fuel is reacted in the stack, with the GT components recovering mainly waste heat from the irreversible losses of the topping SOFC. However as shown in Chapter 2, in aerospace applications where weight and volume are important it can be advantageous to go the other direction. By instead using proportionally smaller SOFC stacks providing lower SOFC utilization U_{FC}, unreacted fuel in the anode exhaust may be burned in the combustor to produce more substantial power through the gas turbine's Brayton cycle. Towards the same weight and volume goals, alternative SOFC materials operating at different temperature ranges might be preferred for the aircraft application. Finally, the changing aircraft ambient conditions with altitude and compressor design will substantially change the operating pressure inside the SOFC.

The result is that the anode exhaust state, instead of just combustion products CO_2, H_2O, and diluent N_2, contains also a variety of additional reformate fuel species, particularly CO and H_2. The available concentrations could significantly alter the local chemical composition and temperature (at a variety of overall pressures) at the combustor injection location. Species like H_2 and CO act like fuels releasing heat whereas others may act like diluents. Potential negative impacts include local hotspots, increased NO_x production, and possible failure of the combustor liner. However, the impact could also be positive: Hot (≈600°C–850°C depending on SOFC material choices) anode exhaust rich in H_2 and CO could be used to enhance combustion stability enabling safe operation at lower overall equivalence ratios that produce less NO_x pollutants. The functional result may depend on the injection strategy applied. Furthermore, as illustrated in Figure 4.1, there are a number of different flow conditions beyond the anode exhaust that result from a GT/SOFC configuration that need to be integrated into the combustor immediately downstream.

The actual impacts are difficult to determine, since the makeup of the exhaust gases is not well established—and accordingly their effects on combustion performance characteristics like ignition, stability limits, and burning velocities. While there are examples of hybrid turbine/fuel cell systems in the literature that investigate off-gas combustion [109, 110], they are most often for ground-based systems with different combustor design priorities and different expected operating condi-

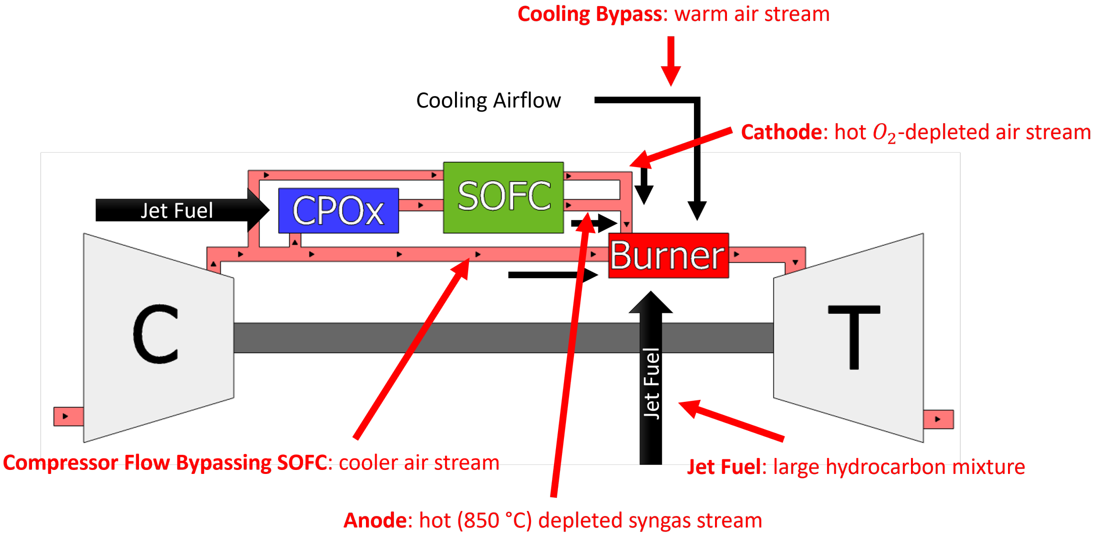

Figure 4.1: Schematic Illustration of Flows Entering GT/SOFC Combustor

tions. One of the rare examples of an aerospace-focused system found is recent work from the German Aerospace Center [33, 34], which has developed a GT/SOFC emulator test rig.

Considering the cost of experimental work, computational combustion is a reasonable first approach for these questions. In that field, most investigations of syngas fuel stream dilution so far tend to focus on the effect of single diluents [111–114] or different concentrations of carbon monoxide [115] and water [116] as opposed to the multiple diluents and CO contents produced by the fuel cell. A broad finding amongst these papers is that computational combustion methods tend to have trouble matching experiment with elevated temperatures and pressures, regardless of the specific reaction mechanism (the set of chemical reactions accounted for through the computation) used.

The closest investigations found are by Zhang et. al. [117] which assesses lean syngas/air flames with N_2 and CO_2 diluents but does not consider water that will be present in the flow, and Cipriani [118] which addresses a variety of syngas mixtures though still neglecting water as a diluent. Mixtures including heavier fuel species such as in jet fuel can be more difficult to simulate, though attempts at extrapolation from experimental results are available [119], as well as some numerical models [48, 120, 121]. Even considering these studies, no known work discusses how SOFC exhaust may impact combustor performance for aircraft, or any that specifies the range of gas turbine combustor conditions that could be expected, aside from a conference paper by our lab group which forms the basis of this chapter [55].

Therefore, in this Chapter we will take the first steps into an examination of the conditions of turbine/fuel cell hybridization that impact the design and operation of the gas turbine's combustor. This will be accomplished using a two-step process. The first step is to use the model of a hybrid turbine/fuel-cell system developed in Chapter 3 to identify a range of fuel cell exhaust conditions/compositions that one could reasonably expect in hybrid GT/SOFCs of various sizes and operating conditions. These include chemical composition as well as thermodynamic and mass flow states.

The second step is to evaluate the potential impact of the fuel cell exhaust integration into the combustor by studying the effect of integrating the SOFC and compressor exhaust streams on basic combustion characteristics (e.g. laminar flame speed, extinction strain rate). These are then compared with more common air/fuel combustor conditions to provide some initial insight into what sorts of effects may or may not be worth further study.

This section will not attempt to consider either of these steps exhaustively; the potential range of GT/SOFC design configurations (e.g. reformer type), operating points (particularly stack temperature, pressure, and utilization), flow compositions, and flow integration methods represent an immense space of analysis that itself requires substantial effort to properly define. Instead, the intent of this chapter is to identify broad classes of potential impacts for combustion characteristics and design scenarios that deserve further study.

4.1 Expected Combustor Inputs

The GT/SOFC model described in Chapter 3 is used here with data from the model's use in prior work [29, 55] to predict the fuel cell exhaust composition. The most important factors to this scenario are the choice of reformation method, degree of recycle (if any) inside the SOFC subsystem, fuel cell operating temperature, and fuel utilization (also referred to as % Oxidation) by the fuel cell. In this work, to limit the number of free parameters we will focus on CPOx reformation with no recycle as developed in previously [64]. For future work, this leaves more efficient (and correspondingly more complex and hardware-intensive) fuel processing methods such as autothermal reformation (ATR) or steam reformation that depend on recycled SOFC exhaust flows or other sources of water. Additionally, a single operating temperature of 850°C is defined for the exhaust from the fuel cell stack, built around a YSZ-based MEA material.

Even given these constraints, an aircraft GT/SOFC system can have a wide

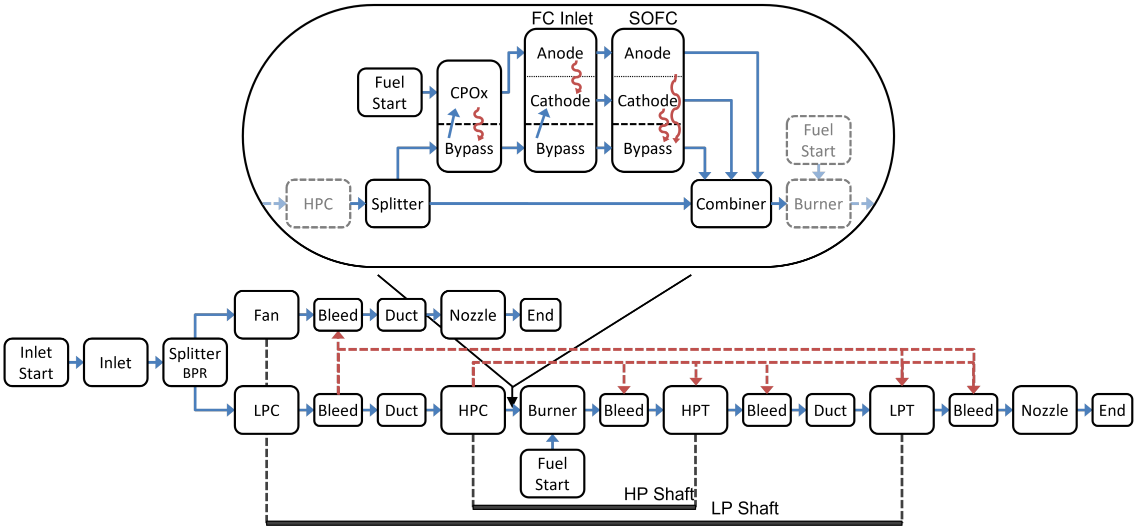

Figure 4.2: NPSS Model Block Diagram for a Two-Spool Turbofan GT/SOFC. SOFC electrical power generated applied to secondary (non-propulsive) applications. Figure reproduced from prior works with slight modifications [29, 31, 55]

range of potential operating conditions inside the combustor, based both on (1) the precise design configuration and (2) the varying flight conditions over the course of a mission. The variation may be seen in both the intensive (e.g. temperature, pressure, composition) and extensive (e.g. flow rate) properties of the material going into the combustor. Fortunately, modeling from prior work [64] and as described in Chapter 3 can give us some insight into those conditions.

To be more specific, the model that generated the combustor input data is for a two-spool GT/SOFC turbofan, for which an NPSS model block diagram is provided in Figure 4.2. The SOFC in this model generates electrical power for secondary applications on board the aircraft such as avionics or fly-by-wire controls.

All this being said however, the turbofan/secondary-electric-power configuration should not be an important factor in determining the composition or state of the resulting SOFC subsystem exhaust streams; the scaling of the energy generated by the GT and SOFC thermodynamic cycles and the incoming ambient conditions should produce similar results to other configurations (e.g. a Fan Supporting GT/SOFC or an All-Electric GT/SOFC, as described in Chapter 3) so long as the SOFC subsystem inputs and GT thermodynamic cycle is the same.

Two sets of model results employing this model are used in this work, each varying a different parameter across a wide range. In the first, the size of the SOFC (and the resulting power output) was increased from an initial GT-only condition with a constant fuel utilization. In the second, a GT/SOFC with constant SOFC electric power output (50 kW) has the target fuel utilization of the SOFC varied from 58% to 75%.

4.1.1 Intensive Properties

The prior NPSS modeling has provided a set of flow conditions for the anode, cathode, and bypass streams. The most important compositional characteristics are those of the fuel-carrying anode stream; the cathode and bypass will provide only air at some temperature and some degree of lower oxygen content in the cathode depending on the excess air ratio (EAR), i.e. the ratio of air flow rate in the cathode to that needed to react with the fuel stream stoichiometrically. In most cases this ratio approximately between two and five, so even with high values of fuel utilization the cathode will still contain a fair amount of oxygen.

For the NPSS model, the equilibrium chemistry assumption results in the anode flow becoming the equilibrium distribution of chemical species based on the elemental composition and operating conditions (i.e. temperature and pressure) as calculated by the Chemical Equilibrium with Applications (CEA) package [82]. The equilibrium assumption is often reasonable for fuel cells since the Ni-based anode material is an effective reformation catalyst that allows the anode gas flows to approach their equilibrium state.

As one step to simplify the conditions we need to consider, we can look to see if the resulting anode flow composition varies substantially for different aircraft operating conditions (i.e. pressure ratio, flight speed, and altitude) such as we might experience. Figure 4.3 provides results with consistent utilization and temperature conditions for a High-Altitude, Long Endurance (HALE) aircraft and a Regional Transport Jet aircraft, both as described in prior work [29, 55]. Given that we target specific SOFC operating temperatures and utilizations within the designs for each of these conditions, the meaningful differences here is the range of reformer and SOFC operating pressures (between 2.3 atm to 18.2 atm) brought on by different altitudes, flight speeds, and compressor pressure ratios.

Notably, there is very little difference in the anode exhaust composition across the range of operating conditions examined, i.e. the equilibrium mixture resulting from the reformer/SOFC subsystem is not substantially sensitive to input pressure differences. This is helpful at the moment as it allows us to consider data from the HALE cruise condition only going forward for setting baseline gas mixtures.

Temperature conditions are often required to remain in a range designed for the MEA materials chosen for the SOFC. While only one SOFC operating temper-

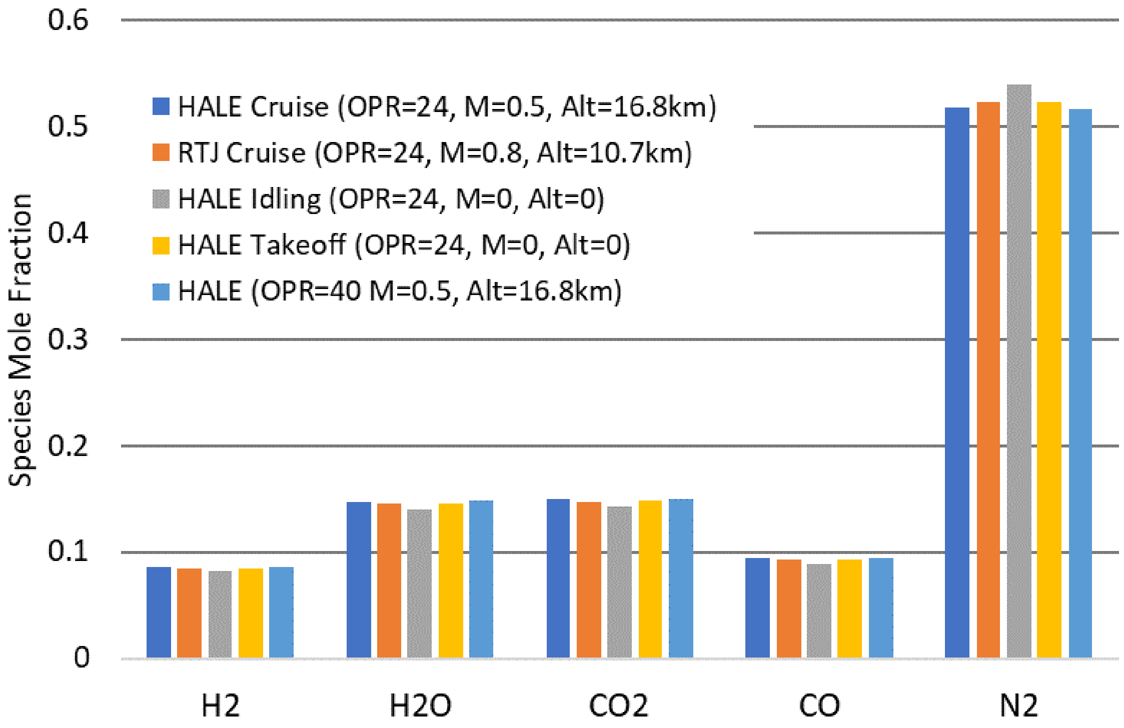

Figure 4.3: Anode exhaust species mass fractions for several operating conditions and engine designs, 850 °C and 75% fuel utilization. Figure reproduced from author's work [55]

ature here (850°C) has been used for generating anode exhaust data, adjusting the equilibrium result with temperature should be consistent with a target utilization in terms of the elements present in the mixture, and as such equilibrium can simply be recalculated for the same input flow at a different temperature.[i]

On the other hand, the SOFC exhaust composition is sensitive to the fuel utilization, per Figure 4.4. As the utilization value increases, more elemental oxygen is transferred across the membrane into the anode from the cathode, shifting the resulting species equilibrium towards product species H_2O and CO_2. As an interesting point of reference, all of the fuel and product species are about 12% mole fraction at 67% fuel utilization.

We now have a range of input flow thermodynamic and compositional conditions that are representative of a reasonable range of SOFC exhaust conditions that has accounted for temperature and pressure variations, and most importantly fuel utilization as the most impactful parameter. Recall that one of the motivations for this section was that fuel utilization inside a GT/SOFC designed for an aircraft can vary or be designed for a wider range of values than ground-based GT/SOFC systems.

Next, we'll use the same set of NPSS modeling results (HALE Cruise conditions of $M = 0.5$ and 16.8km altitude at $OPR = 24$) to investigate the sort of relative

---

[i] At first glance, it seems as though the same argument could be made for pressure variations at the SOFC exhaust. However, the pressure state from the flight condition also affects the equilibrium chemistry inside the CPOx reformer upstream of the SOFC, which targets the minimum AFR above soot formation to maximize the fuel content. Pressure affects that equilibrium [64, Fig. 12], and so the elemental content of the anode exhaust. In contrast, the SOFC exhaust temperature does not *necessarily* impact the reformer input conditions—though they may be interrelated for design optimization.

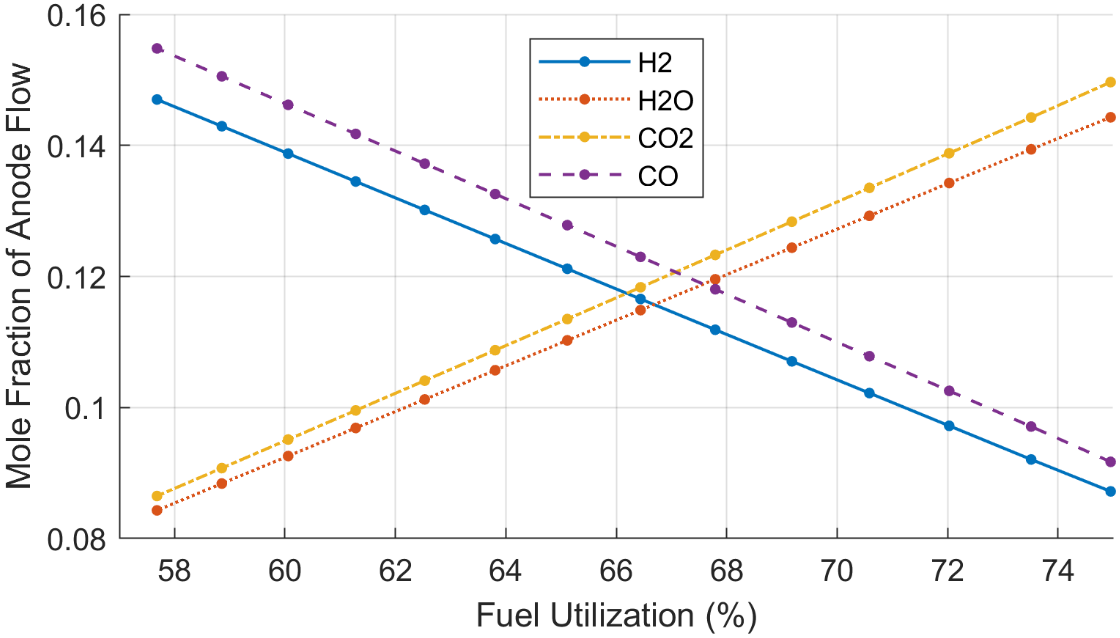

Figure 4.4: GT/SOFC Anode Exhaust Component Mole Fractions for a HALE aircraft (Mach 0.5, Altitude of 16.8 km, OPR of 24) at varying target SOFC fuel utilization. The SOFC operates at 850°C and 2.3 atm. N_2 content not shown, and represents vast majority of remaining mole fraction at every utilization value.

flow rates, and other extensive properties such as enthalpy (with values provided by NPSS via CEA), that we might expect for different relative sizes of SOFC and GT.

4.1.2 Extensive Properties

If we're considering the effective ways to integrate different flows into a single combustion, two main parameters of interest are the mass flow rates of each of those separate flows, and the enthalpy provided in each of those flows—particularly the SOFC anode exhaust, and combustor fuel injection, which contain fuel species. For those two parameters of interest, we'll consider the effects of two variables; (1) the fuel utilization, and (2) the relative scales of the SOFC and GT power outputs in the overall cycle.

For the first, in the previous section we showed that the composition of the anode exhaust varies with fuel utilization, and as such we might expect fuel utilization to affect these extensive parameters in the overall system as well. For the second, we saw in Chapters 2 and 3 that another main design parameter for a GT/SOFC is the relative size of the two main systems in the overall cycle.

So far, we have defined this parameter in terms of $\theta = w_{FC}/w_{GT}$ for analytical purposes, but the parameter can also be specified in terms of an electric power fraction[ii] $\zeta = \dot{W}_{elec}/\left(\dot{W}_{FC} + \dot{W}_{GT}\right)$. This can be more easily specified for an input parameter. Furthermore, for a constant total power target (as used here) ζ will track linearly with the SOFC power output even near complete SOFC or GT contribution.

Our first set of results in Figure 4.5 shows the mass flow rate fractions (here on a log scale) of the different SOFC input flows as a function of anode exhaust fuel oxidation target. For the relatively small SOFC ($\zeta \approx 10\%$), the exhaust from the compressor (bypassing the reformer/SOFC entirely) is the largest component, accounting for 80%–90% of the flow. The second largest flow rate is the cooling bypass flow, accounting for about 10% of the flow at 58% fuel oxidation, though this drops with increased fuel utilization due to the constant AFR of 15 (relative to the fuel injected into the reformer) diverted into the reformer/SOFC subsystem.

For the CPOx reformer with a relatively high degree of air dilution, the cathode and anode exhausts are of a similar mass flow rate, though again for a consistent power output by the SOFC, the flow rates drop by about half from a utilization of 58% to 75%, as more of the fuel is utilized for electric power. The flow rates in the anode and cathode reduce more quickly than the utilization increases because SOFC power is only generated in the SOFC, but the reformer before the SOFC has already utilized 30%-40% of the fuel's oxidative capacity in the reformation process. As such, we expect the fuel utilization's effect on flow rate to be reduced for more efficient reformation processes. Finally, the burner's new fuel flow rate represents approximately 2% of the total flow rate, and increases slowly as the anode fuel utilization increases in order to counteract the reduced enthalpy contribution from

---

[ii] In prior work the SOFC was used to produce electrical power for secondary applications on board the aircraft, such that the term "electric power fraction" implied that some part of the power is used for electrical production (usually the SOFC, or alternatively the standard mechanical generator) and another for thrust (usually the GT). In this work however, we'll use ζ as defined in the text, which merely separates out the part of the GT/SOFC cycle from which power is drawn.

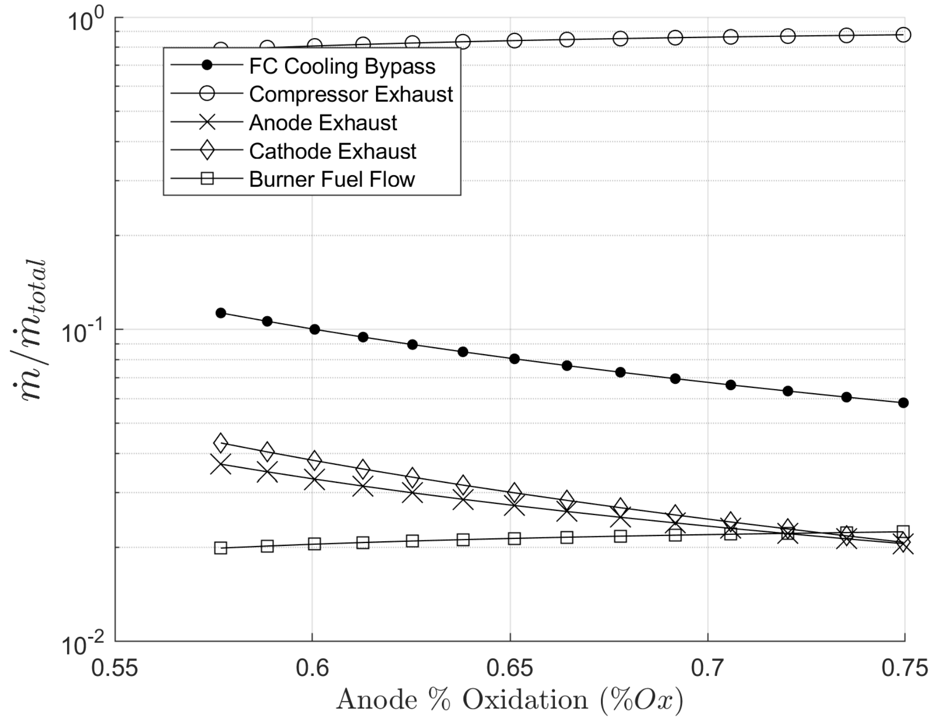

Figure 4.5: Combustor Mass Flow Inputs for Varying SOFC Anode % Oxidation for a HALE aircraft ($M = 0.5$, 16.8 km altitude, OPR = 24, $\zeta = 10\%$).

the anode exhaust.

Enthalpy contributions in this scenario are from the values reported by the CEA thermodynamic package in NPSS, with the coldest air stream (post-compressor flow in all cases) set as the zero baseline. The enthalpy fraction of each stream with varied fuel utilization is provided in Figure 4.6.Notably, 80%–90% of the enthalpy is provided by the burner flow, increasing at greater fuel utilization, also to make up for the lower energy content of the SOFC anode exhaust. On the other end of the scale, the cathode and SOFC cooling bypass flows carry relatively little enthalpy; the cathode flow enthalpy drops with the reduction in mass flow rate, while the cooling bypass absorbs more heat from the SOFC and fuel content (for the constant global AFR) with greater fuel utilization, rather than that enthalpy remaining in the fuel on the way to the burner.

As the other fuel flow, the anode exhaust carries the second-most enthalpy, starting at about 14% of the total at low anode fuel utilization even for the low SOFC power output. At higher values of fuel utilization however, this drops to about 5% similarly, dropping by about two-thirds over the range of fuel utilization. This is slightly more than the drop in anode mass flow rate due to the greater degree of oxidation of the flow itself resulting in less enthalpy addition per unit of flow. Even for a relatively small electric power fraction ($\zeta \approx 10\%$) the SOFC exhaust can represent a wide range of the enthalpy fraction injected into the burner.

All of the results so far were for a single electric power fraction. If we instead lock the % oxidation at 75%, and vary the size of the SOFC subsystem relative to that of the GT, we generate the results in Figures 4.7 and 4.8. In Figure 4.7,

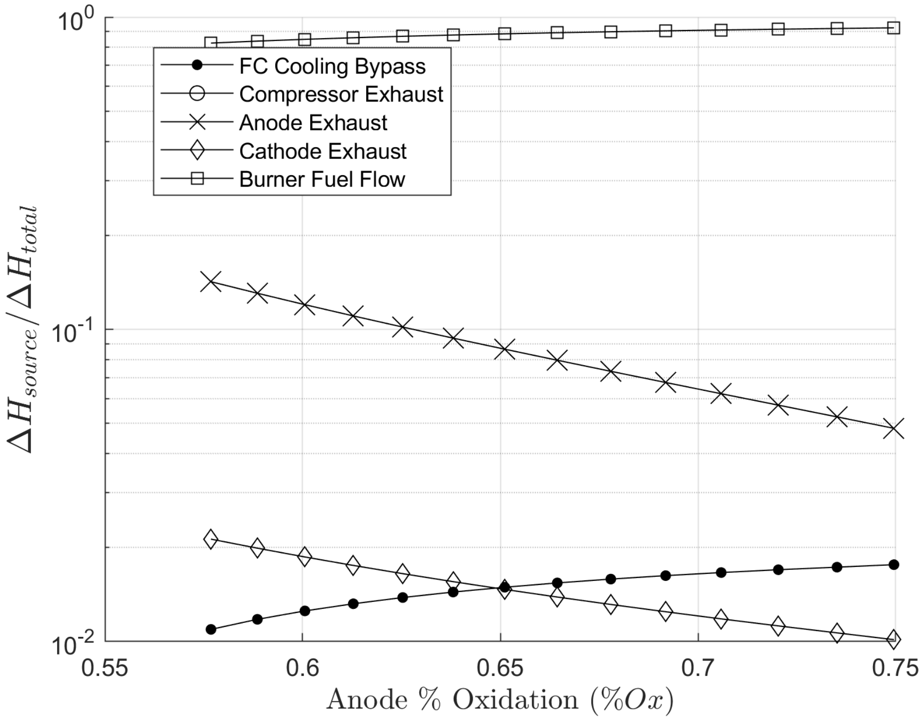

Figure 4.6: Combustor Enthalpy Inputs for Varying SOFC Anode % Oxidation for a HALE aircraft ($M = 0.5$, 16.8 km altitude, OPR = 24, $\zeta = 10\%$).

unsurprisingly the mass fraction of the SOFC subsystem flows (anode, cathode, cooling bypass) become larger with ζ, with slightly exponential behavior since the total power output of the system increases in this scenario as the SOFC is generating secondary electrical power while the GT produces thrust via a turbofan.

For an initial $\zeta \approx 10\%$ at 50 kW, increasing ζ to around 40% brings down the compressor exhaust flow to become around 30% of the total flow rate. Approximately 40% of the flow rate is cooling bypass, dictated by the global AFR value through the SOFC subsystem as a reasonable target for cooling. The anode and cathode flow rates go from about 2% each of the total flow rate to about 15% each. The burner flow rate remains small, dropping from around 2% to 1% of the total flow through the system.

Broadly similar trends can be observed for enthalpy in Figure 4.8. With the compressor exhaust as the baseline value for enthalpy, the two main enthalpy contributions are from the burner and anode flows, with the anode flow providing $\approx 30\%$ of the enthalpy into the combustor at $\zeta \approx 40\%$. Finally, the cathode exhaust provides about 5% (by virtue of being heated to the SOFC operating temperature) and the cooling bypass flow providing about 10% (by virtue of absorbing SOFC waste heat) of the total for the same ζ.

Altogether, we see some general trends for the GT/SOFC flows. First, lower fuel utilization targets that may be attractive for high power-density SOFCs increase the flow rates through the reformer/SOFC subsystem significantly, almost doubling from the high % Oxidation baseline of 75% to the low end of 58%. At the same time, increasing the electric power fraction also increases the proportional flow rates

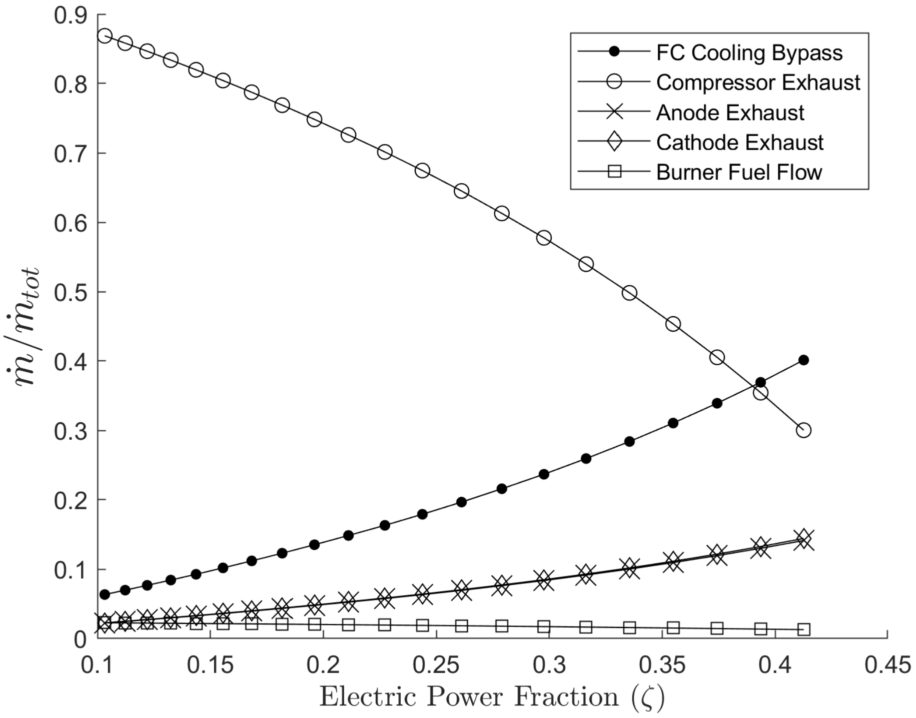

Figure 4.7: Combustor Mass Flow Inputs for Varying Electric Power Fraction (ζ) for a HALE aircraft ($M = 0.5$, 16.8 km altitude, OPR = 24, $\%Ox = 75\%$).

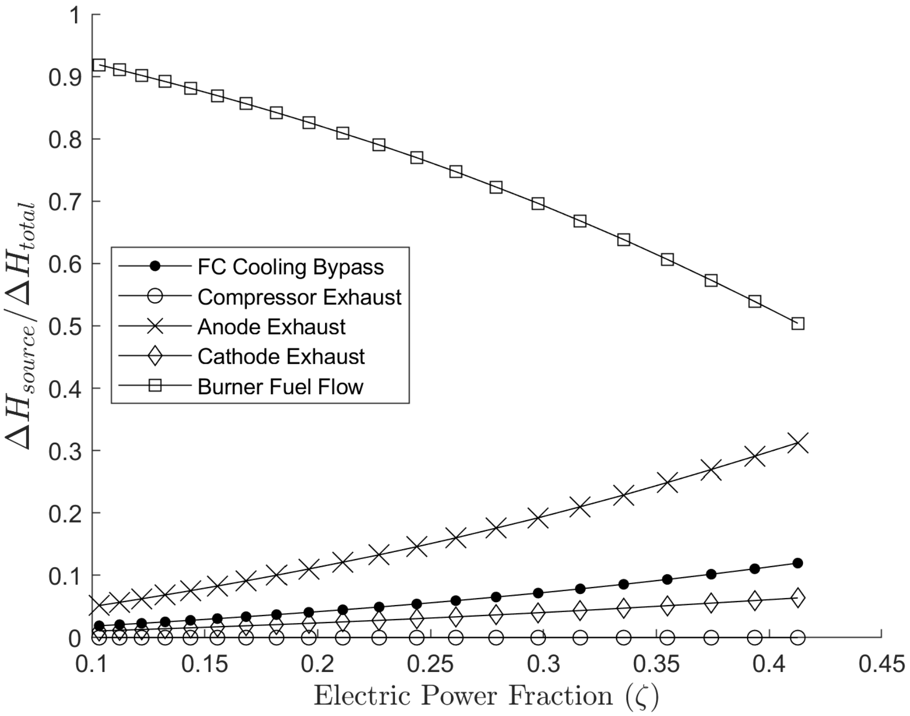

Figure 4.8: Combustor Enthalpy Inputs for Varying Electric Power Fraction (ζ) for a HALE aircraft ($M = 0.5$, 16.8 km altitude, OPR = 24, $\%Ox = 75\%$).

for the reformer/SOFC such that we already have designs where the SOFC anode represents approximately 30% of the fuel power added into the combustor.

As a point of reference, the electric power fraction of 40% investigated here matches approximately to the Fan-Support systems analyzed for Section 3.6 for the largest SOFC subsystems ($\theta \approx 0.6$). Given that general performance improved as the relative size of the SOFC is increased (subject to the specific power of the reformer/SOFC subsystem), substantial flows of the size and type described in this section would likely be encountered in practical GT/SOFC combustor on board an aircraft. At these scales, the reformer/SOFC streams are not small enough to be subsumed into the air and fuel mixture without changing the overall state and composition substantially.

We've now characterized representative conditions for both the intensive and extensive properties of the novel flows leading into the GT/SOFC combustor. The next question is what sort of behaviors might we expect in terms of combustion. As such, we'll next identify possible effects of integration through computational combustion analyses.

4.2 Combustion Modeling

The process of integration into the combustor will involve the combining of all the different flows that, in the ideal case, fully combust fuel and air to a uniform turbine inlet temperature with minimal pressure loss during the heat release process. Because of the high flow rates paired with size and volume constraints, the combustor will be relatively small with short residence times. Additional (though not exhaustive) requirements are for stability over a wide operating range (due to varying throttle and flight conditions), long term survivability of the combustor hardware, and low emissions of smoke or other pollutants [122, p. 9-10].

Typically, fulfilling these requirements is already challenging for binary air and fuel mixtures, with decades of work having gone into improving modern combustor performance across a variety of metrics. For our purposes here however, we will identify some indicators for problems and opportunities that might occur as we bring the different flows together to help determine whether additional investigation is warranted for GT/SOFC hybrid combustors specifically. Immediately considering the potential for interesting mixtures, we have Table 4.1 that provides a matrix of the general interactions we expect for mixing each of the flows from Figure 4.1.

Table 4.1: Expected results of various GT/SOFC combustor input mixtures

	Compressor	Bypass	Anode	Cathode	Comb. Fuel
Compressor	X	Preheat	Combustion	Depletion, Preheat	Combustion
Bypass	X	X	Combustion	Depletion, Preheat	Combustion
Anode	X	X	X	Combustion	Reformation, Evaporation
Cathode	X	X	X	X	Combustion
Comb. Fuel	X	X	X	X	X

The immediate concerns are hot-spots and premature ignition from the combustion cases, particularly the mixing of the SOFC anode exhaust with other streams. At the same time, the hot and easily-ignited gas could also be used to improve flammability limits overall, ensuring ignition where desired inside the combustor.

One means to evaluate the potential for hot spots is the adiabatic flame temperature for mixtures at varying equivalence ratio in order to evaluate the worst-case heating scenario. We may expect these to occur with either mixtures of anode with either cathode or bypass flows (or some mixture thereof). Next, the risks of premature ignition can be evaluated using ignition delay time calculations of similar mixtures. Laminar flame speed calculations provide a general baseline of flammability that is easily compared to other scenarios, while finally an extinction strain rate calculation provides information about the stability of flames using different flows into the GT/SOFC combustor.

Each of these calculations and their results are elaborated in subsequent sections, but all are carried out using Cantera, an open-source toolbox for chemical kinetics, thermodynamics, and transport processes similar in use to CHEMKIN [123]. By default, we will use the FFCM-1 reaction mechanism which serves as an improvement on the venerable GRI-Mech 3.0 mechanism [124].

4.2.1 Adiabatic Flame Temperatures

The Brayton cycle generally benefits from higher temperatures at the peak of the thermodynamic cycle, which are produced by the combustor at the turbine entrance (i.e. the TIT). Practically speaking however, the temperature is limited by the material constraints of the combustor and turbine[iii] that need to survive these conditions for long periods of time. Even if a mixture of air and fuel may be calculated to reach a survivable temperature overall, a non-uniform distribution of the temperatures inside the combustor may actually occur, with some regions much hotter (or cooler, though this is less destructive) than intended for any number of reasons. These hotter regions are also described as "hot spots" and can destroy the combustor during operation.

The SOFC exhaust flows represents a flux of pre-heated and (in the case of the anode) combustible gases into the combustor, with hydrogen as one of the primary fuel species that reacts quickly. Both of these properties may be expected to result in higher local temperatures if no precautions are taken. At the same time, the hottest anode and cathode flows are also diluted by nitrogen for reformation, and the transfer of oxygen within the SOFC respectively. The question is how these effects balance out.

The adiabatic flame temperature (AFT) is the temperature achieved if all of the energy released during an exothermic chemical reaction is retained by the reactants [122, p.71-72]. In practice, real flames lose energy through radiation and convection, so any results may be considered to be upper-limit estimates of the temperatures experienced in an actual system. As such, it is useful for evaluating the potential formation of hot spots inside a combustor if we consider the range of equivalence ratios for mixtures of interest. *A priori* the mixtures we've generated here are effectively vitiated air, which we can expect for any combination of flows to result in a lower maximum AFT at a molar equivalence ratio of unity [122, p. 72].

Figure 4.9 confirms that *a priori* expectation, showing that the AFT with a

---

[iii] Higher combustor temperatures also encourage the formation of NOx pollutants ("thermal NOx"), but this is a less fundamental concern, and often an issue caused by higher temperatures through *part* of the combustor before dilution to the target TIT value.

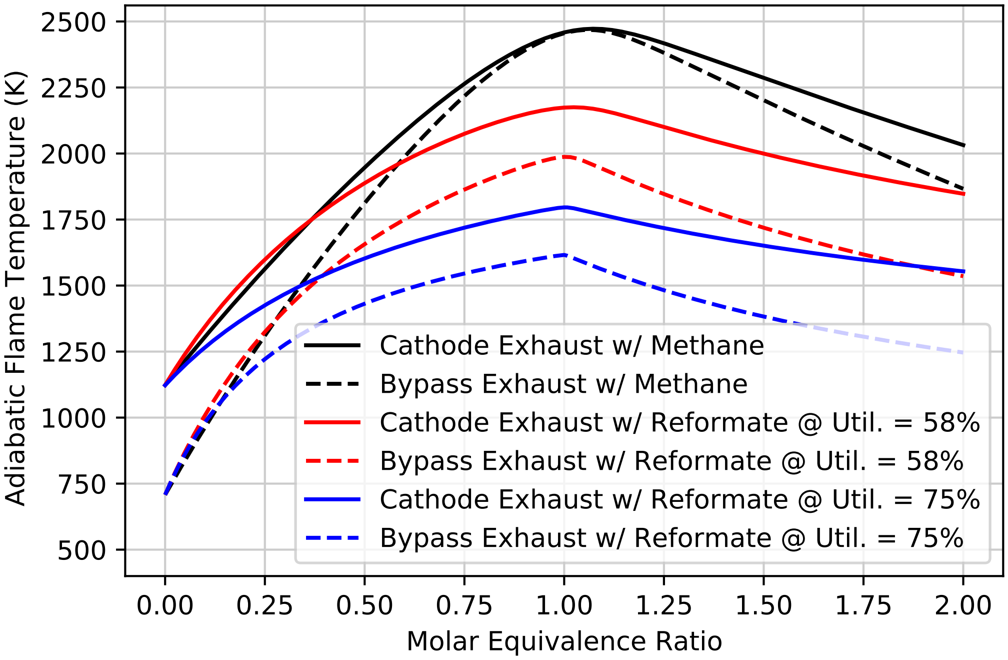

Figure 4.9: Adiabatic Flame Temperature of Exhaust Components and Methane.

pure fuel species (here methane) will reach higher temperatures than the vitiated air mixtures. Additionally, the higher temperatures of the cathode exhaust results in higher AFT values than cooler, but more oxygen-rich, bypass flows. The fuel utilization also has a substantial impact on the AFT, resulting in about 300K–400K differences in the near-stoichiometric region.

However, the lower AFT values still represent substantial heat release, as approximately 500K temperature rises are achieved for all of the bypass mixtures at $\phi = 0.25$, and all cathode mixtures except for the cathode mixture with highly-utilized reformate, which is the most vitiated case.

4.2.2 Ignition Delay Time

The AFT is the ideal result of heat released by combustion to the point of chemical equilibrium. AFT however does not account for the rates at which that heat is released, if the combustion reactions even occur spontaneously, which is a result of chemical kinetics in addition to thermodynamics. One parameter that accounts for these rates is the Ignition Delay Time (IDT), which represents the time between which a fuel and air mixture is combined and the onset of a flame.

Empirical correlations of the IDT with temperature and pressure have previously been made using the Wolfer equation, which takes the form of Equation 4.1 [122, p. 64]. For Equation 4.1, t_i is the IDT, P is the pressure, ϕ is the equivalence ratio of the mixture, E is the activation energy, R is the gas constant, and T_{mix} is the initial mixture temperature. The remaining variables A, n, and m are constants found to fit experimental data.

$$t_i = AP^{-n}\phi^{-m}\exp\left(E/RT_{mix}\right) \tag{4.1}$$

In the absence of those empirical variables (as is the case here), an IDT can also be calculated computationally in Cantera, here using the FFCM-1 mechanism for the chemical kinetics. To determine the IDT, the initial fuel and oxidant mixture's reaction rates (for each reaction in the mechanism) are calculated, then integrated over a timestep before repeating the process. The resulting mixture conditions are tracked over each timestep until a rapid release of heat (or other indicator of flame

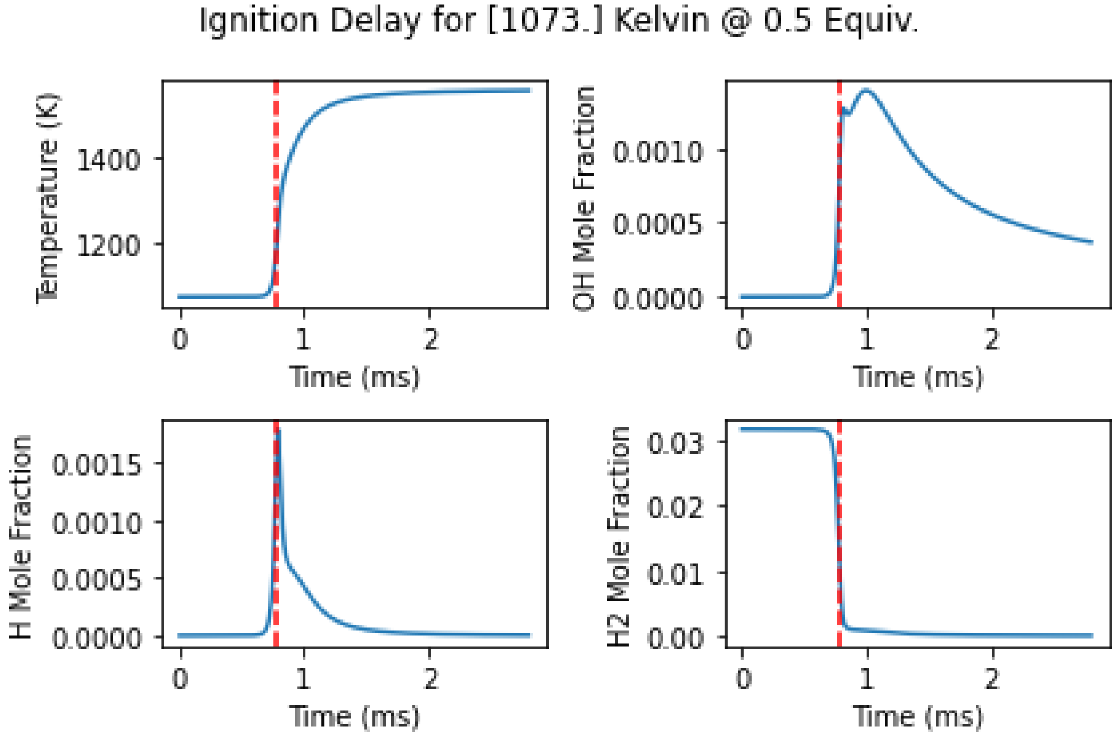

Figure 4.10: Several Indicators for Ignition Delay Time Identification. Red vertical line shows the identified IDT. Mixture provided for Anode/Cathode flows at 58% fuel utilization at 800°C

formation) is observed in the mixture, with some additional timesteps recorded in order to confirm the observation of peaks. An example of these different indicators across the same time range for an ignition can be seen in Figure 4.10, where the ignition time was identified algorithmically.

All of these indicators ideally occur at similar times, but can be difficult to spot algorithmically over wide-ranging timescales. In this work however, the primary indicator is the maximum *rate* of hydroxyl group (OH) creation, calculated as the difference in hydroxyl concentration between timesteps, normalized by the duration of the timestep.

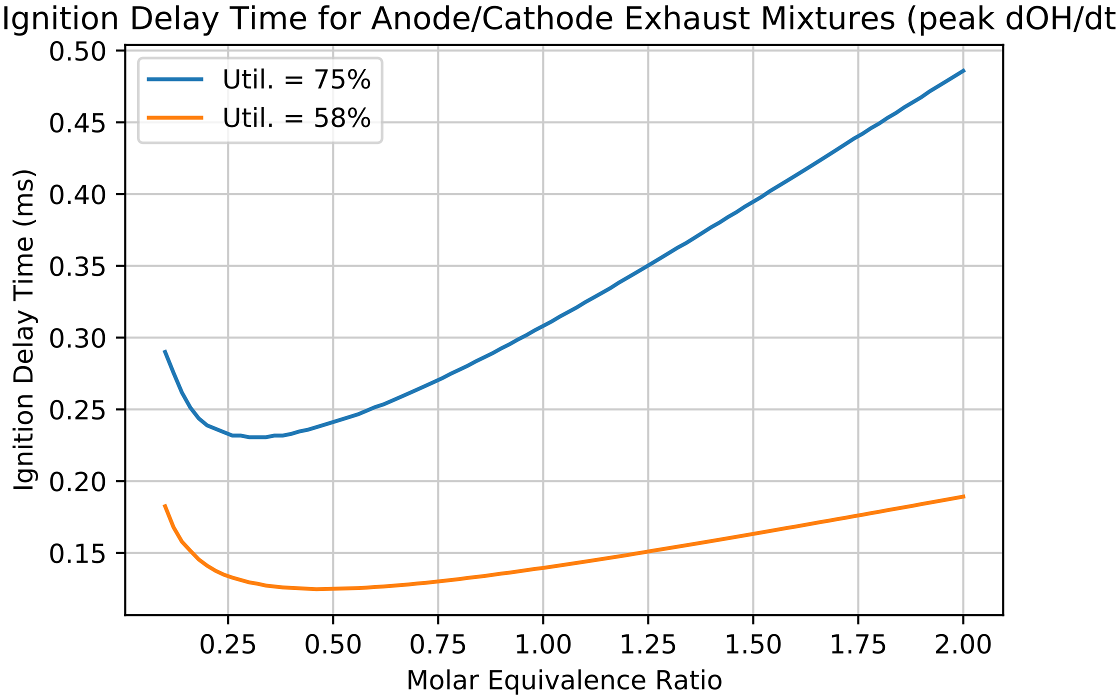

Figure 4.11: Ignition Delay Time of Anode/Cathode Exhaust at Varying Equivalence Ratios for two different fuel utilizations at 800°C.

To try and bound the question as much as possible, we can first consider mixtures of anode and cathode exhaust since these mixtures will have the highest temperature (a sensitive parameter per Equation 4.1). Figure 4.11 shows the IDT of these mixtures at a representative temperature of the SOFC exhaust across a range of equivalence ratios. The specific mixtures are for GT/SOFC exhaust compositions at the highest and lowest solved utilization values (75% and 58% respectively), again to bound the range of solutions.

Immediately, we observe that the ignition delay times are less than 0.5ms over the range of mixture fuel utilization and equivalence ratios, with a minimum under

0.15ms between equivalence ratios of 0.25–0.5. Effectively, at these conditions the mixtures ignite instantaneously. The presence of a minimum is somewhat inconsistent with the observations of other fuel-air mixtures, but there are wide disagreements between experimenters. This may be due however to the physical processes of fuel-air mixing dominating the scenario initially [122, p. 67-69]. The immediate consequences of this observation are that the anode and cathode exhausts cannot be difficult to safely combine upstream of the combustor or near the SOFC, unless intended as part of the SOFC temperature control scheme.

However, Figure 4.11 is only for a single operating temperature; the SOFC exhaust streams might be cooled by various means after the SOFC, and ignition is sensitive to temperature. Figure 4.12 provides results for a single equivalence ratio of 0.5 for the upper and lower ranges of fuel utilization. For varying temperature, it is suggested to use an inverse temperature parameterization for the x-axis, and a logarithmic y-axis, which per Equation 4.1 should result in linear trends [122, p. 66].

And in fact, Figure 4.12 does show such trends, though with changing slopes over three temperature regions. These regions are approximately 1200K–1050, 1050K–1000K, and below 1000K, though the ranges shift to lower temperatures with lower fuel utilization. Following the Wolfer equation, the changing slopes indicate a shift in the activation energy of the rate-limiting reaction step(s). What those specific reactions are has not been immediately identified.

Finding a numerical result for the IDT calculation does not necessarily indicate spontaneous ignition in practice. At least one source provides residence times for an aircraft combustor to be on the order of tens of milliseconds [125]. As such, ignition

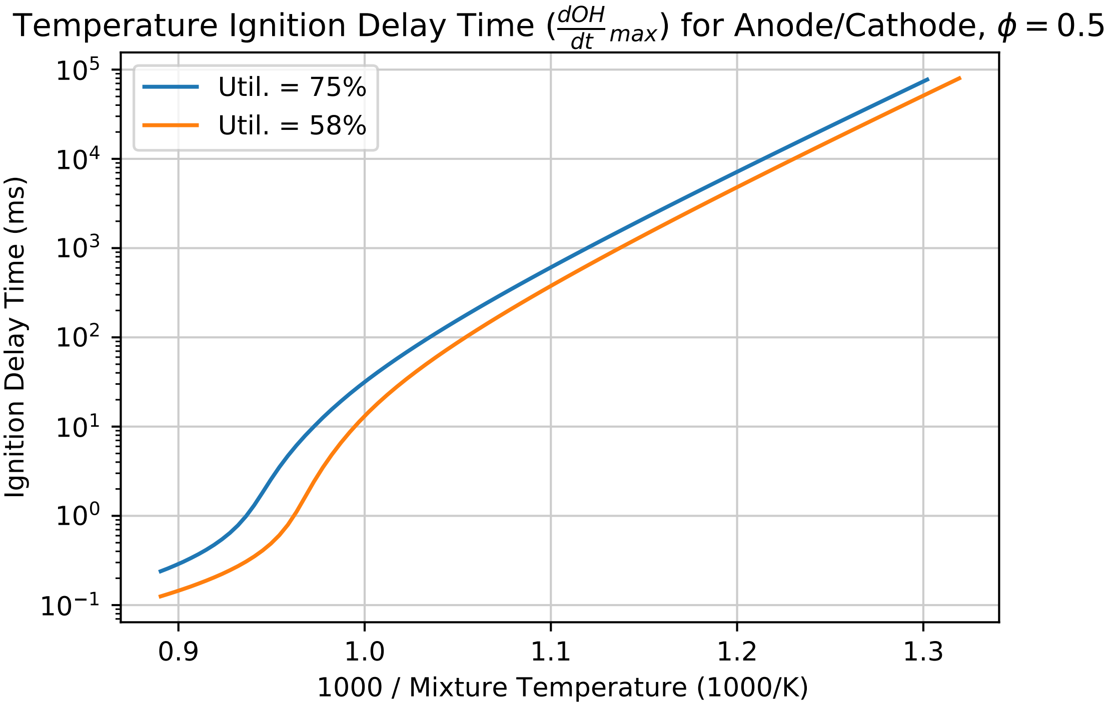

Figure 4.12: Ignition Delay Time of Anode/Cathode Exhaust at Varying Temperature for two different fuel utilizations at $\phi = 0.5$.

times in the 1–10 seconds range are generally meaningless in the context of a jet engine. In that case, it appears that mixture temperatures above approximately 950K ($IDT < 100$ms) will spontaneously ignite. This corresponds to 680°C, below many (though not all) SOFC operating temperatures.

At higher temperatures, there is therefore reason to avoid premixing anode and cathode exhaust to avoid spontaneous ignitions. However, the lower AFTs mixed with spontaneous ignition over combustor residence times suggests that these mixtures may be useful in sustaining combustion inside the combustor itself. To this end, another IDT analysis can be performed that includes three-component mixtures, including now methane as a fuel species. A ternary contour plot can show characteristics for any **mass-fraction** combination of the three flows, here mixtures of bypass flow, anode exhaust, and methane fuel. The bypass and anode exhaust flows are taken to be at their calculated temperatures and compositions for 58% utilization, while the methane is considered to have been preheated to the bypass flow temperature. All three flows are taken to be at one atmosphere of pressure.

In the ternary plots, every point represents a different mixture of the three components, while each edge represents a balance between only two of the components. The resulting mixtures have a range of initial relevant conditions that all may have an effect on IDT, or combustibility in general. These conditions include their initial temperature, molar equivalence ratio, and adiabatic flame temperature.

The initial temperatures are given in Figure 4.13, which are important due to the high sensitivity of IDT to temperature. Given that the methane temperature is taken to match that of the bypass, the temperature is mostly dependent on the

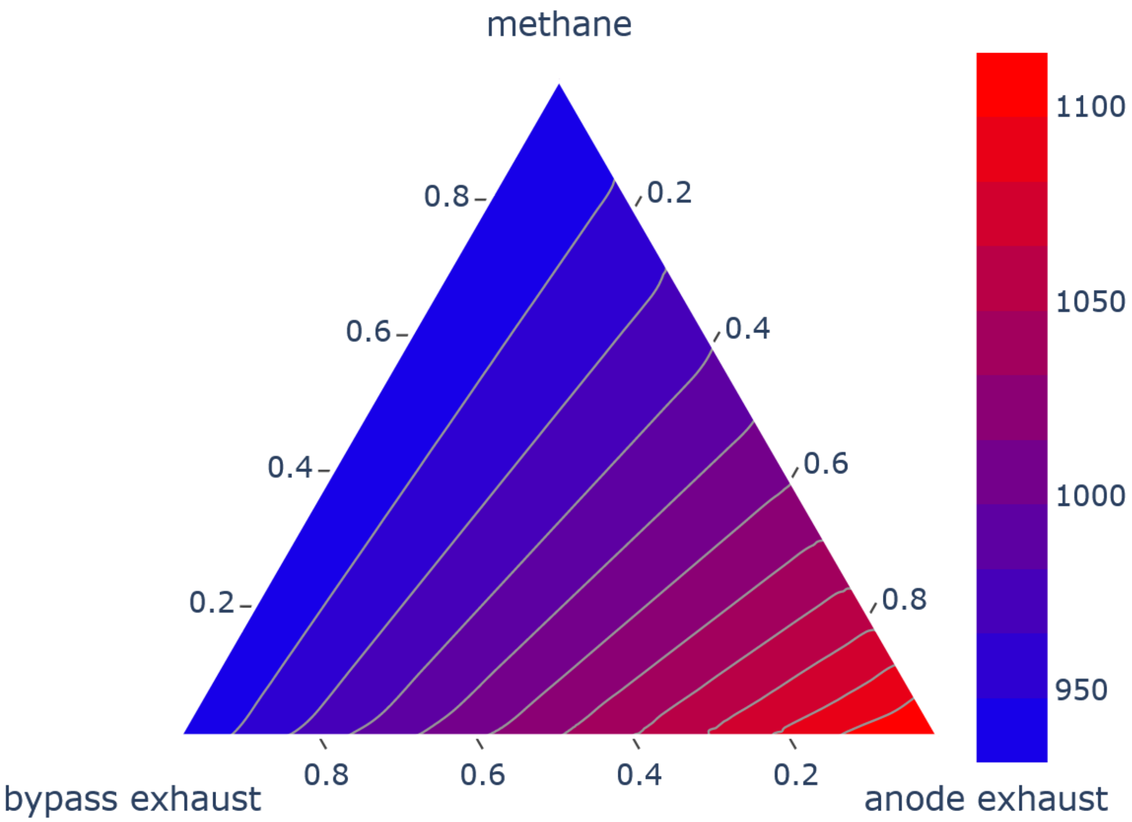

Figure 4.13: Initial Mixture Temperatures (K) of 58% fuel utilization Anode Exhaust, Bypass Exhaust, and Methane Mixtures at Varying Composition.

anode exhaust temperature. The bias for cooler temperatures with larger fractions of methane is due to methane's specific heat being higher than that of air. The temperature of the bypass air is already almost 950K, such that purely anode/bypass exhaust mixtures are likely to ignite spontaneously per Figure 4.12.

The molar equivalence ratios of the mixtures are given in Figure 4.14. Note that in this figure, all values of ϕ above 7 are colored similarly; scaling the contours otherwise is difficult. In general the contours are flat, normal to the methane corner of the ternary plot as methane is a pure fuel. At points with low methane content, the contours become biased by the anode exhaust which also contains some fuel

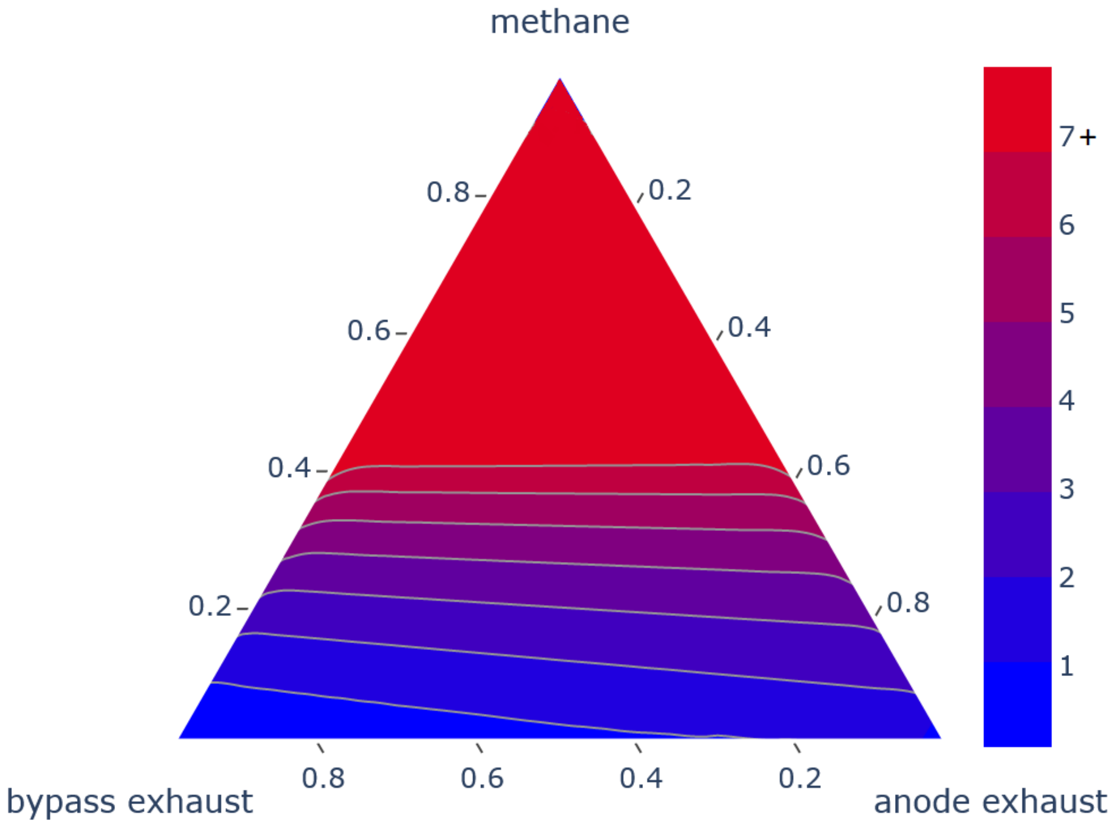

Figure 4.14: Molar Equivalence Ratio of 58% fuel utilization Anode Exhaust, Bypass Exhaust, and Methane Mixtures at Varying Composition.

species. Pure anode exhaust is in a molar equivalence ratio between 1 and 2 (which is consistent with a fuel utilization of 58%). However, most combustion scenarios are intentionally run lean. This makes the most relevant portion of the plot the lower left-hand corner of the bypass exhaust, with only small proportions of anode exhaust and methane.

The stoichiometric contour ($\phi = 1$) in Figure 4.14 is also reflected in the adiabatic flame temperatures given in Figure 4.15. The maximum temperatures around 2500K are achieved roughly along the stoichiometric contour, with two mild peaks

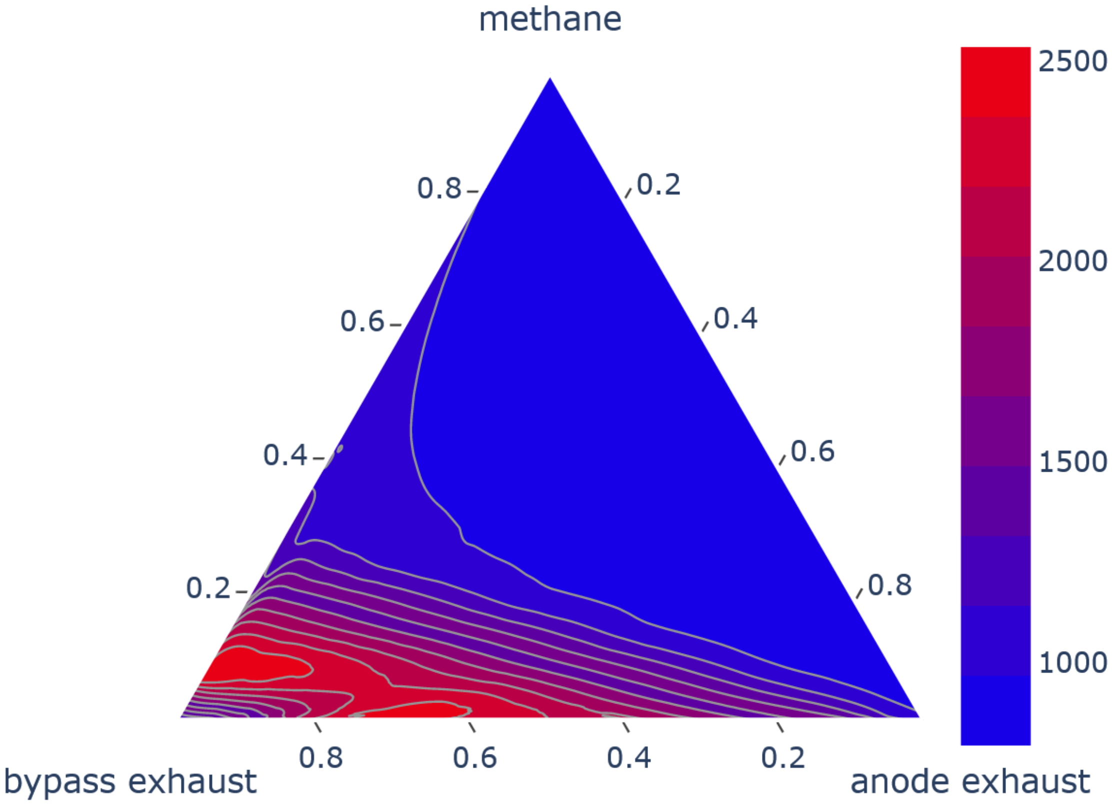

Figure 4.15: Adiabatic Flame Temperature (K) of 58% fuel utilization Anode Exhaust, Bypass Exhaust, and Methane Mixtures at Varying Composition. Scale in $\log_{10}$(ms).

close to pure bypass/methane and bypass/anode mixtures. Again, this indicates our area of interest is for majority-bypass mixtures.

Finally, we consider Figure 4.16 for the IDT results. Note that the figure units are base-10 logarithmic such that our threshold of interest is roughly for values 3 (equivalent to 1 second) and below. As such, all IDTs above 1 second have been omitted entirely, and a line-contour graph used for clarity due to limitations in the ternary-plot software package. The first thing we notice is that the plot is relatively sparse. The only portion of the plot with IDTs below the 1-second threshold are

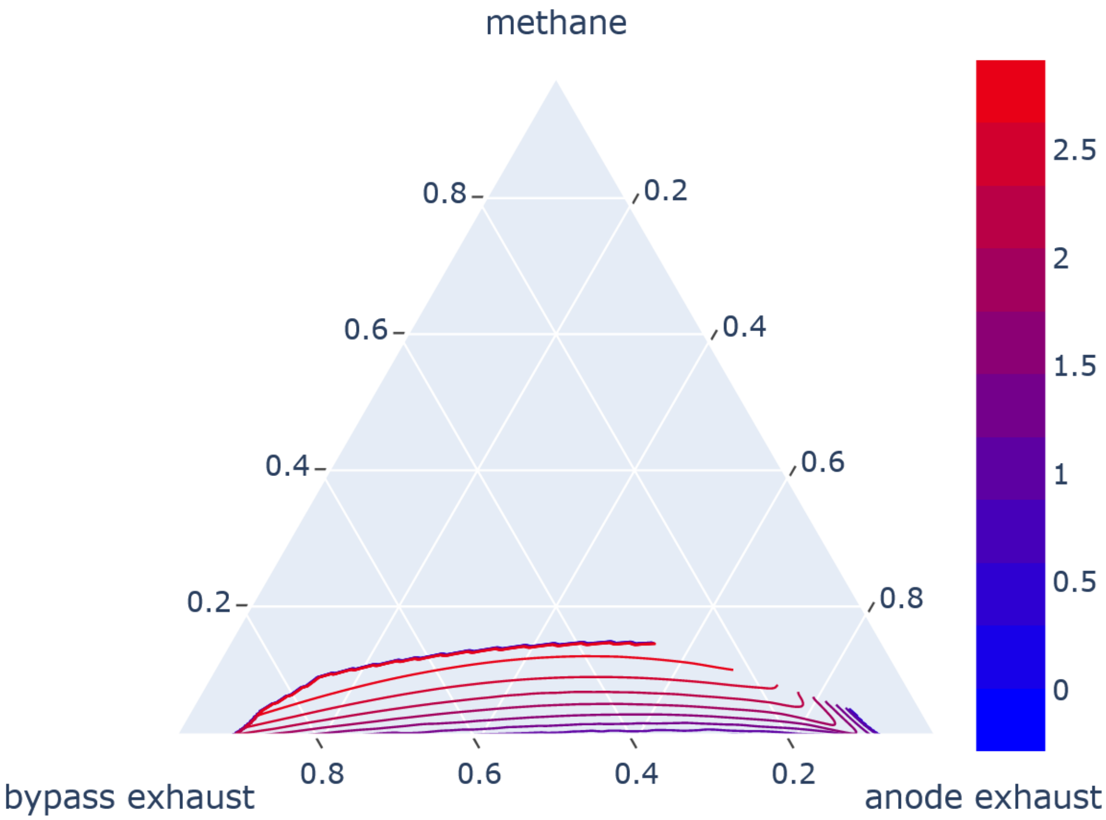

Figure 4.16: Ignition Delay Time of 58% fuel utilization Anode Exhaust, Bypass Exhaust, and Methane Mixtures at Varying Composition. Scale in $\log_{10}$ (ms).

mixtures below approximately 15% methane by mass, in a wide swath between 90% anode and 90% bypass mixtures. Of the two AFT peaks in Figure 4.15, only the anode exhaust peak will spontaneously ignite. While that mixture is primarily additional anode exhaust, small amounts of methane can spontaneously ignite as well, which is untrue for mixtures without the anode exhaust.

While this is only an initial survey of the scenario, it appears that mixtures of anode exhaust with pure fuel species can encourage ignition. Considering the mass fractions for different combustor inputs in Figure 4.7, the mass flow rate of the anode exhaust tends to exceed that of the fuel flow rate several times over. As such, the IDT characteristics explored here may find use in further analysis of GT/SOFC combustors on aircraft.

4.2.3 Laminar Flame Speed

The next combustion characteristic to be considered is the premixed Laminar Flame Speed (LFS), which is the speed at which a plane flame front will propagate through a premixture of fuel and oxidant species. LFS is a basic combustion characteristic that is applied in numerous other estimations and relationships for flame stabilization and rates of heat release [122, p. 41-42]. The main parameters affecting the flame speed of any given mixture are equivalence ratio, temperature and pressure

The premixed LFS is calculated using the Cantera FreeFlame model. In the model a flame is initiated for a mixture of fuel and oxidant, with a reaction mechanism (here again FFCM-1) determining the release of heat and products into the premixture, leaving hot product species behind. The inlet velocity of new premixture gas is adjusted until the flame front remains stationary in the given domain. For the stationary flame, the inlet velocity is effectively the flame speed. Figure 4.17 provides a representative profile of a flame temperature and composition.

While the LFS of most fuel species peak at rich but near-stoichiometric equivalence ratios, syngas components H_2 and CO are exceptions which peak at equivalence ratios around two [122, p. 42].

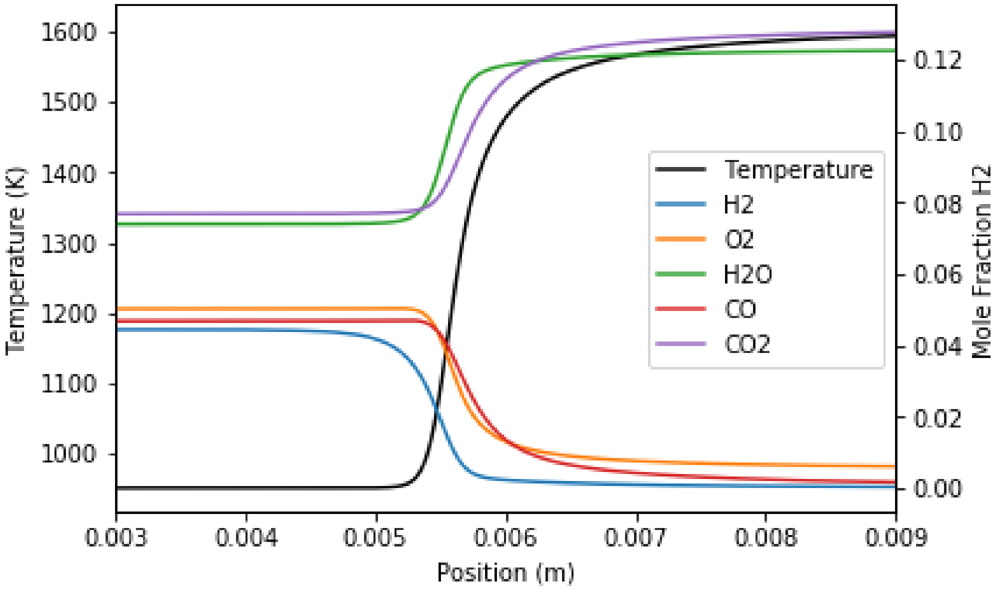

Figure 4.17: Representative Laminar Flame Temperature and Composition 1-D Profile. Syngas and air mixture provided.

In addition to equivalence ratio, the major parameter specific to the GT/SOFC is the fuel utilization. Figure 4.18 gives LFS results for a range of temperatures and a variation in pressure, across the range of SOFC fuel utilization compositions found previously.

In general, we observe trends for temperature and pressure that are consistent with the literature [122, p. 42]. In particular, the laminar flame speed seems inversely proportional with pressure to some (empirical) root, while temperature increases have mild positive exponential impact. More data however will need to be calculated or collected to determine values for the empirical exponential values in both cases.

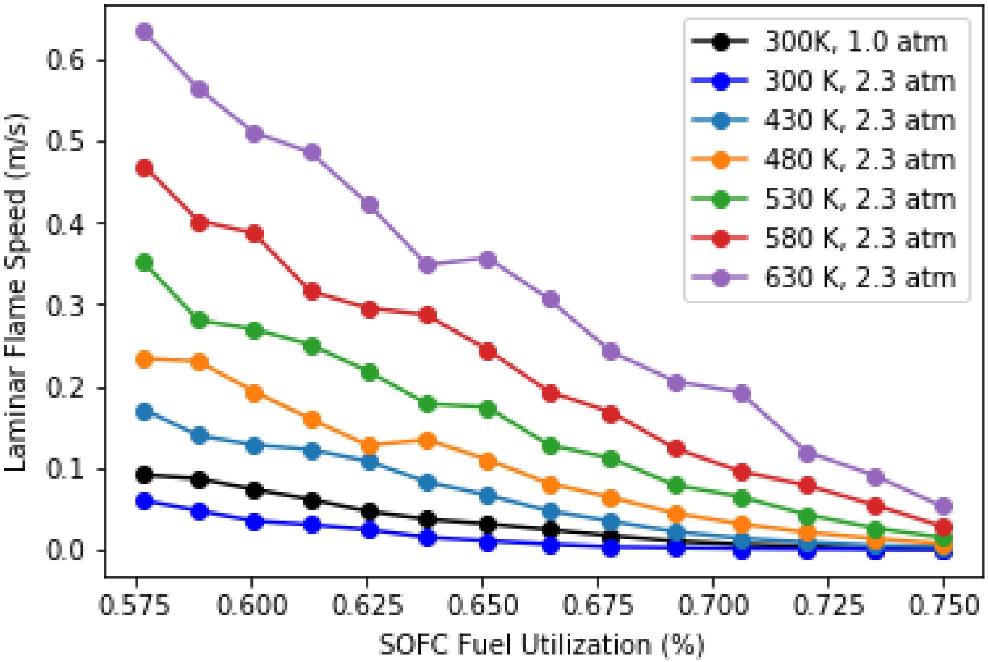

Figure 4.18: Laminar Flame Speed with SOFC Fuel Utilization for Different Temperature and Pressures.

4.2.4 Extinction Strain Rates

The final combustion characteristic considered in this chapter is the non-premixed Extinction Strain Rate (ESR). In the context of a gas turbine combustor, the ESR is relevant for flameholding behavior; i.e. a higher ESR indicates a greater capability to maintain heat release (such as for fuel injection points) even under extremely turbulent conditions inside the combustor.

One computational model for ESR is Cantera's CounterflowDiffusionFlame (similar to OPPDIF in ChemKin). In the model, separate fuel and oxidant streams are directed towards each other with some speed which then spreads out radially at the central plane of contact. The radial spreading changes the length-scale of the fuel and oxidant interface at a certain rate, described as strain, which can be interpreted as a velocity divided by the length scale for units of inverse time. The induced strain rate affects the reactions occurring at the oxidant/fuel interface—and consequently the rate at which heat is released. Figure 4.19 provides a representative profile of the opposed streams with composition and temperature as a function of axial position. Temperature and combustion products peak in the center of the system, where the flame is generated.

"Extinction" occurs when the strain rates are such that reactions do not occur quickly enough to release sufficient heat to sustain and encourage further reactions—or in other words, to cause any flame to go extinct. In the Non-premixed counterflow diffusion flame scenario, the strain rate is a function of the speed of the incoming flows. To calculate the ESR, the CounterFlowDiffusionFlame calculation is run for

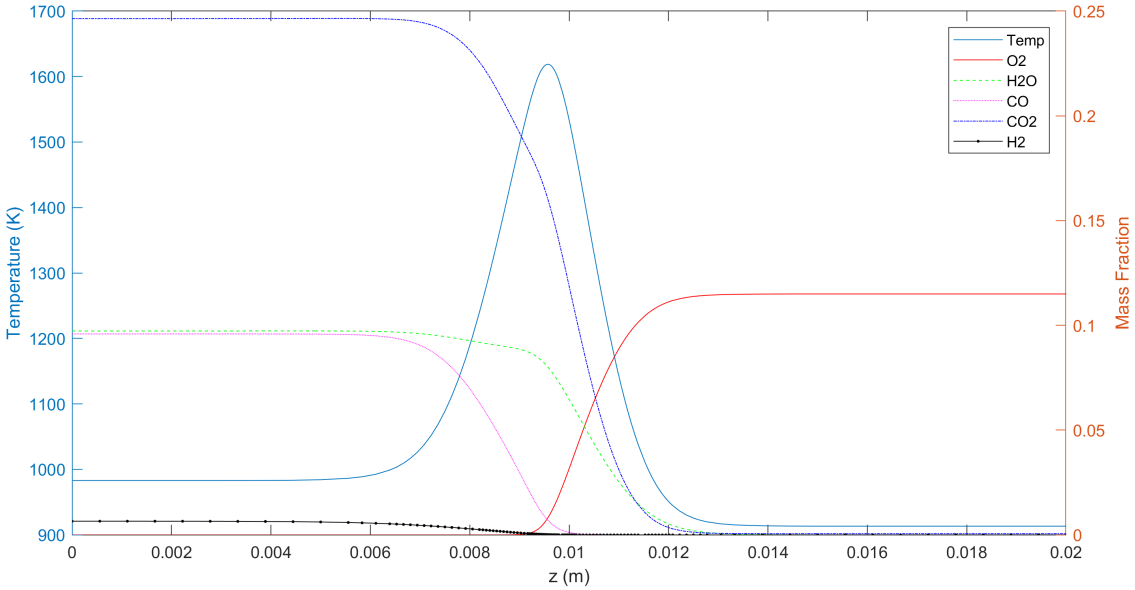

Figure 4.19: Representative CounterflowDiffusionFlame Analytical Profile. Anode and Cathode exhausts (75% Utilization) shown here. Nitrogen content of both flows neglected for clarity.

a relatively low-flow rate scenario where a flame is generated. This can be indicated by a substantial temperature rise close to the expected AFT value. The flow rates of fuel and oxidant are then progressively increased, generating higher and higher strain rates in the calculation. This process continues until the peak temperature rise in the flame drops to some specified threshold, here 5K above the initial higher flow temperature. Figure 4.20 illustrates this progression for a single set of incoming flows. Note that the ESR is shown progressing along a log plot, as possible ESR values may exist along several orders of magnitude.

For each strain rate scenario, a new flame profile must be solved numerically. To help in this process, scaling rules may be applied to estimate the necessary changes to improve calculation speed and stability. In this work, scaling rules from

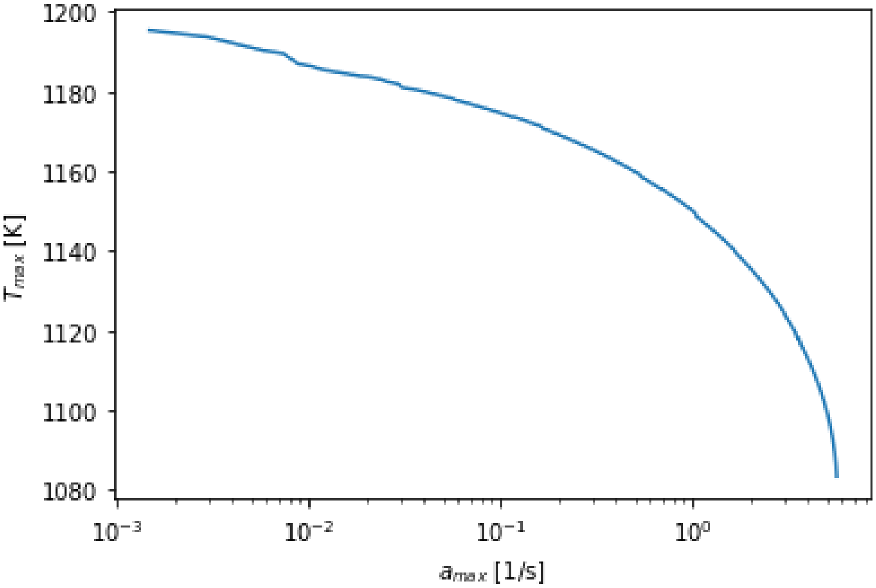

Figure 4.20: Representative ESR calculation progression. Flows are 75% fuel utilization Anode and Cathode composition and temperatures, 1 atm.

Fiala and Sattelmayer were used to calculate the ESR values [126].

As an initial pass, we consider here anode and cathode exhaust flows in their initial proportional amounts and temperature conditions (850°C). The ESR was calculated for anode and cathode exhaust flows at the range of utilizations, and at a variety of pressures (2.3–18.3 atm). Results are shown in Figure 4.21. Immediately we see that the ESR falls with fuel utilization in all cases, up to an order of magnitude at relatively high pressures, such as might be experienced at takeoff. This trend is consistent with the lower concentration of fuel species in the anode exhaust, and subsequent lower temperature rise with combustion reactions.

What *is* interesting is the variation of ESR with pressure. The general trend is toward higher sensitivity to fuel utilization with higher operating pressures, though

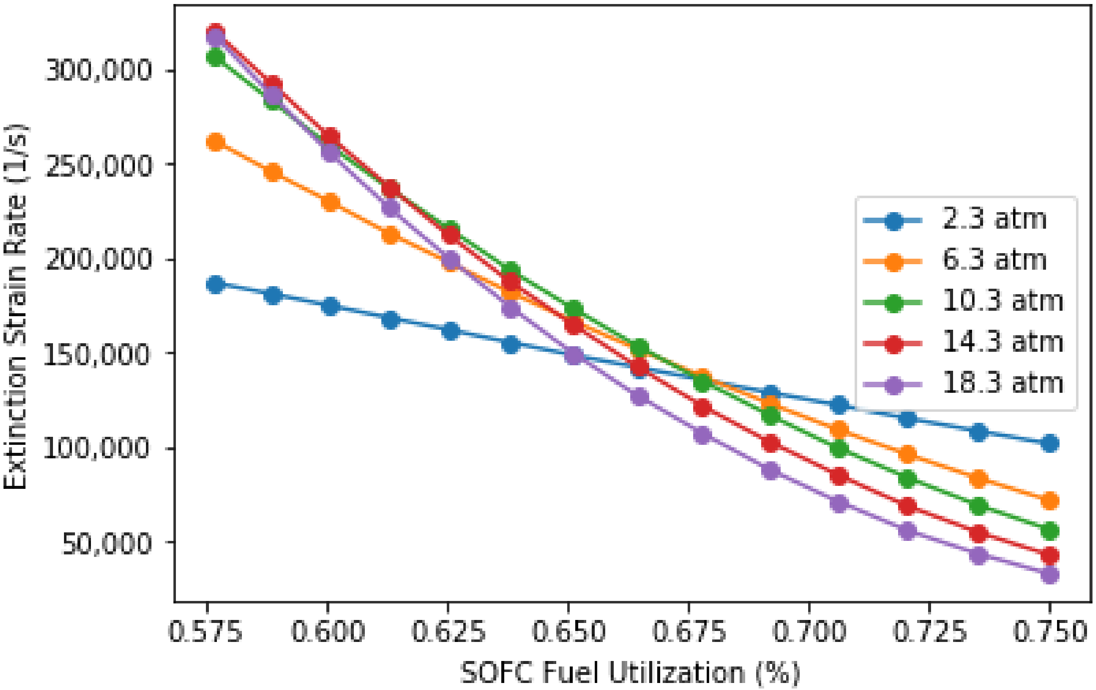

Figure 4.21: Extinction Strain Rate with SOFC Fuel Utilization for Different Pressures.

not necessarily an average change in ESR across the range of utilization. At 65%–67% utilization, the ESR is relatively stable across pressures, serving as a crossover point for the reduction in ESR with increasing fuel utilization. This implies that the design fuel utilization of the SOFC subsystem will have a varying impact on strain-rate effects wherever it may be integrated into the combustor. In this case, an understanding of the different exhaust behavior will need to be accounted for differently depending on the varying ambient conditions over the course of a flight.

4.3 Conclusions and Future Work

In this chapter, we considered that the different fuel and air mixtures expected in a GT/SOFC represented a potential problem—and opportunity—for GT/SOFC combustor design. On mass- and volume-constrained aircraft in particular, combustion must be fast, efficient, and reliable, and is complicated enough to manage for standard fuel and air combinations.

To evaluate the problem, first we set a baseline for the composition and thermodynamic states of the SOFC drawing from prior NPSS GT/SOFC models. We noted immediately that there is very little difference in the intensive properties of SOFC exhaust streams between different flight conditions, so long as the SOFC configuration (e.g. the CPOx reformer, etc.), design exhaust temperature, and fuel utilization are consistent (Figure 4.3). As such, we set the intensive conditions for anode, cathode, and cooling bypass exhaust streams for a range of target utilization targets.

Extensive properties were also investigated in reference to the prior NPSS modeling results for a range of SOFC subsystem sizes parameterized by the electric power fraction, ζ (practically equivalent to varying σ_{FC} per Chapter 2). The resulting system solutions provided the flow rates of each of the combustor inputs. From that information we can note that both the mass flow rates and heating values of the SOFC exhaust streams can be comparable at electric power fractions above approximately 30%, with greater heating values for lower SOFC fuel utilization. At the higher end, the SOFC flows represented up to 70% of the total mass flow and up to 50% of the total net heat release.

We then turned to an initial survey of relevant combustion characteristics. The AFT of the vitiated anode and cathode flows were reduced, though still significant temperatures (up to 2200K) at equivalence ratios near unity. This suggested that hotspots were a possible concern. Underscoring this problem, an IDT analysis suggested that the SOFC exhaust streams would spontaneously combust if mixed at the SOFC operating temperature. However, when three-stream mixtures of anode, bypass, and methane were considered in an IDT analysis, the inclusion of the anode exhaust (including light fuel species of hydrogen gas and carbon monoxide) allowed for spontaneous ignition at lean equivalence ratios. This scenario suggests that the anode exhaust may be useful in ensuring the lightoff or stability of hydrocarbon flames.

An initial survey of LFS performance provided a baseline for future study, with initially lower achieved velocities likely due to the syngas fuel species being highly diluted. However the LFS varied by as much as 500% across the range of exhaust utilizations (58%-75%) suggesting that combustion behavior (such as flashback) may be dependent on SOFC design parameters. Finally, a similarly brief ESR survey showed reducing sensitivity to fuel utilization with increasing pressure, and a wide variation in ESR values with fuel utilization, up to an order of magnitude for pressures above 10 atmospheres for the mixed, hot, anode/cathode flow. The highest values calculated for the ESR were around 300,000s^{-1} at the highest checked pressure (18 atmospheres).

Altogether, we see that the flows created in a GT/SOFC can be widely varied in composition, state, and relative size, and need to be accounted for when designing the combustor.

However, the best means of integrating the different flows (such as the various injection points in Figure 4.22) to avoid problems or enhance performance remains to be determined as one of many avenues for future work. Another avenue is a more rigorous expansion of the possible exhaust composition, temperature, and pressure conditions beyond the ones covered in this chapter. Differences may be especially for varying output temperature and fuel utilization, as well as alternative design strategies such as anode recirculation. In terms of testing, even the metrics showed in this work should receive further attention, such as pressure variation effects in IDT calculations, or the effects of the equivalence ratio on LFS and ESR results. For the LFS in particular, the peak may be broadened by the presence of hydrogen and CO.

The wider range of conditions will also need an expanded analytical capability to include larger hydrocarbons such as traditional jet fuel or injected liquids which

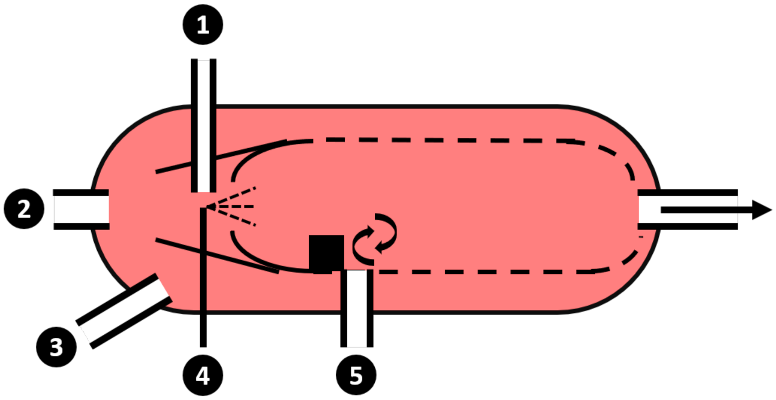

Figure 4.22: Combustor illustration with notional integration points.

need to evaporate. This may be done in part by switching to a reaction mechanism that includes these fuels, though traditional combustion mechanisms for large hydrocarbon fuels typically face many problems. One possible option however is the HyChem mechanism, which is equipped to handle both the decomposition of large hydrocarbon chains such as in jet fuels, as well as the subsequent oxidation reaction kinetics [48].

Chapter 5: Conclusions and Future Work

5.1 Summary and Key Findings

In this dissertation, we've considered the use of a GT/SOFC hybrid propulsion system to reduce fuel burn on aircraft. This represents a shift away from the modern trend of turbofans with increasingly high pressure ratios, which achieve better thermal cycle efficiency at the cost of flow-specific work—amongst other limitations. Prior work has shown that the hybrid cycle including the SOFC within the hot section of a Brayton cycle device can be effective for auxiliary power generation due to a number of synergies within the system. These synergies may improve the performance of the SOFC components sufficiently to counterbalance the increased mass they typically represent. More recently, work has begun to investigate combined power and propulsion schemes, especially in tandem with the increased electrification of aircraft. In this Dissertation, we have set out to address several aspects of the GT/SOFC hybrid system for aircraft, with a particular focus on its use in providing power for propulsion.

First we developed a simplified analytical model to help identify intuitive design parameters and cycle performance trends within the hybrid system. The result is a fast and relatively intuitive model that can provide guidance for system optimization across a wide design space. The main drawback of the model is that the simplicity comes at the cost of static input parameters for SOFC performance. As such, the model may need to iterate with more complex SOFC and GT/SOFC models to account for interactions between the SOFC subsystem performance and the rest of the cycle.

In part to address this issue, we applied and expanded upon previously-developed models in NPSS to model GT/SOFC systems where the electric power generated by the SOFC was used for propulsion. This was examined in two forms, the first being an augmented turbofan engine driven by the hybrid GT, and a second that acted as a airborne powerplant to produce electrical power intended to drive electric-motor fan propulsion schemes. The results matched trends observed in the simple analytical model, and showed improvements in both thermal and propulsive efficiency via an increased bypass ratio. The increased bypass ratio was also mostly achieved by reducing the core flow rate such that the fan was not necessarily becoming overly-large for the aircraft. From a range calculation using steady-state results however showed that while the TSFC always improved with the relative size of the SOFC, the range capability for the aircraft dropped off when the specific power of the SOFC was below approximately $1\text{kW}\,\text{kg}^{-1}$.

Finally, we considered the integration of all the different GT/SOFC flows into the mass- and volume-constrained aircraft combustor. Our initial survey of representative intensive and extensive conditions for the SOFC exhaust flows used an SOFC with a CPOx reformer across a range of relative GT and SOFC scalings. We found that the new flows from the SOFC exhaust could become a significant portion of both the mass flow rates and the heating value going into the combustor. Worryingly, we noted the potential for spontaneous combustion using anode exhaust, and accompanying hotspots. However, at the same time we noted the ability to support ignition of at least simple hydrocarbon fuels (here methane) in mixtures of anode exhaust and air.

5.2 Contributions

For Chapter 2, the idealized GT/SOFC cycle analysis was wholly original work by the author, building initially off of the standard Brayton cycle derivation process.

In Chapter 3, the original NPSS models developed by Daniel Waters [31] were improved by the author for NPSS in numerous ways for stability, performance, and improved capability. A model for an autothermal reformer, as well as the two power-for-propulsion models in this work were also developed by the author.

Finally, in Chapter 4 the author is the first to his knowledge to consider GT/SOFC combustor integration issues specific to an aircraft scenario.

5.3 Future Work

While each chapter has greater detail regarding next steps and future work for their respective subjects, there are some broader directions for future work on GT/SOFC hybrids going forward.

While the precise threshold value will almost certainly depend on the rest of the system configuration, the low specific power of the SOFC remains one of its primary challenges for adoption on aircraft. Future work is recommended to improve SOFC specific power for the transportation context, minimizing mass and volume with constant power output. This is a relatively underinvestigated direction for fuel cells, which are generally designed for maximum efficiency in a ground-based scenario.

For detailed modeling via NPSS, future work is suggested to enable better looping capability for flows. As NPSS operates in a linear fashion, it is not well-suited to multiple characteristics, such as flows with varying compositions, temperatures, and pressures looping into different parts of the system—especially when those components may be slow to execute. This may be addressed in multiple ways, such as combining multiple SOFC components into subsystems that can be solved without the black-box methodology of NPSS, or with fast-iterating performance maps of previously designed SOFC stacks and other components.

Finally, in order to handle the SOFC integration concerns, specific strategies need to be identified and evaluated in order to move forward.

Appendix A: Fundamentals of Gas Turbines[i]

A gas turbine (GT) is an open-cycle heat engine that uses the Brayton heat cycle to convert some source of heat into either torque on a spinning shaft, or kinetic energy of the working fluid through a nozzle, or some combination of the two—depending on the particular application. The most common scenarios use the combustion of a fuel injected into air, which together become the hot-side working fluid of the cycle.

As a device, the gas turbine has five major components, including an inlet, compressor, combustor, turbine, and nozzle, represented in Figure A.1. The function of these components are as follows. Air from the environment enters the inlet to be fed to the compressor. The compressor uses energy to raise the pressure of the air before the flow enters the combustor. In the combustor, heat is added to the flow, usually by burning an added fuel of some kind, while maintaining an approximately constant pressure. The hot gases then enter the turbine, which extracts energy from the flow passing through, which manifests as a drop in pressure. The energy extracted by the turbine is first used to drive the compressor earlier in the cycle, but some portion of the energy added by raising the temperature remains available in

---

[i] This appendix serves as a brief primer on gas turbines drawn from a more complete and elaborate explanation available from Mattingly [71, Ch. 4].

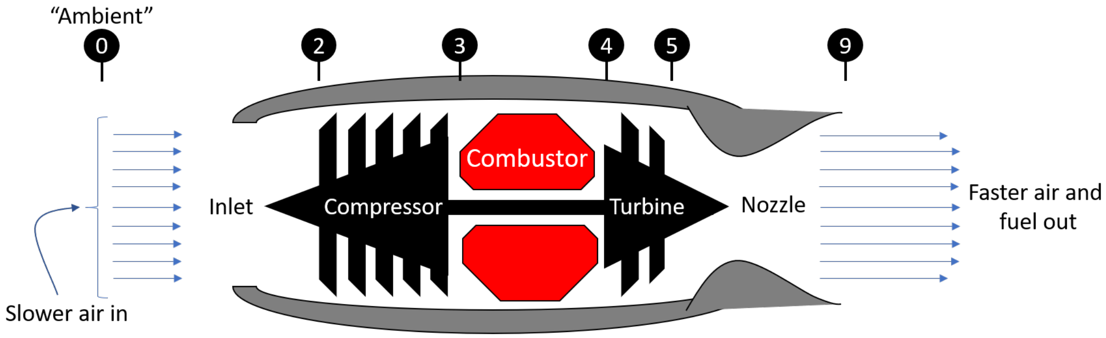

Figure A.1: Simplified Layout of an Axial Gas Turbine as a Turbojet. Includes standard station numbers in black dots.

the remaining heat and pressure of the turbine exhaust relative to the environment. Whichever method applied to make use of the available energy, the gas flow is then released back into the environment, completing the open cycle.

In Figure A.1, that method is the nozzle, which converts the raised temperature and pressure flow energy of the turbine exhaust into kinetic energy (KE) via the nozzle. The change in momentum that the added KE represents is conserved via Newton's second law of motion by changing the momentum of the gas turbine through a force acted upon the nozzle, pushing the engine "forward" as the exhausted gases travel "backwards."

The final application of the remaining useful energy in the flow leaving the turbine classifies Figure A.1 to be a turbojet engine, but an alternative increases the size of the turbine to extract more or all of the difference in pressure between the combustor exhaust and the environment. The extracted energy is transmitted to the spinning shaft of the turbine, which can be applied to a variety of different purposes (see Figure A.2) such as a fan or propeller (a "turbofan" or "turboprop" engine respectively) or some other not-directly-propulsive purpose for the shaft power such as an electrical generator (a “turboshaft” engine).

The underlying physics behind gas turbines is the basic ideal cycle for all heat engines (Equation A.1), which relates the work produced to the heat added $\dot{Q}_{in}$ and rejected $\dot{Q}_{out}$ during the process, in keeping with the conservation of energy. Furthermore, the thermal efficiency of the heat cycle η_T is defined as the proportion of $\dot{W}_{GT}$ to the heat added (Equation A.2).[ii]

$$\dot{W}_{GT} = \dot{Q}_{in} - \dot{Q}_{out} \tag{A.1}$$

$$\eta_T = \frac{\dot{W}_{GT}}{\dot{Q}_{in}} \tag{A.2}$$

The Brayton cycle is a variation of the heat engine that progresses through four processes (with indicators of the associated stations on the turbojet in Figure A.1). These processes can be represented in terms of temperature and entropy (the so-called T-S diagram), plotted here in Figure A.3.

1. Isentropic Compression (0→3)
2. Constant-Pressure Heat Addition (3→4)
3. Isentropic Expansion (4→9)

[ii] In this work we generally follow the convention that for properties whose values may depend on the mass or mass flow rate represented, upper-case letters represent extensive properties while the lower-case equivalent letters represent intensive properties—for example, W_{GT} refers to the net work output of a given gas turbine with some particular mass flow rate $\dot{m}$, while $w_{GT} = W_{GT}/\dot{m}$ refers to the specific net work, i.e. the work output per unit of mass flow through the gas turbine.

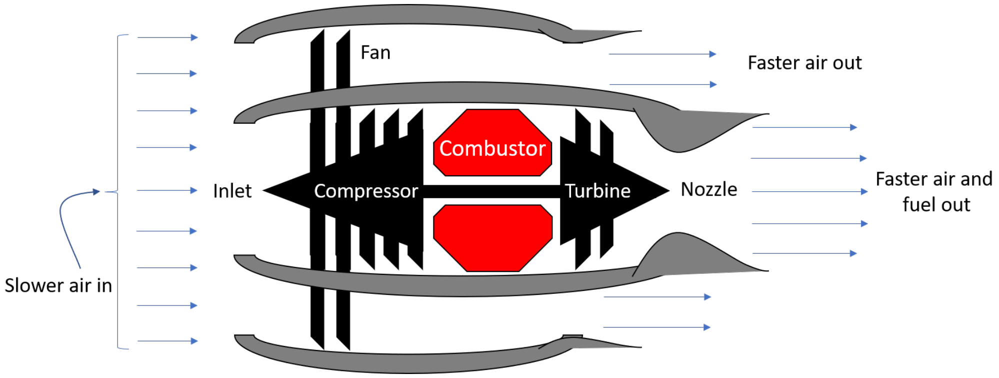

(a) Representation of Turbofan Engine

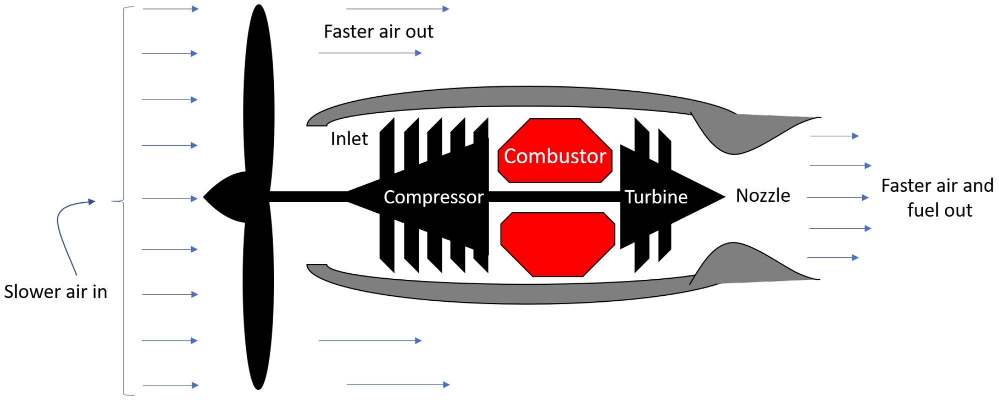

(b) Representation of Turboprop Engine

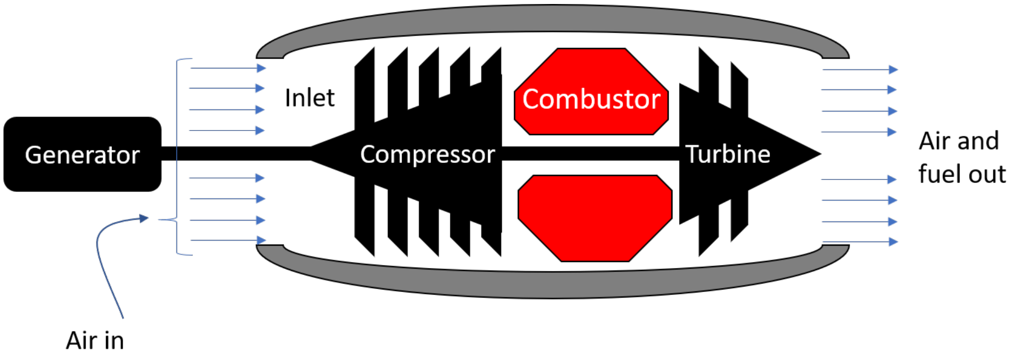

(c) Representation of Turboshaft Engine

Figure A.2: Different Varieties of Gas Turbine Engines.

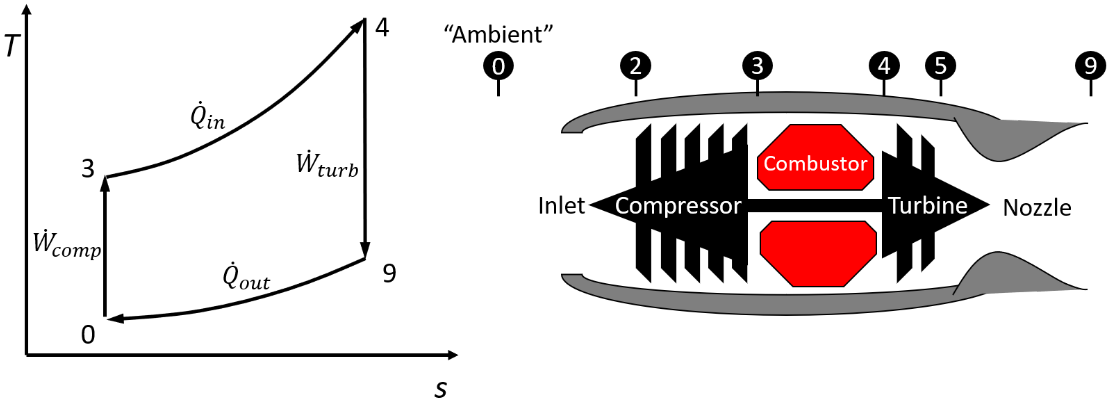

Figure A.3: Temperature-Entropy (T-S) Diagram Representation of Brayton Cycle. GT diagram with station numbers included for reference

4. Constant-Pressure Heat Rejection (9→0)

For the Brayton cycle, heat is added and rejected at constant pressure such that if we assume a calorically perfect gas, that heat is equivalent to a change in temperature between different stations in the cycle, multiplied by the mass flow rate through the system and the now-constant specific heat at constant pressure c_p. The result is Equation A.3.[iii]

$$\dot{W}_{GT} = \dot{m}c_p(T_4 - T_3) - \dot{m}c_p(T_9 - T_{amb}) \tag{A.3}$$

We should note that under the same assumptions this is an equivalent statement to finding the net work generated by the Brayton cycle in terms of the difference between the work generated by the turbine $\dot{W}_{turb}$ and the work consumed by the compressor $\dot{W}_{comp}$.[iv]

[iii] Note that we may use the subscript "amb" for the ambient conditions of station zero, to avoid confusion with the total conditions of a flow that often use a subscripted zero as well.

$$\dot{W}_{GT} = \dot{W}_{turb} - \dot{W}_{comp} \rightarrow \dot{W}_{GT} = \dot{m}c_p(T_4 - T_9) - \dot{m}c_p(T_3 - T_{amb}) \tag{A.4}$$

Recalling the isentropic relationships between temperatures T and pressures P, such that $(P_a/P_b)^{(\gamma-1)/\gamma} = T_a/T_b$ (where γ is the ratio of the specific heat at constant pressure to the specific heat at constant volume, approximately 1.4 for air) for the isentropic compression and expansion processes, and the fact that (ideally) the ratio of high- and low-pressures PR are equal for both of those processes (i.e. $PR = P_3/P_{amb} = P_4/P_9$), we can derive that the ideal thermal efficiency of the Brayton cycle is related specifically to PR (Equation A.5).

$$\eta_T = 1 - \left(\frac{1}{PR}\right)^{(\gamma-1)/\gamma} \tag{A.5}$$

As such, we can see that higher pressure ratios (usually achievable with larger, heavier, and more expensive compressors and turbines) yield higher efficiency operation, which (for the same ambient conditions) implies higher compressor exit temperatures T_3. It may be shown also that the maximum amount of work per unit of mass flow through the GT (an important sizing factor) is achieved when $T_3/T_{amb} = \sqrt{T_4/T_{amb}}$.

Since the main practical constraint on gas turbines is the material limitations on the turbine inlet temperature (TIT) at T_4 (to avoid melting the engine entirely)

[iv] For the purposes of simplifying this description, presume that this is a turboshaft as in Figure A.2c such that all available work is extracted by the turbine rather than a combined turbine/nozzle stage with power potentially extracted two ways.

and the available ambient temperature T_{amb}, the implication is that not only is there a maximum cap on efficiency ($T_3 = T_4$) at any given moment, but after a certain optimal point, increasing efficiency comes at the cost of specific work.

Appendix B: Fuel Cell Fundamentals[i]

B.1 Basic Description

Fuel cells are a class of energy conversion devices like heat engines, generating some form of power from the chemical potential energy stored in a fuel material. Like batteries but unlike heat engines, fuel cells extract electrical power directly from fuel and oxidant materials that indirectly participate in a chemical reduction-oxidation ("redox") reaction. The redox reaction is distinguished by a transfer of electrons (or at least a change in formal oxidation state) between reactants.

In a redox reaction, the reactant(s) losing electrons (adding to the oxidation charge since electrons are negatively charged) are said to be oxidized, while the reactant(s) gaining electrons (losing oxidation charge) are said to be reduced.[ii] We can consider the loss and gain through so-called "half-reactions" of oxidation (Equation B.1) and reduction (Equation B.2).

$$H_2 + \frac{1}{2}O_2^{2-} \rightarrow H_2O + 2e^- \tag{B.1}$$

---

[i] The material in this section is largely drawn from a more extensive description available from Li [24, Ch. 1,9].

$$\frac{1}{2}O_2 + 2e^- \rightarrow \frac{1}{2}O_2^{2-} \tag{B.2}$$

A simple diagram of a fuel cell is provided in Figure B.1. The fuel cell enables reduction and oxidation half-reactions to occur on two separate "electrodes" which are conductive to reactants, electrons, and ions all at once. The necessary electrons for both half-reactions are accounted for by transferring the electrons oxidized from one electrode (the "anode") to the other (the "cathode") through a wire with some kind of electrical load in between, driven by the chemical potential difference between the two reactions. At the same time, the overall charge is conserved by also passing (i.e. "conducting") some ionized species between the anode and cathode through an electrically-insulating "electrolyte" layer separating the two. Collectively, these three layers are called the membrane electrode assembly, or MEA.

The ion species passed across the electrolyte depends on the fuel cell design and reactions, but can be positive such as a proton in a proton exchange membrane fuel cell (PEMFC) or negative such as an oxygen ion in a solid-oxide fuel cell (SOFC). Equations B.1 and B.2, as well as Figure B.1 are written to presume an oxygen ion species passing through the electrolyte, appropriate for the SOFC focused upon in the rest of this work.

When two balanced half-reactions are combined, we have a full redox reaction with reactants and products with no generation of free electrons—such as may be

---

[ii] The confusing gaining-electrons-is-reduction is due to the historical convention (since Ben Franklin!) of arbitrarily assigning a negative charge to the electron. The convention is too entrenched to change easily even if it would line up the concepts of charge and electrons. However to manage as best we can, the useful mnemonic for reduction and oxidation is "LEO the lion goes GER", for "Loss of Electrons is Oxidation, Gain of Electrons is Reduction"

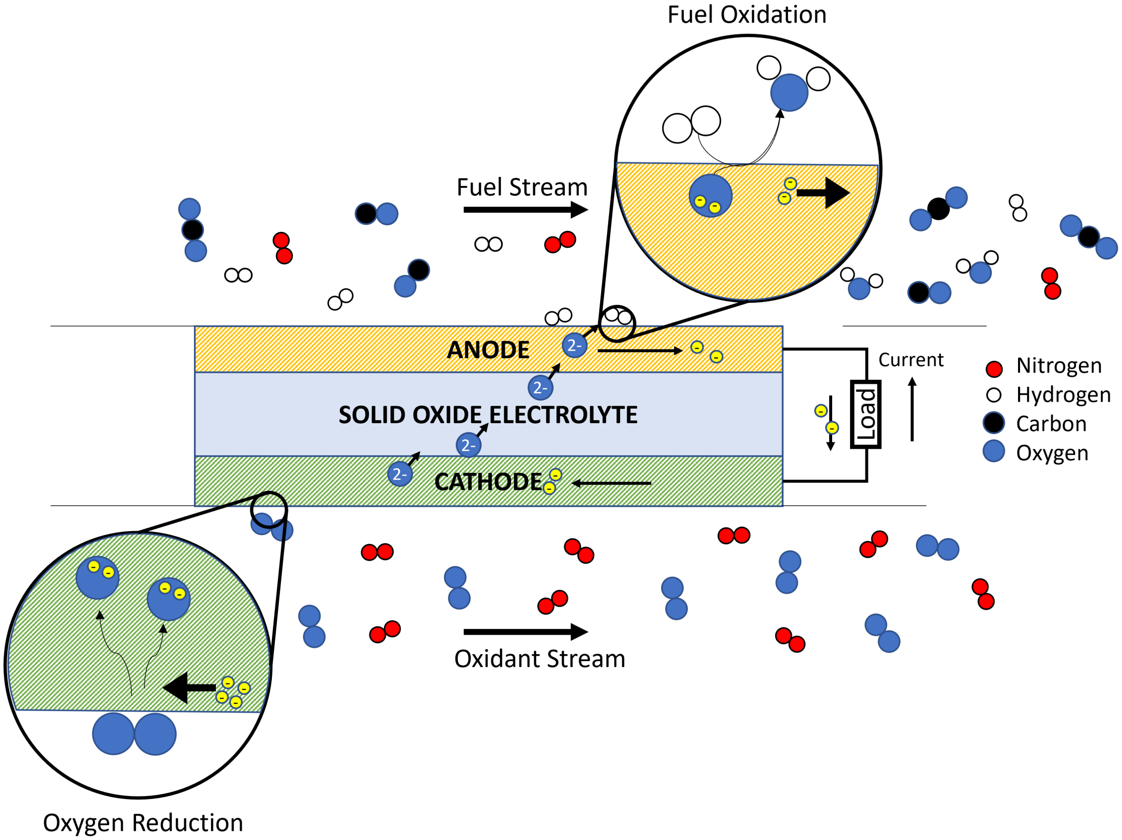

Figure B.1: Basic Schematic of a Fuel Cell (based on an SOFC).

observed if the reactants were processed in a single location, though the electron transfer still occurs (Equation B.3). A heat engine may in fact use the same fundamental chemical reaction as a fuel cell as the source of energy (released in the single combustor location), in which case the electron transfer occurs at the level of the particle rather than through a wire, releasing the energy instead wholly as heat, i.e. kinetic energy of the resulting particle(s).

$$\frac{1}{2}O_2 + H_2 \rightarrow H_2O \tag{B.3}$$

However, in contrast with batteries but similar to heat engines like gas turbines, fuel cells are a power generation device only, and do not have any inherent energy storage, e.g. reactants held within the anode and cathode materials as is often done with batteries. As such, fuel cells are reliant on some kind of external source (storage tanks, the external environment, etc.) and separate flow manifolds and channels to provide streams of fuel and oxidant[iii] to the anode and cathode respectively.

B.2 Solid Oxide Fuel Cells

An SOFC is a subtype of fuel cell that is characterized first by its electrolyte, which is made of a rock-like ceramic oxide material. At sufficiently high temperatures (approximately 550-1000Celsius), the oxygen ions held inside the electrolyte begin to move freely by shuffling between vacancies within the internal structure of

---

[iii] An "oxidant" here is a material that causes the oxidation of some other reactant; the oxidant itself is usually reduced (i.e. it gains electrons) to achieve that effect.

the oxide while the bulk material remains an electrical insulator.

The high operating temperature of the SOFC has several associated impacts; first, the catalyst material that is often used at electrode surfaces to enhance the rates of reaction can be nickel rather than more expensive options like platinum. Second, the catalyst is less susceptible to being poisoned[iv] by any carbon monoxide (CO) in the fuel flow.

[iv] "Poisoned" in this case refers to the loss of chemically-reactive locations on the anode surfaces, due to the binding of carbon monoxide to the surface. At lower (non-SOFC) temperatures and with platinum catalysts, the carbon monoxide forms stronger bonds at the surface sites than hydrogen, and requires a higher potential to oxidize than hydrogen. As such, so long as hydrogen is present, the hydrogen will be oxidized first and more quickly such that any carbon monoxide present will remain at the sites and accumulate, degrading the rate of reactions on the anode surface as CO surface coverage increases [24, p. 408].

Appendix C: Energy Storage and Power Generation

Put another way, the overall motivating problem is one of the energy storage and power generation (ESPG), just specifically for the aircraft application. Taken in the abstract, “energy storage” refers to the total amount of energy that must be carried by the aircraft, in whatever form that may take, which will be sufficient to carry out its mission. “Power generation” refers to the means by which the stored energy is actually employed by the aircraft (both for propulsion and for any other secondary load as the mission demands) as power provided at some needed rate. Different conversion systems may be able to use more or less of the stored energy (as well as produce different kinds and amounts of emissions) to achieve the same level of power generation, which we usually call the “efficiency” of the conversion system.

As a concrete example, we can consider a modern airliner as depicted in Figure C.1: The mass of jet fuel m_f is the energy storage, while the jet engine is the power generation system. The jet engine that burns jet fuel at a certain rate $\dot{m}_f$ to produce a certain amount of thrust power P_{thrust} in flight to balance against the drag on the aircraft $\dot{m}_f$ (for steady flight) that is created by the airplane body moving at a certain flight speed U, with the efficiency η_{over} representing the proportional

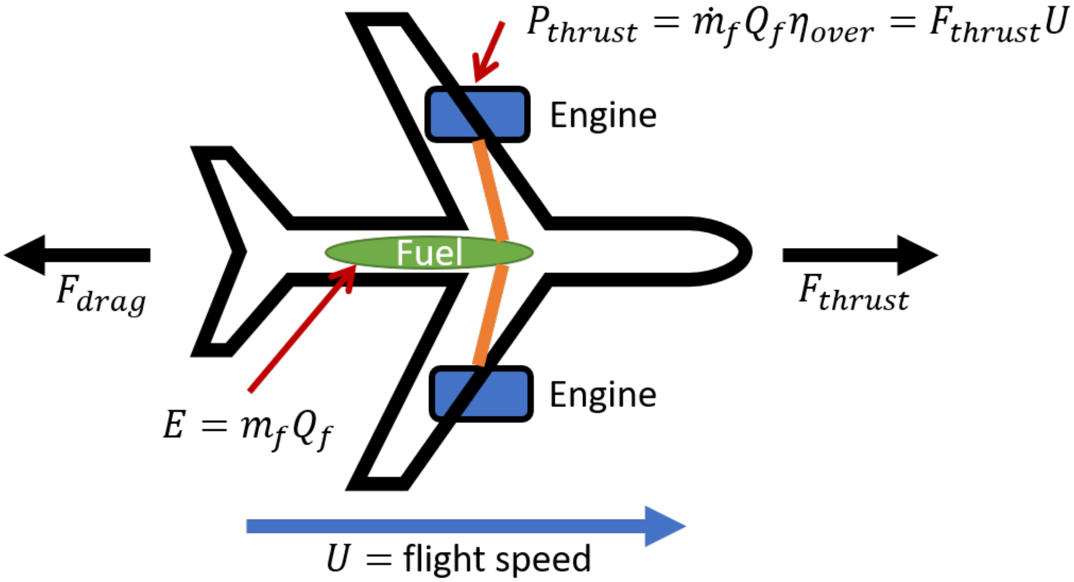

Figure C.1: Basic Energy Storage and Power Generation Relationships on Aircraft.

difference between the chemical potential energy from burning the jet fuel in the air per unit mass Q_f and the thrust force F_{thrust} exerted on the aircraft times its flight speed.

Conversion efficiency can be described in different ways depending on the end use, starting with a fundamental thermodynamic efficiency just illustrated, which relates the total useful energy provided by the power generation system, normalized by the total energy stored. As an alternative example for fuel-driven aircraft it can also be provided in the rate of fuel consumption $\dot{m}_f$ normalized by the force ("thrust") generated by the engine F_{thrust}, also known as the thrust-specific fuel consumption (TSFC).[i]Similarly, the energy storage performance can be measured by the specific energy (and energy density when volume is important) of the fuel,

. Finally, we can take the power generation system mass and volume into account as well through the specific power and power density—i.e. the power produced, normalized by the mass and volume of the generating system respectively.

This may all seem unnecessarily abstracted from the concept of an engine with a fuel tank, but it is helpful in ensuring apples-to-apples comparisons are made when considering vastly different ESPG architectures. As an example for producing aircraft thrust, contrast a hydrocarbon-fuel turbojet along with a battery-motor-fan setup. In the first case, the liquid jet fuel is the energy storage medium, with conversion of the chemical potential energy of the fuel with (free) environmental air into heat, which is applied in the Brayton thermodynamic cycle of the turbojet. The useful work that comes out of the Brayton cycle at some resulting efficiency is converted into a change in the momentum of the airflow leaving the turbine directly through a nozzle (see Figure C.2).

In the second case, the energy storage fundamentally comes from the chemical potential energy present between the anode and cathode materials contained within the battery, most commonly using some kind of reaction involving Lithium. The rest of the battery components (electrolyte, current collector, protective circuits, housings, etc.) and design dictate how quickly and efficiently the potential energy is converted to electricity. Afterwards, the electricity is used by an electric motor to drive a fan which changes the momentum of airflow passing through it (see Figure C.3).

---

[i] The TSFC is also an example of an incomplete metric for ESPG performance, since it ignores the variation in thrust required to account for changes in aircraft mass if the engine mass—the conversion system itself—changes.

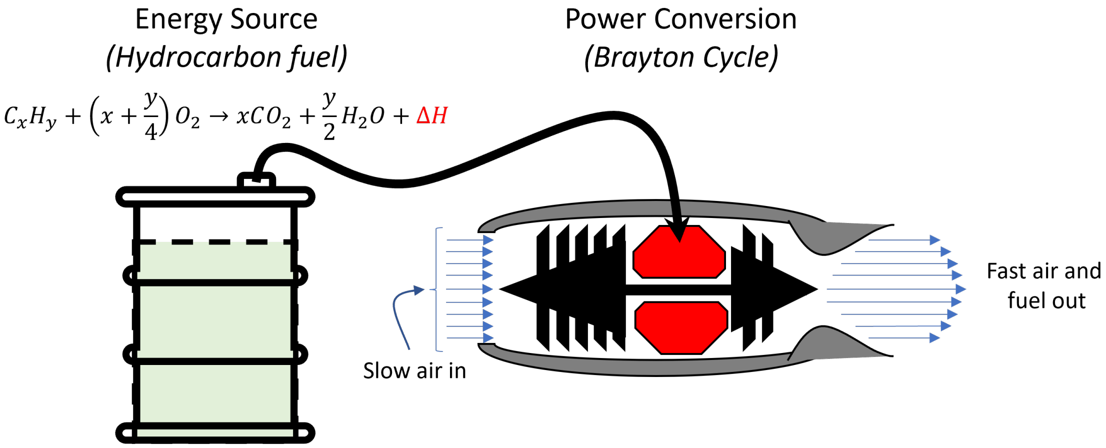

Figure C.2: Basic Fuel-Turbojet ESPG Representation of Major Components.

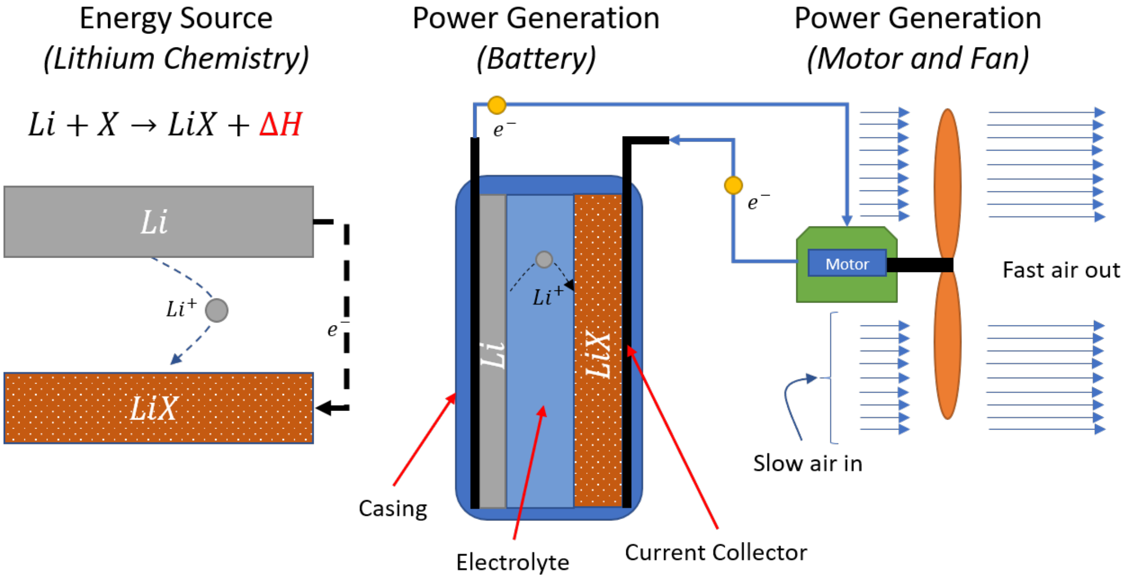

Figure C.3: Basic Battery-Fan ESPG Representation of Major Components.

In both of these examples, there are actually very similar fundamental forms of energy storage (i.e. accessing chemical potential energy from a chemical reaction using an amount of material) and different layers of conversion. For the turbojet, conversion takes place through a heat cycle to produce torque to drive a gas through a nozzle to exhaust at high speed. For the battery-fan, conversion begins in the battery where all of the components exist to constrain the chemical reaction into an electrical circuit by separating the movement of atoms and electrons in the reaction. The electricity is then converted into a change in momentum of air by converting the electricity to torque on a shaft driving a fan via an electric motor.

The problem in making appropriate apples-to-apples comparisons can occur since in practice one is tempted to treat batteries as energy storage similarly to fuel; i.e. I need X number of batteries to have enough energy to fly Y mission—even though this ignores all of the battery design choices that may impact the availability of the fuel energy, and distorts the specific energy value by “miscounting” the non-reactive battery components.[ii]

Beyond making appropriate comparisons, keeping in mind the concept of an ESPG can be helpful in scenarios (such as in this work) where it might otherwise be difficult to evaluate overall system performance from the individual components in hybridized systems with multiple storage or conversion mechanisms that inter-operate. While the different component capabilities can of course be discussed, and remain important, they may or may not directly impact the ESPG performance in

---

[ii] To be fair, fuel-based ESPGs too have gray-areas as well, such as the fuel storage tank and plumbing that normally require corrections to an effective specific power that can change at different size scales.

the same intuitive manner as, say, compressor efficiency as a simple multiplier on the Brayton cycle thermodynamic efficiency.

Furthermore, for many ESPG systems the scale of the overall system or individual components can have an effect on performance; for example, internal combustion engines tend to become less efficient and generate less specific power at smaller scales, for a variety of reasons including construction tolerances, incomplete combustion, and increasing heat losses via the square-cube law [16].

One solution to account for each of these concerns is to ensure that we are accounting for the entire ESPG system when comparing performance for different system architectures that might be used. One means of doing so is with a Ragone plot.

Ragone plots compare the specific power and specific energy of *the whole* ESPG (*not* the metrics of storage and conversion individually), with different technologies carving out particular curves or areas of capability depending on the relative scaling of the energy storage and power generation component characteristics. In cases such as those we will consider with multiple storage and conversion sources (or with the variation of other design characteristics), we can generate area-swaths on the plot corresponding to different relative scalings of energy storage and power conversion.

If we look at a toy example Ragone plot in Figure C.4, we can see at the extreme edges along the y-axis you have scenarios where energy storage dominates, generally representing a case where the ESPG is almost wholly fuel (moderated by the mass of fuel containment and conversion efficiency) with a vanishingly small conversion system by comparison. Along the x-axis are scenarios where the conversion

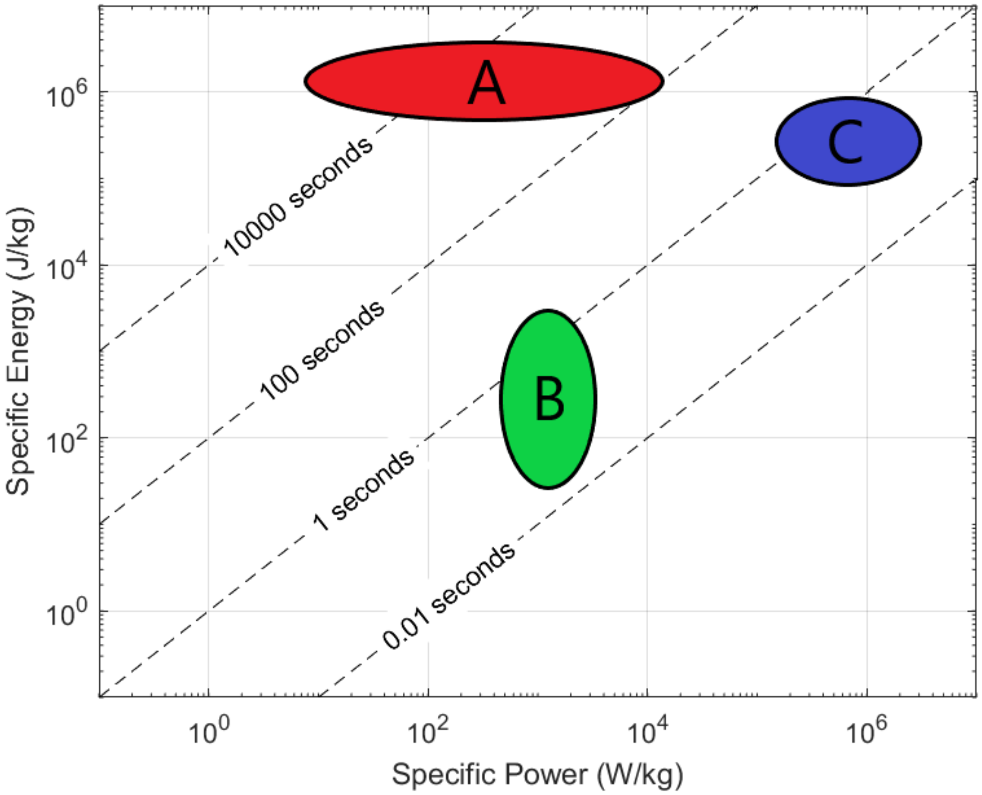

Figure C.4: Example of a Ragone Plot for Three Arbitrary ESPG Architectures A, B, and C.

system dominates, large amounts of power are generated for very short durations. The optimal locations for any ESPG will depend on the mission at hand (also setting an absolute scaling of the ESPG), but generally speaking greater specific power and specific energy values are better. Additionally, when both axes are plotted on a logarithmic scale, straight lines of operational endurance (i.e. the duration over which the ESPG will provide power) can be drawn. For missions with a target endurance, this can provide a direct comparison between two ESPGs, with the (theoretically) superior system existing further along the line of constant endurance.

In practice, Ragone plots or any other discussion involving ESPG components can be easily distorted or misunderstood by underlying assumptions for the specific scenario, or by varying accounting for the performance or inclusion of different components one might consider. Power and energy performance metrics may be conflated even in archival literature (see Figure 1 of [127]), plotting the energy density and specific energy of different fuel cell types along with batteries without any scaling context. For example, a Ragone plot including both a battery and a natural-gas turboshaft *should* include either the mass of an electrical generator on the turboshaft, or an electric motor attached to the battery (and in both cases, likely some electrical power conversion equipment), with the choice depending on whether the Ragone plot is meant to represent an electrical or shaft power output.

Overall, we can use Ragone plots to establish the different capabilities of ESPG systems, but great care must be taken to make sure that the values used on the plot for different ESPG architectures represent the same scenario in terms of output type, scale, and any other factors important for the application at hand that can help constrain the scenario.

Appendix D: Custom NPSS Component/Solver Modifications

D.1 Solid Oxide Fuel Cell

D.1.1 Additional Modes

As part of the author's work, additional operating modes have been added to the SOFC model. Since in general the SOFC model is computationally expensive, "Simplified" and button cell modes have been added for better design and performance estimation and evaluation, especially for comparison to analytical results per Chapter 2. In the Simplified mode, the SOFC uses static efficiency and utilization values that are set rather than calculated from a particular reformer/stack design and MEA parameters. This is very useful for finding reasonable initial conditions for the rest of the integrated system since the more physically-determined "Standard" SOFC model mode requires substantial runtime. As such, in most cases this simplified mode is used with the rest of the GT/SOFC to reach an initial convergence, then re-run in the full physics-based mode to ensure that we are close to a reasonable solution.

The "button cell" mode eliminates the effects of concentration and temperature gradients in the anode and cathode flows. It does this within the existing

SOFC model by increasing anode/cathode flow rates and active areas such that the composition and temperature in the anode and cathode flow passages are spatially uniform. This mode is useful for testing and establishing the parameters and performance maps of any given electrochemical model, such as the results provided in Figures 3.15 and 3.16.

D.1.2 SOFC Model Solver Stability

One of the main efforts in this work has been to improve the stability of the SOFC model for wider ranges of problems. As originally implemented, the SOFC model could easily yield non-physical results during the normal solver process for a wide array of possible causes. Some examples include division by zero errors if one or another fuel species was missing entirely (such as by a CEA rounding error), or if too much oxygen is transferred in a single segment.

Additionally, high or low operating temperatures increase or decrease the SOFC current density respectively for a particular operating voltage. Both of these scenarios are reinforcing cycles since the heat release inside the SOFC is what maintains the SOFC's operating temperature. Very rapidly, the SOFC electrochemistry solver can overshoot any safe operating temperature of the SOFC. out-of-bound temperature operation. For all of these types of problems, "guardrails" have been put up to prevent runaway scenarios or divide-by-zero errors.

Internally to the component, there were many instances where the internal Newton-solver used to find a solution could oscillate around a solution, getting caught in a loop. Each step would overshoot a converged solution of temperature and current density. This occurs because of the high sensitivity that current density and temperature have on each other within the SOFC segment. Altering the step size used to determine the first-derivative did not consistently improve a scenario. As such, a Newton-solver damping scheme was implemented to ensure that each iterative step would become closer to a converged value. In addition, should convergence of temperature and current density within an SOFC channel segment take more than a set number of iteration, the solver will switch to using a central difference scheme rather than a first-order forward difference scheme for calculating first derivatives.

D.1.2.1 Electrochemical Performance Maps

As part of the NPSS model development process, the electrochemical model tends to be slow and unstable to calculate and converge. This is especially true for the aircraft GT/SOFC scenario due to (1) the larger hybrid model featuring an SOFC stack with recirculation, and (2) greater variation in conditions over the course of operation than ground-based SOFC systems. One solution to this problem is to calculate the electrochemical performance ahead of time.

In this case, we have generated maps of the electrochemical performance of the SOFC MEA at the range of conditions that might be expected for the GT/SOFC, allowing for varying levels of reformation and recirculation (though not direct steam injection). For a particular fuel and MEA material arrangement (e.g. JP-5 with Ni-

YSZ/YSZ/LSM as in this work), we can find the MEA current density as a function of six variables:

- Temperature
- Pressure
- Utilization
- Mass Ratio of Nitrogen to Oxygen in the Anode flow (decreasing as anode flow is utilized)
- Mass Ratio of Oxygen to Nitrogen in the Cathode flow (decreasing as cathode flow is utilized)
- Operating Voltage (may also switch as input/output with current density)

The assumptions of the map are that the temperatures and pressures in the anode and cathode are close to matching, and that equilibrium is approached at all times. As such, for a given fuel and MEA material, the six variables above should be able to specify all possible conditions that the MEA will experience. Additional factors of stack design and heat transfer specific to different SOFC systems are handled externally to this performance map, which is a useful feature for generalizing the use of these maps.

The MEA performance maps are created using the MapGenerator functions built into NPSS; as such they should integrate directly with any future NPSS modeling seamlessly. The MapGenerator iterates over a range of values given for each of the six variables as inputs to the "button cell" mode of our SOFC model unit test, which removes pressure-loss and energy-balance (i.e. heating) from the calculation.

Once generated for a particular fuel, the MEA performance map is currently best used to provide an initial estimate of the current density for a given voltage, or vice versa, for the electrochemical solver at each segment of the MEA. The only current difficulty is the large size of the map at any resolution above 3-5 delineations per input variable. Since the map size scales to the power of the number of variables, a map with 5 steps per variable represents over 15,000 points. At sufficient resolution however will allow the electrochemical calculation to be removed from the model entirely, reducing computational cost further. However, it should be noted that this does not elminate many of the iterative solver loops that are involved in the design of the entire SOFC *stack*. Unfortunately the overall model has many more unspecified design variables, though stack performance maps do exist for set designs or empirical devices [108].

D.2 Catalytic Partial Oxidation Reactor

D.2.1 Alternative Fuel/Reformation Capabilities

As part of this work, the fuel and fuel-reformation capabilities of the CPOx model have been expanded. First, data has been tabulated for methane (CH_4) to be used as a fuel instead of JP-5 in prior work. This new tabulation was created using the NASA CEA coefficients to solve for the minimum AFR before coking (C(gr) formation above 0.00001 mole fraction) using the Cantera chemical thermodynamics and kinetics toolbox [123].

In addition, the tabulation was expanded to include a third “oxygen boost” parameter to account for increased oxygen content that may be present if anode exhaust is recirculated. This is a likely form for aircraft ATR systems, which generally avoid direct steam injection because of the substantial additional weight of the necessary water. Exhaust recirculation instead returns a portion of SOFC anode exhaust to the reformer, which carries steam as part of the combustion products generated inside the SOFC. The anode exhaust contains fuel and air species in their original ratios, as well as additional oxygen that was transferred across the SOFC electrolyte from the cathode flow.

When the anode exhaust is injected into the reaction zone along with the new fuel and air, the resulting elemental composition is the same as an AFR value, with the addition of some proportion of oxygen. The added oxygen can be parameterized as a relative boost to the amount of oxygen added with the air which will drive up the air-equivalent, depending on how much air is recycled.

D.2.2 Bypass Heating

As an update for this work, the bypass exhaust temperature is updated after each segment to inform the heat transfer calculation of subsequent segments. This improves the accuracy in scenarios where the temperature rise in the bypass is significant over the course of the CPOx.

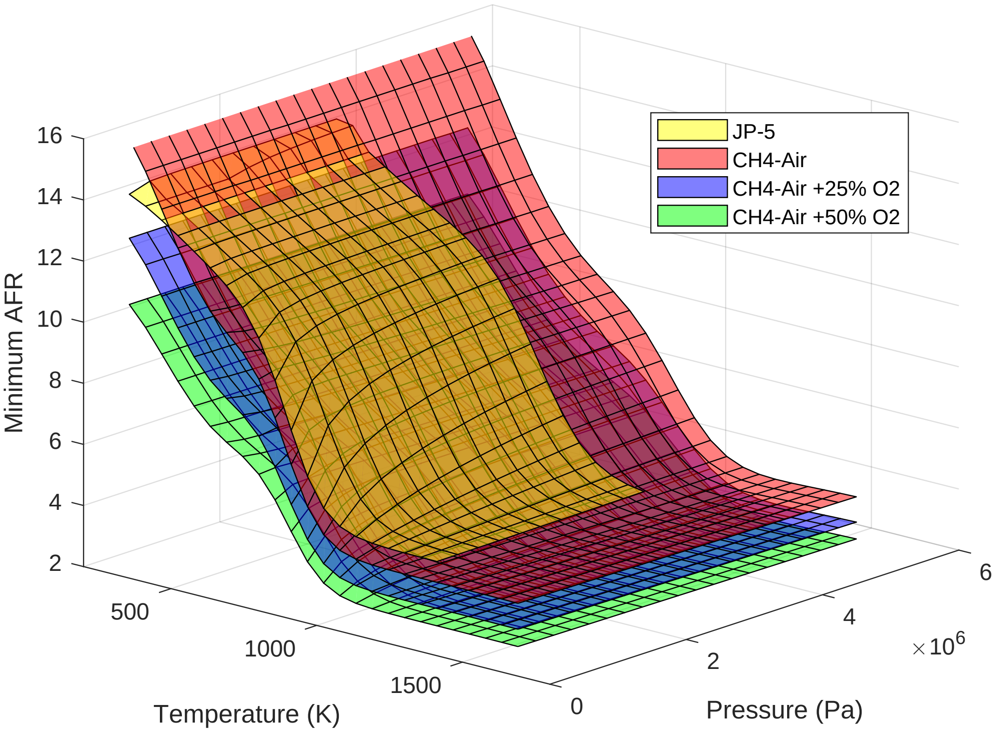

Figure D.1: Minimum Air-Fuel Ratio Mappings for Methane and JP-5.

Bibliography

[1] National Academy of Sciences. *Commercial Aircraft Propulsion and Energy Systems Research*. National Academies Press, Washington, D.C., 2016.

[2] Alan H. Epstein. Aeropropulsion for commercial aviation in the twenty-first century and research directions needed. *AIAA Journal*, 52(5):901–911, 2014.

[3] Alan H. Epstein and Steven M. O'Flarity. Considerations for Reducing Aviation's CO2 with Aircraft Electric Propulsion. *Journal of Propulsion and Power*, 35(3):572–582, may 2019.

[4] John Holladay, Zia Abdullah, and Joshua Heyne. Sustainable Aviation Fuel: Review of Technical Pathways. Technical report, US Department of Energy, Washington, D.C., sep 2020.

[5] Industry Statistics - Fact Sheet. Technical Report December, International Air Transportation Association, 2019.

[6] David S. Lee, David W. Fahey, Piers M. Forster, Peter J. Newton, Ron C.N. Wit, Ling L. Lim, Bethan Owen, and Robert Sausen. Aviation and global climate change in the 21st century. *Atmospheric Environment*, 43(22-23):3520–3537, jul 2009.

[7] Inventory of U.S. greenhouse gas emissions and sinks: 1990-2018. Technical report, United States Environmental Protection Agency, 2020.

[8] Valerie J. Lyons. Aerospace power technology for potential terrestrial applications. In *2012 IEEE Energytech*, number November, pages 1–5. IEEE, may 2012.

[9] Office of Transportation and Air Quality. U.S. Transportation Sector Greenhouse Gas Emissions, 1990-2018. Technical report, U.S. Environmental Protection Agency, jun 2021.

[10] International Civil Aviation Organization Council. Consolidated statement of continuing ICAO policies and practices related to environmental protection – Global Market-based Measure (MBM) scheme, oct 2016.

[11] Stacy Davis and Robert Boundy. Transportation Energy Data Book: Edition 39. Technical report, Oak Ridge National Laboratory (ORNL), Oak Ridge, TN (United States), feb 2021.

[12] Ralph Sims, Roberto Schaeffer, Felix Creutzig, Xochitl Cruz-Núñez, Marcio D'Agosto, Delia Dimitriu, Maria Josefina Figueroa Meza, Lew Fulton, Shigeki Kobayashi, Oliver Lah, Alan McKinnon, Peter Newman, Minggao Ouyang, James Jay Schauer, Daniel Sperling, and Geetam Tiwari. Transport. In Ottmar Edenhofer, Ramón Pichs-Madruga, Youba Sokona, Ellie Farahani, Susanne Kadner, Kristin Seyboth, Anna Adler, Ina Baum, Steffen Brunner, Patrick Eickemeier, Benjamin Kriemann, Jussi Savolainen, Steffen Schlömer, Christoph von Stechow, Timm Zwickel, and Jan C. Minx, editors, *Climate Change 2014: Mitigation of Climate Change. Contribution of Working Group III to the Fifth Assessment Report of the Intergovern- mental Panel on Climate Change*, chapter 8, pages 599–670. Cambridge University Press, Cambridge, United Kingdom and New York, NY, USA, 2014.

[13] Adam J Head. Performance Trends of High-Bypass Civil Turbofans. Technical report, Delft University of Technology, 2015.

[14] International Civil Aviation Organization. ICAO Environmental Report 2016. Technical report, United Nations, nov 2016.

[15] S. Menon and Christopher P. Cadou. Scaling of Miniature Piston-Engine Performance, Part 1: Overall Engine Performance. *Journal of Propulsion and Power*, 29(4):774–787, 2013.

[16] S. Menon and Christopher P. Cadou. Scaling of Miniature Piston Engine Performance Part 2: Energy Losses. *Journal of Propulsion and Power*, 29(4):788–799, jul 2013.

[17] Lucas M. Pratt. *Gas Turbine / Solid Oxide Fuel Cell Hybrids: Investigation of Aerodynamic Challenges and Progress Towards a Bench-Scale Demonstrator*. Master's thesis, University of Maryland, College Park, 2019.

[18] Rolls-Royce. *Turbines.* John Wiley & Sons, 5th edition, 2015.

[19] V Madonna, Student Member, P Giangrande, and M Galea. Electrical Power Generation in Aircraft : review , challenges and opportunities. (May), 2018.

[20] J. A. Rosero, J. A. Ortega, E. Aldabas, and L. Romeral. Moving towards a more electric aircraft. *IEEE Aerospace and Electronic Systems Magazine*, 22(3):3–9, 2007.

[21] Scott W Ashcraft, Andres S Padron, Kyle a Pascioni, Gary W Stout Jr., and Dennis L Huff. Review of Propulsion Technologies for N+3 Subsonic Vehicle Concepts. Technical Report October, 2011.

[22] Arun K. Sehra and Woodrow Whitlow. Propulsion and power for 21st century aviation. *Progress in Aerospace Sciences*, 40(4-5):199–235, may 2004.

[23] Marty K Bradley and Christopher K Droney. Subsonic Ultra Green Aircraft Research Phase II: N+4 Advanced Concept Development. Technical Report NASA CR-2012-217556, NASA, 2012.

[24] Xianguo Li. *Principles of Fuel Cells*. Taylor & Francis, New York, 1st edition, 2006.

[25] F. Yin and A. Gangoli Rao. Performance analysis of an aero engine with inter-stage turbine burner. *The Aeronautical Journal*, 121(1245):1605–1626, nov 2017.

[26] Thomas H Bradley, Blake a Moffitt, Thomas F Fuller, Dimitri Mavris, and David E Parekh. Design Studies for Hydrogen Fuel Cell Powered Unmanned Aerial Vehicles. pages 1–16, 2006.

[27] Moritz Henke, Caroline Willich, Christina Westner, Florian Leucht, Robert Leibinger, Josef Kallo, and K. Andreas Friedrich. Effect of pressure variation on power density and efficiency of solid oxide fuel cells. *Electrochimica Acta*, 66:158–163, apr 2012.

[28] Venkata Adithya Chakravarthula, Rory A. Roberts, and Mitch Wolff. Dynamic Model of Solid Oxide Fuel Cell Integrated with Fan and Exhaust Nozzle. In *14th International Energy Conversion Engineering Conference*, pages 1–14, Reston, Virginia, jul 2016. American Institute of Aeronautics and Astronautics.

[29] Daniel F Waters, Lucas M Pratt, and Christopher P Cadou. Gas Turbine/Solid Oxide Fuel Cell Hybrids for Aircraft Propulsion and Power. *Journal of Propulsion and Power*, 37(3):349–361, mar 2021.

[30] Mohammad Ali Azizi and Jacob Brouwer. Progress in solid oxide fuel cell-gas turbine hybrid power systems: System design and analysis, transient operation, controls and optimization. *Applied Energy*, 215(August 2017):237–289, apr 2018.

[31] Daniel Francis Waters. *Modeling of Gas Turbine - Solid Oxide Fuel Cell Systems for Combined Propulsion and Power on Aircraft*. PhD thesis, Ph.D. Dissertation, Department of Aerospace Engineering, University of Maryland, 2015.

[32] Ji Hye Yi, Joo Hwan Choi, and Tong Seop Kim. Comparative evaluation of viable options for combining a gas turbine and a solid oxide fuel cell for high performance. *Applied Thermal Engineering*, 100:840–848, 2016.

[33] Timo Lingstädt, Felix Grimm, Aurelia Drude, Peter Kutne, and Manfred Aigner. Numerical Investigation of a Jet-Stabilized Combustion System Operated with Low-Calorific SOFC Off-Gas. In *AIAA Scitech 2019 Forum*, number January, pages 1–18, Reston, Virginia, jan 2019. American Institute of Aeronautics and Astronautics.

[34] Timo Lingstädt, Felix Grimm, Thomas Krummrein, Peter Kutne, and Manfred Aigner. Atmospheric Experimental Investigations of a Jet-Stabilized SOFC Off-Gas Combustor for a Hybrid Power Plant operated with Biogas. In *AIAA Scitech 2019 Forum*, number January, pages 1–18, Reston, Virginia, jan 2019. American Institute of Aeronautics and Astronautics.

[35] Stephan Eelman, Isabel del Pozo y de Poza, and Tobias Krieg. Fuel Cell APU's in Commercial Aircraft – an Assessment of SOFC and PEMFC Concepts. In *24th International Congress of the Aeronautical Sciences*, pages 1–10, 2004.

[36] Karen Swider-Lyons, Richard Stroman, Gregory Page, Michael Schuette, Joseph Mackrell, and Joseph Rodgers. Hydrogen Fule Cell Propulsion for Long Endurance Small UVAs. In *AIAA Centennial of Naval Aviation Forum "100 Years of Achievement and Progress"*, number October 2009, pages 1–9, Reston, Virigina, sep 2011. American Institute of Aeronautics and Astronautics.

[37] Lockheed Martin. Stalker XE UAS, 2018.

[38] Kaushik Rajashekara, James Grieve, and David Daggett. Solid Oxide Fuel Cell/Gas Turbine Hybrid APU System for Aerospace Applications. In *Conference Record of the 2006 IEEE Industry Applications Conference Forty-First IAS Annual Meeting*, volume 5, pages 2185–2192. IEEE, oct 2006.

[39] Kaushik Rajashekara, James Grieve, and David Dagget. Hybrid Fuel Cell Power in Aircraft. *IEEE Industry Applications Magazine*, 14:54–60, 2008.

[40] M.D. Fernandes, S.T. de P. Andrade, V.N. Bistritzki, R.M. Fonseca, L.G. Zacarias, H.N.C. Gonçalves, A.F. de Castro, R.Z. Domingues, and T Matencio. SOFC-APU systems for aircraft: A review. *International Journal of Hydrogen Energy*, 43(33):16311–16333, aug 2018.

[41] Tina Stoia, Chellappa Balan, Shailesh Atreya, and Patrick O'Neil. Solid Oxide Fuel Cell - Steam Reformation Power System Configuration Options for an All-Electric Commuter Airplane Flight Demonstrator. In *2018 Aviation Technology, Integration, and Operations Conference*, pages 1–8, Reston, Virginia, jun 2018. American Institute of Aeronautics and Astronautics.

[42] Junye Wang. System integration, durability and reliability of fuel cells: Challenges and solutions. *Applied Energy*, 189:460–479, 2017.

[43] Keiichi Okai, Takehiro Himeno, Toshinori Watanabe, Hiroshi Nomura, and Takeshi Tagashira. Investigation of FC/GT Hybrid Core in Electrical Propulsion for Fan Aircraft. In *51st AIAA/SAE/ASEE Joint Propulsion Conference*, pages 1–2, Reston, Virginia, jul 2015. American Institute of Aeronautics and Astronautics.

[44] Keiichi Okai, Takehiro Himeno, Toshinori Watanabe, Hiroshi Nomura, Takeshi Tagashira, and Akira Nishizawa. Potential of Aircraft Electric Propulsion with SOFC/GT Hybrid Core. In *52nd AIAA/SAE/ASEE Joint Propulsion Conference*, pages 1–14, Reston, Virginia, jul 2016. American Institute of Aeronautics and Astronautics.

[45] Keiichi Okai, Hiroshi Nomura, Takeshi Tagashira, and Akira Nishizawa. Effects of Fuel Type on Aircraft Electric Propulsion with SOFC/GT Hybrid Core. In *53rd AIAA/SAE/ASEE Joint Propulsion Conference*, number July, pages 1–13, Reston, Virginia, jul 2017. American Institute of Aeronautics and Astronautics.

[46] Shinichi Hashimoto, Tomohisa Hirota, Kenji Suzuki, Tomoaki Namioka, Hibiki Ito, Ryuichi Miyata, Keiko Kobayashi, Keiji Yashiro, Hitoshi Takamura, Tatsuya Kawada, Kyosuke Yoshimi, Norito Kijima, Takaaki Manabe, Tetsuo Tsuchiya, Takayuki Kojima, and Keiichi Okai. Material Development Strategy of Lightweight Solid Oxide Fuel Cells for Airplane System Electrification. *ECS Transactions*, 91(1):311–318, 2019.

[47] Shin-ichi Hashimoto, Ryuichi Miyata, Keiko Kobayashi, Keiji Yashiro, Hitoshi Takamura, Kyosuke Yoshimi, Norito Kijima, Takaaki Manabe, Tetsuo Tsuchiya, Tomohisa Hirota, Kenji Suzuki, Tomoaki Namioka, Hibiki Ito, Takayuki Kojima, and Keiichi Okai. A New Development Strategy of Light Wight Solid Oxide Fuel Cells for Electrified Airplane System. In *AIAA Propulsion and Energy 2019 Forum*, volume 08, pages 1–7, Reston, Virginia, aug 2019. American Institute of Aeronautics and Astronautics.

[48] Hai Wang, Rui Xu, Kun Wang, Craig T. Bowman, Ronald K. Hanson, David F. Davidson, Kenneth Brezinsky, and Fokion N. Egolfopoulos. A physics-based approach to modeling real-fuel combustion chemistry - I. Evidence from experiments, and thermodynamic, chemical kinetic and statistical considerations. *Combustion and Flame*, 193:502–519, jul 2018.

[49] Zhixing Ji, Jiang Qin, Kunlin Cheng, Chaolei Dang, Silong Zhang, and Peng Dong. Thermodynamic performance evaluation of a turbine-less jet engine integrated with solid oxide fuel cells for unmanned aerial vehicles. *Applied Thermal Engineering*, 160(92):114093, 2019.

[50] Alfonso F. Ibarreta and Chih Jen Sung. Optimization of Jet-A fuel reforming for aerospace applications. *International Journal of Hydrogen Energy*, 31(8):1066–1078, 2006.

[51] R. J. Braun, M. Gummalla, and J. Yamanis. System Architectures for Solid Oxide Fuel Cell-Based Auxiliary Power Units in Future Commercial Aircraft Applications. *Journal of Fuel Cell Science and Technology*, 6(3):031015, aug 2009.

[52] G. A. Whyatt and L. A. Chick. Electrical Generation for More-Electric Aircraft using Solid Oxide Fuel Cells. (April):110, 2012.

[53] Ji Hye Yi and Tong Seop Kim. Effects of fuel utilization on performance of SOFC/gas turbine combined power generation systems. *Journal of Mechanical Science and Technology*, 31(6):3091–3100, jun 2017.

[54] Brandon L. Litherland, Nicholas K. Borer, and Steven Geuther. A Study on the Use of Solid-Oxide Fuel Cells for Increased Power Generation on Small Aircraft. In *AIAA Aviation 2019 Forum*, number June, pages 1–17, Reston, Virginia, jun 2019. American Institute of Aeronautics and Astronautics.

[55] Lucas M. Pratt and Christopher P. Cadou. Possible Effects of Turbine/Fuel Cell Integration on Combustor Operation. In *AIAA Propulsion and Energy 2020 Forum*, pages 1–13, Reston, Virginia, aug 2020. American Institute of Aeronautics and Astronautics.

[56] Mallika Gummalla, Arun Pandy, Robert Braun, Thierry Carriere, Jean Yamanis, Thomas Vanderspurt, Larry Hardin, and Rick Welch. Fuel Cell Airframe Integration Study for Short-Range Aircraft Volume 1 : Aircraft Propulsion and Subsystems Integration Evaluation. Technical Report September, 2006.

[57] Joshua E. Freeh, Joseph W. Pratt, and Jacob Brouwer. Development of a Solid-Oxide Fuel Cell/Gas Turbine Hybrid System Model for Aerospace Applications. In *Volume 7: Turbo Expo 2004*, number May 2004, pages 371–379. ASMEDC, jan 2004.

[58] Joshua E. Freeh, Christopher J. Steffen, and Louis M. Larosiliere. Off-Design Performance Analysis of a Solid-Oxide Fuel Cell/Gas Turbine Hybrid for Auxiliary Aerospace Power. In *3rd International Conference on Fuel Cell Science, Engineering and Technology*, volume 2005, pages 265–272. ASMEDC, jan 2005.

[59] Christopher J. Steffen, Joshua E. Freeh, and Louis M. Larosiliere. Solid Oxide Fuel Cell/Gas Turbine Hybrid Cycle Technology for Auxiliary Aerospace Power. In *Volume 5: Turbo Expo 2005*, number May 2005, pages 253–260. ASME, jan 2005.

[60] Robert Tornabene, Xiao-Yen Wang, Christopher J. Steffen, and Joshua E. Freeh. Development of Parametric Mass and Volume Models for an Aerospace SOFC/Gas Turbine Hybrid System. In *Volume 5: Turbo Expo 2005*, volume M, pages 135–144. ASMEDC, jan 2005.

[61] Jürgen Dollmayer, Nicola Bundschuh, and Udo B. Carl. Fuel mass penalty due to generators and fuel cells as energy source of the all-electric aircraft{star, open}{star, open}This article was presented at the German Aerospace Congress 2005.{star, open}{star, open}{star, open}{star, open}The article was publis. *Aerospace Science and Technology*, 10(8):686–694, 2006.

[62] Ananda Himansu, Joshua E. Freeh, Christopher J. Steffen, Robert T. Tornabene, and Xiao-Yen J. Wang. Hybrid Solid Oxide Fuel Cell/Gas Turbine System for High Altitude Long Endurance Aerospace Missions. In *ASME 2006 Fourth International Conference on Fuel Cell Science, Engineering and Technology, Parts A and B*, volume NASA TM-20, pages 573–583. ASMEDC, jan 2006.

[63] P. Aguiar, D. J.L. Brett, and N. P. Brandon. Solid oxide fuel cell/gas turbine hybrid system analysis for high-altitude long-endurance unmanned aerial vehicles. *International Journal of Hydrogen Energy*, 33(23):7214–7223, 2008.

[64] Daniel F. Waters and Christopher P. Cadou. Engine-integrated solid oxide fuel cells for efficient electrical power generation on aircraft. *Journal of Power Sources*, 284:588–605, jun 2015.

[65] Marty K Bradley and Christopher K Droney. Subsonic Ultra Green Aircraft Research : Phase I Final Report. Technical Report NASA CR-2011-216847, NASA CR-2011-216847, 2011.

[66] Esteban A. Valencia, Victor Hidalgo, Laskaridis Panagiotis, Devaiah Nalianda, Riti Singh, and Chengyuan Liu. Design Point Analysis of an Hybrid Fuel Cell Gas Turbine Cycle for Advanced Distributed Propulsion Systems. In *51st AIAA/SAE/ASEE Joint Propulsion Conference*, Reston, Virginia, jul 2015. American Institute of Aeronautics and Astronautics.

[67] M. Hanasaki, C. Uryu, T. Daio, T. Kawabata, Y. Tachikawa, S. M. Lyth, Y. Shiratori, S. Taniguchi, and K. Sasaki. SOFC Durability against Standby and Shutdown Cycling. *Journal of The Electrochemical Society*, 161(9):F850–F860, jun 2014.

[68] Eric D. Wachsman and Kang Taek Lee. Lowering the temperature of solid oxide fuel cells. *Science*, 334(6058):935–939, 2011.

[69] Penyarat Chinda and Pascal Brault. The hybrid solid oxide fuel cell (SOFC) and gas turbine (GT) systems steady state modeling. *International Journal of Hydrogen Energy*, 37(11):9237–9248, 2012.

[70] Brian Tarroja, Fabian Mueller, Jim Maclay, and Jacob Brouwer. Parametric thermodynamic analysis of a solid oxide fuel cell gas turbine system design space. *Journal of Engineering for Gas Turbines and Power*, 132(7):1–11, 2010.

[71] Jack D. Mattingly. *Elements of Propulsion: Gas Turbines and Rockets.* American Institute of Aeronautics and Astronautics, Reston ,VA, jan 2006.

[72] Robert J. Kee, Huayang Zhu, and David G. Goodwin. Solid-oxide fuel cells with hydrocarbon fuels. *Proceedings of the Combustion Institute*, 30(2):2379–2404, jan 2005.

[73] Dang Saebea, Suthida Authayanun, Yaneeporn Patcharavorachot, and Amornchai Arpornwichanop. Effect of anode-cathode exhaust gas recirculation on energy recuperation in a solid oxide fuel cell-gas turbine hybrid power system. *Energy*, 94:218–232, 2016.

[74] Philip Graham Hill and Carl R. Peterson. *Mechanics and Thermodynamics of Propulsion.* Addison-Wesley, Reading, MA, 2nd edition, 1992.

[75] Daniel Raymer. *Aircraft Design: A Conceptual Approach.* American Institute of Aeronautics and Astronautics, Inc., Washington, DC, 2nd edition, aug 2012.

[76] Annamaria Buonomano, Francesco Calise, Massimo Dentice D'Accadia, Adolfo Palombo, and Maria Vicidomini. Hybrid solid oxide fuel cells-gas turbine systems for combined heat and power: A review. *Applied Energy*, 156:32–85, 2015.

[77] Colin F. McDonald, Aristide F. Massardo, Colin Rodgers, and Aubrey Stone. Recuperated gas turbine aeroengines, Part I: early development activities. *Aircraft Engineering and Aerospace Technology*, 80(2):139–157, mar 2008.

[78] Colin F. McDonald, Aristide F. Massardo, Colin Rodgers, and Aubrey Stone. Recuperated gas turbine aeroengines. Part III: engine concepts for reduced emissions, lower fuel consumption, and noise abatement. *Aircraft Engineering and Aerospace Technology*, 80(4):408–426, jul 2008.

[79] Colin F. McDonald, Aristide F. Massardo, Colin Rodgers, and Aubrey Stone. Recuperated gas turbine aeroengines, part II: engine design studies following early development testing. *Aircraft Engineering and Aerospace Technology*, 80(3):280–294, may 2008.

[80] Scott M Jones. An introduction to thermodynamic performance analysis of aircraft gas turbine engine cycles using the numerical propulsion system simulation code. Technical Report NASA TM-2007-214690, NASA Glenn Research Center, 2007.

[81] Michael L Belair, Charles J Sarmiento, Thomas M Lavelle, and Nasa Glenn. Nuclear Thermal Rocket Simulation in NPSS. pages 1–15, 2018.

[82] Sanford Gordon and Bonnie J. McBride. Computer Program for Calculation of Complex Chemical Equilibrium Compositions and Applications. Technical report, 1994.

[83] Carl C. Ciepluch, Donald Y. Davis, and David E. Gray. Results of NASA's Energy Efficient Engine Program. *Journal of Propulsion and Power*, 3(6):560–568, nov 1987.

[84] Ralph Jansen, Yaritza De Jesus-Arce, Peter Kascak, Rodger W. Dyson, Andrew Woodworth, Justin J. Scheidler, Ryan Edwards, Erik J. Stalcup, Jarred Wilhite, Kirsten P. Duffy, Paul Passe, and Sean McCormick. High Efficiency Megawatt Motor Conceptual Design. In *2018 Joint Propulsion Conference*, pages 1–9, Reston, Virginia, jul 2018. American Institute of Aeronautics and Astronautics.

[85] Ralph Jansen, Peter E. Kascak, Rodger W. Dyson, Andrew Woodworth, Justin J. Scheidler, Andrew Smith, Erik J. Stalcup, Thomas Tallerico, Yaritza De Jesus-Arce, David Avanesian, Kirsten P. Duffy, Paul Passe, and Gerald M. Szpak. High Efficiency Megawatt Motor Preliminary Design. In *AIAA Propulsion and Energy 2019 Forum*, Reston, Virginia, aug 2019. American Institute of Aeronautics and Astronautics.

[86] David Kenneth Hall, Edward M Greitzer, Aidan Patrick Dowdle, Jonas J Gonzalez, Warren W Hoburg, M. Ilic, Jeffrey H Lang, J S Sabnis, Zoltán S Spakovszky, Brian Yutko, Christopher Courtin, William Thalheimer, Lauren Trollinger, J Tylko, N Varney, Alejandra Uranga, Saakar Byahut, and Michael Kruger. Feasibility of Electrified Propulsion for Ultra-Efficient Commercial Aircraft, Final Report. Technical Report December 2019, NASA CR—2019-220382, 2018.

[87] W M (William Morrow) Kays and A L (Alexander Louis) London. *Compact Heat Exchangers*. McGraw-Hill, New York SE - xv, 335 pages : illustrations ; 24 cm, 3rd ed. edition, 1984.

[88] Jaroslaw Milewski and Andrzej Miller. Influences of The Type and Thickness of Electrolyte on Solid Oxide Fuel Cell Hybrid System Performance. *Journal of Fuel Cell Science and Technology*, 3(4):396–402, nov 2006.

[89] Robert J. Kee, Huayang Zhu, A. Mary Sukeshini, and Gregory S. Jackson. Solid Oxide Fuel Cells: Operating Principles, Current Challenges, and the Role of Syngas. *Combustion Science and Technology*, 180(6):1207–1244, may 2008.

[90] Huayang Zhu, Robert Kee, and Gregory Jackson. Solid Oxide Fuel Cells Using Syngas. In *Synthesis Gas Combustion*, chapter 11, pages 329–374. CRC Press, Boca Raton, 1st edition, sep 2009.

[91] Huayang Zhu, Robert J. Kee, Vinod M. Janardhanan, Olaf Deutschmann, and David G. Goodwin. Modeling Elementary Heterogeneous Chemistry and Electrochemistry in Solid-Oxide Fuel Cells. *Journal of The Electrochemical Society*, 152(12):A2427, 2005.

[92] Huayang Zhu and Robert J. Kee. The influence of current collection on the performance of tubular anode-supported SOFC cells. *Journal of Power Sources*, 169(2):315–326, jun 2007.

[93] Huayang Zhu and Robert J. Kee. A general mathematical model for analyzing the performance of fuel-cell membrane-electrode assemblies. *Journal of Power Sources*, 117(1-2):61–74, may 2003.

[94] Huayang Zhu and Robert J. Kee. Thermodynamics of SOFC efficiency and fuel utilization as functions of fuel mixtures and operating conditions. *Journal of Power Sources*, 161(2):957–964, oct 2006.

[95] Huayang Zhu and Robert J. Kee. Modeling Distributed Charge-Transfer Processes in SOFC Membrane Electrode Assemblies. *Journal of The Electrochemical Society*, 155(7):B715, 2008.

[96] Mason E. A. and A P Malinauskas. *Gas transport in porous media : the dusty-gas model / E.A. Mason and A.P. Malinauskas.* Elsevier Scientific Pub. Co Amsterdam ; New York, 1983.

[97] Clifford K. Ho and Stephen W. Webb, editors. *Gas Transport in Porous Media*, volume 20 of *Theory and Applications of Transport in Porous Media*. Springer Netherlands, Berlin, Heidelberg, 2006.

[98] Yeqing Fu and M Z Bazant. Theoretical and Experimental Study of Solid Oxide Fuel Cell (SOFC) Using Impedance Spectra. *Chemical Engineering*, Doctor of(2006):107, 2014.

[99] Yeqing Fu, Yi Jiang, Sophie Poizeau, Abhijit Dutta, Aravind Mohanram, John D. Pietras, and Martin Z. Bazant. Multicomponent Gas Diffusion in Porous Electrodes. *Journal of The Electrochemical Society*, 162(6):F613–F621, 2015.

[100] A. Bertei and C. Nicolella. Common inconsistencies in modeling gas transport in porous electrodes: The dusty-gas model and the Fick law. *Journal of Power Sources*, 279:133–137, apr 2015.

[101] E Onat and G W Klees. A method to estimate weight and dimensions of large and small gas turbine engines. Technical Report NASA CR-159481, NASA, 1979.

[102] Gabriel D. Roy. Novel Approaches to Control Emissions from Marine Diesel and Gas Turbine Engines. *Journal of Propulsion and Power*, 22(5):1068–1074, sep 2006.

[103] Ralph H Jansen, Kirsten P Duffy, and Gerald V Brown. Partially Turboelectric Aircraft Drive Key Performance Parameters. 2017.

[104] Keiichi Okai, Takehiro Himeno, Toshinori Watanabe, Hiroshi Nomura, and Takeshi Tagashira. Investigation of FC/GT hybrid core in electrical propulsion for fan aircraft. *51st AIAA/SAE/ASEE Joint Propulsion Conference*, pages 1–2, 2015.

[105] Shailesh Atreya, Marianne Mata, Russ Jones, and Lisa Kohout. Power System Comparisons for a High Altitude Long Endurance (HALE) Remotely Operated Aircraft (ROA). In *AIAA 5th ATIO and16th Lighter-Than-Air Sys Tech. and Balloon Systems Conferences*, number September 2005, pages 1–13, Reston, Virigina, sep 2005. American Institute of Aeronautics and Astronautics.

[106] Range Extenders for Electric Aviation With Low Carbon and High Efficiency (REEACH) — Initial Announcement, 2019.

[107] Peter G Batterton. Energy Efficient Engine Program Contributions to Aircraft Fuel Conservation. Technical report, NASA, 1984.

[108] J. Hartvigsen. Development of an SOFC Stack Performance Map for Natural Gas Operation. *ECS Proceedings Volumes*, 1999-19(1):1135–1141, jan 1999.

[109] Li Zhang, Yaohua Xing, Hong Xu, Hongtao Wang, Jie Zhong, and Jin Xuan. Comparative study of solid oxide fuel cell combined heat and power system with Multi-Stage Exhaust Chemical Energy Recycling: Modeling, experiment and optimization. *Energy Conversion and Management*, 139:79–88, may 2017.

[110] Roland Peters, Robert Deja, Maximilian Engelbracht, Matthias Frank, Van Nhu Nguyen, Ludger Blum, and Detlef Stolten. Efficiency analysis of a hydrogen-fueled solid oxide fuel cell system with anode off-gas recirculation. *Journal of Power Sources*, 328:105–113, oct 2016.

[111] Hsin-Yi Shih. Computed extinction limits and flame structures of H2/O2 counterflow diffusion flames with CO2 dilution. *International Journal of Hydrogen Energy*, 34(9):4005–4013, may 2009.

[112] J. Natarajan, T. Lieuwen, and J. Seitzman. Laminar flame speeds of H2/CO mixtures: Effect of CO2 dilution, preheat temperature, and pressure. *Combustion and Flame*, 151(1-2):104–119, oct 2007.

[113] Michael P. Burke, Frederick L. Dryer, and Yiguang Ju. Assessment of kinetic modeling for lean H2/CH4/O2/diluent flames at high pressures. *Proceedings of the Combustion Institute*, 33(1):905–912, 2011.

[114] Jinhua Wang, Zuohua Huang, Hideaki Kobayashi, and Yasuhiro Ogami. Laminar burning velocities and flame characteristics of CO-H 2-CO2-O2 mixtures. *International Journal of Hydrogen Energy*, 37(24):19158–19167, 2012.

[115] Robin John Varghese, Harshal Kolekar, Vishnu Hariharan, and Sudarshan Kumar. Effect of CO content on laminar burning velocities of syngas-air premixed flames at elevated temperatures. *Fuel*, 214(May 2017):144–153, 2018.

[116] Deepti Singh, Takayuki Nishiie, Saad Tanvir, and Li Qiao. An experimental and kinetic study of syngas/air combustion at elevated temperatures and the effect of water addition. *Fuel*, 94:448–456, apr 2012.

[117] Yang Zhang, Wenfeng Shen, Hai Zhang, Yuxin Wu, and Junfu Lu. Effects of inert dilution on the propagation and extinction of lean premixed syngas/air flames. *Fuel*, 157:115–121, oct 2015.

[118] Francesco Cipriani. Numerical Analysis of Use of Syngas for Combustion Systems and in Solid Oxide Fuel Cells. (October 2011), 2013.

[119] Kian Eisazadeh Far, Farzan Parsinejad, and Hameed Metghalchi. Flame structure and laminar burning speeds of JP-8/air premixed mixtures at high temperatures and pressures. *Fuel*, 89(5):1041–1049, may 2010.

[120] Philippe Dagaut and Michel Cathonnet. The ignition, oxidation, and combustion of kerosene: A review of experimental and kinetic modeling. *Progress in Energy and Combustion Science*, 32(1):48–92, 2006.

[121] Rui Xu, Kun Wang, Sayak Banerjee, Jiankun Shao, Tom Parise, Yangye Zhu, Shengkai Wang, Ashkan Movaghar, Dong Joon Lee, Runhua Zhao, Xu Han, Yang Gao, Tianfeng Lu, Kenneth Brezinsky, Fokion N. Egolfopoulos, David F. Davidson, Ronald K. Hanson, Craig T. Bowman, and Hai Wang. A physics-based approach to modeling real-fuel combustion chemistry – II. Reaction kinetic models of jet and rocket fuels. *Combustion and Flame*, 193:520–537, 2018.

[122] Arthur H Lefebvre and Dilip R Ballal. *Gas Turbine Combustion*. CRC Press, 3rd edition, apr 2010.

[123] David G. Goodwin, Raymond L. Speth, Harry K. Moffat, and Bryan W. Weber. Cantera: An Object-oriented Software Toolkit for Chemical Kinetics, Thermodynamics, and Transport Processes, 2021.

[124] Gregory P. Smith, Y. Tao, and Hai Wang. Foundational Fuel Chemistry Model Version 1.0 (FFCM-1), 2016.

[125] Hejie Li, Ahmed ElKady, and Andrei Evulet. Effect of Exhaust Gas Recirculation on NOx Formation in Premixed Combustion System. In *47th AIAA Aerospace Sciences Meeting including The New Horizons Forum and Aerospace Exposition*, number January, pages 1–13, Reston, Virigina, jan 2009. American Institute of Aeronautics and Astronautics.

[126] Thomas Fiala and Thomas Sattelmayer. Nonpremixed Counterflow Flames: Scaling Rules for Batch Simulations. *Journal of Combustion*, 2014:1–7, 2014.

[127] Anna Evans, Anja Bieberle-Hütter, Jennifer L.M. Rupp, and Ludwig J. Gauckler. Review on microfabricated micro-solid oxide fuel cell membranes. *Journal of Power Sources*, 194(1):119–129, 2009.